Technical University of Denmark

Roll-to-Roll Fabricated Polymer Solar Cells: Towards Low Environmental Impact and Reporting Consensus

Trofod, Thue; Krebs, Frederik C

Publication date:
2013

Document Version
Publisher's PDF, also known as Version of record

Link back to DTU Orbit

Citation (APA):
Larsen-Olsen, T. T., & Krebs, F. C. (2013). Roll-to-Roll Fabricated Polymer Solar Cells: Towards Low Environmental Impact and Reporting Consensus. Department of Energy Conversion and Storage, Technical University of Denmark.

Roll-to-Roll Fabricated Polymer Solar Cells

Towards Low Environmental Impact and Reporting Consensus

Ph.D Thesis

Thue Trofod Larsen-Olsen

October 2013

Preface

This Ph.D. Thesis presents the main results obtained during my 3-year Ph.D.-project at the Technical University of Denmark (DTU), from October 1 2010 to September 30 2013. The vast majority of the work was carried out at the Solar Energy/Functional Organic Materials section in the Department of Energy Conversion and Storage, located at Risø in Denmark. My work was funded by the Danish National Research Foundation (Grant no. 51011130028), as part of the Danish-Chinese Center for Organic-based photovoltaic cells with morphology control. The work was thus carried out in close collaboration with scientists in China, both at the Zhejiang University (ZJU) in Hangzhou, and at the Institute of Chemestry at the Chines Academy of Sciences (ICCAS) in Beijing, as well as AAU in Aalborg. I was also fortunate enough to visit our Chinese collaborators on several occasions. Most notably I did a 3 months external study based at ZJU, but which included the visit to more than 15 laboratories around China, a very rewarding experience which served to broaden my cultural understanding, both scientifically and personal.

During my Ph.D., I have contributed to 19 peer-review publications, of which I have only include 9 in this thesis. These 9 included papers are the ones which have taken up the most of my time, and which, to my opinion, best defines my Ph.D. project.

Acknowledgements

First of all I wish to thank my supervisor Prof. Frederik C. Krebs for entrusting this Ph.D. project to me, and for his inspiring enthusiasm and guidance throughout. I also wish to thank my colleagues in the Danish-Chinese centre for making this a strong team effort. A special thanks to my fellow Ph.D. students for being great colleagues, not least Arvid Böttiger, Birgitta Andreasen and Thomas Rieks Andersen for all our many collaborations and some good times in China. Another thanks should go to the R2R coating team; Mikkel Jørgensen, Roar Søndergaard and Markus Hösel, for an endless supply of solar cells. I also thank the rest of the people at FOM/SOL for creating a pleasant working environment.

I also wish to thank my collaborators in China for their invaluable help and hospitality during my stay in China, especially Prof. Hongzhen Chen and Zhuowei Gu at ZJU and Prof. Xiaowei Zhan and Yao Liu at ICCAS.

Birgit Oksbjerg is thanked for proof reading.

I also would like to thank my family and friends for support and understanding during the long periods of radio silence.

Finally, I owe a special thank you to my girlfriend Line Mundt. You have been there for my all the way through, not least when going with me to China and lending me your invaluable expertise and companionship. For that I am grateful.

Abstract

The sun is by far the largest source of renewable energy available; consequently solar cells, which are able to convert light into electricity, have the technical potential to cover the global energy needs. Polymer solar cells (PSCs) on flexible plastic substrate have a low embodied energy and can be processed by fast roll-to-roll (R2R) methods, using earth abundant materials, and thus deliver the prospects to fulfil this potential.

A strong polarization in PSC research efforts have led to diverging and non-comparable results: While very high power conversion efficiencies (PCEs) above 10% have been demonstrated for small area devices prepared by batch processing, the demonstration of PSCs fabricated in large quantities using high thoughput R2R fabrication of large are solar cells have presented much lower PCEs.

This thesis primarily focuses on lowering the cost and environmental impact of polymer solar cell mass fabrication, by the substitution of toxic solvents for water, and eliminating the use of rare earth indium which accounts for 90 % of the embodied energy in state-of-the-art R2R fabricated devices based on ITO. Secondly, a scheme to potentially raise the efficiency of PSCs is explored, through R2R processing of tandem PSCs. A final focus area of the thesis is the investigation into the extrinsic variability in standard J-V characterizations done on PSCs, and towards ways to minimize it.

Organic solvents are predominant process solvents used for fabricating the active layer of a PSC. In this thesis, aqueous dispersions of polymer:PCBM blend nanoparticles are fabricated by the miniemulsion method, and utilized as active layer inks in both small area devices and fully R2R processed large area polymer solar cells.

An aqueous dispersion of P3HT:PCBM blend nanoparticles is also employed in conjunction with PEDOT:PSS in R2R double slot-die coating, a process that demonstrates the simultaneous formation of a P3HT:PCBM/PEDOT:PSS bilayer on a substrate comprising PET/ITO/ZnO. Devices are subsequently completed with a metal electrode demonstrating working solar cells.

A third way of utilizing the aqueous nanoparticle inks is demonstrated in fully R2R processed polymer tandem solar cells, in which the second junction is coated from the nanoparticle dispersion. The use of water as an orthogonal solvent is shown to be necessary when upscaling the process from small glass-based devices to large area devices based on flexible PET.

Also described in this thesis, is the development of an all-solution processed alternative to ITO as transparent conductor in PSCs. In its simples form the electrode consist of high conductive

PEDOT:PSS R2R coated on a PET substrate. To enable functional devices, the completed solar cells are exposed to a short burst of high voltage in a R2R post process. The working mechanism of the ‘switching’ is found to be an in-situ formation of a charge-selective interface layer.

To enable scalability the PEDOT:PSS is combined with several types of silver grids and utilized in large area PSCs. The use of a flexographically (flexo) printed grid is shown to be superior to both embedded grids and ink jet printed grid, especially in terms of processing speed.

The scalability of the PEDOT:PSS/flexo grid electrode, the flextrode, is tested, and shown to be superior to ITO in terms of both performance and processing, demonstrating >1% efficiency on the total module area and a >50% fill-factor on a >100 cm^2 module, while also demonstrating a significant reduction in materials cost and processing time.

Finally the thesis includes two examples of round robin studies, one conducted in Europe and a second one across China. These studies investigate the extrinsic variations in PCE values obtained under standardized test conditions. The first study demonstrate how the round robin method can be used to evaluated and obtain consensus values on the PCEs of high efficiency devices. The second round robin included 15 laboratories in China. The inter-laboratory variations led to an overall relative standard deviation in PCE of 12%, primarily owing from variations in the current.

Resumé

Solen udgør langt den største fornybare energikilde vi har, og solceller som kan konvertere lys om til elektricitet, har derfor potentialet til at levere energi nok til at dække hele verdens behov. Polymersolceller trykt på fleksible plast-substrater har en lav indlejret energi og kan fabrikeres via hurtige rulle-til-rulle(R2R)-metoder, udelukkende ved brug af materialer med rigelig tilgængelighed. Dette gør at polymersolceller leverer muligheden for indfrielse of solcellens potentiale.

En stærk polarisering inden for PSC forskningsindsatsen har ført til divergerende og ikke-sammenlignelige resultater: Mens meget høje konverterings effektiviteter (PCEer) på over 10% er blevet påvist for meget små polymersolceller fabrikeret i batch processor, så har den sideløbende demonstration af polymersolceller fremstillet ved egentlig masseproduktion via R2R præsteret meget lavere PCEer .

Denne afhandling fokuserer primært på metoder til at sænke omkostninger og de miljømæssige konsekvenser forbundet massefabrikation af polymersolceller: Dette gøres ved substitution af giftige opløsningsmidler til fordel for vand, samt ved elimineringen af brugen af den sjældne jordart indium som tegner sig for godt 90% af den indeholdte energi i state-of-the-art R2R fabrikerede polymersolceller baseret på ITO . Derudover udforskes en metode til potentiel at hæve effektiviteten af polymersolceller; gennem R2R fabrikation af tandem polymersolceller. Et sidste fokusområde i afhandlingen er undersøgelsen den ydre variabilitet i en standard J-V karakterisering af polymersolceller, samt måder hvorpå denne kan minimeres.

Organiske opløsningsmidler er den mest brugte type opløsningsmidler, ved fremstilling af det aktive lag i en PSC. Som en del af denne afhandling, fremstilles vandige dispersioner af polymer:PCBM blandings-nanopartikler, ved brug af miniemulsion metoden. Disse udnyttes efterfølgende til udformningen af de aktive lag i både små polymersolceller og fuldt-ud R2R fabrikerede store polymersolceller .

En vandig dispersion af P3HT:PCBM blandings-nanopartikler anvendes ligeledes i forbindelse med PEDOT:PSS i R2R dobbelt slot-die coating, en proces der demonstrerer simultan dannelse af et P3HT:PCBM/PEDOT:PSS dobbeltlag oven på et substrat omfattende PET/ITO/ZnO. Ved efterfølgende påførsel af en metalelektrode, demonstrere virkende solceller.

En tredje måde at udnytte de vandige nanopartikel- dispersion demonstreres ved fuldt-ud R2R fabrikeret polymer tandem solceller, hvori den bagerste junction er trykt fra nanopartikel-dispersion. Brugen af vand som et ortogonalt opløsningsmiddel viser sig nemlig at være nødvendigt, når opskaleringsprocessen fra små glas -baserede solceller til stor- areal-solceller baseret på fleksibelt PET.

Udviklingen af et trykkebart alternativ til ITO som den gennemsigtige elektrode i polymersolceller, er også beskrevet i denne afhandling. I sine simpleste form består elektroden af højtledende PEDOT:PSS som er R2R coatet på et PET-substrat. For at opnå funktionelle solceller, skal de færdige solceller først udsættes for en kort puls af høj spænding, hvilket bliver vist integreret i en R2R proces. Dem underlæggende mekanisme for dette ’skift’ bliver anslået til at være en ’in-situ’ dannelse af en ladnings-selektivt grænseflade.

For at opnå skalerbarhed bliver PEDOT:PSS elektroden kombineret med flere typer af sølv gitre, og testes ved anvendt i stor-areal polymersolceller. Det fleksografisk (flexo) trykt gitter vises at være bedre end både det indlejrede gitter og det inkjet-trykte gitter, især med hensyn til fabrikationshastighed.

Samtidig demonstreres skalerbarheden af den førnævnte PEDOT:PSS/flexo elektrode, kaldet flextroden, og denne viser sig at være væsentlig bedre end en tilsvarende ITO-elektrode i ydeevne.

Endelig indeholder afhandlingen to eksempler på såkaldte round robin studier, den første i Europa og den anden i Kina. Begge studier undersøger variationer i PCE-værdier opnået under standardiserede testbetingelser . Den første undersøgelse viser, hvordan round robin metode kan bruges til at evaluere og fastlægge konsensus PCE-værdier for højeffektive polymersolceller.Den anden round robin omfattede 15 laboratorier i Kina. De observerede variationer førte til en samlet relativ standardafvigelse i PCE på 12 %, primært som følge af variationer i strømmen.

Contents

List of Abbreviations

BHJ	Bulk hetero junction
CB	Chlorobenzene
CF	Chloroform
D/A	Donor/acceptor
DCB	*Ortho*-dichlorobenzene
DSD	Double slot-die (coating technique)
e-h	electron-hole (pair)
EJ	Exajoule = 10^{18} J
E_g	Semiconductor band gap (e.g. HOMO-LUMO energy difference)
EQE	External quantum efficiency (equivalent to IPCE)
ETL	Electron transport layer/Hole blocking layer
Flexo	Flexographic printing
HOMO	Highest occupied molecular orbital
HTL	Hole transport layer/Electron blocking layer
IPCE	Incident Photon to Current Efficiency (equivalent to EQE)
ITO	Indium tin oxide
LiF	Lithium fluoride
LUMO	Lowest unoccupied molecular orbital
NP	Nano particle
OPV	Organic photovoltaics

PSC	Polymer solar cells
P3HT	Poly(3-hexylthiophene)
P5010	PEDOT:PSS, Orgacon EL-P 5010 from Agfa
PCBM, PC[60]BM	[6,6]-Phenyl-C61-butyric acid methyl ester
PC[70]BM	[6,6]-Phenyl-C71-butyric acid methyl ester
PCE	Power conversion efficiency
PEDOT:PSS	Poly(3,4-ethylenedioxythiophene):poly(styrenesulfonate)
PET	Poly(ethylene terephthalate)
PFN	poly [(9,9-bis(3´-(N,N-dimethylamino)propyl)-2,7-fluorene)-*alt*-2,7-(9,9–dioctylfluorene)]
PH1000	PEDOT:PSS, Clevios PH 1000 from Heareus
PSC	Polymer solar cell (i.e. OPV having polymers as donor material)
PV	Photovoltaics
R2R	Roll-to-roll (coating and printing)
RL	Recombination layer (in serially connected tandem devices)
RR	Round robin
SAXS	Small-angle x-ray scattering
SC	Spin Coating
STC	Standard test conditions (defined in section 2.3.1)
W_p	Watt-peak: The maximum power output of a PV system at standard test conditions (i.e. AM1.5G 1000 W m^{-2}, 25°C)

1 Introduction

1.1. The energy challenge within planetary boundary conditions

The world is faced with serious challenges regarding the future sustainability and progress of modern human civilization, as the expanding global population and economic growth increases the anthropogenic pressure exerted on Earth's natural systems. This is manifested through the emergence of visible planetary boundary conditions which challenges the unregulated business-as-usual approach to progress. One very clear boundary appears, as scientific reports, by and large, have now converged on the nature of global warming as an anthropogenic alteration of the planetary radiation balance caused by the burning of fossil fuels and the resulting emission of green-house gases [1]. Hence, it is clear that what lies at the heart of these challenges is humanity's need for energy.

Through the work of the UN's Intergovernmental Panel on Climate Change (IPCC) on summarizing and collating relevant research, it has been made clear that immediate actions are needed to keep the rise in global average temperature within 2°C towards 2100 [2]. This temperature range defines the likely boundaries within which anthropogenic climate change can be 'handled', and beyond which lies increased negative impacts on factors such as freshwater cycles, ocean circulation, ocean acidity, ecosystems and crop production, leading to increased flooding, droughts, loss of biodiversity, famine and mass migrations [1,2]. Other less tangible but no less disconcerting implications are the prospects of progression beyond so-called 'tipping-points', defined as thresholds at which a small perturbation can lead to abrupt and/or irreversible change, as part of the Earth system goes through a phase transition [1,3]. Such prospects arise from the inherent unpredictability and non-linear nature of these climatic mega-systems, and as such the tipping-points are hard to pin-point, and likewise the implications of the end-state [3]. However, it is clear that such shifts could lead to global catastrophe [3,4].

These predictions on the impact of human activities on the future state of the planet, disturbing as they are, form the argument for change on a global scale, as being the rational and only choice rather than 'just' the moral humanistic imperative.

So, what should be changed? To mitigate climate change and keep the temperature rise acceptable, models predict that CO_2-emissions will have to peak between 2015 and 2020 followed by a rapid decline [1]. This implies a swift change from the current complete dependence on fossil resources, with which we have fuelled the rise of modern society since the beginning of the industrial revolution, to an increasing reliance on renewable energy sources instead [5,6]. The transition will likely be augmented by market forces, as reserves of oil and natural gas dwindle, causing increased price volatility of main primary energy sources [7]. But as studies by the International Energy Agency (IEA), IPCC and others suggest, this will be far from enough [5–7]. Instead extensive and global policies and regulations are required, with emphasis on several areas such as research and development of energy technology, energy efficiency in all sectors, and setting a global price on the emission of main pollutants [1,5,6].

The shift from fossil fuel dependence will have the added effect of also alleviating geopolitical tension and concerns regarding the future security of energy supply, arising from the exhaustion of fossil energy reserves and hence the distribution of precious resources on fewer and fewer hands. Which, as studies suggest, might otherwise have dystopian repercussions for the future of global society [7,8].

One thing is certain, however: with an increasing global population and a projected increase in living standards, the global energy demand will increase, using what sources are available. It is projected that the worlds annual primary energy consumption will rise from the 2010 level of 500 EJ [9], to an estimated 800-1000 EJ in 2050 [10], a daily increase of roughly 1 GW or the equivalent of the power production capacity of a large coal-driven power plant. On top of this, the existing capacity must be substituted as well, adding another 1 GW pr. day.

So, to counter the energy needs of the future while still operation safely within the planetary boundary conditions, the world needs clean and renewable energy sources that can produce GW's-a-day-scale with a minimal environmental footprint.

1.2. Renewable energy: A heliocentric vision

From the previous section, it becomes clear that all choices with regards to major investments in future supply must be rational and well thought through, as both resources and time are limited. In this regard, it serves to look at the available sources of energy, and in this respect one source of energy dwarfs all other, namely the sun. Solar energy reaches earth in the form of electromagnetic radiation, hitting the atmosphere with a constant flux of 10^5 TW. A staggering amount of energy, driving most dynamic processes on earth, in turn also fuelling most of earth's available renewable energy sources: Through photosynthesis it delivers biomass and biofuels, while the temperature fluctuations in our atmosphere create wind, waves, and the precipitation that drives hydropower. Being only weekly coupled systems, these sources of energy are unlikely to present the most efficient harvesting of the sun light. This can be seen by estimating the amount of energy which is technically possible to harvest from the different renewable sources as shown in Table 1.1. Of these only geothermal power is completely decoupled from solar radiation, while "ocean" energy includes both wind and gravitational (tidal) effects.

Table 1.1: Estimates of the technical potential for electric power generation for different renewable energy sources. All figures are annual averages, and based on assumptions which infer a high degree of uncertainty [10,11].

	Available energy flow (TW) [10]	Technical potential, Electric power (TW) [11]	2010 Electric power generation (GW) [12]
Solar PV	10^5	53.7	3.7
Solar CSP	10^5	31.5	0.2
Hydro	5	1.6	392
Wind total (offshore)	10^3	12.7 (0.7)	39
Ocean	22	10.4	0.1
Geothermal	41	1.4	7.8
Biomass	92	8 [13]	36

Comparing the available energy from the different sources with the incoming solar flux, hints towards very low conversion efficiencies for these natural energy couplings. So, from a thermodynamics point of view, the soundest choice would be to seek out methods to harvest the solar radiation directly. A straightforward way would be by means of heating (E.g. solar CSP in the table) of water, thus driving a conventional turbine. But such a process involves two conversion steps, and would be limited in efficiency. So again thermodynamics bids us favour a one-step conversion if available, and this indeed is possible through the photovoltaic effect utilized by solar PV technology through solar cells.

1.3. Solar PV power generation

As is clearly seen in Table 1.1, PV shows the by far largest technical potential among the listed renewable energy sources. As an energy technology PV is unique: It is fuelled only by sun light and has no moving parts that need maintenance. Furthermore, it is inherently scalable due to its modular nature provided by its fundamental power production unit; the solar cell. As illustrated in Figure 1.1, this modular nature enables truly scalable power generation; from the powering of small electronics, through residential power installation, to large scale grid connected solar parks generating many MW's of electricity.

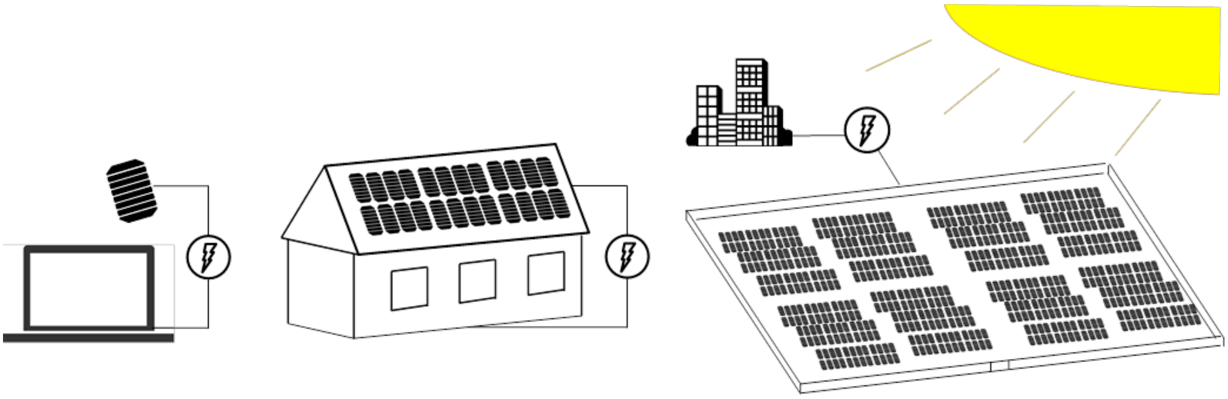

Figure 1.1: Schematic illustration of the scalable nature of solar cell power generation. From low power equipment (left) to residential (middle) and large scale solar parks (right).

This scalability also makes solar cells ideal for small-scale power generation in rural or isolated areas, especially in developing countries with limited power-grid infrastructure [14–16], and where nearly 1.3 billion people are still without access to electricity [5]. This is effectively illustrated by the graph in Figure 1.2 showing the number of people without access to electricity and the global population vs. the annual solar irradiation on an optimally inclined surface: About one third of all people living in the regions of Earth with the highest insolation do not have access to electricity. For all these regions, off- or mini-grid PV systems are very economical solutions for power generation [16]. In this way PV can be a powerful societal development tool, and a step towards escaping poverty for a significant part of the global population.

The overview given by Figure 1.2 also sustains two other important arguments for PV power generation: Most people generally live in areas with relatively high insolation (annual global mean of ~2000 kWh m^{-2} vs. ~1300 kWh m^{-2} for northern Europe), thus electricity can be produced locally. Furthermore, it is evident that very few people live in regions of very high insolation (i.e. above 2300 kWh m^{-2} $year^{-1}$), e.g. desserts, meaning that vast areas of uninhabited land, unsuitable for crop production, is available, and relatively close by.

Present day is seen as a renaissance for PV power generation. After flat-line conditions in the installed capacity since the 1970s, the last 5 years have brought the installed peak-capacity from 7 GW_p to 100 GW_p in 2012 [17]. Despite this and all the before mentioned benefits of PV, most realistic predictions on the future of the global energy mix, places PV to play a part equally shared with other renewables, such as wind and hydro power: For instance the IEA predicts that PV will account for somewhere between 11% and 25% of the global electricity production by 2050, depending on the degree of implementation of renewables in general, as governed by e.g. energy policies and price developments [18]. This relatively small part as compared to the technical potential (Table 1.1), is partly due to the technical difficulties related to having large amounts of fluctuating energy sources in the energy mix and the uncertainties related to how well these challenges can be met [18]. However, the biggest challenge for PV along with all other renewables remains cost. And, hence, the present growth rates of installed PV capacity are largely an effect of governmental subsidies; e.g. though beneficial financing schemes, and feed-in tariffs [18,19].

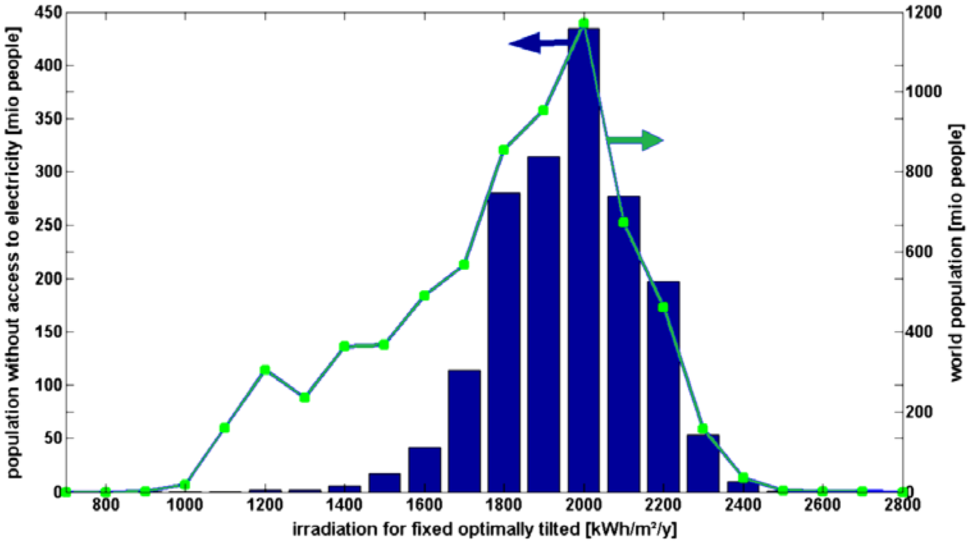

Figure 1.2: Population without access to electricity in dependence of respective local solar irradiation on module surfaces of fixed optimally tilted photovoltaic systems. The line refers to the right axis and represents distribution of world population. The bars refer to the left axis and represent population without access to electricity. Reproduced with permission from ref. [14] Copyright © 2012 John Wiley & Sons, Ltd.

1.4. Overview of PV technology

The PV market is dominated by so-called 1st generation solar cells, which are based on crystalline silicon (c-Si) as semiconductor, today accounting for more than 85% of the worldwide installed capacity [17]. This first generation of solar cells was developed in the Bell laboratories during the 1950's, and is generally characterized by high power conversion efficiencies (PCEs) (current average module efficiency of 14-15% [19]) and long operational lifetimes [20]. 1st generation PV is as mature technology, and thus prices are not predicted to fall significantly due to the inherently costly and energy intensive production of the high grade silicon wafers needed [18,21].

This problem has been partially addressed by the development of 2nd generation, so-called thin film, solar cells. These are based on more amorphous, stronger absorbing materials, which can be made thinner and at lower temperatures, thus enabling a lower embodied energy [18,22]. Mainly three types of cells are counted as 2nd generation thin-film cells; the amorphous silicon (a-Si) based, cadmium-telluride (Cd-Te) based, and the Copper-Indium-Gallium-Selenide (CIGS) based cells. All these types are commercially available, with average module PCEs around 6%, 10% and 12%, for the a-Si, Cd-Te and CIGS types respectively [19], while lifetimes are expected to compare with c-Si modules [18]. However, when considering very large scale fabrication, especially the Cd-Te but also CIGS types have serious challenges with regards to toxicity and/or abundance of materials [18,21]. The a-Si types, so far, suffer mainly from the low efficiencies as compared to the c-Si counterpart, a gap which it does not fully make up for in terms of processing benefits [23].

As of now, neither the 1st generation or 2nd generation solar cells has the potential of pushing the cost of electricity drastically below 1 € W_p^{-1} [21], being hindered by either costly and energy intensive fabrication and/or abundance/toxicity issues. Hence neither can be expected to drastically change the future prospects of PV as global energy source. Exactly such prospects are sought provided by next (3rd) generation solar cells, especially by organic-based PV (OPV) which will be the subject of this thesis [24,25].

1.5. Organic photovoltaics: a 3rd generation of solar cells

OPV differ from the 1st and 2nd generation solar cells the introduction of organic semiconductors in place of inorganic semiconductors as light absorbing material. The benefits of OPV are given by the unique characteristics of this class of materials: Organic semiconductors are strong absorbers, which means that solar cells can be made very thin (<100 nm) allowing for flexibility while saving on material usage [26]. They can be easily processed, e.g. by solution, and at low temperatures, enabling the use of cheap and flexible plastic substrates and fast roll-to-roll (R2R) processing techniques known from the printing industry [27]. Materials can be synthesized in an endless variety, to fit a given need, while the use or earth abundant elements ensures no problem with scalability [25].

As research has progressed, several distinct categories have emerged within the field of OPV, several of which will not be considered further in this thesis: One is based on the combination of organic and inorganic semiconductor materials, in so-called hybrid devices [28] including dye-sensitized solar cells (DSC) [29], a category which is often not considered to be part of the OPV field. Another distinction can be made towards OPV which focuses on the use of small organic molecules processed by vacuum techniques [30], as this type of OPV does not inherit the processing benefits offered by pure solution processing.

Instead the emphasis will be on OPV which are fully solution processable and mainly based on the combination of semiconducting polymers and fullerene derivates as light absorbing material [31]. Hence this category is what best encompass the benefits of OPV as listed above. For simplicity, this type is denoted as polymer solar cells (PSCs).

1.6. PSCs: Current state and challenges

A solar cell is conveniently benchmarked within three main areas; PCE, stability, and ease of processing. The convergence of these three categories has been termed the unification challenge and is seen as the major goal for any solar cell technology [32]. Most PSC research however, still focuses above all on maximizing PCE: The devices are typically very small (<0.1 cm^2 of active area) where the device fabrication and testing is done in an inert atmosphere using generally non scalable fabrication methods and processes such as spin coating and high vacuum thermal evaporation. PSCs of this type include the 'hero' devices of the field, which have presented a near doubling in PCE over the last 5 years, to the current level just above 10 % [33]. These outstanding achievements raise the PSC banner high for the world to see. But in terms of the unification challenge this is far from the goal, as there is generally little reported on stability and scalability of these hero devices.

At the other end of the scale are the R2R fabricated devices. This type of PSC have also seen remarkable development in terms of processing [34] and stability [35]. While challenges remains in terms of upscaling [36,37] and the dormant efficiency around 2% [36].

1.7. Project outline

To summarize: The aim of developing carbon-neutral and sustainable energy technologies such as solar cells is a race against the clock; as the threat of climate change grows and the reserves of fossil fuels dwindle, while the projected increase in energy demand towards 2050 is around 1 GW a day. PSCs have the ambitious potential to cover most of our future energy needs [25]. In order to enable fabrication of solar cells on such a massive scale, the paradigm is low cost, minimal environmental footprint, and high throughput production, while working towards higher and scalable efficiencies. This thesis covers four themes, each constituting an attempt towards this vision for PSCs:

Chapter 2 introduces the basic principles of polymer solar cells; from principles of operation to the solar cells structure.

Chapter 3 presents the efforts towards a water processable BHJ by the use of aqueous nanoparticles. The experiments constituted a novel approach to aqueous R2R processed solar cells, with the potential to significantly reduce the environmental impact of PSCs.

Chapter 4 describes the upscaling of tandem polymer solar cells, from small spin-coated devices to a complete R2R process. Tandem cells is a proven concept for increasing the achievable efficiencies, and the experiments presented here are the first to demonstrate fully R2R processed tandem PSCs.

Chapter 5 describes the development of PEDOT:PSS-based transparent electrodes for ITO-free PSCs. The elimination of ITO significantly lowers the cost and environmental impact of PSCs.

Chapter 6 demonstrates the Round Robin method as a low-cost tool to improve consensus in reported efficiency data, which is shown to be otherwise poor but equally so, globally.

Chapter 7 presents a short summarizing conclusion and outlook.

1.8. References

[1] I. Allison, N.L. Bindoff, R.A. Bindschadler, P.M. Cox, N. de Noblet, M.H. England, et al., The Copenhagen Diagnosis: Updating the world on the latest climate science, (2011).

[2] IPCC, Climate Change 2007 Synthesis report: An Assessment of the Intergovernmental Panel on Climate Change, (2007) 12–17.

[3] T.M. Lenton, H. Held, E. Kriegler, J.W. Hall, W. Lucht, S. Rahmstorf, et al., Tipping elements in the Earth's climate system., Proceedings of the National Academy of Sciences of the United States of America. 105 (2008) 1786–93.

[4] W. Steffen, K. Noone, E. Lambin, T.M. Lenton, M. Scheffer, C. Folke, et al., Planetary Boundaries : Exploring the Safe Operating Space for Humanity, (2009).

[5] IEA, WORLD ENERGY OUTLOOK 2012, in: 2012.

[6] IPCC, Climate Change 2007: Mitigation of Climate Change, 2007.

[7] P.D. Raskin, C. Electris, R. a. Rosen, The Century Ahead: Searching for Sustainability, Sustainability. 2 (2010) 2626–2651.

[8] A. Correljé, C. van der Linde, Energy supply security and geopolitics: A European perspective, Energy Policy. 34 (2006) 532–543.

[9] BP, BP Statistical Review of World Energy, (2013).

[10] P. Moriarty, D. Honnery, What is the global potential for renewable energy?, Renewable and Sustainable Energy Reviews. 16 (2012) 244–252.

[11] M. Hoogwijk, W. Graus, Global potential of renewable energy sources: A Literature assessment, EcoFys. (2008).

[12] IEA, World Energy Outlook 2012, (2012).

[13] G. Resch, A. Held, T. Faber, C. Panzer, F. Toro, R. Haas, Potentials and prospects for renewable energies at global scale, Energy Policy. 36 (2008) 4048–4056.

[14] C. Breyer, A. Gerlach, Global overview on grid-parity, Progress in Photovoltaics: Research and Applications. 21 (2013) 121–136.

[15] F.C. Krebs, T.D. Nielsen, J. Fyenbo, M. Wadstrøm, M.S. Pedersen, Manufacture, integration and demonstration of polymer solar cells in a lamp for the “Lighting Africa” initiative, Energy & Environmental Science. 3 (2010) 512.

[16] A. Gerlach, M. Hlusiak, C. Peters, P. Adelmann, J. Winiecki, S. Tsegaye, et al., Electrifying the Poor: Highly Economic Off-Grid PV Systems in Ethiopia - A Basis for Sustainable Rural Development, in: 24th European Photovoltaic Solar Energy Conference , 21-25 September 2009 , Hamburg , Germany, 2009: pp. 21–25.

[17] REN21, Renewables 2013 Global Status Report, REN21 Secretariat, Paris, 2013.

[18] IEA, Solar Energy Perspectives, OECD Publishing, 2011.

[19] Fraunhofer institute - Photovoltaic report, (2012).

[20] D.C. Jordan, R.M. Smith, C.R. Osterwald, E. Gelak, S.R. Kurtz, Outdoor PV Degradation Comparison, 2011.

[21] M. Raugei, P. Frankl, Life cycle impacts and costs of photovoltaic systems: Current state of the art and future outlooks, Energy. 34 (2009) 392–399.

[22] J. Nelson, The Physics of Solar Cells, 1st ed., Imperical College Press, London, 2004.

[23] A.G. Aberle, Thin-film solar cells, Thin Solid Films. 517 (2009) 4706–4710.

[24] C.J. Brabec, J.A. Hauch, P. Schilinsky, C. Waldauf, Production Aspects of Organic Photovoltaics and Commercialization of Devices, MRS Bullitin. 30 (2005).

[25] N. Espinosa, M. Hösel, D. Angmo, F.C. Krebs, Solar cells with one-day energy payback for the factories of the future, Energy & Environmental Science. 5 (2012) 5117.

[26] H. Hoppe, N.S. Sariciftci, Organic solar cells: An overview, Journal of Materials Research. 19 (2004) 1924–1945.

[27] R.R. Søndergaard, M. Hösel, D. Angmo, T.T. Larsen-Olsen, F.C. Krebs, Roll-to-roll fabrication of polymer solar cells, Materials Today. 15 (2012) 36–49.

[28] K.D.G.I. Jayawardena, L.J. Rozanski, C. a Mills, M.J. Beliatis, N.A. Nismy, S.R.P. Silva, “Inorganics-in-Organics”: recent developments and outlook for 4G polymer solar cells., Nanoscale. (2013).

[29] M. Grätzel, Dye-sensitized solar cells, Journal of Photochemistry and Photobiology C: Photochemistry Reviews. 4 (2003) 145–153.

[30] P. Peumans, A. Yakimov, S.R. Forrest, Small molecular weight organic thin-film photodetectors and solar cells, Journal of Applied Physics. 93 (2003) 3693.

[31] B.C. Thompson, J.M.J. Fréchet, Polymer-fullerene composite solar cells., Angewandte Chemie (International Ed. in English). 47 (2008) 58–77.

[32] M. Jørgensen, K. Norrman, F.C. Krebs, Stability/degradation of polymer solar cells, Solar Energy Materials and Solar Cells. 92 (2008) 686–714.

[33] L. Dou, J. You, Z. Hong, Z. Xu, G. Li, R.A. Street, et al., 25th Anniversary Article : A Decade of Organic / Polymeric Photovoltaic Research, Advanced Materials. (2013) 1–30.

[34] F.C. Krebs, S. a. Gevorgyan, J. Alstrup, A roll-to-roll process to flexible polymer solar cells: model studies, manufacture and operational stability studies, Journal of Materials Chemistry. 19 (2009) 5442.

[35] M. Jørgensen, K. Norrman, S.A. Gevorgyan, T. Tromholt, B. Andreasen, F.C. Krebs, Stability of polymer solar cells., Advanced Materials. 24 (2012) 580–612.

[36] F.C. Krebs, T. Tromholt, M. Jørgensen, Upscaling of polymer solar cell fabrication using full roll-to-roll processing., Nanoscale. 2 (2010) 873–86.

[37] N. Espinosa, R. García-Valverde, A. Urbina, F.C. Krebs, A life cycle analysis of polymer solar cell modules prepared using roll-to-roll methods under ambient conditions, Solar Energy Materials and Solar Cells. 95 (2010) 1293–1302.

2 Basics of polymer solar cells

2.1. Principles of operation

A solar cell converts a photon flux into an electrical current by a mechanism denoted as the photovoltaic effect. Its discovery is generally ascribed to Becquerel and his report from 1839 [1]. In very general form, the mechanism can be described as follows: A photon incident on a semiconductor, having an energy that exceeds the semiconductor band gap ($E_{photon} \geq E_g$), excites an electron to an unoccupied state above E_g, creating an electron-hole (e-h) pair which is subsequently separated over a built-in gradient in the electrochemical potential of the solar cell, and finally led to recombine after being put to work in an external circuit [2]. There are many excellent reviews covering the intricate details of the working mechanisms of PSCs [3–7], while the complete picture is still very much a work in progress. This text will suffice with a simplistic description, leaving out details to be found in the cited references.

The working mechanisms of different types of solar cells are determined by the type of semiconductors it uses. PSCs, as mentioned, utilize organic semiconductors, both polymers and molecules, commonly characterized by having a π-conjugated electronic system. The π-conjugation that leads to the semiconducting properties originates from the alternating occurrence of double and single carbon-carbon bonds in the chemical structure. This structure infers delocalization of the π-electrons across overlapping p-orbitals, creating a highly polarizable electronic structure, which can be tuned to offer strong absorption in the UV-visible range [8]. Although they are semiconductors, the physical properties of organic semiconductors differ substantially from those of inorganic counterparts such as Si, and hence effecting how they function in solar cells.

Inorganic semiconductors form very ordered structures which are highly periodic; resulting in highly degenerate energy levels and the formation of continues energetic bands. Organics however, are characterized by inherent disorder, due to the low energy of inter-molecular interactions in the bulk and the high degree of conformational freedom of organic macromolecules [9]. For one, E_g of an organic semiconductor is not a regular 'band'-gap but rather the difference in energy of the highest occupied molecular orbital (HOMO) and the lowest unoccupied molecular orbital (LUMO) of the organic molecule or polymer. Furthermore, both the dielectric constant and charge carrier mobility is inherently low in organic semiconductors. The low dielectric constant in the bulk of the semiconductor means that electric fields are poorly screened, and thus the mutual coulomb-attraction of the photoexcited e-h pair is much stronger than in inorganic solar cells where photoexcitation effectively produces free charges. Upon photoexcitation in PSCs however, the result is the formation of a quasi-stable charge complex called a Frenkel-exciton, with an estimated e-h binding energy around 0.4-0.5 eV [3,4,6], more than a magnitude larger than thermal energies around 300 K. For this reason a large energetic driving force, roughly as large as the exciton binding energy, is needed to separate the charges. Exactly this challenge was limiting the success of early OPV research from its beginning in the 1950s to around the mid-1980s where devices were simply made from a single layer of organic semiconductor sandwiched between two electrodes of different work function as illustrated in Figure 2.1a [10].

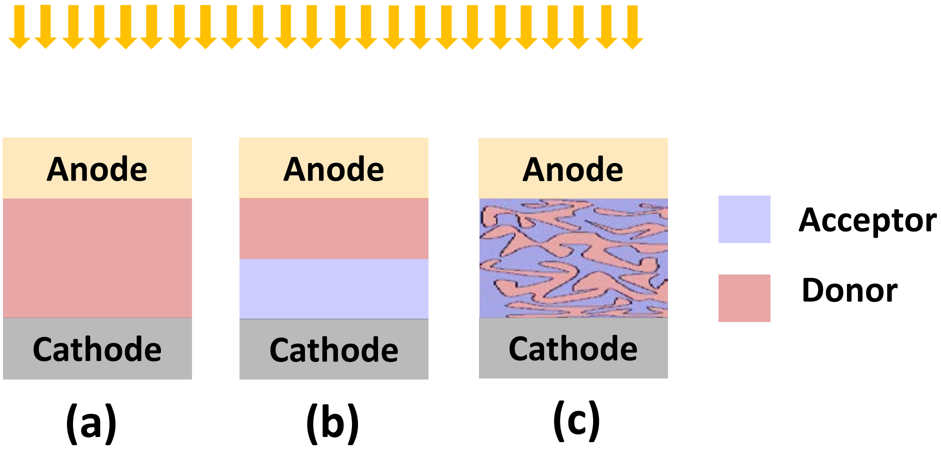

Figure 2.1: Schematic illustration of the three approaches to PSCs. (a) a single organic semiconductor sandwiched between two electrodes. (b) The introduction of the D/A heterojunciton in a bi-layer device. (c) The BHJ approach, distributing the D/A interface throughout the bulk of the PSC.

The solution was the combining of two types of organic semiconductor having a difference in electron affinity to match the exciton binding energy in a bi-layer heterojunction device, as first reported by Tang in 1986 [11]. In PSCs the material with the lower affinity is called the (electron) donor while high affinity material is called the acceptor, and the combined approach is referred to as a donor/acceptor (D/A) heterojunction (Figure 2.1b). Typical donor materials are conjugated polymers which are predominantly responsible for the light absorption, due to the success of acceptor materials based on the weakly absorbing C_{60} molecule. The first D/A combination of conjugated polymer and C_{60} was demonstrated by Sariciftci et al. in 1992 [12,13].

A limiting factor for all types of solar cells is the limited lifetime of photo-excited charges, as they will eventually recombine to the ground state. In PSCs the chance of recombination is much higher due to the inherent disorder and poor screening in the constituting materials, resulting in effective exciton lifetimes of around 1 ns [4]. For a typical donor polymer this translates to an exciton diffusion length on the order of 5-10 nm [3], within which a D/A interface must be reached in order to avoid recombination. For a bi-layer heterojunction PSC this means that only excitons which are generated on the order of this diffusion length from the D/A interface can be harvested efficiently, and while most polymer donors are very strong absorbers they will still need 50-100 nm of material in order to absorb most of the available photons. This effectively limits the efficiency of the bi-layer device. Moreover, from a solution processing point of view the bi-layer is impractical, as the first processed layer of semiconductor must be insoluble in the solvent of the second layer.

This challenge was resolved in 1995 when Yu et al. reported the bulk heterojunction (BHJ) [14]. By distribution the D/A heterojunction throughout the bulk of the solar cell with a nanoscale structure as illustrated in Figure 2.1c, in principle all excitons can be harvested efficiently. Also from a processing point of view, the BHJ approach is very strong, as it can be formed by a single mixed solution of donor and acceptor. Though the morphology of the BHJ is all-determining and has proven very difficult to control [15], the BHJ approach remains the state of the art of PSCs.

From this, an overview of the PSC operational mechanism can be given, following the illustration in Figure 2.2:

1) **Light absorption and exciton diffusion**
   a) Photon absorption when $E_{photon} \geq E_g$, where E_g corresponds to the HOMO-LUMO gap of the donor. As illustrated, the acceptor can also contribute to the absorption as is e.g. the case for C_{70} –based acceptors.
   b) The charge neutral exciton moves by diffusion, until it reaches a D/A interface or recombines.
2) **Exciton dissociation and charge transport**
   a) As the exciton encounters the D/A interface it will dissociate provided that the charge transfer is energetically favorable, e.g. that the D/A LUMO-LUMO difference is on the order of the exciton binding.
   b) The separation into free charges is often described as a two-step process including an intermediate state referred to as the charge transfer complex [4]. Here the electron is situated on the acceptor and the hole on the donor, still close enough to being coulomb-bound thus increasing likelihood of recombination.
   c) Upon complete separation of electron and hole, further charge transport in the respective donor- and acceptor-phases occurs via hopping due to the disordered nature of the organic semiconductors. Microscopic descriptions are given by e.g. Marcus theory [4], however ample macroscopic description has been made e.g. using a drift and diffusion model [16].
3) **Charge collection at electrodes**

a) The charge extraction process is very dependent on the type of contact between the semiconductor and the electrode and how well the acceptor LUMO and donor HOMO aligns with the cathode and anode work functions respectively. Most often it is necessary to add a semiconducting hole transport layer (HTL) at the anode and/or electron transport layer (ETL) at the cathode, as illustrated in Figure 2.3, in order to optimize carrier extraction.

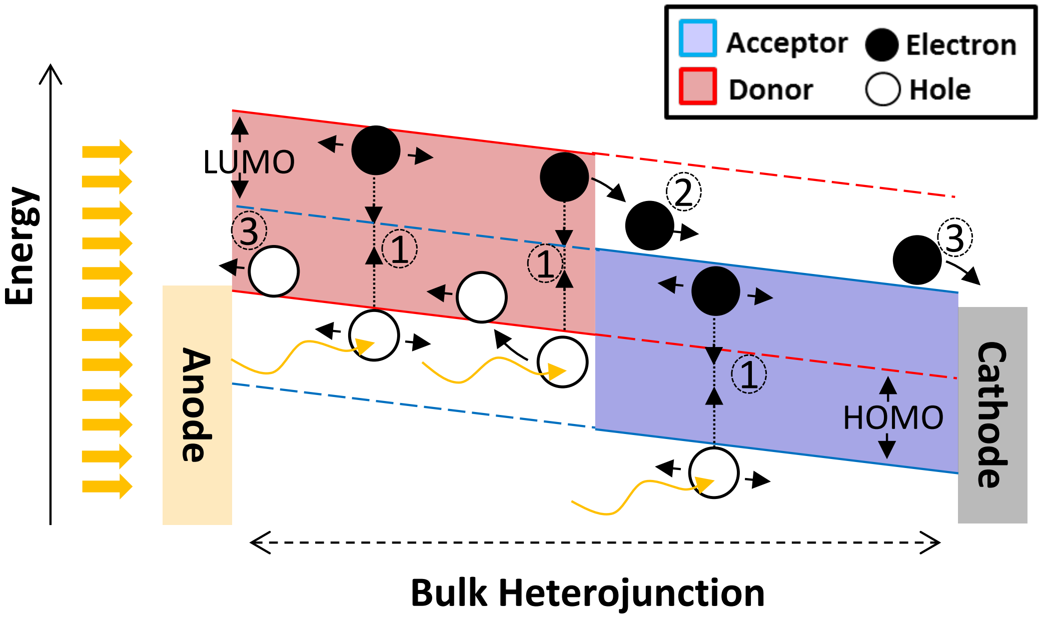

Figure 2.2: Instructive (energy) diagram explaining the basic working mechanism of current generation in a BHJ PSCs operating at short circuit conditions: (1) Photo excitation and exciton diffsion -> (2) charge separation over the D/A interface -> (3) Charge collection at respective electrodes. The dashed lines illustrates that the D/A interface is distributed throughout the bulk of the solar cell.

2.2. The basic PSC structure

Polymer solar cells are sandwich-like structures; build layer by layer, using solution processing by spin coating or various R2R methods, while metal and oxide layers can be deposited by thermal evaporation. Individual layer thicknesses are most often measured in tens of nm's, though the substrate is kept thick in order to enable handling. In PSC research one refers to the geometry or configuration of the cell as being either 'normal' or 'inverted', with reference to the layer sequence and hence the direction of current, as can be seen in Figure 2.3a and b respectively, where some typical examples of materials used for the different layers are also listed.

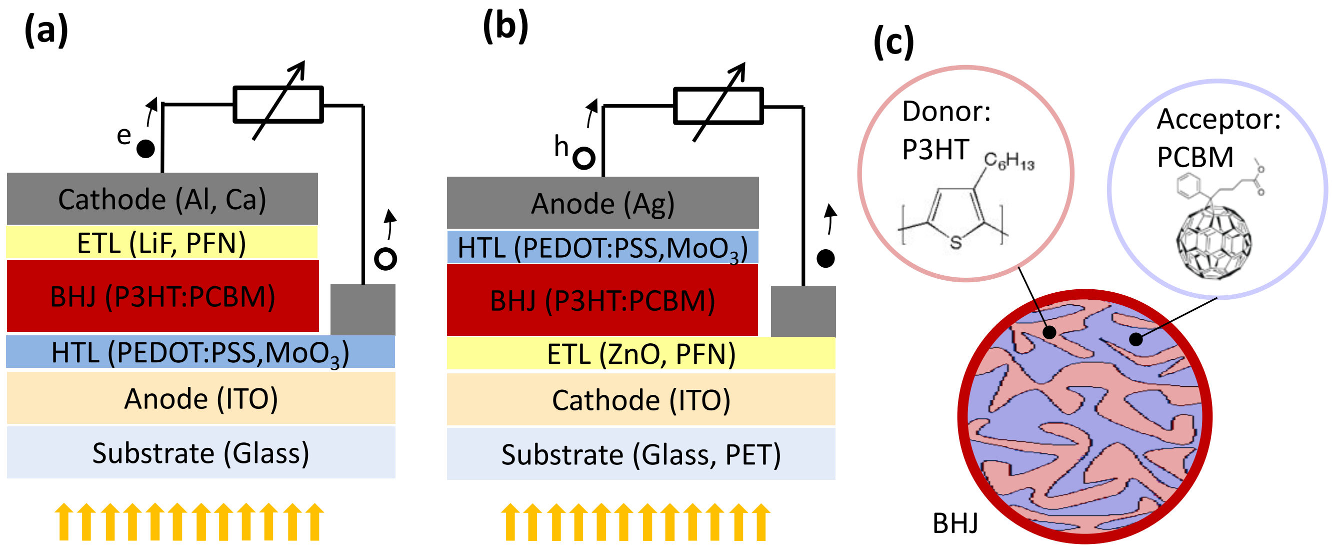

Figure 2.3: Generalized solar cell layer stack with some materials examples shown in parenthesis, of (a) normal geometry PSCs and (b) Inverted geometry PSCs. (c) shows a blow-up of the BHJ active layer, illustrating the interpenetrating D/A heterojunction.

The normal geometry was, hence the name, the first geometry to be used for PSCs [11,13,14]. Typically, it is based on a rigid glass substrate with a layer of ITO functioning as transparent electrode. A typical HTL of PEDOT:PSS ensures good contact with the BHJ [17]. Figure 2.3c shows the BHJ, often termed the active layer, with the archetypical materials combination of P3HT and PCBM. The normal geometry PSCs most often uses a low work function metal sometimes modified by a thin buffer layer <1 nm of LiF [18].

The inverted geometry is very useful in a processing point of view, as the inverted layer sequence allows for the use of higher work function metals as top electrode, e.g. Ag, which can be solution processed. This makes the inverted geometry very well suited for high throughput PSC fabrication [19,20]. These R2R fabricated cells have primarily been based on a flexible PET/ITO substrate, with ZnO as ETL, P3HT:PCBM as active layer, PEDOT:PSS as HTL, and the back metal electrode processed from a Ag paste. A PSC design known as ProcessOne as reported by Krebs et al. [21].

Considerable research has also been put towards finding and optimizing ETL and HTL materials [22]. A notable ETL example is the polymer PFN reported by the group of Cao [23,24], while HTLs based on transition metal oxides such as MoO_x have also been used with success [25–28].

2.3. Electrical characteristics

PSCs are ultimately constructed to be put to work in some external circuit. For this reason the electrical characteristics of the PSC under illumination is used as the main measure to gauge the device performance. Furthermore electrical characterization serves as the main characterization tool in PSC research. By electrical characteristics is meant, how the current of the solar cells evolves as a function of applied voltage, measured by a current density – voltage (J-V) characterization, as is illustrated in Figure 2.4.

A PSC is much like a diode, therefor without photoinduced current (J_{ph}), the J-V curve of a well behaving PSC has the typical rectifying diode characteristics (dashed curve in Figure 2.4). Upon illumination the dark curve of a perfect solar cell is shifted downward in the J-V diagram by $-J_{ph}$, but otherwise retains its characteristics. However PSCs perform far from the ideal and the exposure to light can significantly alter the J-V characteristics of the solar cell.

Zero bias is referred to as short-circuit conditions, and the y-axis intersect is called the short-circuit current density (J_{sc}). Again for a perfect solar cell $J_{sc}=J_{ph}$ but due to non-perfect charge extraction and internal resistive losses in the solar cell, J_{sc} can be substantially smaller than J_{ph}.

The bias at J=0 is called the open circuit voltage (V_{oc}), or the maximum voltage that the cell can deliver. The V_{oc} is proportional with the potential difference of the photogenerated electrons and holes as they 'leave' the solar cell, which for PSCs is related to the energy difference of the donor HOMO-level and the acceptor LUMO-level, often referred to as the effective band-gap.

A PSC produces power to the external circuit in the 4th quadrant of the J-V diagram, when $0<V<V_{oc}$. The largest power is defined as the maximum power point (P_{max}), and the power conversion efficiency (PCE) of the solar cell is the ratio between P_{max} and the incident solar power (P_{sun}):

$$\mathrm{PCE} = \frac{\mathrm{P_{max}}}{\mathrm{P_{sun}}}$$

As the incident solar irradiance (I_{sun}) is rated at 1000 W m^{-2} at standard test conditions, it is convenient to write the expression in terms of densities, and also the ratio between the ideal solar cell and the actual solar cell, called the fill-factor (FF) defined as the ratio between the two dotted squares in Figure 2.4:

$$\mathrm{PCE} = \frac{\mathrm{J_{mpp}V_{mpp}}}{\mathrm{J_{sc}V_{oc}}}\frac{\mathrm{J_{sc}V_{oc}}}{\mathrm{I_{sun}}} = \mathrm{FF}\frac{\mathrm{J_{sc}V_{oc}}}{\mathrm{I_{sun}}}$$

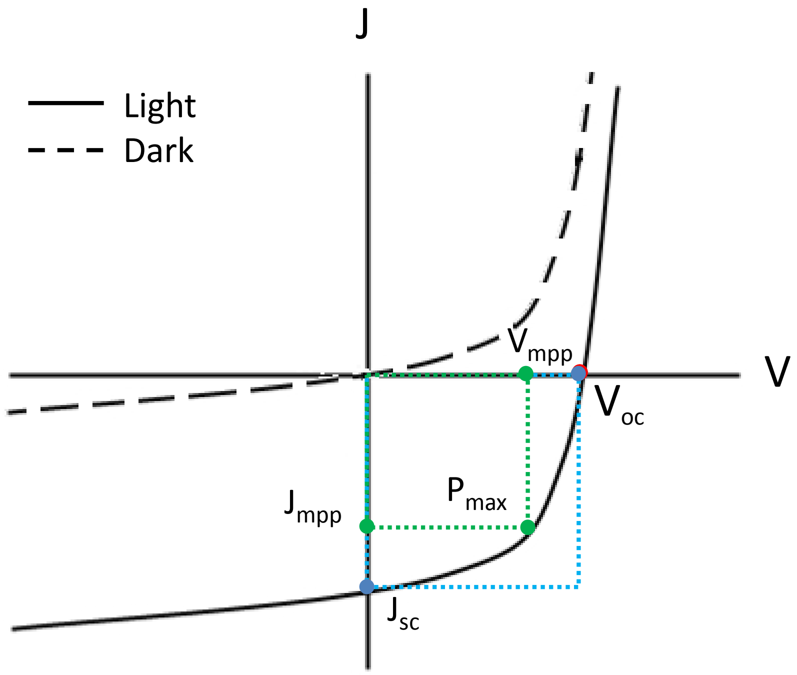

Figure 2.4: J-V characteristics of a PSC under illumination, with the definitions of the PV parameters as indicated. Further it is indicated how the parallel and series resistances can be estimated.

2.3.1. The solar spectrum and standard test conditions

At normal incidence the energy flux hitting the atmosphere is 1366 W m^{-2}, a figure known as the solar constant. The spectral distribution is defined by the 'air-mass-0' (AM0) spectrum, almost perfectly described by black-body radiation at 5250 °C, and shown by the black curve in Figure 2.5b. However, more interesting for solar cells is the terrestrial solar spectrum. For nominal PCE ratings of solar cells the air-mass 1.5 global (AM1.5G) spectrum is used, simulating the solar spectrum at an angle of 44.2° from zenith (in Figure 2.5a), and where AM1.5 referres to the traversing of roughly 1.5 times the average thickness of the atmosphere while G indicates the inclusion of simulated diffuse light.

The standard test conditions (STC) for solar cells is the AM1.5G spectrum with an irradiance of 1000 W m^{-2} and a temperature of 25 °C. For this thesis the STC are slightly modified as the nominal temperature during indoor J-V characterization was 85±5 °C.

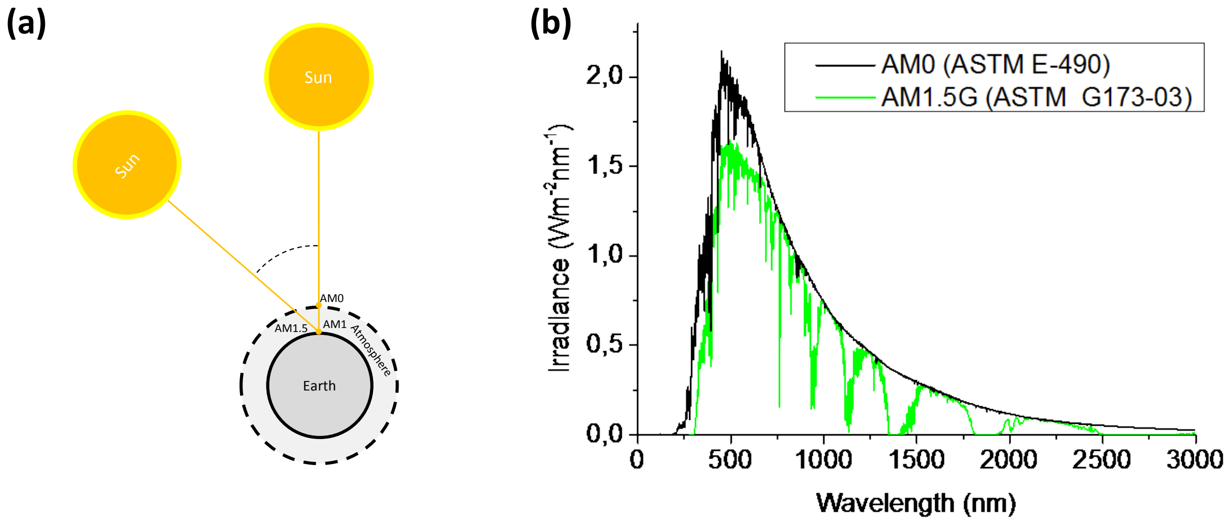

Figure 2.5: (a) Graphical representation of the definition of "air mass" (AM). (b) Standard irradiance spectrum from ASTM, comparing the extraterrestrial (AM0) spectrum with the AM1.5G spectrum used under standard test conditions.

2.4. **References**

[1] A.E. Becquerel, Photoelctrochemical effect, CR Acad. Sci. Paris9. 14 (1839).

[2] J. Nelson, The Physics of Solar Cells, 1st ed., Imperical College Press, London, 2004.

[3] B.C. Thompson, J.M.J. Fréchet, Polymer-fullerene composite solar cells., Angewandte Chemie (International Ed. in English). 47 (2008) 58–77.

[4] C. Deibel, V. Dyakonov, Polymer–fullerene bulk heterojunction solar cells, Reports on Progress in Physics. 73 (2010) 096401.

[5] J. Nelson, Polymer : fullerene bulk heterojunction solar cells The efficiency of solar cells made from a conjugated polymer blended, 14 (2011) 462–470.

[6] P.W.M. Blom, V.D. Mihailetchi, L.J.A. Koster, D.E. Markov, Device Physics of Polymer:Fullerene Bulk Heterojunction Solar Cells, Advanced Materials. 19 (2007) 1551–1566.

[7] J. Bisquert, G. Garcia-Belmonte, On Voltage, Photovoltage, and Photocurrent in Bulk Heterojunction Organic Solar Cells, J. Phys. Chem. Lett. (2011) 1950–1964.

[8] H. Hoppe, N.S. Sariciftci, Organic solar cells: An overview, Journal of Materials Research. 19 (2004) 1924–1945.

[9] R. Noriega, J. Rivnay, K. Vandewal, F.P. V. Koch, N. Stingelin, P. Smith, et al., A general relationship between disorder, aggregation and charge transport in conjugated polymers, Nature Materials. 12 (2013) 1–7.

[10] G. a. Chamberlain, Organic solar cells: A review, Solar Cells. 8 (1983) 47–83.

[11] C.W. Tang, Two-layer organic photovoltaic cell, Applied Physics Letters. 48 (1986) 183.

[12] N.S. Sariciftci, L. Smilowitz, A.J. Heeger, F. Wudi, Photoinduced Electron Transfe from a Conducting Polymer to Buckminsterfullerene, Science. 258 (1992) 1474–1476.

[13] N.S. Sariciftci, D. Braun, C. Zhang, V.I. Srdanov, A.J. Heeger, G. Stucky, et al., Semiconducting polymer-buckminsterfullerene heterojunctions: Diodes, photodiodes , and photovoltaic cells, Applied Physics Letters. 62 (1993) 585–587.

[14] G. YU, J. GAO, J.C. HUMMELEN, F. WUDL, A.J. HEEGER, Polymer photovoltaic cells : enhanced efficiencies via a network of internal donor-acceptor heterojunctions, Science. 270 (1995) 1789–1791.

[15] C.J. Brabec, M. Heeney, I. McCulloch, J. Nelson, Influence of blend microstructure on bulk heterojunction organic photovoltaic performance., Chemical Society Reviews. 40 (2011) 1185–99.

[16] L.J.A. Koster, E. Smits, V.D. Mihailetchi, P.W.M. Blom, Device model for the operation of polymer/fullerene bulk heterojunction solar cells, Physical Review B. 72 (2005) 1–9.

[17] C.J. Brabec, a. Cravino, D. Meissner, N.S. Sariciftci, T. Fromherz, M.T. Rispens, et al., Origin of the Open Circuit Voltage of Plastic Solar Cells, Advanced Functional Materials. 11 (2001) 374–380.

[18] C.J. Brabec, S.E. Shaheen, C. Winder, N.S. Sariciftci, P. Denk, Effect of LiF/metal electrodes on the performance of plastic solar cells, Applied Physics Letters. 80 (2002) 1288.

[19] F.C. Krebs, T. Tromholt, M. Jørgensen, Upscaling of polymer solar cell fabrication using full roll-to-roll processing., Nanoscale. 2 (2010) 873–86.

[20] R.R. Søndergaard, M. Hösel, D. Angmo, T.T. Larsen-Olsen, F.C. Krebs, Roll-to-roll fabrication of polymer solar cells, Materials Today. 15 (2012) 36–49.

[21] F.C. Krebs, S. a. Gevorgyan, J. Alstrup, A roll-to-roll process to flexible polymer solar cells: model studies, manufacture and operational stability studies, Journal of Materials Chemistry. 19 (2009) 5442.

[22] E.L. Ratcliff, B. Zacher, N.R. Armstrong, Selective Interlayers and Contacts in Organic Photovoltaic Cells, J. Phys. Chem. Lett. 2 (2011) 1337–1350.

[23] Z. He, C. Zhong, X. Huang, W.-Y. Wong, H. Wu, L. Chen, et al., Simultaneous Enhancement of Open-Circuit Voltage, Short-Circuit Current Density, and Fill Factor in Polymer Solar Cells., Advanced Materials (Deerfield Beach, Fla.). (2011) 4636–4643.

[24] Z. He, C. Zhong, S. Su, M. Xu, H. Wu, Y. Cao, Enhanced power-conversion efficiency in polymer solar cells using an inverted device structure, Nature Photonics. 6 (2012) 593–597.

[25] V. Shrotriya, G. Li, Y. Yao, C.-W. Chu, Y. Yang, Transition metal oxides as the buffer layer for polymer photovoltaic cells, Applied Physics Letters. 88 (2006) 073508.

[26] K. Zilberberg, H. Gharbi, A. Behrendt, S. Trost, T. Riedl, Low-Temperature, Solution-Processed MoOx for Efficient and Stable Organic Solar Cells, Applied Materials & Interfaces. (2012).

[27] F. Cheng, G. Fang, X. Fan, H. Huang, Q. Zheng, P. Qin, et al., Enhancing the performance of P3HT:ICBA based polymer solar cells using LiF as electron collecting buffer layer and UV–ozone treated MoO3 as hole collecting buffer layer, Solar Energy Materials and Solar Cells. 110 (2013) 63–68.

[28] J. Meyer, S. Hamwi, M. Kröger, W. Kowalsky, T. Riedl, A. Kahn, Transition metal oxides for organic electronics: energetics, device physics and applications., Advanced Materials (Deerfield Beach, Fla.). 24 (2012) 5408–27.

3 Water processing

3.1. Introduction

When considering the up-scaling of the fabrication of polymer solar cells from laboratory meters to meaningfully-sized industrial production, one must consider very carefully the toxicity and environmental footprint of all materials and processes involved in the making of the solar cells. This is significantly important in the case of polymer solar cells, due to what is often pointed out to be their strongpoint; they can potentially be made very cheaply. And polymer solar cells should be cheap, as they will likely not be able to compete with other PV technologies on factors such as efficiency and lifetime. For such low cost/value, highly disseminatable devices, probably with a low lifetime, considerations of toxicity and environmental impact are of utmost importance. As is the case for all up-scaling efforts: The earlier such considerations are somehow incorporated into the paradigm of PSC development, the more scalable the technology will become. This will also make for a much more transparent and market-wise attractive technology, increasing the likelihood of capital investment, from industry and in company start-ups.

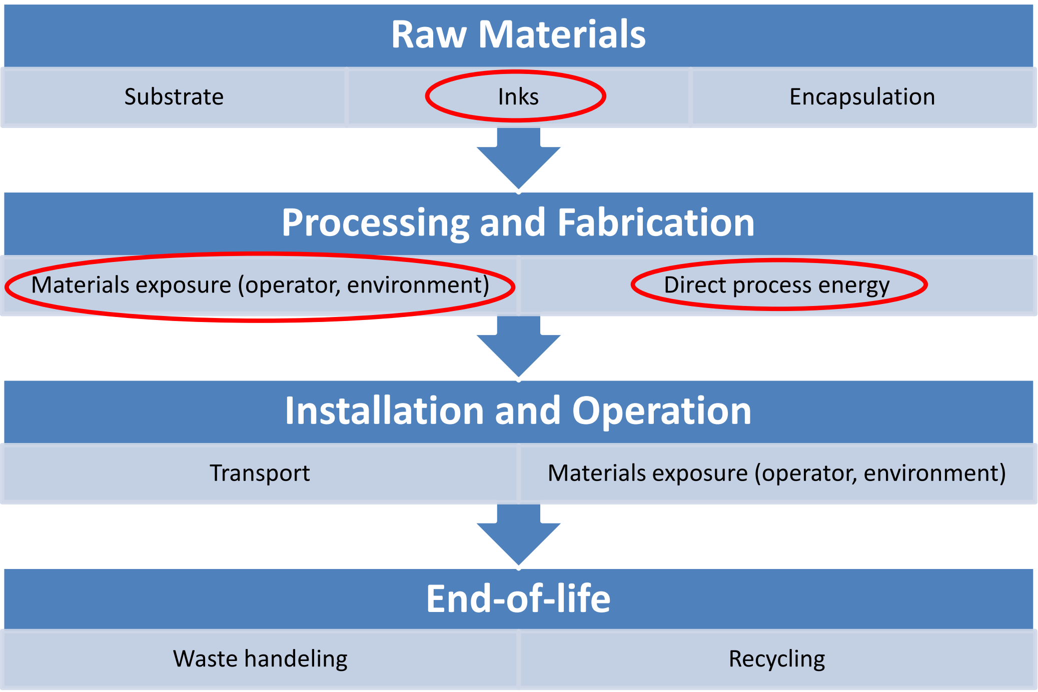

Figure 3.6: Rough overview of areas that need to be considered in terms of environmental impact in order to evaluate the environmental impact of PSCs. The areas considered in this chapter are inks, materials exposure during processing, and direct process energy.

As outlined in Figure 3.6, there are many factors that influence the total environmental impact of polymer solar cells. Most of which have been subjected to review in life-cycle- and environmental assessments [1–7]. This chapter focuses on the inks used in solution processing of the different layers constituting the solar cell stack, in particular the efforts towards the use of aqueous processing of the active layer.

The vision of the polymer solar cell as formulated by our group[3] is of a technology that offers to deliver in the 1 GW_p/day scale, and which is fabricated using relatively low-tech equipment, such that factories might be easily distributed across the globe, fabricating solar cells where they are needed. For such a vision, the chosen processing solvent is of great importance with regards to the complexity of the factory infrastructure and machinery operation necessary to accommodate for general health and environmental concerns. In this view it is clear that the use of water would be a very beneficial route, also in terms of embodied energy[3] and, as will be discussed in section 3.3, direct process energy.

Since the first reports of solution processed organic solar cells, aromatic and chlorinated solvents which are all toxic, some more than others, have been used almost exclusively for the processing of the BHJ layer. This is likely linked to the fact that devices mostly are made and optimized for science and not for bulk energy production. Thus, device fabrication has evolved around the inert environment of the glove box, resulting in highly efficient devices which unfortunately are very sensitive to oxygen and water through a multitude of degradation pathways[8].

Even now, as the science moves closer to real application, there are still relatively few reports concerned with substituting toxic solvents with more benign ones, for processing the active layer[9–19], where many are hybrid cells [10,12,19–21]. This has to do with the intricate relationship between solvent, solubility, morphology and device performance, and so to switch the solvent type, researchers would have to redo polymer designs and process optimization procedures, and thus would have to settle for efficiencies much below the record cells of today, at least for a time.

3.1.1. Polymer nanoparticles via emulsification

A facile and versatile route for fabricating aqueous polymer nanoparticle inks was pioneered by Landfester et al. [14,22–24] based on the water-in-oil miniemulsion method[25,26]. The route produces a stable aqueous dispersion of polymer nanoparticles, as sketched in Figure 3.7: A two-phase solution (I) containing a hydrophobic polymer-phase and an aqueous phase containing the anionic surfactant SDS. High shear is then exerted on the two-phase solution by sonication, promoting the formation of micelles (II) containing the polymer phase still in solution, suspended in the water. Depending on the boiling-point of the organic solvent used for the polymer solution, heating will cause the solvent in the micelles to evaporate, leaving behind micelles containing solid nanoparticles, held in aqueous suspension by the amphiphilic SDS molecules (III).

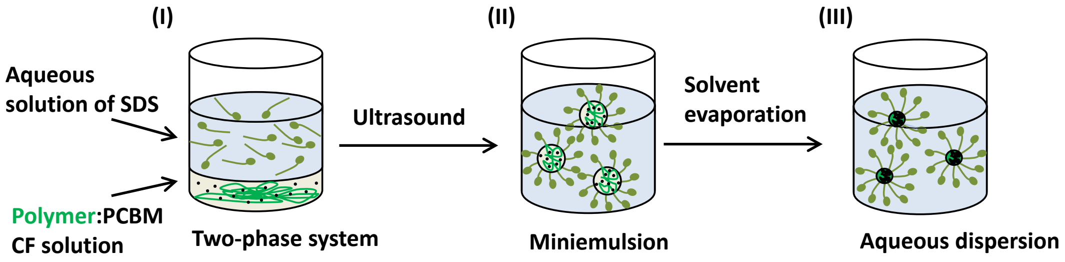

Figure 3.7: Production of polymer:pcbm blend nanoparticles in aqueous suspension, through miniemulsification of a CF-water two-phase system using the surfactant SDS and sonication.

The polymer phase can consist of either a single type of polymer or a blend of materials soluble in a common organic solvent (and insoluble in water), resulting in either single-phased particles or multi-phased particles respectively. In this way, the method constitutes a possible route for controlling the morphology in a layer formed by such nanoparticles, as would be very useful e.g. in a BHJ.

In order to obtain morphology control through the use of these nanoparticles, one must have control of their size, and in the case of multiphased particles, their internal structure. As also reported by Landfester et al., the particle diameter can be controlled by the concentration of the surfactant as well as the concentration of the hydrophobic phase in the approximate range of 30-500 nm [14], such that more surfactant and less polymer both results in smaller particles. Furthermore, we found that the surfactant/size relationship and the accessible size range seemed very dependent on the type of dissolved polymer [15].

Kietzke et al. compared PV devices, based on either a mixture of single-phased poly(9,9-dioctylfluorene-co-N,N-bis(4-butylphenyl)-N,Ndiphenyl-1,4-phenylenediamine) (PFB) and poly (9,9-dioctylfluorene-co-benzothiadiazol) (F8BT) or two-phased particles made from a PFB:F8BT blend [24], revealing very different relations between PFB:F8BT ratios and PV performance explained by less intimate contact between the phases in the case of single component particles resulting in too large domains relative to the exciton diffusion length. Whereas it is proposed that the two-phase particles have a Janus-particle composition combined with a large degree of phase intermixing. The Janus-like particle morphology is further supported by a later paper by Kietzke et al. [27] using TEM and PL spectroscopy. Recently however, Dastoor and his team [28,29] also prepared PV devices using similarly fabricated PFB:F8BT nanoparticles, obtaining much higher device efficiencies by depositing multiple layers sequentially, as is possible due to the collapse of the micelles upon film formation.

Furthermore they found that the particles exhibited a core-shell morphology, rather than the Janus-morphology, where again the large degree of phase mixing results in functional devices.

3.2. Device fabrication using polymer:PCBM blend nanoparticles

The miniemulsion approach to water processing of the BHJ active layer has several great advantages. One relates to the recuirement of orthogonal solubility in multilayer solution processing, as the layer formed by the aqueous nanoparticles becomes insoluble in water after filmformation due to the collabs of the micelles. This allows for the subsequent processing of other aqueous inks, such as PEDOT:PSS, without damaging the active layer. This also opens for possibilities in the area of multijunction solar cells, which will be explored in the next chapter.

A second great advantage of this nanoparticle approach is that it allows for the inclusion of the large existing portfolio of highly efficient polymers and fullerenes. To probe this advantage, we thus fabricated a series of nanoparticle inks based on a set of previously published low band-gap polymers as well as the all-time favorite model polymer of P3HT. All were combined with PCBM in a 1:1 weight ratio, to form two-phase particles. The results presented in the following can for the most part be found in ref. [15] (appendix 2).

3.2.1. Ink and film characterization

All inks were characterized by SAXS in order to obtain the particle size. Further characterization of solid films formed by spin coating the inks was done using AFM.

For the detailed fabrication procedure specific for the inks in Table 3.2, please refer to refs. [15,16]

Table 3.2: The particle diameter of the different nanoparticle inks.

Materials	Particle diameter (est. standard deviation) [nm]		Active layer thickness[c] (est. standard deviation) [nm]
	SAXS[a]	AFM[b]	AFM
P3HT:PCBM	(2 x) 46	NA	NA
PSBTBT [30]	32 (10)	69 (47)	500 (25)
TQ1 [31]	87 (21)	120 (82)	612 (22)

a: in solution. b: in solid film. c: Referring to the R2R devices.

3.2.2. Roll-to-roll large area devices fabrication

Large area devices were fabricated by R2R slot-die coating, following the well-known ProcessOne [32] only with the usual CLB-based active layer ink substituted with the aqueous nanoparticle ink. The processing of the aqueous inks was challenging at first, where detrimental dewetting was observed as shown in Figure 3.8(a-c). The phenomenon is ascribed to surface poisoning during coating by the dynamic nature of the ink itself; as the ink dries the micelles collapses and the nanoparticles becomes hydrophobic which poisons the surface and causes the dewetting. This is why a thin layer, most likely a monolayer of particles, can be observed in Figure 3.8c covering the whole width of the stripe.

This problem was solved by the addition of the non-ionic fluorosurfactant (FSO-100) to the ink. This resulted in nice and smooth films as can be seen in Figure 3.8(d-e). Later, similar results have been obtained using a more environmentally friendly wetting agent (TWEEN80, Sigma-Aldrich).

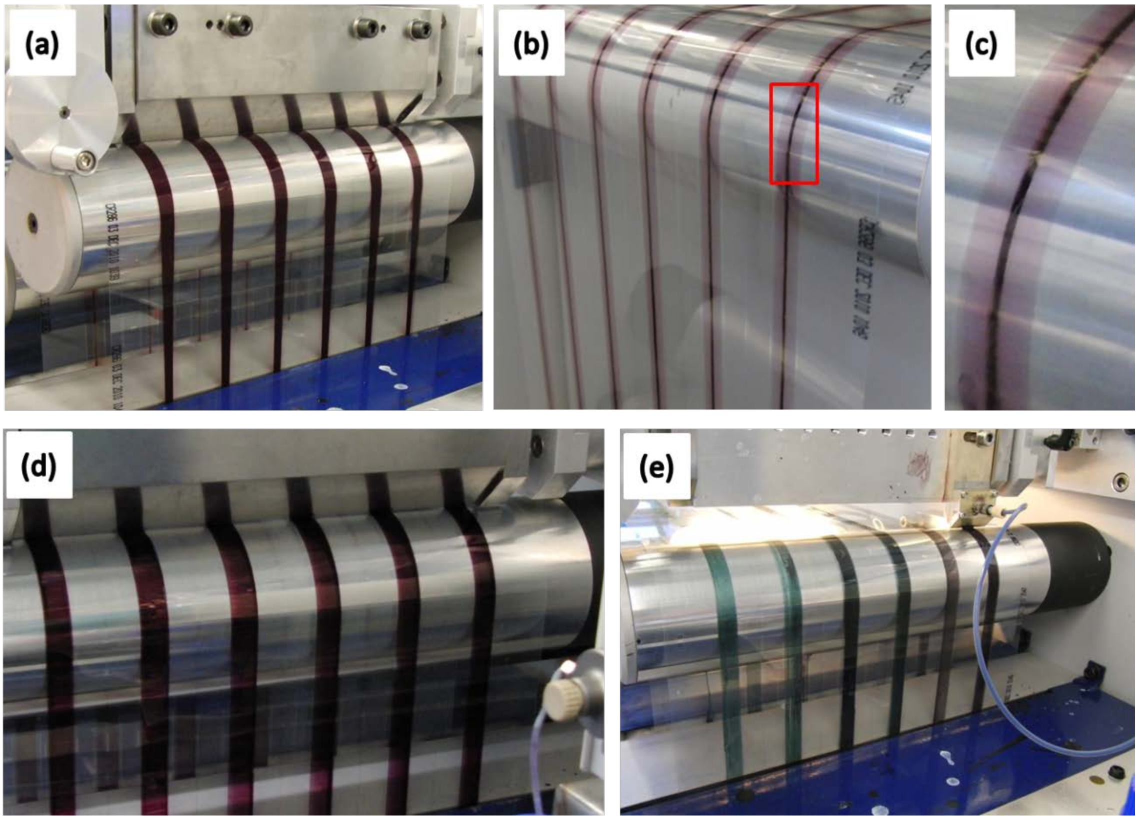

Figure 3.8: Dewetting during slot-die coating of the aqueous nanoparticle ink, showing the progression from (a) wide lines right after coating to (b) the stripe has pulled up into a thin line, with (c) showing a magnification of the outlined area. Examples of successful slot-die coating of (d) six simultaneous stripes of P3HT-based NPs, and (e) low band-gap polymer NPs one stripe at the time.

3.2.3. Small spin-coated devices

The standard approach to PSC device fabrication is spin coating. The same is the case for previously reported application of the aqueous nanoparticle inks for OPV devices [14]. Thus, in order to obtain more comparable data, as well as having a platform for small scale testing, devices were also fabricated using spin coating. The device structure was kept at the same inverted type as was used in the R2R process, only based on rigid Glass/ITO substates instead: Glass/ITO/ZnO/NP-ink (active layer)/PEDOT:PSS/Ag. The same dewetting issues were also present when spin-coating, and thus it was natural to use the same inks as was used for slot-die coating.

3.2.4. Device performance

The devices were subjected to J-V characterization using STC, and the results are shown in Figure 3.9(a-c) and summarized in Table 3.3 : Summary of J-V characterizationi of the nanoparticle based solar cells.. As can be seen by comparing Figure 3.9a and c, the SC and the R2R devices follow similar trends, with the PSBTBT-based devices performing best and the TQ1 devices performing worst. In both cases the PSBTBT-based cells show a significant factor of two better performance, mainly due to a higher short-circuit current, but also a higher open-circuit voltage. These results were amongst the highest reported performances for water-processed active layer, and furthermore constituted the first reported aqueous R2R-processing of the active layer in a PSC. In all cases, however, the performance is significantly less than what has been achieved with the same polymers processed by regular spin coating and using chlorinated solvents, where devices based on both PSBTBT [33] and TQ1 [31] mixed with PCBM with up to 5% in PCE have been reported albeit under optimized conditions and for very small devices, while P3HT is well known to give above 3% in PCE. Such lower performance is not unexpected, as this nanoparticle approach constitutes a new way of forming the BHJ, and the performance is bound to be very dependent on the internal morphology of the two-component particles, as well as the interparticle contact and packing density. In the same way, the relatively higher performance of the PSBTBT nanoparticle devices might be due to a combination of favourable particle morphology and size, where referring to Table 3.2 suggests that smaller particle size leads to higher performance. Furthermore, if the two-phase particle has a core-shell morphology the performance might be very sensitive to the miscibility of the fullerene in the different polymers, as has also recently been suggested by Dastoor et al. [34,35]. A quantitative comparison of the miscibility of PCBM in the polymers was beyond the scope here, but studies by Collins et al. have found good miscibility in the amorphous part of P3HT and PSBTBT films [36,37], while a study by Lindqvist et al. [38] suggests low miscibility of PCBM in TQ1. This might be a contributing factor in the large observed difference in performance, as well as in the stability of the R2R devices under continuous illumination at 85 °C shown in Figure 3.9b, where TQ1 peaks after only 14 min followed by a rapid degradation. Contrary, the difference in degradation patters are likely not linked to photochemical degradation as all polymer-fullerene blends have been found to be quite stable in this regard [39].

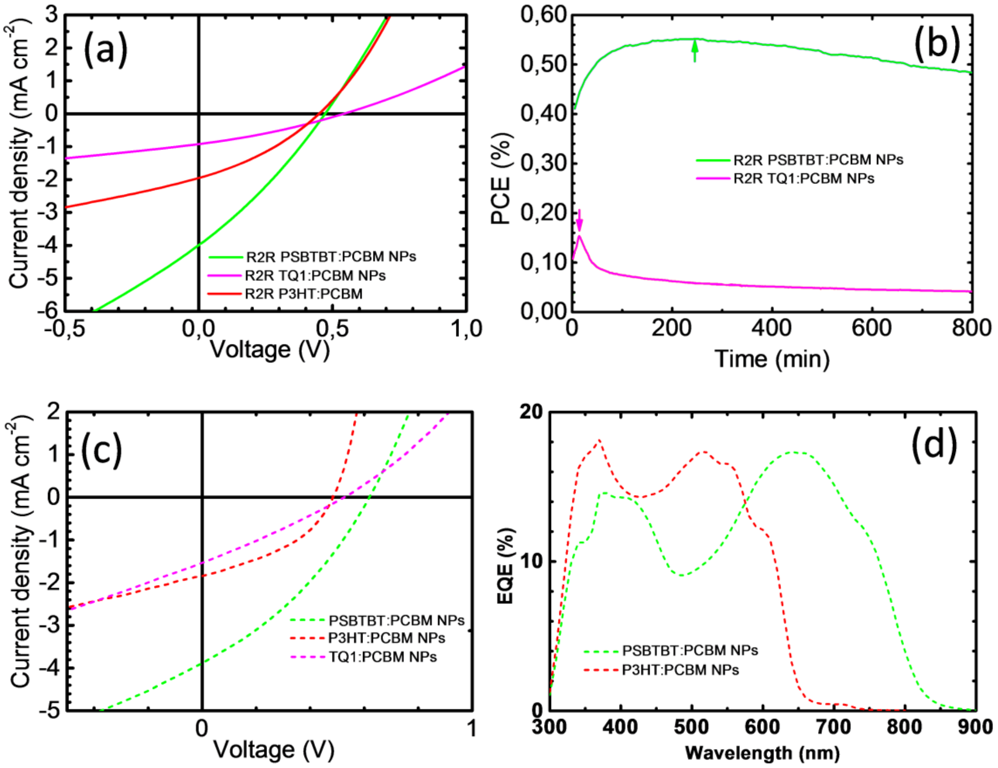

Figure 3.9: J-V curves of Large area R2R coated devices under STC, where (a) shows the best J-V curves, taken from (b) a performance-time study of large area devices, as indicated by the arrows (after 145 min and 14 min for the PSBTBT and TQ1 respectively). (c) J-V curves of the best spin-coated polymer:PCBM NP-based devices, fabricated on Glass/ITO. (d) EQE data of the PSBTBT- and P3H-based devices.

Table 3.3 : Summary of J-V characterizationi of the nanoparticle based solar cells.

Polymer	Proc. method	PCE (%)	V_{oc} (V)	J_{sc} (mA cm^{-2})	FF (%)
P3HT	SC	0.58	0.48	2.95	40.2
	R2R	0.29	0.45	1.95	33.1
PSBTBT	SC	1.29	0.62	6.21	33.5
	R2R	0.55	0.47	3.99	29.3
TQ1	SC	0.32	0.52	2.45	27.5
	R2R	0.15	0.54	0.92	30.8

3.3. Simultaneous multi-layer formation by double slot-die coating

A large part of the energy that goes into making PSCs via R2R, is consumed in the drying of the different layers [3]. As part of the upscaling of fabrication production speed, i.e. web speed, must increase, and so must the size of the drying equipment. One way to dramatically cut down on the number of drying steps would be to coat several layers at the same time. One way to do this is using slot-die coating. The simplest example is the formation of two simultaneous layers, for example by so-called double slot-die (DSD) coating, the concept of which is shown in Figure 3.10.

The use of DSD coating possibly has other unique advantages: Some of which relates to the difficulties regarding solvent orthogonality, as two layers soluble in a common solvent could be coated simultaneously to form a bilayer which could not have been formed with single layer coating. Furthermore, the intermixed region formed between the two layers will result in a diffuse bilayer structure with large interfacial area, which could be utilized in a donor-acceptor bilayer device. The diffuse nature will also increase the adhesion between the simultaneously formed layers, which can have great beneficial influence on the stability and durability of the final device [40,41].

The latter example is of importance in the work presented in the following, where we utilize the aqueous P3HT-PCBM nanoparticle active layer ink together with an aqueous PEDOT:PSS (Agfa Orgacon EL-P 5010 diluted with water 2:1 w/w) to test double slot-die coating for the simultaneous formation of active layer and HTL in a PSC.

Coating two wet films on top of each other, is of course no easy task. For one it entails the use of highly viscos inks in order to prevent intermixing during film formation. The PEDOT:PSS can be made very viscous, while the active layer inks are normally limited by the solubility. By using a nanoparticle suspension, the solid concentration could possibly be made much higher. For this experiment, however, we ‘only’ succeeded in making a 60 mg ml^{-1} active layer ink.

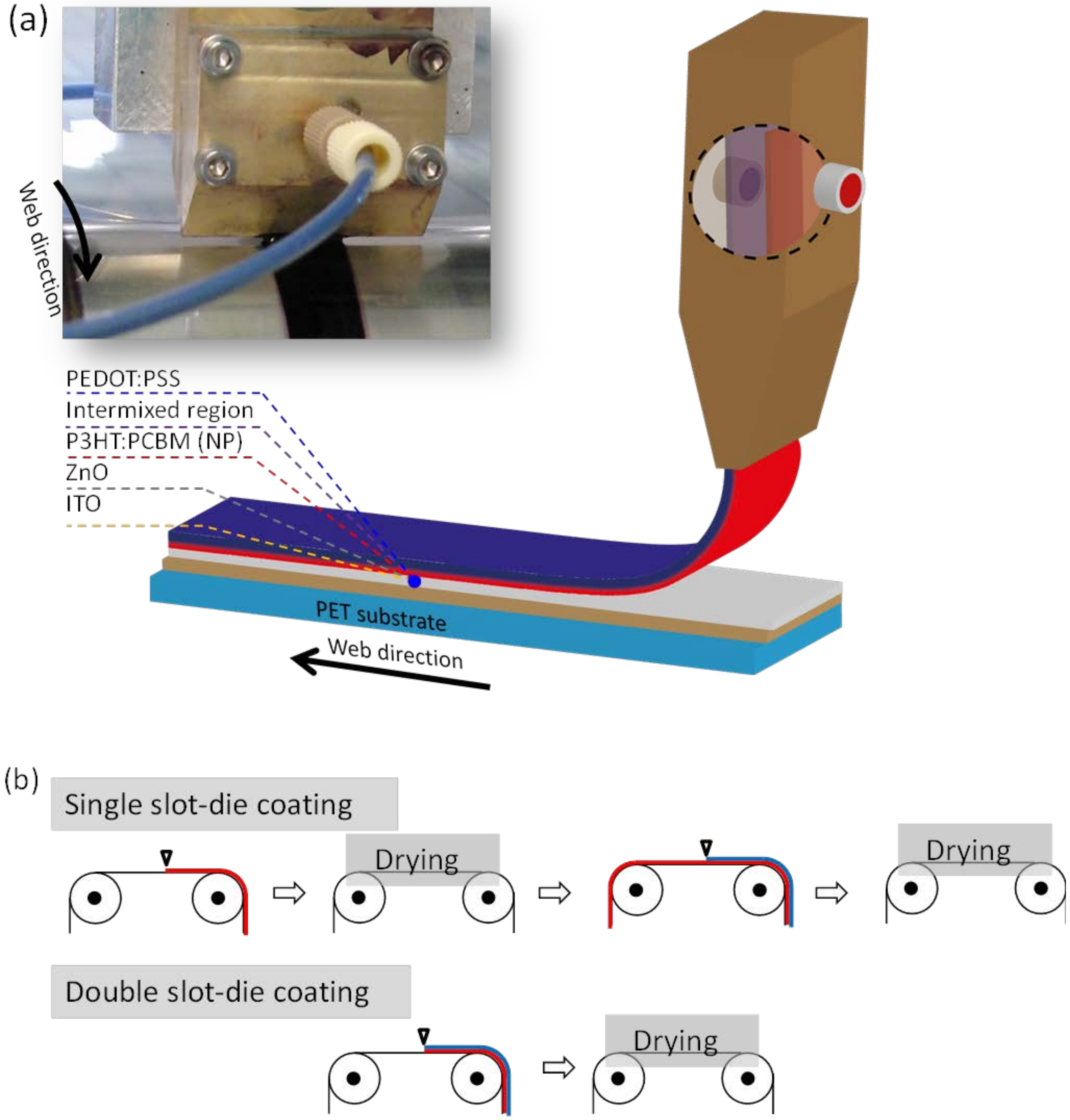

Figure 3.10: (a) Illustration of the DSD coating experiment, where the photo-insert shows the actual coating experiment. (b) Shows how both a coating and a drying-step is eliminated by using DSD coating.

3.3.1. Characterization of the bilayer

In order to verify that the DSD coating indeed did result in a bilayer structure, several methods were employed. The strongest evidence came from combined visual and chemical confirmation: First a piece of DSD coated film was submerged in an aqueous solution of NaOH, where after a while a discreet layer of PEDOT:PSS simply delaminated and floated off, exposing the underlying layer of P3HT:PCBM. Figure 3.11a shows a picture of the experiment, where the colours of the floating film (dark blue) and substrate (red) indicates the materials of the respective layers as shown in Figure 3.11b. To verify the chemical species, a TOF-SIMS experiment was conducted on the piece of film, probing the vertical chemical composition of the stack at the place indicated by the green arrow in Figure 3.11a. The results are plotted in Figure 3.11c and confirm the stacking order, where ionic markers for PEDOT:PSS, P3HT:PCBM and ZnO/ITO, were S^-, SO_x^- and InO^- respectively. However, neither S^- nor SO_x^- are unique to PEDOT:PSS and P3HT:PCBM respectively, and thus it was not possible to say anything conclusive of the extension of the intermixed region between the two layers. It is clear, however, that a bilayer is formed, and as it was not possible to delaminate the PEDOT:PSS layer in a simple tape-test which otherwise completely delaminates the corresponding single-layer coated PEDOT:PSS/P3HT:PCBM interface, at least the interlayer adhesion is greatly improved.

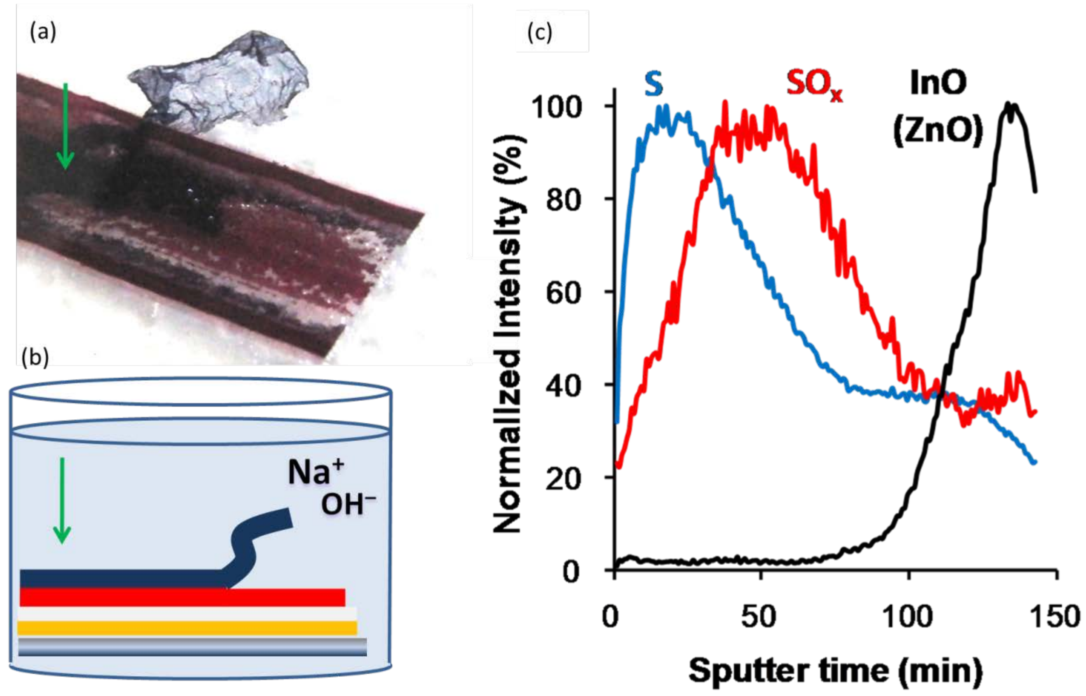

Figure 3.11: (a) Shows a piece of DSD coated stack on PET, where the PEDOT:PSS layer has delaminated from the underlying P3HT:PCBM layer due to a submersion in an aqueous NaOH solution. (b) shows the setup, while (c) shows the results of a TOF-SIMS experiment on the same piece of foil, confirming the bilayer structure, and where the green arrows in (a) and (b) marks the sputter area.

3.3.2. Device performance

Devices were finalized with an electrode being either a piece of Cu tape or a layer of evaporated Ag. J-V curves were recorded under STC and are shown in Figure 3.12 where they are compared to a reference device coated using the usual single slot-die technique. The results are summarized in Table 3.4. Blank devices of PET/ITO/ZnO/PEDOT:PSS/Cu-tape and PET/ITO/ZnO/P3HT:PCBM/Cu-tape were also prepared (not shown) and showed no measurable PV activity. Although the DSD devices perform significantly worse than the reference for all PV parameters, they do show clear PV activity, and in the case of the evaporated Ag electrode device a non-linear rectifying behaviour in forward bias. From the J-V behaviour it is clear that the devices are resistive in nature, owing from a high series resistance and a low shunt resistance. The latter is likely the cause of shunting of PEDOT:PSS through the active layer due to the nature of the DSD coating. In the case of the Cu-tape device, the shunting is supressed possibly by a preferential contacting to the top-most part of the PEDOT:PSS, while the device is limited by the PEDOT:PSS/Cu contact resistance in forward bias.

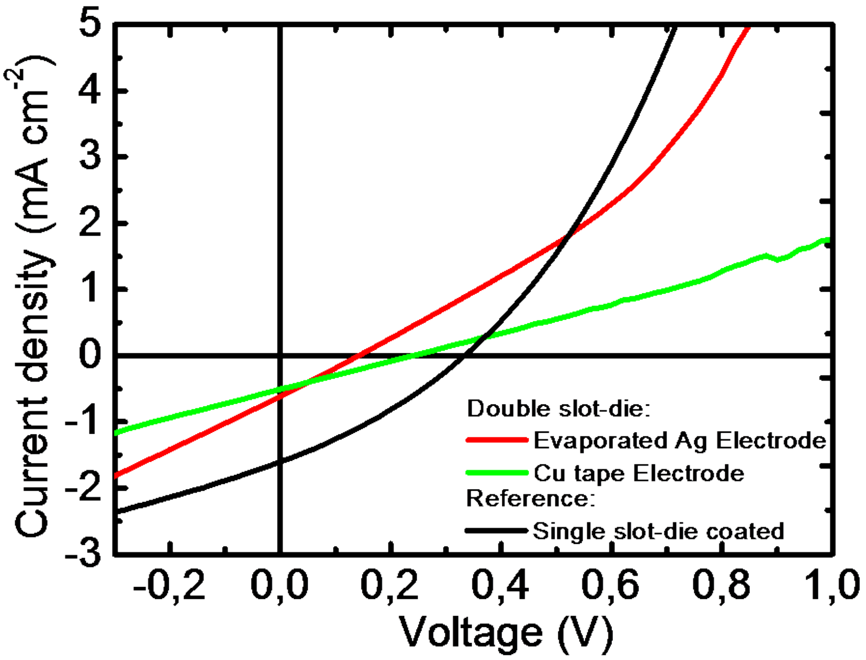

Figure 3.12: J-V Curves of devices prepared from the DSD coated stack, and compared with a reference devices prepared with regular single slot-die coating.

Table 3.4: Summary of J-V characterization of the DSD coated devices and the reference.

Device	J_{sc} (mA cm^{-2})	V_{oc} (V)	FF (%)	PCE (%)
Cu-tape	0.5	0.24	25	0.03
Ag evap	0.61	0.14	25.6	0.02
Reference	1.95	0.45	33.1	0.29

3.4. Conclusion

The miniemulsion method was used to fabricate aqueous dispersions of polymer:PCBM blend nanoparticles using the LBG polymers TQ1 and PSBTBT, in addition to P3HT. These dispersions were made into aqueous active layer inks, and utilized in fully R2R fabricated polymer solar cells following the well-known ProcessOne, constituting the first reported aqueous R2R processing of the active layer of polymer solar cells. The highest efficiencies of 0.55% for large-area R2R cells and 1.29% for smaller area spin-coated cells were obtained with the polymer PSBTBT. A generally lower performance of the large area solar cells compared to the spin-coated cells was observed, likely a result of the complex task of R2R slot-die coating the aqueous inks, a process which has yet to be completely optimized.

The aqueous inks were also employed in R2R double slot-die coating of polymer solar cells, where PEDOT:PSS and P3HT was simultaneously coated into a bilayer, completing the polymer solar cell stack of PET/ITO/ZnO/P3HT:PCBM/PEDOT:PSS. This novel technique in the context of solar cells, produced working devices with J_{sc} of around 0,5 mAcm^{-2} and V_{oc} up to 0.24 V. The bilayer stack was visually confirmed by physical delamination, and chemically identified using TOF-SIMS. Although the PV performance was significantly lower than comparable single slot-die coated R2R cells, the experiment proves the concept of DSD and the possible advantages of coating two layers at once, such as less energy for drying and increased interlayer adhesion.

3.5. References

[1] N. Espinosa, F.O. Lenzmann, S. Ryley, D. Angmo, M. Hösel, R.R. Søndergaard, et al., OPV for mobile applications: an evaluation of roll-to-roll processed indium and silver free polymer solar cells through analysis of life cycle, cost and layer quality using inline optical and functional inspection tools, Journal of Materials Chemistry A. (2013).

[2] B. Azzopardi, C.J.M. Emmott, A. Urbina, F.C. Krebs, J. Nelson, Economic assessment of solar electricity production from organic-based photovoltaic modules in a domestic environment, Energy & Environmental Science. 4 (2011) 3741–3753.

[3] N. Espinosa, M. Hösel, D. Angmo, F.C. Krebs, Solar cells with one-day energy payback for the factories of the future, Energy & Environmental Science. 5 (2012) 5117.

[4] N. Espinosa, R. García-Valverde, A. Urbina, F. Lenzmann, M. Manceau, D. Angmo, et al., Life cycle assessment of ITO-free flexible polymer solar cells prepared by roll-to-roll coating and printing, Solar Energy Materials and Solar Cells. 97 (2011) 3–13.

[5] C.J.M. Emmott, A. Urbina, J. Nelson, Environmental and economic assessment of ITO-free electrodes for organic solar cells, Solar Energy Materials and Solar Cells. 97 (2011) 14–21.

[6] N. Espinosa, R. García-Valverde, F.C. Krebs, Life-cycle analysis of product integrated polymer solar cells, Energy & Environmental Science. 4 (2011) 1547.

[7] N. Espinosa, R. García-Valverde, A. Urbina, F.C. Krebs, A life cycle analysis of polymer solar cell modules prepared using roll-to-roll methods under ambient conditions, Solar Energy Materials and Solar Cells. 95 (2010) 1293–1302.

[8] M. Jørgensen, K. Norrman, S.A. Gevorgyan, T. Tromholt, B. Andreasen, F.C. Krebs, Stability of polymer solar cells., Advanced Materials. 24 (2012) 580–612.

[9] K.-S. Chen, H.-L. Yip, C.W. Schlenker, D.S. Ginger, A.K.-Y. Jen, Halogen-free solvent processing for sustainable development of high efficiency organic solar cells, Organic Electronics. 13 (2012) 2870–2878.

[10] Z. Chen, H. Zhang, W. Yu, Z. Li, J. Hou, H. Wei, et al., Inverted Hybrid Solar Cells from Aqueous Materials with a PCE of 3.61%, Advanced Energy Materials. 3 (2013) 433–437.

[11] Q. Qiao, J.T. McLeskey, Water-soluble polythiophene⁄nanocrystalline TiO2 solar cells, Applied Physics Letters. 86 (2005) 153501.

[12] Z. Chen, H. Zhang, X. Du, X. Cheng, X. Chen, Y. Jiang, et al., From planar-heterojunction to n–i structure: an efficient strategy to improve short-circuit current and power conversion efficiency of aqueous-solution-processed hybrid solar cells, Energy & Environmental Science. 6 (2013) 1597.

[13] R.R. Søndergaard, M. Helgesen, M. Jørgensen, F.C. Krebs, Fabrication of Polymer Solar Cells Using Aqueous Processing for All Layers Including the Metal Back Electrode, Advanced Energy Materials. 1 (2010) 68–71.

[14] T. Kietzke, D. Neher, K. Landfester, R. Montenegro, R. Güntner, U. Scherf, Novel approaches to polymer blends based on polymer nanoparticles., Nature Materials. 2 (2003) 408–12.

[15] T.R. Andersen, T.T. Larsen-Olsen, B. Andreasen, A.P.L. Böttiger, J.E. Carlé, M. Helgesen, et al., Aqueous Processing of Low-Band-Gap Polymer Solar Cells Using Roll-to-Roll Methods., ACS Nano. 5 (2011) 4188–4196.

[16] T.T. Larsen-Olsen, B. Andreasen, T.R. Andersen, A.P.L. Böttiger, E. Bundgaard, K. Norrman, et al., Simultaneous multilayer formation of the polymer solar cell stack using roll-to-roll double slot-die coating from water, Solar Energy Materials and Solar Cells. 97 (2012) 22–27.

[17] T.T. Larsen-Olsen, T.R. Andersen, B. Andreasen, A.P.L. Böttiger, E. Bundgaard, K. Norrman, et al., Roll-to-roll processed polymer tandem solar cells partially processed from water, Solar Energy Materials and Solar Cells. 97 (2012) 43–49.

[18] Y.-X. Nan, X.-L. Hu, T.T. Larsen-Olsen, B. Andreasen, T. Tromholt, J.W. Andreasen, et al., Generation of native polythiophene/PCBM composite nanoparticles via the combination of ultrasonic micronization of droplets and thermocleaving from aqueous dispersion, Nanotechnology. 22 (2011) 475301.

[19] Q. Dong, W. Yu, Z. Li, S. Yao, X. Zhang, B. Yang, et al., All-water-solution processed solar cells based on PPV and TiO2 nanocrystals, Solar Energy Materials and Solar Cells. 104 (2012) 75–80.

[20] L. Baeten, B. Conings, J. D'Haen, A. Hardy, J. V. Manca, M.K. Van Bael, Fully water-processable metal oxide nanorods/polymer hybrid solar cells, Solar Energy Materials and Solar Cells. 107 (2012) 230–235.

[21] B. Park, Y. Chan Kim, S.H. Yun, All-solution-processed inverted polymer solar cells with low temperature, water-processable hybrid electron-collecting layers, Journal of Materials Chemistry A. 1 (2013) 2030.

[22] K. Landfester, The Generation of Nanoparticles in Miniemulsions, Advanced Materials. 13 (2001) 765–768.

[23] K. Landfester, R. Montenegro, U. Scherf, R. Güntner, U. Asawapirom, S. Patil, et al., Semiconducting Polymer Nanospheres in Aqueous Dispersion Prepared by a Miniemulsion Process, Advanced Materials. 14 (2002) 651–655.

[24] T. Kietzke, D. Neher, M. Kumke, R. Montenegro, K. Landfester, U. Scherf, A Nanoparticle Approach To Control the Phase Separation in Polyfluorene Photovoltaic Devices, Macromolecules. 37 (2004) 4882–4890.

[25] J. Ugelstad, M.S. El-Aasser, J.W. Vanderhoff, Emulsion polymerization: Initiation of polymerization in monomer droplets, Journal of Polymer Science: Polymer Letters Edition. 11 (1973) 503–513.

[26] M.S. El-Aasser, C.D. Lack, Y.T. Choi, T.I. Min, J.W. Vanderhoff, Interfacial aspects of miniemulsions and miniemulsion polymers, Colloids and Surfaces. 12 (1984) 79–97.

[27] T. Kietzke, D. Neher, M. Kumke, O. Ghazy, U. Ziener, K. Landfester, Phase separation of binary blends in polymer nanoparticles., Small (Weinheim an Der Bergstrasse, Germany). 3 (2007) 1041–8.

[28] K.B. Burke, A.J. Stapleton, B. Vaughan, X. Zhou, a L.D. Kilcoyne, W.J. Belcher, et al., Scanning transmission x-ray microscopy of polymer nanoparticles: probing morphology on sub-10 nm length scales., Nanotechnology. 22 (2011) 265710.

[29] A. Stapleton, B. Vaughan, B. Xue, E. Sesa, K. Burke, X. Zhou, et al., A multilayered approach to polyfluorene water-based organic photovoltaics, Solar Energy Materials and Solar Cells. 102 (2012) 114–124.

[30] J. Hou, H.-Y. Chen, S. Zhang, G. Li, Y. Yang, Synthesis, characterization, and photovoltaic properties of a low band gap polymer based on silole-containing polythiophenes and 2,1,3-benzothiadiazole., Journal of the American Chemical Society. 130 (2008) 16144–5.

[31] E. Wang, L. Hou, Z. Wang, S. Hellström, F. Zhang, O. Inganäs, et al., An Easily Synthesized Blue Polymer for High-Performance Polymer Solar Cells, Advanced Materials. 22 (2010) 5240–5244.

[32] F.C. Krebs, S.A. Gevorgyan, J. Alstrup, A roll-to-roll process to flexible polymer solar cells: model studies, manufacture and operational stability studies, Journal of Materials Chemistry. 19 (2009) 5442.

[33] H. Lu, B. Akgun, T.P. Russell, Morphological Characterization of a Low-Bandgap Crystalline Polymer:PCBM Bulk Heterojunction Solar Cells, Advanced Energy Materials. (2011) n/a–n/a.

[34] S. Ulum, N. Holmes, M. Barr, A.L.D. Kilcoyne, B. Bin Gong, X. Zhou, et al., The role of miscibility in polymer:fullerene nanoparticulate organic photovoltaic devices, Nano Energy. (2013) 1–8.

[35] N.P. Holmes, K.B. Burke, P. Sista, M. Barr, H.D. Magurudeniya, M.C. Stefan, et al., Nano-domain behaviour in P3HT:PCBM nanoparticles, relating material properties to morphological changes, Solar Energy Materials and Solar Cells. 117 (2013) 437–445.

[36] B. a. Collins, E. Gann, L. Guignard, X. He, C.R. McNeill, H. Ade, Molecular Miscibility of Polymer−Fullerene Blends, The Journal of Physical Chemistry Letters. 1 (2010) 3160–3166.

[37] B.A. Collins, Z. Li, C.R. McNeill, H. Ade, Fullerene-Dependent Miscibility in the Silole-Containing Copolymer PSBTBT-08, Macromolecules. 44 (2011) 9747–9751.

[38] C. Lindqvist, A. Sanz-Velasco, E. Wang, O. Bäcke, S. Gustafsson, E. Olsson, et al., Nucleation-limited fullerene crystallisation in a polymer–fullerene bulk-heterojunction blend, Journal of Materials Chemistry A. 1 (2013) 7174.

[39] T. Tromholt, M.V. Madsen, J.E. Carlé, M. Helgesen, F.C. Krebs, Photochemical stability of conjugated polymers, electron acceptors and blends for polymer solar cells resolved in terms of film thickness and absorbance, Journal of Materials Chemistry. 22 (2012) 7592.

[40] S.R. Dupont, M. Oliver, F.C. Krebs, R.H. Dauskardt, Interlayer adhesion in roll-to-roll processed flexible inverted polymer solar cells, Solar Energy Materials and Solar Cells. 97 (2012) 171–175.

[41] V. Brand, C. Bruner, R.H. Dauskardt, Cohesion and device reliability in organic bulk heterojunction photovoltaic cells, Solar Energy Materials and Solar Cells. 99 (2012) 182–189.

4 Tandem Solar Cells via orthogonal processing

4.1. Theoretical limits

Solar cell efficiency in general is limited by fundamental loss mechanisms. In this regard the 1961 report by Shockley and Queisser formulating the so-called detailed balance limit as the theoretical upper limits to solar cell efficiency [1]. As can be seen in Figure 4.1a, most energy is lost in the form of unabsorbed photons and in thermalization, i.e. relaxation of hot carriers [2], to an extend very much dependant on the band-gap, and with a maximum efficiency just above 30%. As seen in Figure 4.1b these losses can be alleviated by the stacking of several discreet junctions, into multi-junction solar cells, thus increasing the theoretically achievable efficiency to above 50%.

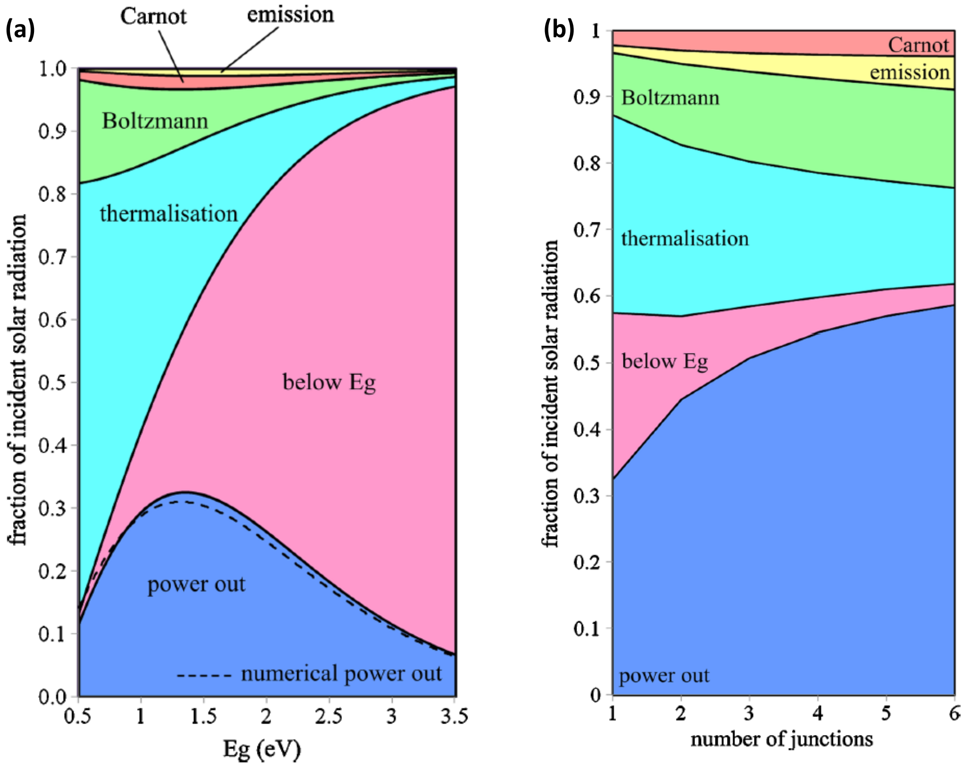

Figure 4.1: (a) Fundamental losses in ideal solar cells divided on processes and power out, as a function of band-gap (Eg). (b) Loss processes and power out in an unconstrained, multijunction device under one sun illumination. Optimal bandgaps are used in each case. All mechanisms are shown to be dependent on the number of junctions. (a,b) As all incident photons are accounted, the y-axis directly translates to the theoretical efficiency limit. Data is from analytical model published by Hirst and Ekins-Daukes in, and reproduced with permission from, ref. [2] **Copyright © 2010 John Wiley & Sons, Ltd.**

In the specific case of organic based solar cells, there are distinct loss mechanisms that need to be considered, e.g. the narrow absorption bands and low carrier mobility's of typical organic semiconductors. The first means that not only sub-band gap photons are lost, but also photons with too high energy. From the low carrier mobility follows that photo-active layers must be kept thin in order not to compromise performance. These distinct loss mechanisms render the multi-junction solution a very promising candidate to increase performance of OPV devices. Using a variety of OPV specific design criteria, the ultimate performance of tandem and triple-junction solar cells have been studied by many [3–9]. Dennler et al. found that the ultimate efficiency could be raised from around 10% in single junction cells, to almost 15% by introducing an extra junction in the PSC [3]. Recently, Minaert et al. applied a more general approach to the investigation of the efficiency merits and limits of organic tandem and triple-junction cells, and found that efficiencies up to 20.5% for the former and 22.7% for the latter, would be possible given the development of materials with the right band gaps and absorption widths [6].

4.2. Experimental advances in solution processing of monolithic multi-junction PSCs

Since the hero tandem PSC of Kim et al. in 2007, presenting a 6.5% efficient, mostly solution processed device [10], tandem PSCs have been identified with record efficiencies, and the increasing scientific interest in the area is epitomised by a relatively large number of reviews [11–14]. Never-the-less, the number of publications dealing with tandem PSCs is still relatively small [15]. This is undoubtedly linked to the processing difficulties connected with realizing monolithic multi-junction cells [16,17], while the efficiency gap between single and tandem record devices is still observed to be minor [18]. With respect to the scalability of device fabrication, where all solution processing and the use of the inverted device architecture are essential, little work prior to that presented in this chapter, had been carried out [19–21]. However, following the establishment of PEDOT:PSS/ZnO as a reliable interconnection layer, a recent surge in the reports on inverted tandem PSCs with more than 5% efficiency has been seen [14], notably by the groups of Yang Yang [17,22–24] and René Janssen [25–27], presenting hero tandem and triple-junction devices, respectively, with above 10% efficiency [24,27]. These very high efficiency devices represent outstanding achievements, nevertheless, being fabricated on rigid glass substrates using spin coating and thermal evaporation and having small active areas (<< 1cm^2), they are still far removed from the vision of the R2R processed polymer solar cells. Furthermore, the technical challenge, and thus the technical nature of tandem PSC fabrication, only removes them further.

This chapter summarizes the efforts undertaken as part of this thesis, towards the realization of scalable tandem PSCs, presenting the first reported all-R2R processed tandem PSC (ref. [16] and appendix 4).

4.3. **Upscaling from spin coating to R2R coating**

As the first step towards fully R2R processed tandem PSCs, initial work was done on development of a robust, R2R-compatible, fabrication route. This involved the use of the inverted configuration and only solution processing. Central to the work was the development of a recombination layer (RL), which would be both impervious to the processing solvent of the second (back) BHJ so as to enable the use of a non-orthogonal solvent, while also ensuring a good electrical (serial) connection of the sub-cells. The effort resulted in a series of inverted tandem PSC devices, published in ref. [21], utilizing a RL consisting of V_2O_5 as HTL and ZnO as ETL as shown in Figure 4.2a. The J-V characteristics of the best tandem devices are presented in Figure 4.2b and Table 4.1. In both cases the tandem solar cells did not represent an increase in performance compared to the best performing sub-cell in a single junction device. However, the V_{oc} of the tandem devices were close to the expected sum of the sub-junction voltages, and the observed inflection point was demonstrated to have only minor influence on the PV performance [21]. The particular V_2O_5/ZnO RL thus presented a viable route for an all solution processed tandem PSC.

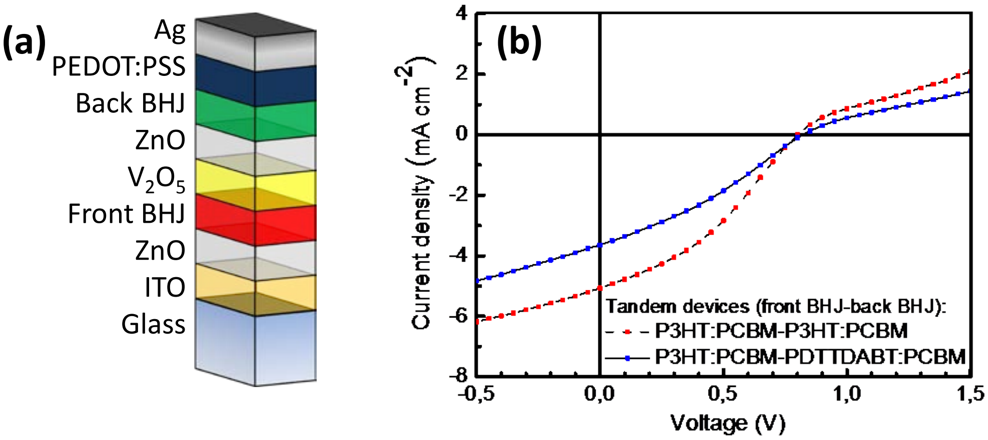

Figure 4.2: (a) The general structure of the tandem solar cells fabricated on glass. (b) The J-V curves of the best tandem PSC devices fabricated from non-orthogonal solvents.

Table 4.1: Summary of PV parameters of inverted tandem PSC devices, based on non-orthogonal solution processing of both BHJ layers, as published in ref. [21]**.**

Device (front BHJ-back BHJ)	PCE (%)	V_{oc} (V)	J_{sc} (mA cm^{-2})	FF (%)
P3HT:PCBM-P3HT:PCBM	1.4	0.80	5.1	36
P3HT:PCBM-PBTTDABT:PCBM	0.94	0.82	3.6	32

The next step was to transfer the process to R2R, by substituting Glass/ITO with flexible PET/ITO, spin coating with slot-die coating, and silver evaporation with screen printing, as illustrated in Figure 4.3. Unfortunately, the experiment resulted in poorly functioning devices, characterized by a low V_{oc} on the order of the single junction value (Figure 4.4d). Subsequent inspection of the layers using optical microscopy (Figure 4.4b) revealed cracks in the solar cell stack, originating in the V_2O_5 layer. Such cracks in the RL would result in solvent permeation during processing of the back BHJ layer, which in turn would re-solubilize the front BHJ and disrupt the integrity of the serial connection, and hence cause the observed low V_{oc} as schematically illustrated in Figure 4.4c. The cause of the cracking is thought to be related to the several steps of heating and cooling (up to 140°C) and/or the bending of the flexible substrate as it passes through the R2R machinery.

While the front BHJ was coated from a CB based solution of P3HT:PCBM, both CB and CF was tested as coating solvent for the back BHJ. As CF has a lower boiling point than CB it was thought that the solvent might evaporate fast enough as to avoid penetration of the RL. The use of CF however, did not improve the tandem device performance.

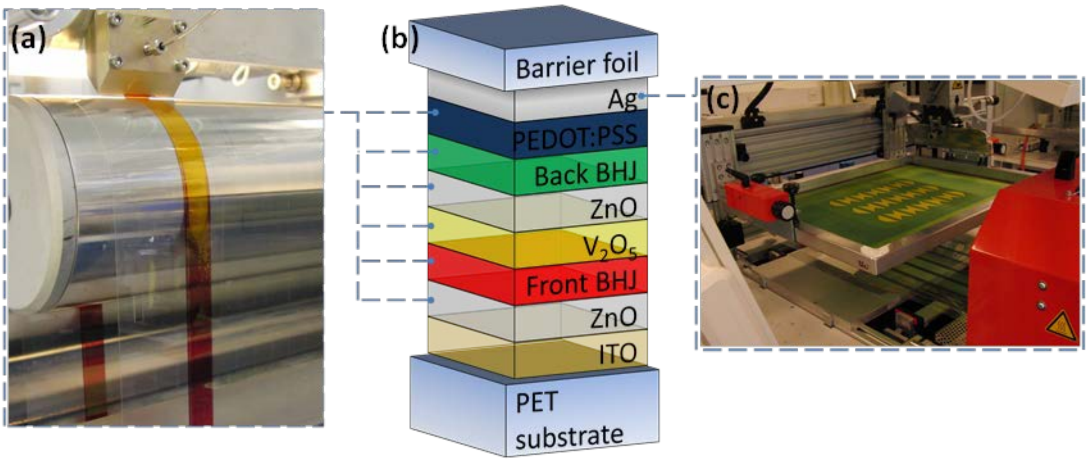

Figure 4.3: (a) Photograph of the slot die coating of the front P3HT:PCBM BHJ, a method used for all the layers indicated by the dashed lines, where (b) shows the completed R2R processed tandem PSC stack, and (c) shows a photograph (by Marcus Hösel) of the R2R screen printing technique used for the final back electrode.

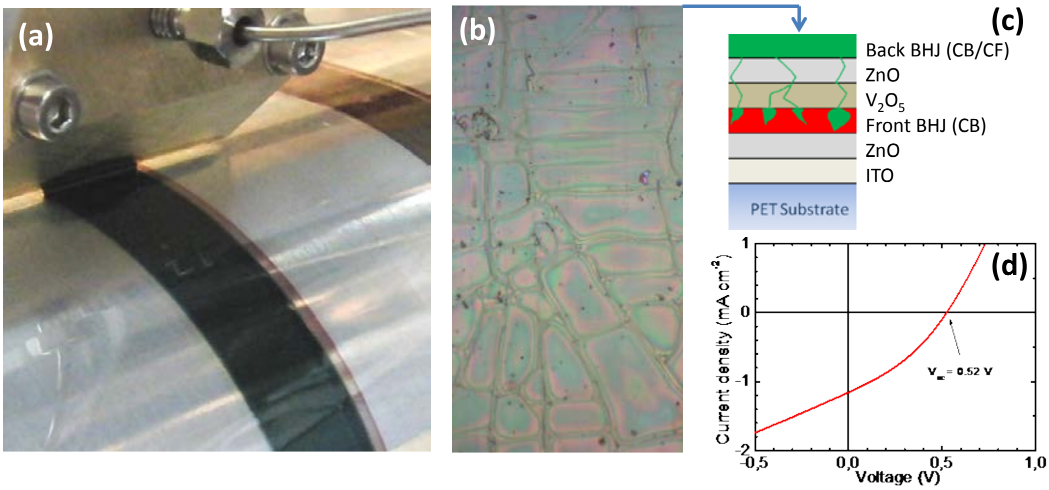

Figure 4.4: (a) Slot-die coating of the back BHJ using a chlorinated non-orthogonal solvent. (b) Micrograph (130 x 250 µm^2) of the back BHJ surface after coating, showing obvious cracks. (c) Schematic of the proposed effect of cracks in the RL during processing of the back BHJ with a non-orthogonal solvent. (d) Shows a typical J-V curve of the resulting R2R tandem devices, having a low V_{oc} of 0.52 V.

4.4. R2R water-based processing of the back BHJ

The use of the water-based inks, presented in the previous chapter, for the processing of the back BHJ offered a possible way to remove the effect of having a less-than-impervious RL.

An aqueous dispersion of TQ1:PCBM-based nanoparticles was thus successfully slot-die coated as the back BHJ of the tandem PSC, as shown in Figure 4.5a. Subsequent microscopy of the back BHJ revealed no cracks (Figure 4.5c), indicating that the tandem structure was intact, in a fashion shown in Figure 4.5b. The completed and encapsulated devices (using edge sealing [28]) were J-V characterized and the best performing tandem device is shown in Figure 4.6a (black circles) together with representative J-V curves for both tandem and back cell reference devices, with and without photo-annealing (800 min). The PV parameters are summarized in Table 4.2, while the time-evolution of J_{sc} and V_{oc} during the photo-annealing is shown in Figure 4.6b.

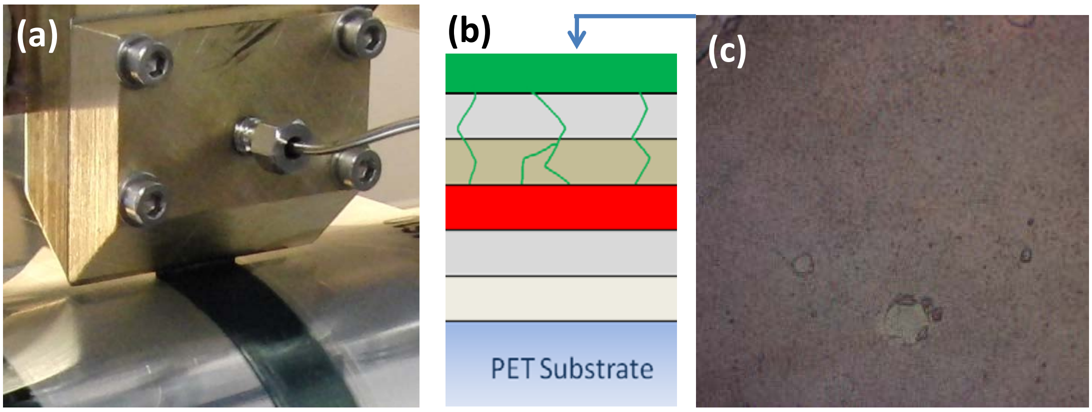

Figure 4.5: (a) Slot-die coating of the aqueous ink for the tandem back BHJ. (b) By using an orthogonal solvent (water) for the back BHJ, the front BHJ is not damaged. (c) Micrograph (180 x 180 µm^2) of the back BHJ after processing, as indicated by the arrow, showing no sign of cracks indicating a less damaged tandem cell compared to Figure 4.4(b).

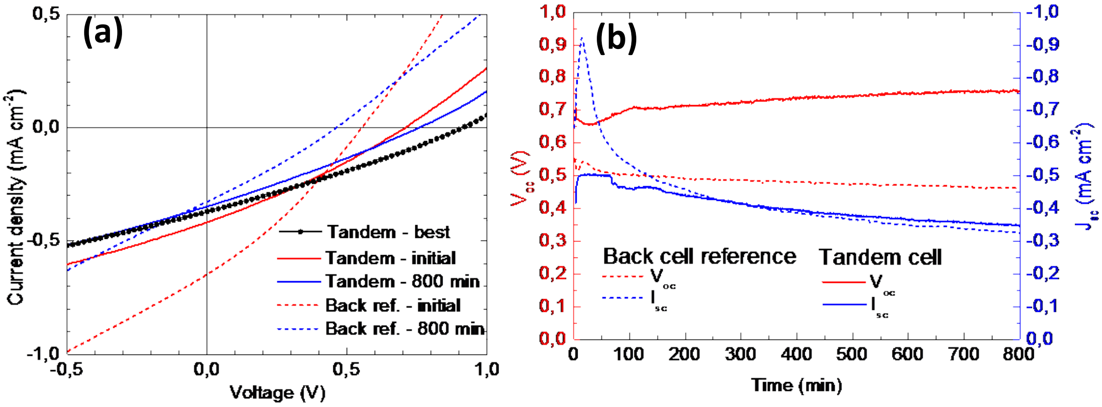

Figure 4.6: (a) J-V characteristics of partially water-processed tandem PSCs and the water-processed back BHJ single junction reference device. (b) Temporal evolution of V_{oc} and J_{sc}, during 800 min photo annealing under STC, of the back BHJ reference device and a representative tandem device, where the start and end of J-V curves are shown in (a).

Table 4.2: Summary of PV parameters of the partially water-processed tandem PSCs, showing the hero device ('best') and an average device ('initial' and '800 min'). The back BHJ single junction reference device is also shown. Results are shown before and after 800 min of photo annealing.

Cell	PCE [%]	V_{oc} [V]	J_{sc} [mA cm^{-2}]	FF [%]
R2R Tandem[a]				
initial	0.09	0.71	-0.42	28.8
800 min	0.07	0.76	-0.35	27.5
best	0.10	0.91	-0.37	28.2
Back cell reference[a]				
initial	0.11	0.55	-0.65	30.2
800 min	0.04	0.46	-0.33	27.7
Front cell reference[b]	1.33	0.50	-6.69	39.7

[a] Cell active area of 4 cm^2. [b] Cell active area of 0.5 cm^2 and structure of Glass/ITO/P3HT:PCBM/V_2O_5/Ag.

To estimate how the tandem cell performs compared to the theoretical expectation, a model for construction of the ideal tandem J-V characteristics, by means of the J-V characteristics of the sub-cell single junction reference devices, was used. The tandem J-V curve is constructed by summing voltages at equal current, following the principle of charge conservation in the serially connected tandem cell, as illustrated in Figure 4.7a [29]. To accommodate for spectral mismatch, i.e. overlapping absorption profiles of the two sub-cells, the current of the back BHJ is simply modified by a factor between 0 and 1, where 1 implies perfect current matching. In the case of the two polymers used here, TQ1 and P3HT, a rough estimate of 50% is used (Figure 4.7b). The constructed J-V curves are plotted in Figure 4.8, showing a 'best case' and a 'worst case', respectively using the 'initial' and '800 min' measurements of the reference back cell (cf. Table 4.2).

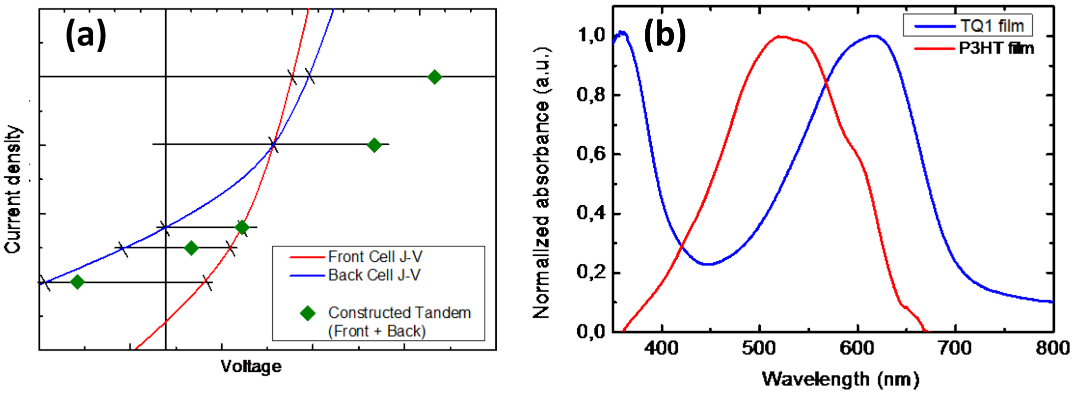

Figure 4.7: (a) Illustration of the principle behind the construction of the resulting tandem curve from two sub-cell reference J-V curves: voltage sums at equal currents. The J-V curves are arbitrary examples. (b) Normalized absorbance data for film of TQ1 and P3HT respectively.

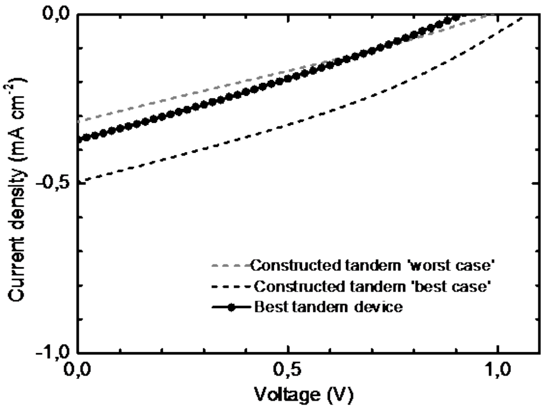

Figure 4.8: Constructed tandem curves, using the 'worst' and the 'best' reference devices respectively, and compared with the best measured tandem device.

Table 4.3: PV parameters of the constructed tandem J-V characteristics. The model assumes that the back cell receives only 50% of the 1 sun intensity due to the front cell blocking.

Model Tandem J-V	PCE (%)	V_{oc} (V)	J_{sc} (mA cm^{-2})	FF (%)
'Worst case'	0.09	0.98	1.3	27
'Best case'	0.17	1.1	2.0	33

As it can be seen in Figure 4.8, the R2R tandem device performance is just within the lower bound of the estimates extracted from the simple model. In the case of the V_{oc}, the measured data is around 0.1 – 0.2 V below the expected. Various loss mechanisms can influence the tandem voltage, of which most are related to the nature of the sub-cell interconnection, i.e. the RL. In this case it is highly probable that the observed cracks in the RL are likely to have a negative influence on V_{oc} considering the mechanism schematically shown in Figure 4.5b, as the formation of shunts across the recombination layer would lower the tandem V_{oc}. Furthermore, the results from the J-V time-study (Figure 4.6b) show that the back reference cell exhibited a decreasing V_{oc} over time, while for the tandem devices the trend is opposite, i.e. increasing V_{oc}. This indicates that the sub-cell interconnection improves over time, possibly due to burning of the shunts across the RL, while the sub-cell voltages decrease as a consequence of degradation, hence the model/measurement discrepancy becomes smaller over time. In this regard, another factor which is disregarded by the model is the V_{oc} dependence on light intensity [30], which for the this R2R tandem cell would mean a lowering of the V_{oc} of the back cell due to the light absorption of the front cell.

With respect to the J_{sc} it is noticeable that the tandem device and the back cell reference device have rather similar J_{sc} values. When considering that the actual back cell will receive much less than 1 sun intensity (½ a sun used in the model) the tandem J_{sc} is considerably higher than the J_{sc} of the back cell. This is explained by the model as a result of substantial current mismatch in sub-cell J_{sc}, with a factor of 10 in difference (cf. Table 4.2): Such an imbalance in sub-cell photocurrent entails a substantial biasing of the sub-cells under operation as explained by the schematic in Figure 4.7a: When the tandem cell is at short circuit conditions, the current-limiting back BHJ will operate in reverse bias (e.g. at -V) while the front BHJ will operate close to open-circuit conditions (at V). From this follows that the tandem J_{sc} is especially dependent on the slope of the J-V curve of the current-limiting sub-cells in reverse bias, as also pointed out by Braun et al. in the case of an inorganic tandem cell [31]. Thus the non-zero slope of the back cell results in the tandem J_{sc} being relatively higher than the J_{sc} of the limiting sub-cell.

4.5. **Further work on small area tandem solar cells**

Further work on tandem solar cells using water-based processing of the back BHJ were later continued on small area tandem solar cells using glass/ITO substrates and spin coating of all layers, except the final silver electrode which was evaporated, i.e. a structure similar to that shown in Figure 4.2a. Here, an aqueous PSBTBT:PCBM nanoparticle ink was used for the back BHJ material, as it yield much better PV performance in single junction devices than the TQ1:PCBM-based counterpart, as presented in chapter 3.

The J-V characterisation is summarised in Figure 4.9b and Table 4.4, where the best and worst device is listed for both tandem and sub-cell reference devices. To enable comparison with the 'ideal' tandem performance, a slightly upgraded version of the model described in the previous section is used: To better estimate the impact of spectral overlap between the sub-cells, the IPCE of the back BHJ is convoluted with the transmittance spectrum of the Front BHJ+RL as shown in Figure 4.9a. Hence the spectral mismatch factor input in the model is calculated as the ratio between the areas under two IPCE spectra in Figure 4.9a. As in the previous section, both a 'best case' and a 'worst case' tandem curve is constructed, using the best and worst reference devices respectively. The results are shown along with the measurements in Figure 4.9b and Table 4.4.

Compared to the R2R processed tandem, these smaller area devices show a 10-fold increase in performance. This increase is obviously driven by the much better performance of the PSBTBT:PCBM NP material as compared to the TQ1:PCBM NPs, reflected in the performance of the respective back BHJ reference devices. When comparing with the constructed curves in Figure 4.9b it is clear the measured tandem devices are close to the lower bound in terms of V_{oc} which was also seen for the R2R tandem, while the J_{sc} for the best tandem device is slightly higher than the 'best case' prediction of the model. This current discrepancy could be both a result of overestimated spectral mismatch, but just as well a result of the low statistics used here: only 8 devices were prepared of each type.

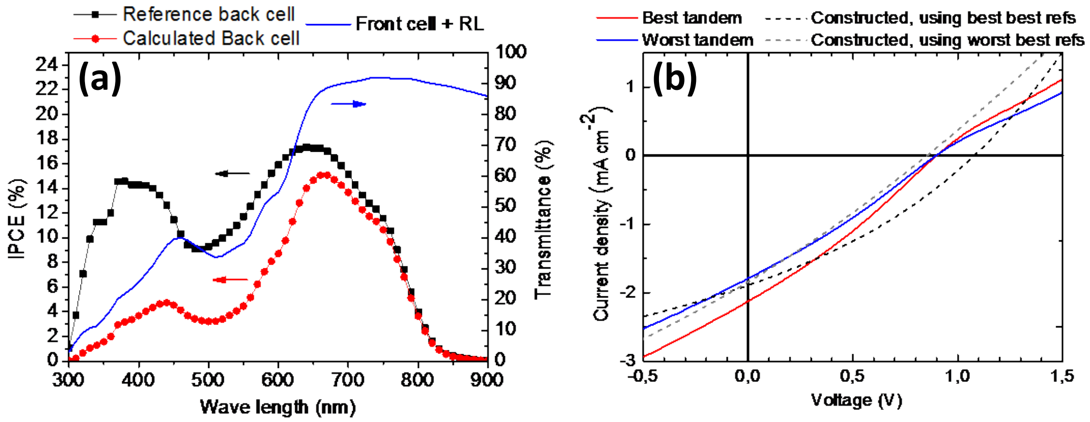

Figure 4.9: (a) The IPCE of a PSBTBT:PCBM-nanoparticle single junction device (black), from which the IPCE of the current-limiting back cell is estimated (red) by convolution with the transmittance of the front cell+RL (blue). (b) The J-V curve of the small area tandem device, shown with two contructed 'ideal' tandem curves using either the best or the worst corresponding single junction reference devices and the spectral mismatch factor of 0.56 calculated from (a).

Table 4.4: Summary of PV parameters of the small area tandem devices and respective single junction reference devices, all having an active area of 0.5 cm^2. The PV parameters of the 'ideal' constructed tandem J-V characteristics are also shown.

Cell	PCE [%]	V_{oc} [V]	J_{sc} [mA cm^{-2}]	FF [%]
Tandem[a]				
Best	1.1	0.90	-4.25	28.9
Worst	0.9	0.90	-3.58	28.4
Front BHJ reference[b]				
Best	1.33	0.50	-6.69	39.7
Worst	0.72	0.50	-5.18	27.9
Back BHJ reference[c]				
Best	0.84	0.56	-5.04	29.9
Worst	0.44	0.35	-4.74	26.8
Contructed tandem				
Best	1.27	1.06	-3.81	31.3
Worst	0.85	0.85	-3.69	27.0

[a] Cell structure of Glass/ITO/P3HT:PCBM(1:1,CB)/V_2O_5/ZnO/ PSBTBT:PCBM(NP,H_2O)/PEDOT:PSS/Ag. [b] Cell structure of Glass/ITO/P3HT:PCBM/V_2O_5/Ag. [c] Cell structure: Glass/ITO/ZnO/PSBTBT:PCBM(NP,H_2O)/ PEDOT:PSS/Ag.

Another notable feature of the tandem J-V characteristics are the inflection points just around V_{oc}. These do not exist in the single junction devices and are thus not reproduced in the constructed tandem J-V curves. Such inflection points were also seen in the earlier work with the V_2O_5/ZnO RL shown in Figure 4.2b, and as reported in ref. [21] the inflection was successfully removed by the insertion of a thin metal interlayer. As reported by Wagenpfahl et al. [32] such an inflection point could be described by a reduced recombination velocity, in this case at the V_2O_5/ZnO interface, causing space charge build-up in forward bias. Furthermore, as the removal of the inflection point in ref [21] did not improve the V_{oc} of the tandem device, it is likely a limitation restricted to biases higher than V_{oc}, and thus to injected carriers. This is substantiated by the dark-curves which show no inflection points.

4.6. Conclusion

This chapter presented the upscaling of tandem PSC processing from small area devices fabricated by spin coating and evaporation, to large area flexible tandem PSCs with all layers processed entirely from solution. This enabled by the use of orthogonal aqueous processing of back BHJ. The multilayer stack on flexible PET substrate comprised a cathode of ITO/ZnO, a recombination layer of V2O5/ZnO, and a PEDOT:PSS/Ag (printed) anode. The two serially connected BHJs was comprised of a P3HT:PCBM front cell processed from CB and a back cell processed from an aqueous dispersion of TQ1:PCBM nanoparticles. The V_{oc} of the best tandem device was 0.9 V. The measured J-V curves were compared to the ideal tandem J-V curves constructed from the sub-cell single junction reference devices, and the tandem device performance was found to deviate only little from the theoretical prediction, confirming a serial connection of the sub cells while the observed voltage losses were ascribed to visible defects in the recombination layer.

Further optimization was done on small area devices based on glass/ITO slides, and processing by spin coating. By substitution of the photo-active polymer used in the aqueously dispersed nanoparticles, TQ1 for PSBTBT, the performance of the tandem cells was increased from 0.1% to 1.1%, due to a much higher performance of the water-processed back BHJ.

4.7. References

[1] W. Shockley, H.J. Queisser, Detailed Balance Limit of Efficiency of p-n Junction Solar Cells, Journal of Applied Physics. 32 (1961) 510.

[2] L.C. Hirst, N.J. Ekins-Daukes, Fundamental losses in solar cells, Progress in Photovoltaics: Research and Applications. 19 (2011) 286–293.

[3] G. Dennler, M.C. Scharber, T. Ameri, P. Denk, K. Forberich, C. Waldauf, et al., Design Rules for Donors in Bulk-Heterojunction Tandem Solar Cells?Towards 15 % Energy-Conversion Efficiency, Advanced Materials. 20 (2008) 579–583.

[4] J. Gilot, M.M. Wienk, R. a J. Janssen, Optimizing polymer tandem solar cells., Advanced Materials (Deerfield Beach, Fla.). 22 (2010) E67–71.

[5] J.D. Kotlarski, P.W.M. Blom, Ultimate performance of polymer:fullerene bulk heterojunction tandem solar cells, Applied Physics Letters. 98 (2011) 053301.

[6] B. Minnaert, P. Veelaert, Guidelines for the Bandgap Combinations and Absorption Windows for Organic Tandem and Triple-Junction Solar Cells, Materials. 5 (2012) 1933–1953.

[7] Y.M. Nam, J. Huh, W.H. Jo, A computational study on optimal design for organic tandem solar cells, Solar Energy Materials and Solar Cells. 95 (2011) 1095–1101.

[8] O. Adebanjo, P. Maharjan, P. Adhikary, M. Wang, S. Yang, Q. Qiao, Triple Junction Polymer Solar Cells, Energy & Environmental Science. (2013).

[9] R. a J. Janssen, J. Nelson, Factors limiting device efficiency in organic photovoltaics., Advanced Materials (Deerfield Beach, Fla.). 25 (2013) 1847–58.

[10] J.Y. Kim, K. Lee, N.E. Coates, D. Moses, T.-Q. Nguyen, M. Dante, et al., Efficient Tandem Polymer Solar Cells Fabricated by All-Solution Processing, Science. 317 (2007) 222–5.

[11] a. Hadipour, B. de Boer, P.W.M. Blom, Organic Tandem and Multi-Junction Solar Cells, Advanced Functional Materials. 18 (2008) 169–181.

[12] T. Ameri, G. Dennler, C. Lungenschmied, C.J. Brabec, Organic tandem solar cells: A review, Energy & Environmental Science. 2 (2009) 347.

[13] S. Sista, Z. Hong, L.-M. Chen, Y. Yang, Tandem polymer photovoltaic cells—current status, challenges and future outlook, Energy & Environmental Science. (2011).

[14] T. Ameri, N. Li, C.J. Brabec, Highly efficient organic tandem solar cells: a follow up review, Energy & Environmental Science. 6 (2013) 2390.

[15] M. Jørgensen, J.E. Carlé, R.R. Søndergaard, M. Lauritzen, N. a. Dagnæs-Hansen, S.L. Byskov, et al., The state of organic solar cells—A meta analysis, Solar Energy Materials and Solar Cells. (2013) 1–10.

[16] T.T. Larsen-Olsen, T.R. Andersen, B. Andreasen, A.P.L. Böttiger, E. Bundgaard, K. Norrman, et al., Roll-to-roll processed polymer tandem solar cells partially processed from water, Solar Energy Materials and Solar Cells. 97 (2011) 43–49.

[17] J. Yang, R. Zhu, Z. Hong, Y. He, A. Kumar, Y. Li, et al., A Robust Inter-Connecting Layer for Achieving High Performance Tandem Polymer Solar Cells, Advanced Materials. (2011) n/a–n/a.

[18] J.E. Carlé, F.C. Krebs, Technological status of organic photovoltaics (OPV), Solar Energy Materials and Solar Cells. (2013) 1–2.

[19] O. Hagemann, M. Bjerring, N.C. Nielsen, F.C. Krebs, All solution processed tandem polymer solar cells based on thermocleavable materials☆, Solar Energy Materials and Solar Cells. 92 (2008) 1327–1335.

[20] S.K. Hau, H.-L. Yip, K.-S. Chen, J. Zou, A.K.-Y. Jen, Solution processed inverted tandem polymer solar cells with self-assembled monolayer modified interfacial layers, Applied Physics Letters. 97 (2010) 253307.

[21] T.T. Larsen-Olsen, E. Bundgaard, K.O. Sylvester-Hvid, F.C. Krebs, A solution process for inverted tandem solar cells, Organic Electronics. 12 (2011) 364–371.

[22] L. Dou, J. You, J. Yang, C. Chen, Y. He, S. Murase, et al., Tandem polymer solar cells featuring a spectrally matched low-bandgap polymer, Nature Photonics. 6 (2012) 180–185.

[23] J. You, C.-C. Chen, Z. Hong, K. Yoshimura, K. Ohya, R. Xu, et al., 10.2% power conversion efficiency polymer tandem solar cells consisting of two identical sub-cells., Advanced Materials (Deerfield Beach, Fla.). 25 (2013) 3973–8.

[24] J. You, L. Dou, K. Yoshimura, T. Kato, K. Ohya, T. Moriarty, et al., A polymer tandem solar cell with 10.6% power conversion efficiency., Nature Communications. 4 (2013) 1446.

[25] V.S. Gevaerts, A. Furlan, M.M. Wienk, M. Turbiez, R. a J. Janssen, Solution Processed Polymer Tandem Solar Cell Using Efficient Small and Wide bandgap Polymer:Fullerene Blends., Advanced Materials (Deerfield Beach, Fla.). (2012) 1–5.

[26] S. Kouijzer, S. Esiner, C.H. Frijters, M. Turbiez, M.M. Wienk, R. a. J. Janssen, Efficient Inverted Tandem Polymer Solar Cells with a Solution-Processed Recombination Layer, Advanced Energy Materials. (2012) n/a–n/a.

[27] W. Li, A. Furlan, K.H. Hendriks, M.M. Wienk, R.A.J. Janssen, Efficient Tandem and Triple Junction Polymer Solar Cells., Journal of the American Chemical Society. (2013) 7–10.

[28] D.M. Tanenbaum, H.F. Dam, R. Rösch, M. Jørgensen, H. Hoppe, F.C. Krebs, Edge sealing for low cost stability enhancement of roll-to-roll processed flexible polymer solar cell modules, Solar Energy Materials and Solar Cells. 97 (2012) 157–163.

[29] a Hadipour, B. Deboer, P.W.M. Blom, Device operation of organic tandem solar cells, Organic Electronics. 9 (2008) 617–624.

[30] T. Tromholt, E. a. Katz, B. Hirsch, A. Vossier, F.C. Krebs, Effects of concentrated sunlight on organic photovoltaics, Applied Physics Letters. 96 (2010) 073501.

[31] A. Braun, N. Szabó, K. Schwarzburg, T. Hannappel, E. a. Katz, J.M. Gordon, Current-limiting behavior in multijunction solar cells, Applied Physics Letters. 98 (2011) 223506.

[32] a. Wagenpfahl, D. Rauh, M. Binder, C. Deibel, V. Dyakonov, S-shaped current-voltage characteristics of organic solar devices, Physical Review B. 82 (2010) 1–8.

5 ITO-Freedom

5.1. Introduction

As conveyed in the introduction, polymer solar cells prize themselves of being a potentially very low cost technology, enabling mass production on a scale that allows for delivering the equivalent of 1 GW_p worth of solar cells pr. day [1]. Since their introduction [2], OPV devices have by and large relied on the use of ITO as the transparent conductor. However, through LCA and economic assessment studies on ITO-based R2R-fabricated OPV, it has been shown that the ITO substrate accounts for roughly 90% of the total energy used[3] and at least 50% of the cost[4,5]. This has to do with both the scarcity of the raw material which is the rare-earth mineral indium and the energy intensive and inefficient vacuum sputtering technique used to fabricate ITO [6]. It becomes very clear from such assessments, that ITO has no future in OPV for energy production [1].

Thus alternatives must be sought that poses the same attributes that makes ITO attractive, i.e. high conductivity ($<50\ \Omega\square^{-1}$) and high transmittance (≥80%), while making up for the shortcomings of ITO with respect to cost and compatibility with fast R2R processing.

Materials-wise ITO-alternatives most often consist of one, or a combination, of four types of materials, either inorganic semiconductor-, polymer-, metal-, or 'carbon'-materials. The latter include carbon nanotubes[7–9] and graphene [10,11]. These materials are highly interesting and show great promise for future application, and for more details the interested reader is kindly referred to recent reviews on the subject [12–15]. The group of inorganic semiconductors are mainly interesting in the context of inorganic solar cells as these materials demand energy intensive fabrication methods [16], hence suffering from the same processing difficulties as ITO (being a member this group of materials), and thus are not compatible with the outlined vision of PSCs.

5.1.1. PEDOT:PSS and silver for transparent electrodes

In terms of cost-effectiveness, so far the most promising results have been presented with the use of conducting polymers and metals, often but not exclusively, in combination. This chapter will focus on the use of PEDOT:PSS and silver and their utilization as transparent electrode in R2R processed PSCs. A few other solutions have been presented using this category of materials however, e.g. Kang et al. [17] who used PEDOT:PSS in combination with various metals, while Zimmermann et al. used PEDOT:PSS and gold [18].

Thus far however, the most widely used materials for ITO substitution is the polymer blend PEDOT:PSS and silver, used either by themselves or in combination [15]. As both are solution processable, they constitute an excellent choice for R2R processing.

The exclusive use of silver have been successfully pursued through the use of solution processed silver nanowires[19,20], while a recent paper by Angmo et al. describes a R2R solution processed semi-transparent continuous silver front electrode [21].

As the traditional layer stack of ITO-based ‘normal geometry’ PSCs is ITO/PEDOT:PSS/BHJ/Cathode, it is natural to simply omit the ITO, and compensate by the use of a higher conductivity PEDOT:PSS, to allow lateral charge transport. This was done in 2002 by Zhang et al. [22], but with inferior performance due to a low conductivity (10^{-3} $\Omega_{\square}$) of the PEDOT:PSS. Later, high conductivity PEDOT:PSS through various modification have enabled much better performance of PEDOT:PSS electrodes[23–26]. Especially the use of newer generations of commercial PEDOT:PSS such as Clevios PH 500 [24,25,27,28] and Clevios PH 1000 [26,29–31] have enabled stand-alone PEDOT:PSS electrodes.

Although conductivities of <100 $\Omega_{\square}$ can be achieved with PEDOT:PSS today, one still need the aid of metallic conductivity (1-10 $\Omega_{\square}$) in order to have a truly scalable and versatile transparent electrode. Otherwise current transport over length scales more than a few mm’s will compromise device performance through series resistance losses [32]. An efficient and adaptable solution has proven to be the use of a silver grids [23,33–35]. The combination of PEDOT:PSS and silver grids have proven especially useful in the context of upscaling, as it has been used in the first demonstrations of R2R processed ITO-free PSCs [33,34]. These first R2R processed ITO-free devices all suffered from the relatively low transmittance of the high-conductivity PEDOT:PSS used, and the low resolution of the screen printing method applied for the silver grid.

The work presented in the following, describes the development of the next generation of PEDOT:PSS/Silver grid electrodes from our group, taking from a number of recent publications [36–39] (Appendix 5-8). This ITO-free transparent electrode has been labelled the *Flextrode* [40], while the complete R2R process is called *iOne* [39], thus taking over as work-horse from the previous ITO-based *ProcessOne* [41]. The process have already shown improved stability [39] and greatly improved energy-budget [42] enabling truly large scale on-grid PSC technology [43].

5.2. Front electrodes for inverted polymer solar cells through a switching mechanism

A flexible electrode, originally intended for "normal" geometry solar cells, were prepared by slot-die coating of hc-PEDOT:PSS (Clevios PH 1000 from Heraeus) (PH1000) on a PET substrate. The inverted PSC stack was completed by sequential spin-coating of ZnO, P3HT:PCBM and PEDOT:PSS (EL-P 5010 from Agfa) (P5010) layers. The devices were finalized with an evaporated Ag electrode, constituting a PSC stack which has previously been reported to yield working devices [25,29]. However, all initial *J-V* characterizations yielded shorted devices as shown in Figure 5.1a. It was then discovered that the application of a short negative bias burst resulted in working devices as illustrated in Figure 5.1(a->b). This was first thought to result from mere burning of physical shunts through the active layer. However, similar shorted devices have never been observed for ITO-based devices. In order to be certain that the effect was not related to the slot-die coating of the PH1000 or the PET substrate itself, the stack was spin-coated on a Glass/ITO substrate, yielding a similarly behaving device, seen as the blue curves in Figure 5.1.

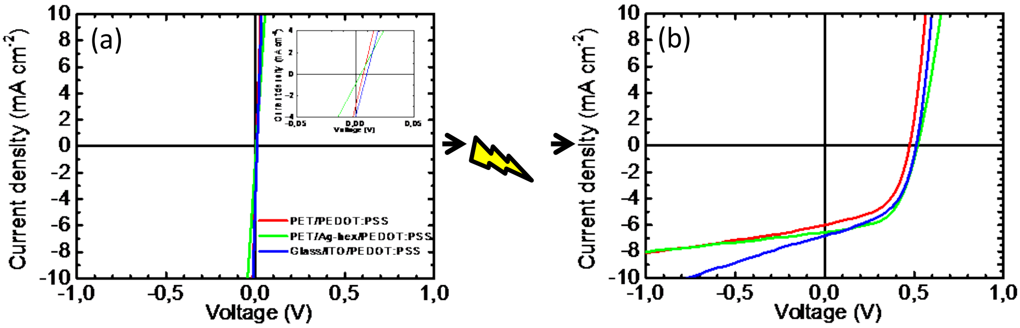

Figure 5.1: *J-V* curves of PV devices with the layer stack of [Front electrode]/ZnO/P3HT:PCBM/PEDOT:PSS/Ag, where the front electrode is given in the legend. (a) Shows the initial J-V curve, showing shorted devices, albeit with less than unity voltage and current as shown in the insert. (b) *J-V* curves after high negative voltage burst of -15 V.

Negative bias treatment have already been reported to efficiently reduce shunting for ProcessOne-type devices by enhancing the hole-blocking functionality of ZnO [44,45]. This could explain the ohmic behavior in the pristine devices, however this was bought to question in a control experiment: By delaminating the device at the Active layer/P5010 interface, and rebuilding the device (i.e. spin-coating PEDOT:PSS and evaporating Ag), we found that the ohmic behavior was reversed, and the device needed to be switched anew. To ensure that the return of the ohmic behavior was not a result of the processing, a second set of switched devices were exposed to water vapor and organic solvent vapor to mimic the fabrication environment, neither resulting in reversing the switching effect. This surely suggests that the observed “switching” phenomenon do not originate at the ZnO interface alone.

Instead our observations fit well with the sustained conductivity loss in PEDOT:PSS reached upon high electric field/high current density exposure as described by Möller et al. [46,47]. The switching is well illustrated with the data shown in Figure 5.2a, were a reverse bias sweep from 0 V to -8 V (20 mV steps) is done on a pristine device under 1 sun illumination. At ~0.8 V the current drops abruptly and reaches a plateau corresponding to a high parallel resistance in the solar cell. The phenomenon is ascribed to the de-doping of the PEDOT from its natural p-doped state to a neutral state by oxygen reduction ($PEDOT^+$ -> $PEDOT^0$) induced by current injection, a process well known from electrochemistry [48]. The de-doped state in pure PEDOT film has been reported to be highly unstable in ambient atmosphere [48], however in the case of the PEDOT:PSS blend the de-doped state of PEDOT is stabilized by the neutralization of the PSS counter-ions (PSS^- -> PSS-H) [46,47]. Xu et al. also found that morphological changes occur upon the switching due to the heating involved, thus enforcing the low-conductivity by the formation of a thin insulating PSS layer [49].

In the case presented here, the formation of the de-doped state promotes the hole selectivity of the P5010 PEDOT:PSS layer, leading to a rectifying solar cell with a high fill factor as seen in Figure 5.2b and d. The process itself is self-containing as charge-injection is hindered by the lower conductivity thus preventing overgrowth of the de-doped layer.

To chemically confirm that de-doping was indeed the cause of the observed switching phenomenon, a TOF-SIMS depth profiling experiment was carried out on the switched and non-switched devices, following delamination of the cells at the active layer/P5010 interface, as sketched in Figure 5.3. The chemical trace of the de-doping would be that of a redox-reaction i.e. quit small. However the neutralization of $PEDOT^+$ and PSS to PEDOT and PSS-H respectively, will change the ionic strength of the medium, thus naturally occurring ionic substances will withdraw from the neutralized interface region towards the more polarized bulk. This was indeed observed in the depth profile as seen in Figure 5.3 for the sodium-ion count.

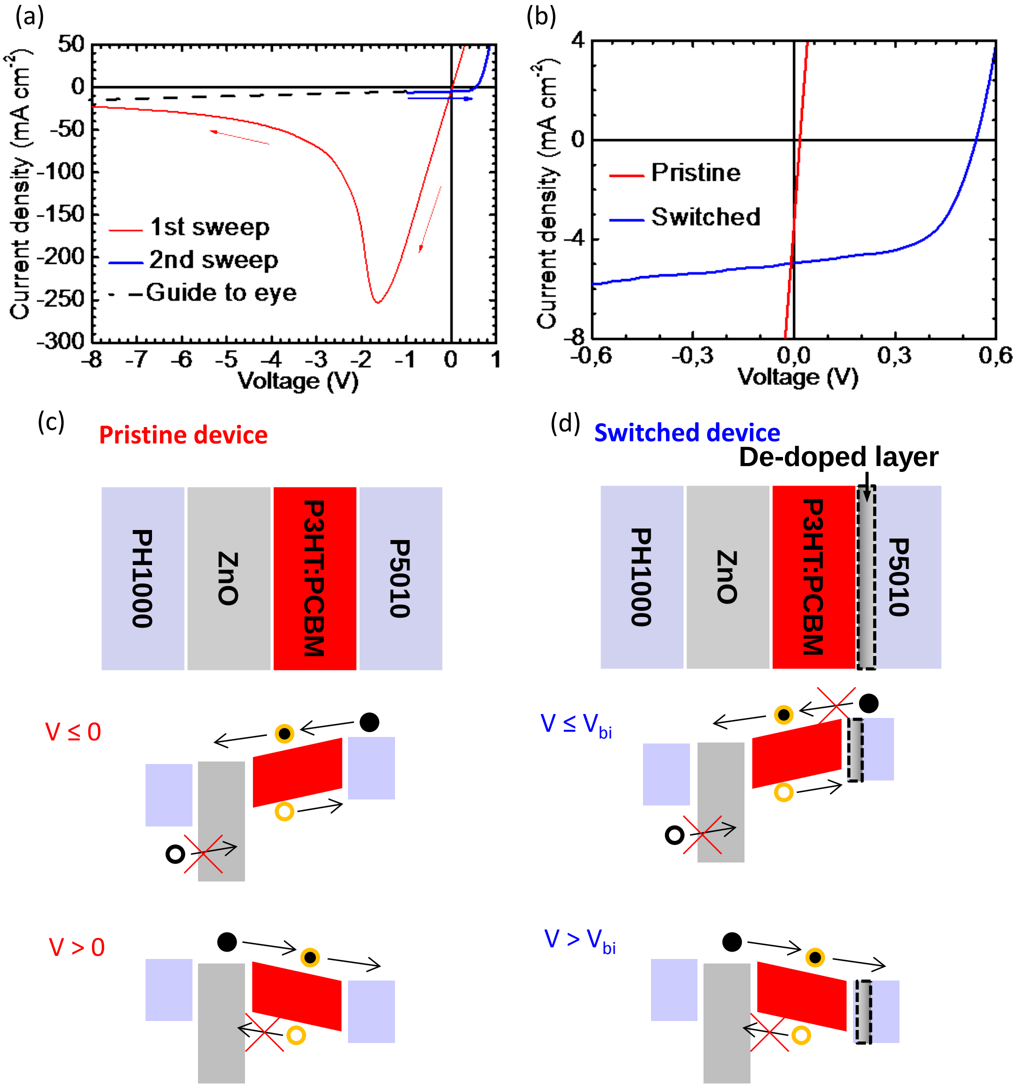

Figure 5.2: (a) *J*-V curve showing the switching by a reverse bias sweep 0 to 8 V followed by a forward sweep from -1 to 1 V. where a close-up on the active quadrant is shown in (b). (c) and (d) shows a graphical explanation of the formation of a hole-selective layer upon switching, where V_{bi} refers to the built-in potential of the solar cell, black circles are electrons, white circles holes, while the orange outline indicates photo-excited charges.

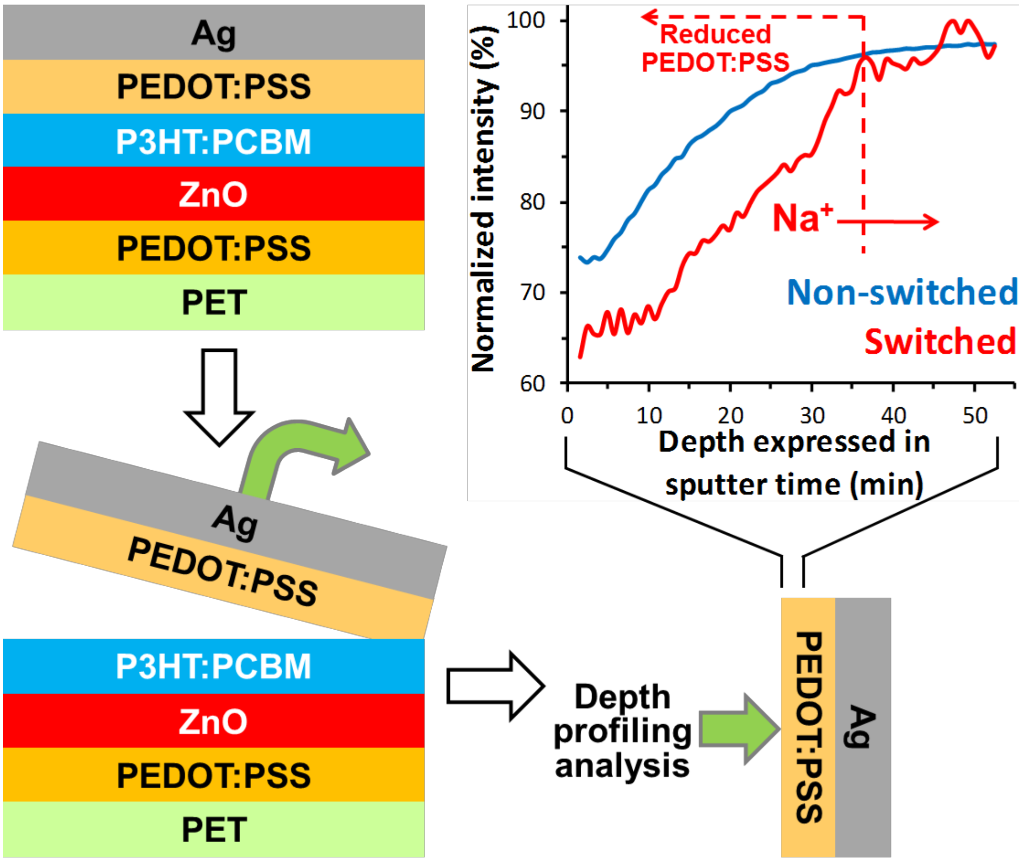

Figure 5.3: Schematic illustration of the TOF-SIMS depth profiling experiment following mechanical delamination of the PSC. The Na-ion count depth profile is plotted showing a shift of ions away from the interface. Illustration is taken from ref. [36]**.**

5.3. ITO- and silver-free Small modules: Towards the all-carbon PSC

5.3.1. Upscaling to R2R fabrication

The development of the Flextrode was a clear example of an upscaling procedure as the starting-point was a R2R processed slot-die coated PET/PH1000 after which the solar cell stack was further processed using spin coating and evaporation. Gradually, one layer at the time, the spin coater, and finally also the evaporator, was substituted with a R2R process, and Figure 5.4 and Table 5.1 describes the J-V characteristics of small area devices in three different stages of this upscaling as shown in the legend of Figure 5.4. Although this upscaling procedure was an efficient way of testing the stack while doing small tweaks and optimizations in layer thicknesses etc. before investing the materials and man-power in large scale printing and coating, the difference in performance when going from spin coater to R2R was not always clear due to the inherent differences in the processing conditions. Later this problem has been solved in our group with the development of the mini roll-coater as substitution for the spin coater, as it mimics the processing conditions in full scale R2R fabrication [50,51].

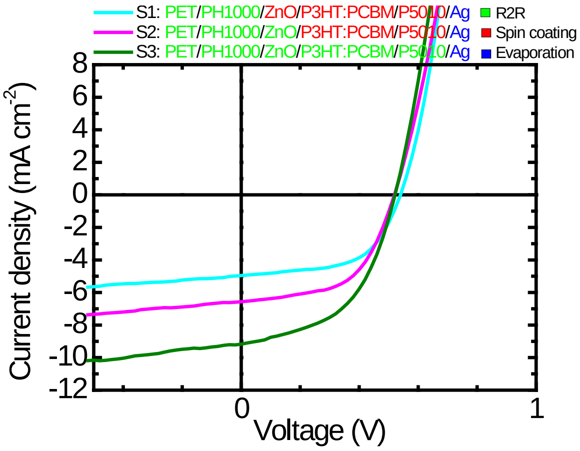

Figure 5.4: Examples of J-V curves of devices at different stages in the upscaling, all with active areas of 25±3 mm^2. Layer thicknesses vary among devices.

Table 5.1: PV performance of small area devices as described in Figure 5.4. The uncertainty is estimated from a ~10% uncertainty in the actual active area.

Device	J_{sc} (mA cm^{-2})	V_{oc} (V)	FF (%)	PCE (%)
S1	5±0.5	0.54	57.6	1.5±0.2
S2	6.6±0.7	0.52	55.5	1.9±0.2
S3	9±1	0.52	50.3	2.4±0.2

5.3.2. Complete R2R processing and switching of small credit card modules

In order to be a true ITO-alternative, the whole process including the switching would have to be scaled to large area (60 cm web with) R2R processing. By choosing a small credit-card sized 16-striped module meant for product integration [52] as the ITO-free test vehicle, having a small aperture width of 2 mm (see Figure 5.5h) we were able to omit not only ITO but also silver, fabricating a nearly all-carbon module while still retaining a high fill factor. The whole R2R printing and coating process is depicted in Figure 5.5(a-e).

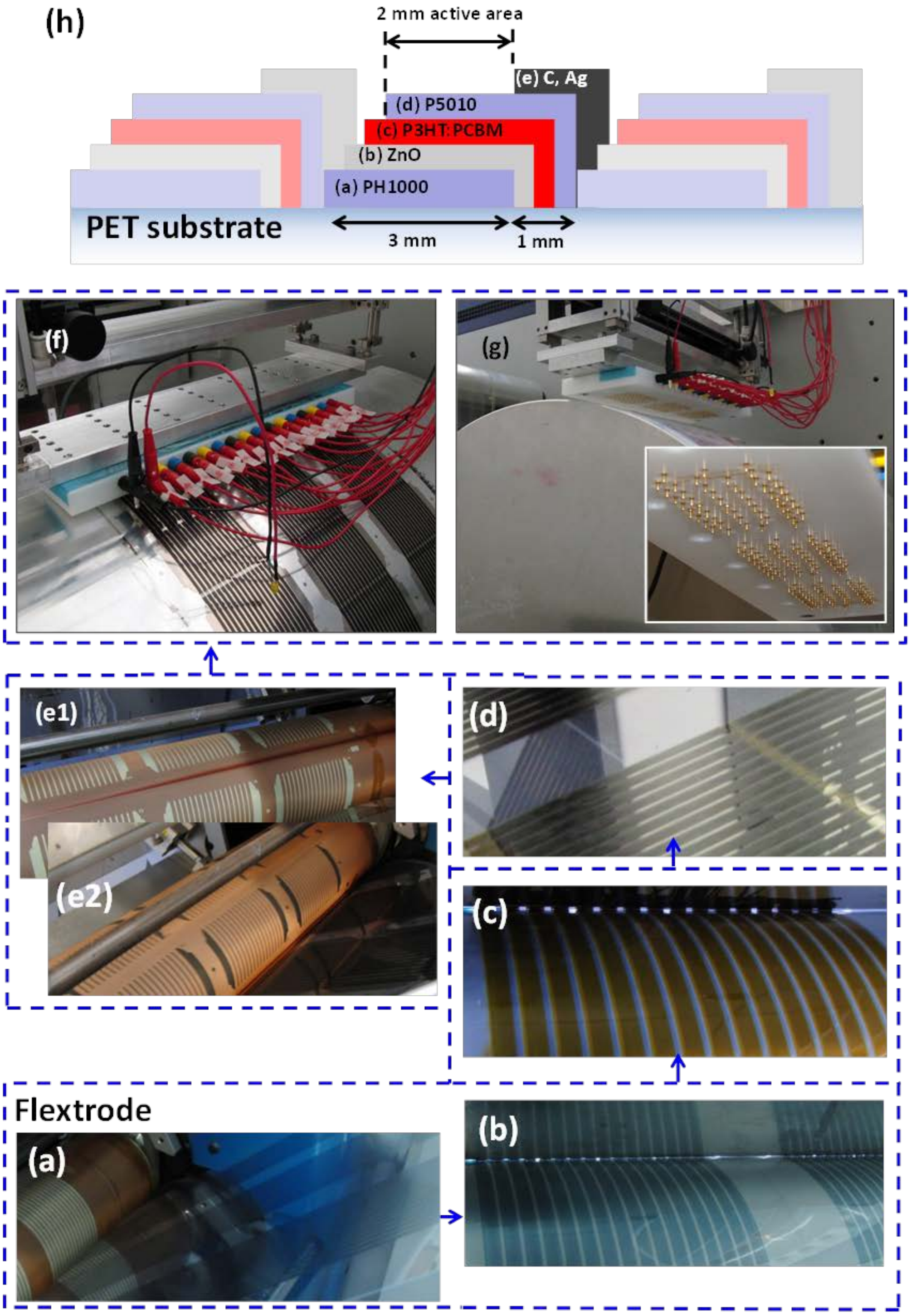

Figure 5.5: Picture of the complete R2R process of small modules, with the PSC stack shown in the bottom left: (a) shows the rotary screen printing of the PH1000 layer on the bare PET foil, followed by (b) slot-die coating of ZnO, (c) slot-die coating of P3HT:PCBM active layer, (d) rotary screen printing of P5010, and finally rotary screen printing of the back electrode either silver (e1) or carbon (e2). (f+g) The roll is then transferred to the R2R switching machine where (f) depicts the machine during switching (contact pad down) of three modules in parallel, while (g) shows the situation between switches (contact pad up), with the gold contacts shown in the insert. (h) Shows a cross-section of the small module stack and the line interconnect by overlap -principle.

To accomplish the R2R switching a new R2R machine was designed and built, using a pneumatically controlled contact pad and a large aluminum drum to dissipate heat as seen in Figure 5.5(f+g). The whole setup was controlled via in-house made computer software, where essential switching parameters e.g. current, voltage, switch-burst time and web-speed could be controlled. The machine was fed with the roll of completed solar cells, switching three modules in parallel at a time in a R2R stop-and-go fashion. An optimized switching step took less than 2 sec, of which the actual switching-burst was on the order of 10 ms using an applied bias of ~20 V with the power-supply running with a current compliance of ~500 mA.

Devices were fabricated, having either silver or carbon bus-bars and electrodes. The J-V curves are shown in Figure 5.6b and the results are summarized in Table 5.2. As can be seen the performance of the carbon-based device is slightly inferior to the silver-based version, owing to the much lower conductivity of the carbon ink (~50 $\Omega_\square$ vs ~1 $\Omega_\square$). Both types of devices, however, performed on par or better compared to ITO-based versions of the same module type [52], while both the processing speed and the overall fabrication cost was lowered by a factor >10 [36,42].

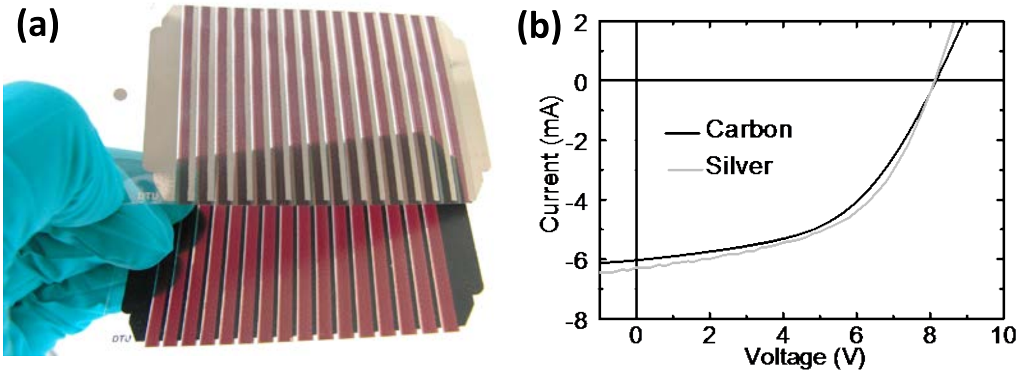

Figure 5.6: (a) A picture of the two types of small ITO-free modules, with the top-most having silver back electroes/bus bars, and the other carbon, as is seen by the contrast in color. (b) Shows the J-V curves, comparing the silver and carbon version.

Table 5.2: PV performance of the small 16-striped modules, having nominal active area of 15.4 cm^2

Device	J_{sc} (mA cm^{-2})	V_{oc} (V)	FF (%)	PCE (%)
Silver	6.5^a	8.2	52	1.9
Carbon	6.2^b	8.1	51	1.6

^{a}Measured at 90 mW cm^{-2}, ^{b}Measured at 100 mW cm^{-2}.

5.4. **Silver front electrode grids for scalability**

As mentioned earlier the sheet resistance of the PEDOT:PSS is only low enough to enable current transport over a few mm's before having negative effects on the device performance through the increase of series resistance. To circumvent this issue and to make a truly scalable electrode, the PEDOT:PSS must be coupled with a grid having metallic conductivity. A feasible choice is silver, as it has a high conductivity and stability while a wide range of commercial inks are available facilitating easy solution processing [4]. The first R2R examples utilized back illumination, where the silver grid was printed using screen printing on top of the solar cell stack [33,34]. A front grid where the silver is printed directly on the plastic substrate does however, have the noticeable advantage of freedom of choice when it comes to processing solvents, and post processing methods such as annealing or UV treatment (section 5.4.3) without risk of damaging underlying layers. There are few reports of such printed silver front grids, one reason being the technical difficulty in printing a smooth enough layer necessary for the complete coverage of the subsequent layers which might be only 10-100 nm thick. Galagan et al. found it necessary to embed the grid into the substrate, in a post process, in order to avoid detrimental shunts from the relatively rough screen printed grids [35]. Later the same authors solved the shunting issues by using ink jet printing, allowing for much smoother grids [53,54]. The previous work on printed front-grids for ITO-free PSCs have been based on small laboratory batch processing. In this section we present work that take the step further by exploring fully R2R processed front grids by several methods.

5.4.1. Embedded vs. raised silver grids

There are many options for fabricating silver grids owing to the multitude of R2R printing and coating methods [55]. In the present work three types of silver front grids were compared belonging to two distinct categories: flexo printed and inkjet printed *raised* grids, and *embedded* grids fabricated by thermal nano-imprint and subsequent silver filling. By embedding the grid in the substrate one has the possibility of controlling the aspect ratio of the line, which is otherwise governed by surface tension during ink printing and drying. Thus it is possible to make grids with a thin outline retaining bulk metallic conductivity as compared with a printed raised grid (see Figure 5.7).

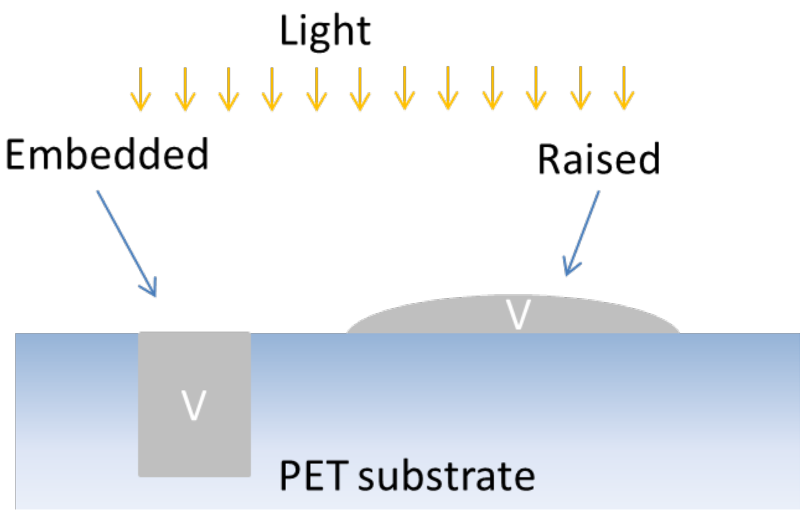

Figure 5.7: The simplistic schematic of the principle idea behind embedding the grid into the substrate: Allowing for a thinner outline, letting more light through for the same volume (V) of silver, compared to the printed raised topography.

5.4.1.1. Grid processing

The embedded grid was fabricated at the collaborating institute KIMM in Korea using a method described elsewhere [56]. Both the flexo- and inkjet printed grids where fabricated at DTU. All grid-types constitute novel electrode types in the context of R2R PSCs.

In terms of processing, all grids were fabricated completely R2R, and using water-based silver inks, the first being a prerequisite for mass fabrication while the latter at the least presents a clear advantage with respect to environmental concerns. The embedded grid was prepared in a two-step process; first the thermal imprint was done forcing a heated nickel master with a raised topography (line width of 15 µm and height of 10 µm) onto the PET substrate, while the filling step consisted of silver being forced into the protrusions in the PET using a squeegee. In the experiment a speed of 0.96 m min^{-1} were used for both steps while an upper limit in terms of speed is estimated at 12 m min^{-1} in an inline process. Micrographs of unfilled and filled imprinted PET can be seen in Figure 5.8c and d respectively.

Both types of raised grids are fabricated in one step, and capable of very fast processing speed. The inkjet printing was done at 2m min^{-1} a relatively low speed necessitated by the length of the drier and the curing time of the ink employed (Figure 5.8a). However, the estimated upper limit is as high as 75 m min^{-1}, pending the necessary ink development. The flexo printing is by far the fastest process, with an estimated top speed of 200 m min^{-1}, while a web speed of 25 m min^{-1} was employed in the experiment (Figure 5.8(b)). Relevant processing details of the three grid types/processing methods are compiled in Table 5.3. Further processing detail can be found in ref. [37].

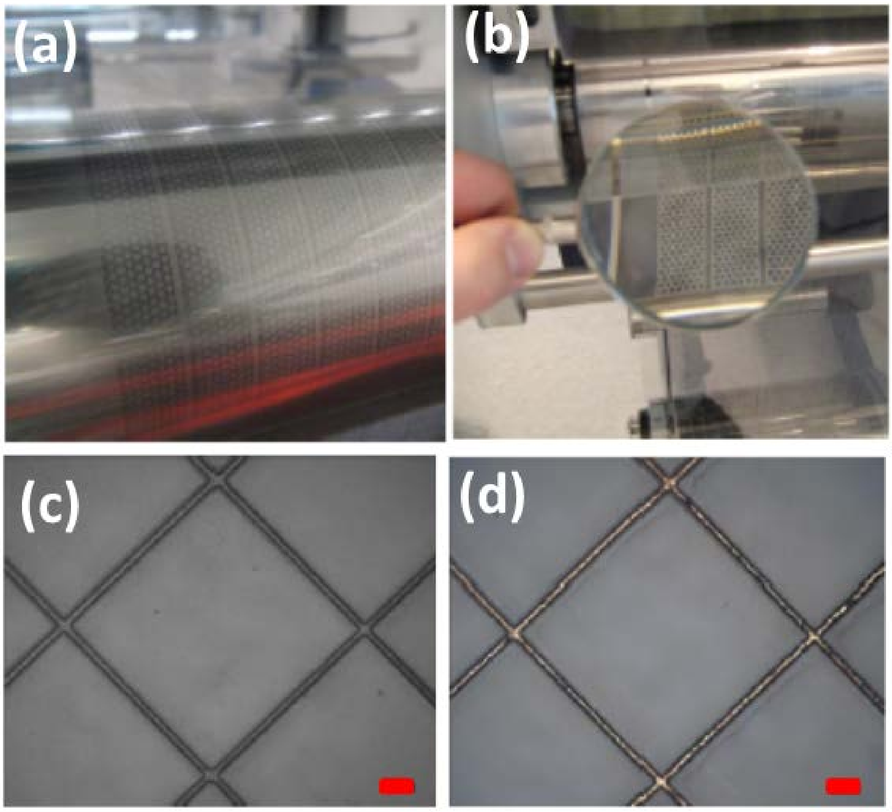

Figure 5.8: a) Flexo printed grid shown as wet film with the red glow from the infrared drier. b) The ink jet printed grid shown after hot air drying. c) Shows the thermal imprinted PET without silver filling, while d) shows the imprint with filling. The red bar corresponds to 100 µm.

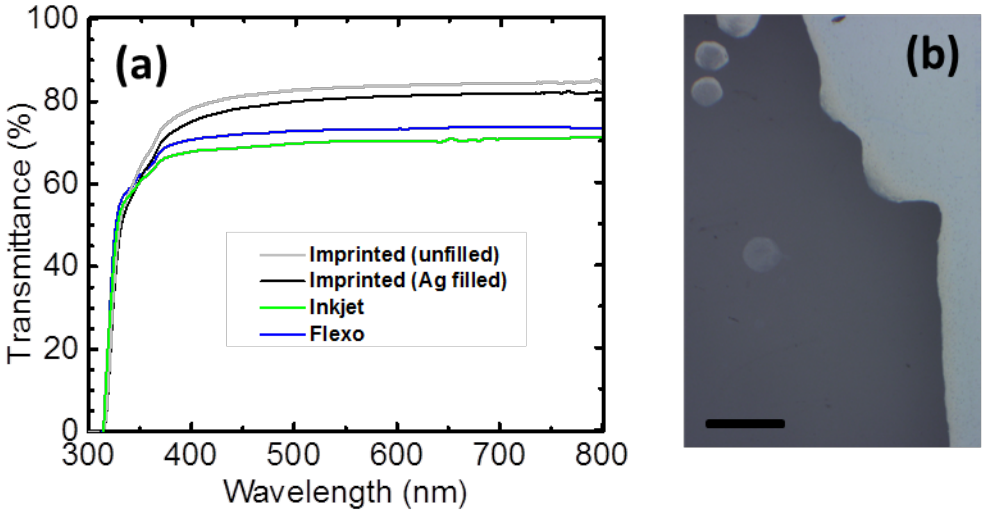

Figure 5.9: (a)Transmittance as measured by UV-vis of the different grid types+PET. The measurements includes reflection/scattering losses. (b) Micrograph zoom-in on examples defects in the inkjet grid due to the occasional misfiring of a jet (scalebar is 50 µm).

5.4.1.2. Grid characterization

The three grid types were characterized by UV-vis (Figure 5.9a), showing a clear advantage for the embedded grid in terms of transmittance allowing ~10% more light to reach the solar cell. The raised grids have close to the same transmittance, with the inkjet grid being slightly hampered occasional defects introduced by the misfiring of jets (Figure 5.9b).

The grids were also characterized with both SEM and confocal microscopy (at KIMM), the results of which is shown in Figure 5.10. SEM images show nicely sintered silver in the case of the flexo print while the inkjet print seems much less sintered. This might be a reason for the much lower conductivity of the inkjet print, as measured with a 4-point probe, compared with both the flexo and imbedded grid (Table 5.3). The embedded grid does not show obvious sintering either, but the material consists of much larger nanoparticles which might explain the higher conductivity compared to the inkjet print. In section 5.4.3 we will show how the conductivity of the inkjet printed silver can be improved by photonic sintering.

Figure 5.10 also shows cross-sectional diagrams of the different grid lines measured by confocal microscopy. These nicely illustrate the much thinner gridlines obtained with the embedding method, and although there is a groove on the order of 1 µm, it seems smooth considering the aspect ratio of the diagram. The inkjet and flexo lines have the same line width, while the inkjet print has the lowest topography of only 300 nm while the flexo print is less smooth displaying a ‘ridge’-like structure reaching close to 1 µm in the center of the line. Fortunately the rise in topography is relatively smooth considering the line width of 130 µm.

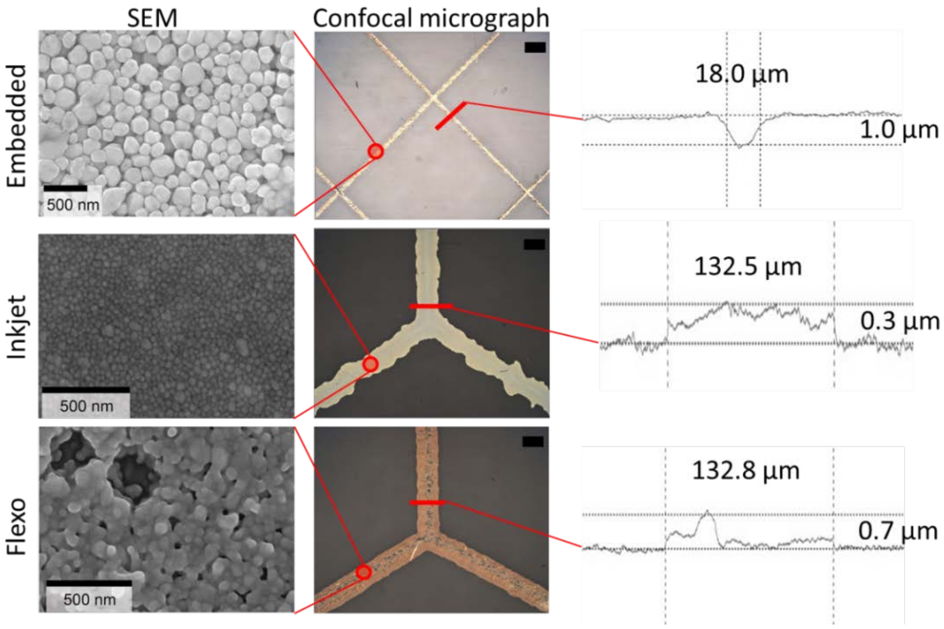

Figure 5.10: SEM images of the nanoparticles for the three different silver electrodes. The embedded grid is shown with a low degree of magnification due to larger particle size. The inkjet printed and flexo printed grids are shown with the same magnification. The middle part shows corresponding optical confocal micrographs (scale bar is 100 µm) with traces across the grid lines showing the typical width and height (from confocal micrograf).

Table 5.3: A comparison between conducting electrodes based on embedded, inkjet printed, and flexo printed grids using parameters covering cost, ease of processing and physical parameters.

	Embedded	**Inkjet**	**Flexo**
Speed (m min^{-1})	0.48[a]	2	25
Max possible speed (m min^{-1})	6[a]	70	200
Number of steps	2	1	1
Ink type	Nanoparticles	Nanoparticles	Nanoparticles
Water as solvent	Yes	Yes	Yes
Cost of master	Medium	Free (digital)	Low
Optical transmittance (PET+grid)	82%	70%	73%
Resolution (micron)[b]	16 (8)	100 (42)	100 (32)
Printed height (nm)	0 ± 25	+150 ± 25	+100 ± 25
Spikes (nm)	20	50	1000
Technical yield	High	High	High
Sheet resistance (Ω square^{-1})	10	60	11

[a] The thermally imprinted grid is prepared in two consecutive steps. Firstly, the pattern is imprinted and secondly, it is filled with silver. The speed was 0.96 m min^{-1} in both steps. The maximum achievable speed in both steps is 12 m min^{-1}. [b] The value in brackets is the highest current resolution achievable, understood as the minimal obtainable distance between two distinguishable points.

5.4.1.3. Solar cell processing and characterization

In order to keep conditions as similar as possible for the different grid types, the three separate PET sections were spliced together, giving one long PET roll on which the solar cell stack, introduced in section 5.3.2, was R2R coated, yielding a solar cells stack as depicted in Figure 5.11a. Further processing detail can be found in ref. [37]. Single devices were cut from the main roll looking as shown in Figure 5.11b, giving them a nominal active area of 6 cm^2.

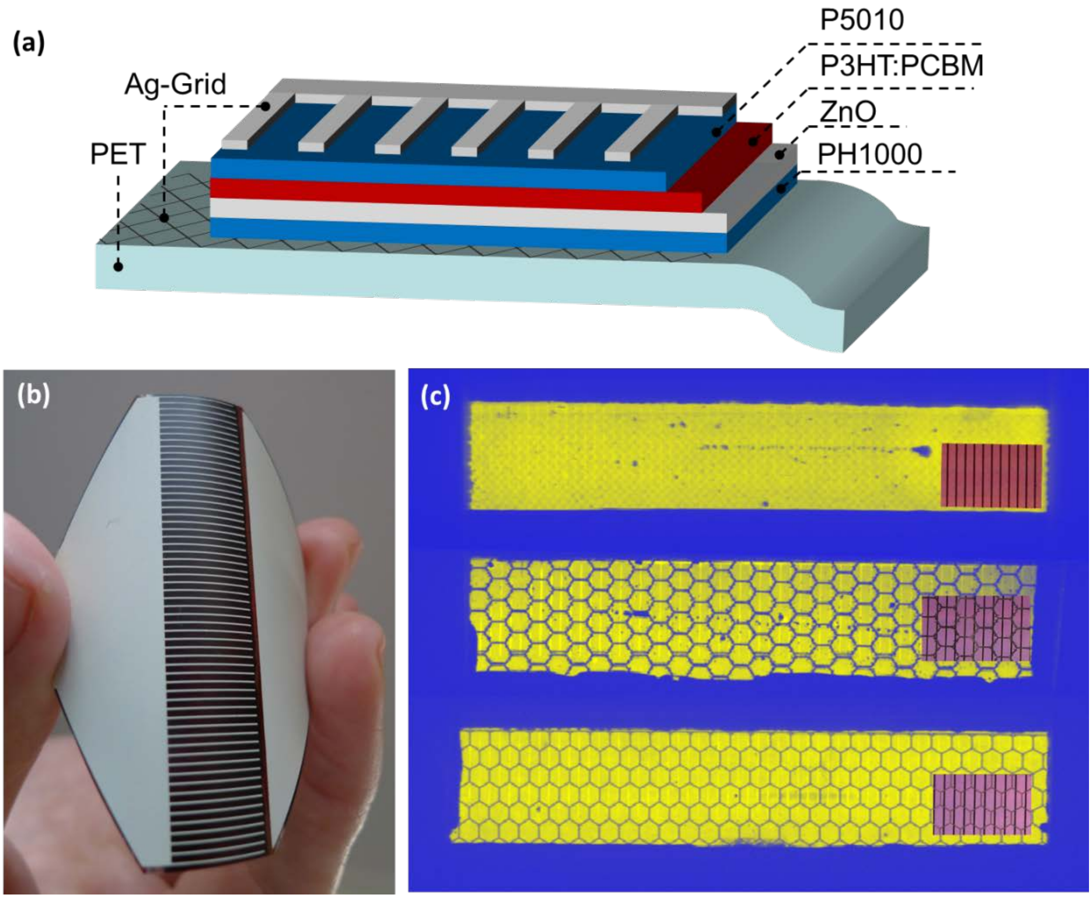

Figure 5.11: (a) A schematic illustration of the complete device stack, here shown with the embedded grid electrode. (b) Device seen from the back side, featuring the screen printed back electrode. (c) LBIC images of devices based on the embedded (top), inkjet (middle), and flexographic (bottom) grid respectively. The small inserts show photos of the particular cell type with strong backlighting.

One point of concern was the ability of the coated layers to cover the protrusions in the silver grid substrate, so as to avoid shunted solar cells. Luckily all grid types performed equally well, after the initial switching procedure showing no signs of shunting, clearly shown by the homogeneous LBIC images in Figure 5.11c. Firstly, it is of course likely that the switching in the case of these grid-based devices double-functions as a shunt burning procedure, and indeed it was seen that sometimes the switching led to physical shunt burning in a few places on the cell during switching (these might be seen as dead spots in the LBIC in Figure 5.11c). Secondly, it is likely that the choice of coating method of the PH1000 layer (first layer coated on the grid) has a major influence on the ability to cover roughness. While methods such as spin coating has a shear field which is parallel to the substrate (i.e. normal to the roughness) which might lead to poor coverage of protrusions, the rotary screen printing method employed here has a shear field which is normal to the substrate while it generally also allows the use of inks with much higher solid content [57], both possibly leading to better coverage of surface roughness.

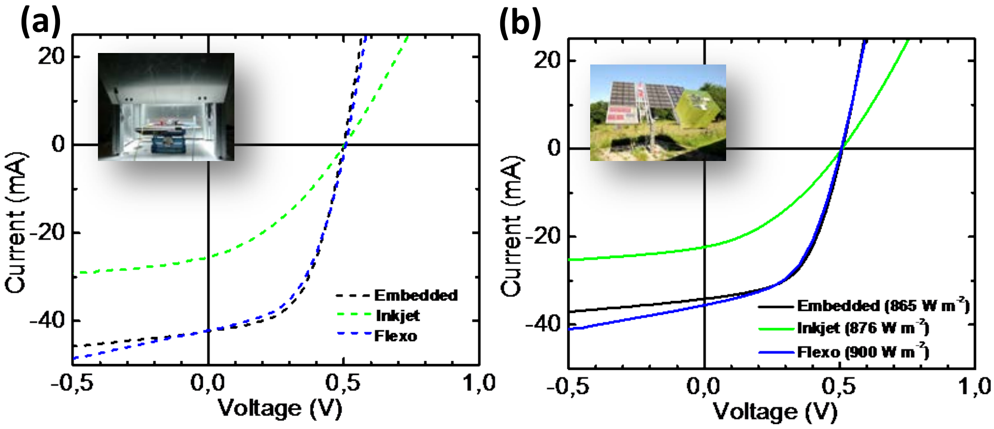

Figure 5.12: J-V characteristics of the three types of devices, as measured in the lab (left) and under the real sun (right), where the number in parenthesis indicates the incident light intensity.

Table 5.4: IV-data comparison for the three device types, measured both under simulated light (lab) and under direct sunlight (outdoor).

	Imprint		**Inkjet**		**Flexo**	
	Lab[a]	**Outdoor**[b]	**Lab**[a]	**Outdoor**[c]	**Lab**[a]	**Outdoor**[d]
PCE (%)	1.92	1.84	0.75	0.79	1.82	1.72
J_{sc} (mA cm^{-2})	-7.06	-5.68	-4.27	-3.72	-7.02	-5.92
V_{oc} (V)	0.50	0.51	0.50	0.51	0.51	0.51
FF (%)	54.5	54.8	35.1	36.5	51.2	51.6

[a] AM1.5G, 1000 W m^{-2}, [b] 865 W m^{-2} (Global), [c] 876 W m^{-2} (Global), d) 900 W m^{-2} (Global).

The three device types were encapsulated between two sheets of barrier foil (Amcor) using UV-curable adhesive (DELO), followed by J-V characterized using indoor STC as well as outdoor on a solar cell tracker. The results are shown in Figure 5.12a and b respectively, and summarized in Table 5.4.

Notably, both device types gives >50% FF which is very high numbers considering that these are large area cells. And with efficiencies just under 2% the devices perform better than comparable ITO-based *ProcessOne* cells [41]. Devices based on the embedded grid performed marginally better than those based on the flexo grid, driven by a higher fill factor. Surprisingly the higher transmittance of the embedded grid does not lead to higher J_{sc} , which might be a result of a significant amount of indirect light, in which case the shadow-loss will be equalized. The inkjet grid-based devices perform quite poorly, clearly a result of the very low sheet resistance of the inkjet print as compared to the two other grid types (Table 5.3). This is also evident from the relative better performance of the inkjet-based devices in outdoor conditions, given a non-linear light-intensity dependence as a result of the high series resistance in the device. Thus the lower light intensity and lower temperature in the outside measurement leads to higher J_{sc} and FF [58].

This successfully demonstrates three methods for the fabrication of scalable ITO-free solar cells based on silver grid electrodes. While the embedded grid did perform best of the three, it does suffer from being a much slower and more cumbersome process, where on the other hand the flexo printed grid performed nearly as well while it allows for extremely fast processing. The embedded grid solution will be the choice when performance is a priority, while flexo grid wins on cost. The inkjet printing proved to produce nice and smooth grids, but its further success depends on whether the conductivity can be raised significantly.

5.4.2. Scalability of solar cell modules based on the flexo grid electrode

In order to further test the performance of the flexo-based *iOne* solar cells, a series of scalability studies were carried out. Instead of single stripe cells, wide-stripe modules were prepared as depicted in Figure 5.13. Please refer to ref. [39] for experimental details. Modules of three different sizes were cut out from the main roll of solar cells and prepared by switching and subsequent double encapsulation. The final devices are shown in Figure 5.14b, with corresponding J-V characteristics shown in Figure 5.14a. Relevant data on the modules are compiled in Table 5.5. As it can be seen from the performance data, all module sizes performed excellent, showing no degrading effect of changing either stripe length or number of stripes. This leads to total area performances >1% which has not previously been reported for completely solution processed ITO-free >100 cm^2 modules. The observed lower performance of the small module might be a consequence of the relatively larger contribution of negative edge effects such as shunts and delamination due to the cutting procedure.

The observed scalability from single cell devices to large area modules, is undoubtedly a testament to the flexo-grid/PH1000 *flextrode*. Especially the FF values >50% is a very notable achievement. This should be compared to the mean FF of <40% for similar-sized ITO-based modules as previously reported by our group[4]. The only area in which the ITO surpases the flextrode is in transmittance, leading to the lower J_{sc} for the modules reported here, as compared to the >8 mA cm^{-2} which have been reported for *ProcessOne* [59]. This is mainly due to the light absorbed by flextrode, especially by the PH1000 (see Figure 6.2 for transmittance). It is, however, likely that this layer can be made thinner and more transparent pending the development of new high conductive PEDOT:PSS formulations.

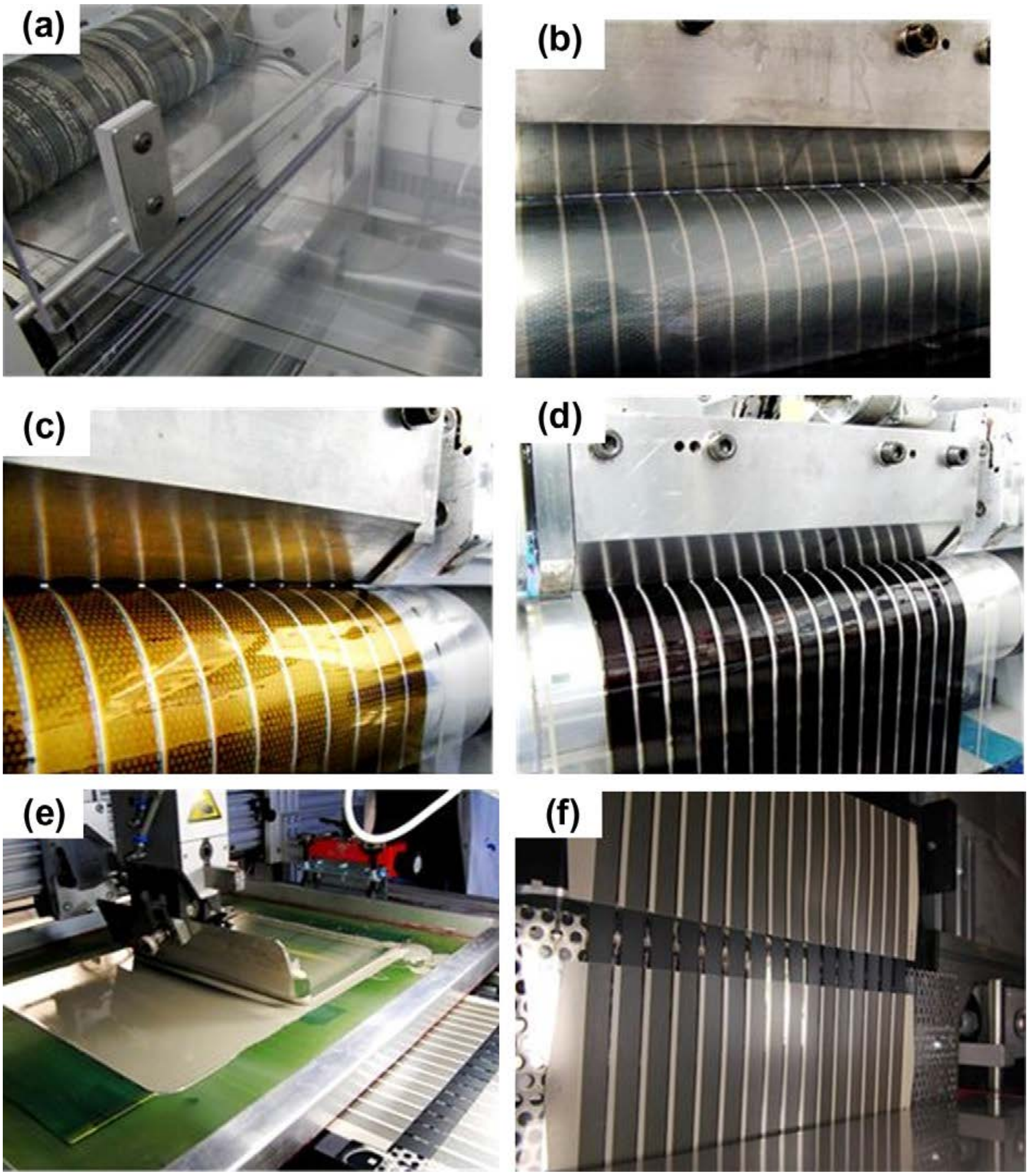

Figure 5.13: Pictures of the different R2R printing and coating steps in fabrication of the modules: (a) flexo printing of Ag grid; (b–d) slot die coating of PH1000, P3HT:PCBM, and P5010 respectively; (e) flat-bed screen printing of Ag paste; and (f) final module. Reproduced with permission from ref. [39]**.**

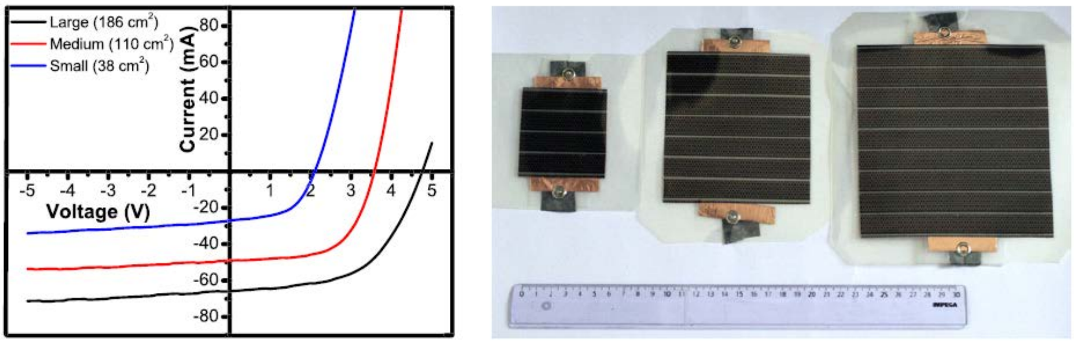

Figure 5.14: (left) J-V curves of ITO-free modules of three different sizes as shown in the photo (right). Reproduced with permission from ref. [39].

Table 5.5: PV parameters and other key data of the three differently sized modules.

Device	A_T[a] (cm^2)	A_A[b] (cm^2)	A_s[c] (cm^2)	No. of stripes	J_{sc} (mA cm^{-2})	V_{oc} (V)	FF (%)	PCE (A_A)	PCE (A_T)
Small	38.28	24	6.00	4	4.84	2.11	53.6	1.36	0.86
Medium	110.47	70	10.3	7	4.85	3.59	61.3	1.60	1.10
Large	186.30	121.5	13.5	9	5.45	4.76	55.6	1.62	1.05

[a] Total area of module, not including encapsulation. [b] Active area of device, including area blocked by front grid.[c] Area of one cell/stripe.

5.4.3. Photonic sintering for improved R2R inkjet printed electrodes

In an effort to improve the front electrode conductivity of the small ITO-free modules described in section 5.3, an inkjet pattern was designed as shown in Figure 5.15c. The experiment built on the work presented in section 5.4.1 showing the first attempt at making PSC front grids by R2R inkjet printing which resulted in relatively low conductivity grids (~60 $\Omega_\square$), not much better than what can be obtained with PEDOT:PSS. The problem was thought to be lack of proper sintering of the nanoparticles during printing and drying as shown in Figure 5.10. At the optimized printing speed of 2 m min^{-1}, the oven length of 2 m resulted in the inkjet print only getting 1 min of annealing at 140 °C, which again lead to high resistivity of ~60 $\Omega_\square$. So to improve the situation, the finished roll was subdued to an additional annealing step of 2 min, leading to a resistivity of 18-20 $\Omega_\square$. Further improvements were sought via so-called photonic sintering by the use of a R2R xenon flash system as described earlier by Hösel and Krebs [60]. The flash ran a 0.5 ms pulse with a maximum pulse energy of 830 J at a frequency of 1.8 Hz. The setup in action is shown in Figure 5.15a. By running the web at three different speeds, we obtained grid which had effectively received 1, 2 and 4 flashes respectively. The subsequent R2R PSC fabrication was identical to that described in Figure 5.5, with further details found in ref. [38].

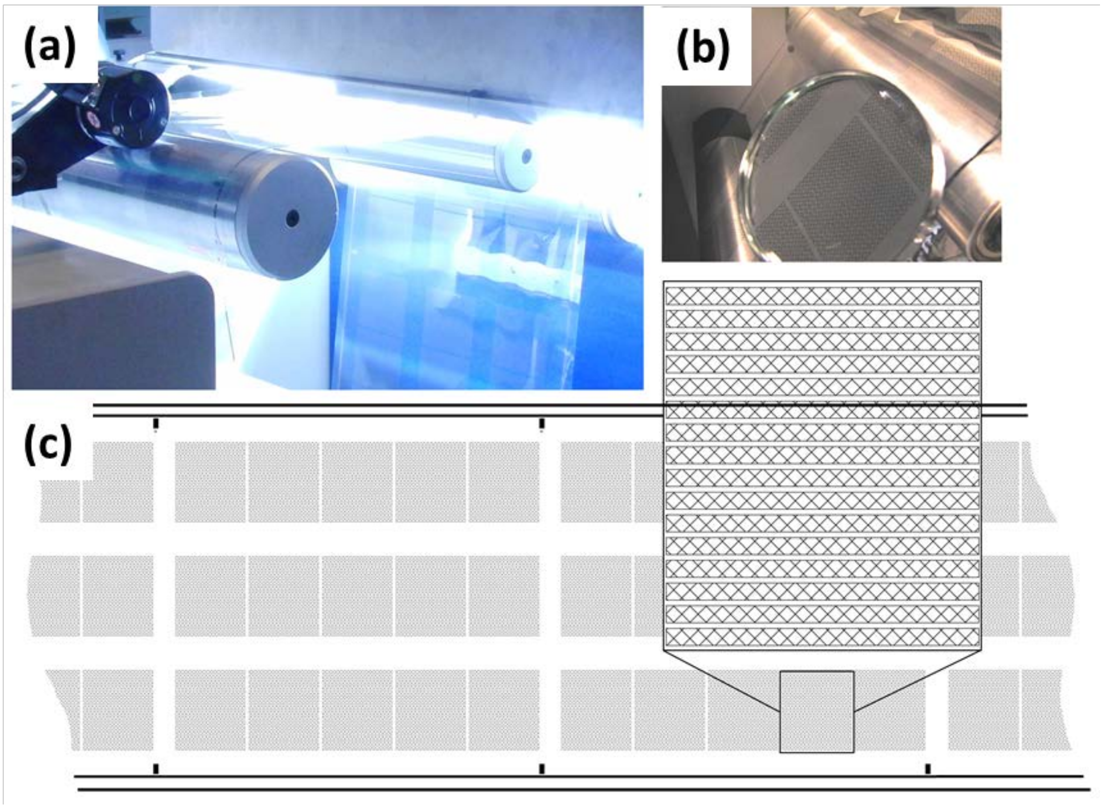

Figure 5.15: (a) Picture of the R2R photonic sintering by UV flashing. (b) picture of the R2R inkjet printed pattern after drying. (c) Illustration of the PET web with the repeated motif comprising 15 induvidual modules with the pattern for the inkjet printed grid showing in the blow-up. Reproduced with permission from ref. [38]**.**

5.4.3.1. Results

The conductivity of the grid was measured by 4-point probe, and the results are listed in Table 5.6. The flashing resulted in improved conductivity with 4 flashes leading to ∼10 Ω/□, clearly a result of the photonic sintering in line with what was reported earlier [60]. The completed PSCs were R2R switched and J-V characterized with the results seen in Figure 5.16 and Table 5.6. As it shows, the photonic sintering leads to minor improvements in the performance, mainly through improvements in the photocurrent, where we see significant improvement when comparing the un-flashed with the 4-x-flashed devices. When comparing the results to the otherwise similar grid-free small modules of section 5.3, one sees that the FF, which would be the factor most directly relatable to the sheet resistivity of the front electrode, is not improved. This is ascribed to the narrow PH1000 lines in the module imposed by the small module design. In contrast the photocurrent is significantly lower in the devices shown here than for the grid-free alternative, clearly due to the shadow-effect of the grid. The improvement in photocurrent with the degree of photonic sintering is, along the same lines, most likely caused by grid shrinkage upon flashing. A secondary positive effect of the photonic sintering is a much improved adhesion to the substrate, where it was observed that just exposure to

1 flash would render the inkjet print resistance to the tape-test, whereas the un-flashed print was completely removed.

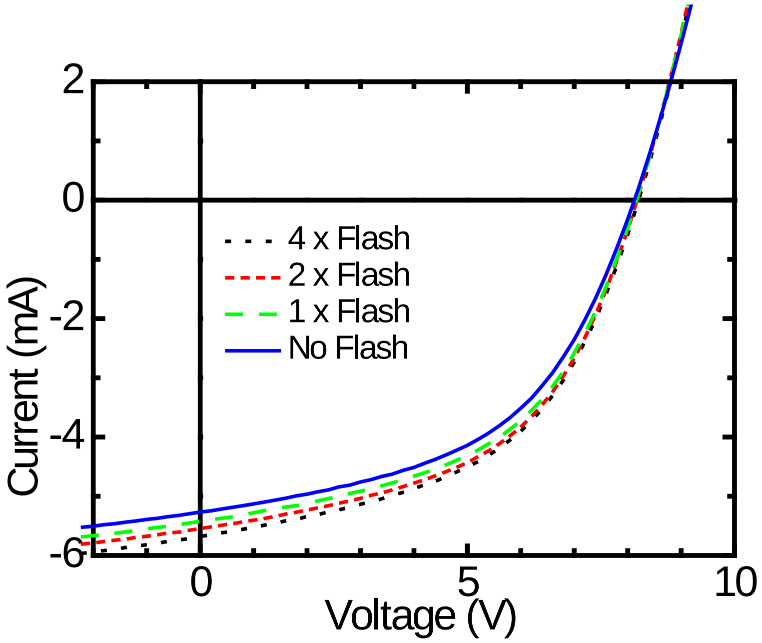

Figure 5.16: J-V characteristics of the small modules having an inkjet printed front grid with varying degree of flash exposure. The curves are averages of 6 modules. The measurements are done at 90 mW cm^{-2}.

Table 5.6: Summary of IV-data of devices with varying degree of photonic sintering (number of flashes). The values are averaged over 6 modules with the standard deviation in parenthesis.

Number of flashes	PCE[a] (%)	I_{sc}[b] (mA)	V_{oc} (V)	FF (%)	R_{sh}[c] (Ω/□)
No flash	1.5 (0.04)	-5.3 (0.2)	8.1 (0.04)	50 (0.6)	18-20
1 x flash	1.6 (0.03)	-5.4 (0.16)	8.2 (0.05)	51 (0.9)	16-17
2 x flash	1.7 (0.1)	-5.5 (0.3)	8.2 (0.03)	51 (0.7)	14-16
4 x flash	1.7 (0.1)	-5.7 (0.3)	8.2 (0.04)	51 (0.9)	9-12

[a] Module active area of 15.4 cm^2 (i.e. not corrected for aperture loss caused by the front grid). [b] Measured at 90 mW cm^{-2}. [c] Sheet resistance of the inkjet printed front grid measured by 4-point probe.

5.5. Conclusion

In conclusion, a scalable and convincing replacement for ITO as transparent electrode in R2R processed PSCs was developed. In its simplest form it consisted of R2R processed highly conductive PEDOT:PSS and ZnO. PSCs based on this PEDOT:PSS electrode only worked after exposure to a short burst of high voltage (5-20 V for <1 s, depending on active area) upon completion. We have described the working mechanism behind this in-situ formation of the rectifying junction, as a result of PEDOT reduction and PSS oxidation, upon which a stable undoped layer of PEDOT:PSS is formed that effectively blocks electron injection.

To achieve true scalability, the PEDOT:PSS front electrode was combined with a conductive metal grid. Three types were compared: embedded, flexo printed and inkjet printed grids: The embedded grid fabricated by thermal nano-imprint in the PET substrate and subsequent filling of silver, excelling by a high transmittance (80%) while retaining a high conductivity. The flexo printed grids had lower transmittance but excelled by very high processing speed. The conductivity was similar to the embedded, and the raised topography did not hinder the successful printing of PSCs. The embedded grid resulted in solar cells with slightly higher performance than the flexo printed grid. PSCs based on the inkjet printed grid initially showed low performance due to a very low conductivity of the grid. Later, however, it was shown how R2R photonic sintering could significantly improve the inkjet grid conductivity, thus levelizing its performance in PSCs with other grid types. All grid types were fabricated by aqueouse inks, and generally using much less time and energy than ITO. However, the flexo grid outperformed the other grid types in terms of processing speed and thus represented the most convincing alternative to ITO. The Flexo grid/PEDOT:PSS electrode was named the *flextrode*

Finally, large PSC modules based on the *flextrode* were fabricated having >1% PCE on the total module area of >100 cm^2 while retaining above 50% FF, showing the highest reported performance on ITO-free PSCs of this size, while clearly outperforming ITO-based devices in terms of scalability.

5.6. References

[1] N. Espinosa, M. Hösel, D. Angmo, F.C. Krebs, Solar cells with one-day energy payback for the factories of the future, Energy & Environmental Science. 5 (2012) 5117.

[2] N.S. Sariciftci, D. Braun, C. Zhang, V.I. Srdanov, A.J. Heeger, G. Stucky, et al., Semiconducting polymer-buckminsterfullerene heterojunctions: Diodes, photodiodes , and photovoltaic cells, Applied Physics Letters. 62 (1993) 585–587.

[3] N. Espinosa, R. García-Valverde, A. Urbina, F.C. Krebs, A life cycle analysis of polymer solar cell modules prepared using roll-to-roll methods under ambient conditions, Solar Energy Materials and Solar Cells. 95 (2010) 1293–1302.

[4] F.C. Krebs, T. Tromholt, M. Jørgensen, Upscaling of polymer solar cell fabrication using full roll-to-roll processing., Nanoscale. 2 (2010) 873–86.

[5] B. Azzopardi, C.J.M. Emmott, A. Urbina, F.C. Krebs, J. Nelson, Economic assessment of solar electricity production from organic-based photovoltaic modules in a domestic environment, Energy & Environmental Science. 4 (2011) 3741–3753.

[6] D. Angmo, F.C. Krebs, Flexible ITO-free polymer solar cells, Journal of Applied Polymer Science. (2012) 1–14.

[7] H. Ago, K. Petritsch, M.S.P. Shaffer, a. H. Windle, R.H. Friend, Composites of Carbon Nanotubes and Conjugated Polymers for Photovoltaic Devices, Advanced Materials. 11 (1999) 1281–1285.

[8] A. Du Pasquier, H.E. Unalan, A. Kanwal, S. Miller, M. Chhowalla, Conducting and transparent single-wall carbon nanotube electrodes for polymer-fullerene solar cells, Applied Physics Letters. 87 (2005) 203511.

[9] M.W. Rowell, M. a. Topinka, M.D. McGehee, H.-J. Prall, G. Dennler, N.S. Sariciftci, et al., Organic solar cells with carbon nanotube network electrodes, Applied Physics Letters. 88 (2006) 233506.

[10] G. Eda, Y.-Y. Lin, S. Miller, C.-W. Chen, W.-F. Su, M. Chhowalla, Transparent and conducting electrodes for organic electronics from reduced graphene oxide, Applied Physics Letters. 92 (2008) 233305.

[11] J. Wu, H. a. Becerril, Z. Bao, Z. Liu, Y. Chen, P. Peumans, Organic solar cells with solution-processed graphene transparent electrodes, Applied Physics Letters. 92 (2008) 263302.

[12] A. Kumar, C. Zhou, The race to replace tin-doped indium oxide: which material will win?, ACS Nano. 4 (2010) 11–4.

[13] V. Singh, D. Joung, L. Zhai, S. Das, S.I. Khondaker, S. Seal, Graphene based materials: Past, present and future, Progress in Materials Science. 56 (2011) 1178–1271.

[14] X. Wan, Y. Huang, Y. Chen, Focusing on energy and optoelectronic applications: a journey for graphene and graphene oxide at large scale., Accounts of Chemical Research. 45 (2012) 598–607.

[15] R. Po, C. Carbonera, A. Bernardi, F. Tinti, N. Camaioni, Polymer- and carbon-based electrodes for polymer solar cells: Toward low-cost, continuous fabrication over large area, Solar Energy Materials and Solar Cells. 100 (2012) 97–114.

[16] C.G. Granqvist, Transparent conductors as solar energy materials: A panoramic review, Solar Energy Materials and Solar Cells. 91 (2007) 1529–1598.

[17] M.-G. Kang, M.-S. Kim, J. Kim, L.J. Guo, Organic Solar Cells Using Nanoimprinted Transparent Metal Electrodes, Advanced Materials. 20 (2008) 4408–4413.

[18] B. Zimmermann, H.-F. Schleiermacher, M. Niggemann, U. Würfel, ITO-free flexible inverted organic solar cell modules with high fill factor prepared by slot die coating, Solar Energy Materials and Solar Cells. 95 (2011) 1587–1589.

[19] J.-Y. Lee, S.T. Connor, Y. Cui, P. Peumans, Solution-processed metal nanowire mesh transparent electrodes., Nano Letters. 8 (2008) 689–92.

[20] L. Hu, H.S. Kim, J. Lee, P. Peumans, Y. Cui, Scalable coating and properties of transparent, flexible, silver nanowire electrodes., ACS Nano. 4 (2010) 2955–63.

[21] D. Angmo, M. Hösel, F.C. Krebs, All solution processing of ITO-free organic solar cell modules directly on barrier foil, Solar Energy Materials and Solar Cells. 107 (2012) 329–336.

[22] B.F. Zhang, M. Johansson, M.R. Andersson, Polymer Photovoltaic Cells with Conducting Polymer Anodes, Advanced Materials. 14 (2002) 662–555.

[23] K. Tvingstedt, O. Inganäs, Electrode Grids for ITO Free Organic Photovoltaic Devices, Advanced Materials. 19 (2007) 2893–2897.

[24] S.-I. Na, S.-S. Kim, J. Jo, D.-Y. Kim, Efficient and Flexible ITO-Free Organic Solar Cells Using Highly Conductive Polymer Anodes, Advanced Materials. 20 (2008) 4061–4067.

[25] S.K. Hau, H.-L. Yip, J. Zou, A.K.-Y. Jen, Indium tin oxide-free semi-transparent inverted polymer solar cells using conducting polymer as both bottom and top electrodes, Organic Electronics. 10 (2009) 1401–1407.

[26] Y.H. Kim, C. Sachse, M.L. Machala, C. May, L. Müller-Meskamp, K. Leo, Highly Conductive PEDOT:PSS Electrode with Optimized Solvent and Thermal Post-Treatment for ITO-Free Organic Solar Cells, Advanced Functional Materials. 21 (2011) 1076–1081.

[27] E. Ahlswede, W. Mühleisen, M.W. bin Moh Wahi, J. Hanisch, M. Powalla, Highly efficient organic solar cells with printable low-cost transparent contacts, Applied Physics Letters. 92 (2008) 143307.

[28] S. Na, B. Yu, S. Kim, D. Vak, T. Kim, J. Yeo, et al., Fully spray-coated ITO-free organic solar cells for low-cost power generation, Solar Energy Materials and Solar Cells. 94 (2010) 1333–1337.

[29] Y. Zhou, H. Cheun, S. Choi, W.J. Potscavage, C. Fuentes-Hernandez, B. Kippelen, Indium tin oxide-free and metal-free semitransparent organic solar cells, Applied Physics Letters. 97 (2010) 153304.

[30] Y. Zhou, C. Fuentes-Hernandez, J. Shim, J. Meyer, A.J. Giordano, H. Li, et al., A universal method to produce low-work function electrodes for organic electronics., Science (New York, N.Y.). 336 (2012) 327–32.

[31] T. Kim, S. Na, S. Oh, R. Kang, B. Yu, J. Yeo, All-solution-processed ITO-free polymer solar cells fabricated on copper sheets, Solar Energy Materials and Solar Cells. 98 (2012) 168–171.

[32] A. Manor, E.A. Katz, T. Tromholt, B. Hirsch, F.C. Krebs, Origin of size effect on efficiency of organic photovoltaics, Journal of Applied Physics. 109 (2011) 1–9.

[33] F.C. Krebs, All solution roll-to-roll processed polymer solar cells free from indium-tin-oxide and vacuum coating steps, Organic Electronics. 10 (2009) 761–768.

[34] M. Manceau, D. Angmo, M. Jørgensen, F.C. Krebs, ITO-free flexible polymer solar cells: From small model devices to roll-to-roll processed large modules, Organic Electronics. 12 (2011) 566–574.

[35] Y. Galagan, J.-E. J.M. Rubingh, R. Andriessen, C.-C. Fan, P. W.M. Blom, S. C. Veenstra, et al., ITO-free flexible organic solar cells with printed current collecting grids, Solar Energy Materials and Solar Cells. 95 (2011) 1339–1343.

[36] T.T. Larsen-Olsen, R.R. Søndergaard, K. Norrman, M. Jørgensen, F.C. Krebs, All printed transparent electrodes through an electrical switching mechanism: A convincing alternative to indium-tin-oxide, silver and vacuum, Energy & Environmental Science. 5 (2012) 9467.

[37] J.-S. Yu, I. Kim, J.-S. Kim, J. Jo, T.T. Larsen-Olsen, R.R. Søndergaard, et al., Silver front electrode grids for ITO-free all printed polymer solar cells with embedded and raised topographies, prepared by thermal imprint, flexographic and inkjet roll-to-roll processes., Nanoscale. 4 (2012) 6032–40.

[38] D. Angmo, T.T. Larsen-Olsen, M. Jørgensen, R.R. Søndergaard, F.C. Krebs, Roll-to-Roll Inkjet Printing and Photonic Sintering of Electrodes for ITO Free Polymer Solar Cell Modules and Facile Product Integration, Advanced Energy Materials. 3 (2013) 172–175.

[39] D. Angmo, S.A. Gevorgyan, T.T. Larsen-Olsen, R. Søndergaard, M. Hösel, M. Jørgensen, et al., Scalability and stability of very thin, roll-to-roll processed, large area, indium-tin-oxide free polymer solar cell modules, Organic Electronics. 14 (2013) 984–994.

[40] M. Hösel, R.R. Søndergaard, M. Jørgensen, F.C. Krebs, Fast Inline Roll-to-Roll Printing for Indium-Tin-Oxide-Free Polymer Solar Cells Using Automatic Registration, Energy Technology. 1 (2013) 102–107.

[41] F.C. Krebs, S. a. Gevorgyan, J. Alstrup, A roll-to-roll process to flexible polymer solar cells: model studies, manufacture and operational stability studies, Journal of Materials Chemistry. 19 (2009) 5442.

[42] N. Espinosa, F.O. Lenzmann, S. Ryley, D. Angmo, M. Hösel, R.R. Søndergaard, et al., OPV for mobile applications: an evaluation of roll-to-roll processed indium and silver free polymer solar cells through analysis of life cycle, cost and layer quality using inline optical and functional inspection tools, Journal of Materials Chemistry A. (2013).

[43] P. Sommer-Larsen, M. Jørgensen, R.R. Søndergaard, M. Hösel, F.C. Krebs, It is all in the Pattern-High-Efficiency Power Extraction from Polymer Solar Cells through High-Voltage Serial Connection, Energy Technology. 1 (2013) 15–19.

[44] A. Manor, E. a. Katz, T. Tromholt, F.C. Krebs, Enhancing functionality of ZnO hole blocking layer in organic photovoltaics, Solar Energy Materials and Solar Cells. 98 (2012) 491–493.

[45] A. Manor, E. a. Katz, T. Tromholt, F.C. Krebs, Electrical and Photo-Induced Degradation of ZnO Layers in Organic Photovoltaics, Advanced Energy Materials. 1 (2011) 836–843.

[46] S. Möller, C. Perlov, W. Jackson, C. Taussig, S.R. Forrest, A polymer/semiconductor write-once read-many-times memory., Nature. 426 (2003) 166–9.

[47] S. Möller, S.R. Forrest, C. Perlov, W. Jackson, C. Taussig, Electrochromic conductive polymer fuses for hybrid organic/inorganic semiconductor memories, Journal of Applied Physics. 94 (2003) 7811.

[48] T. Johansson, L.A.A. Pettersson, O. Ingana, Conductivity of de-doped poly (3 , 4-ethylenedioxythiophene), 129 (2002) 269–274.

[49] X. Xu, R. a. Register, S.R. Forrest, Mechanisms for current-induced conductivity changes in a conducting polymer, Applied Physics Letters. 89 (2006) 142109.

[50] H.F. Dam, F.C. Krebs, Simple roll coater with variable coating and temperature control for printed polymer solar cells, Solar Energy Materials and Solar Cells. 97 (2012) 191–196.

[51] J.E. Carlé, T.R. Andersen, M. Helgesen, E. Bundgaard, M. Jørgensen, F.C. Krebs, A laboratory scale approach to polymer solar cells using one coating/printing machine, flexible substrates, no ITO, no vacuum and no spincoating, Solar Energy Materials and Solar Cells. 108 (2013) 126–128.

[52] F.C. Krebs, J. Fyenbo, D.M. Tanenbaum, S. a. Gevorgyan, R. Andriessen, B. van Remoortere, et al., The OE-A OPV demonstrator anno domini 2011, Energy & Environmental Science. 4 (2011) 4116.

[53] Y. Galagan, B. Zimmermann, E.W.C. Coenen, M. Jørgensen, D.M. Tanenbaum, F.C. Krebs, et al., Current Collecting Grids for ITO-Free Solar Cells, Advanced Energy Materials. 2 (2012) 103–110.

[54] Y. Galagan, E.W.C.C. Coenen, S. Sabik, H.H. Gorter, M. Barink, S.C. Veenstra, et al., Evaluation of ink-jet printed current collecting grids and busbars for ITO-free organic solar cells, Solar Energy Materials and Solar Cells. 104 (2012) 32–38.

[55] R.R. Søndergaard, M. Hösel, D. Angmo, T.T. Larsen-Olsen, F.C. Krebs, Roll-to-roll fabrication of polymer solar cells, Materials Today. 15 (2012) 36–49.

[56] J.-S. Yu, G.H. Jung, J. Jo, J.S. Kim, J.W. Kim, S.-W. Kwak, et al., Transparent conductive film with printable embedded patterns for organic solar cells, Solar Energy Materials and Solar Cells. 109 (2013) 142–147.

[57] F.C. Krebs, Fabrication and processing of polymer solar cells: A review of printing and coating techniques, Solar Energy Materials and Solar Cells. 93 (2009) 394–412.

[58] T. Tromholt, E. a. Katz, B. Hirsch, A. Vossier, F.C. Krebs, Effects of concentrated sunlight on organic photovoltaics, Applied Physics Letters. 96 (2010) 073501.

[59] J. Alstrup, M. Jørgensen, A.J. Medford, F.C. Krebs, Ultra Fast and Parsimonious Materials Screening for Polymer Solar Cells Using Differentially Pumped Slot-Die Coating, ACS Applied Materials & Interfaces. 2 (2010) 2819–2827.

[60] M. Hösel, F.C. Krebs, Large-scale roll-to-roll photonic sintering of flexo printed silver nanoparticle electrodes, Journal of Materials Chemistry. 22 (2012) 15683.

6 Towards Consensus in the characterization of PSCs

6.1. Introduction

The future seems bright for OPV: The record device efficiencies have convincingly progressed beyond 10 % [1–4], while R2R fabrication schemes have evolved towards encompassing true scalability, from gadgets to bulk energy production [6–9]. Unfortunately, however, the two developments have been parallel showing little sign of convergence. The average laboratory efficiencies, be it for either small area OPV prepared by spin coating or large area OPV prepared via R2R coating and printing methods, are still lacking significantly behind the record numbers. This has been shown convincingly in a recent literature overview by Jørgesen et al. [5], collecting and comparing PV data from all OPV publications up to September 2011 (>10000 individual records). Thus it might seem a fact of life within the field of OPV that reproducibility and scalability is relatively poor. Two distinct factors can be said to contribute to this: One is intrinsically inherent to the OPV device, coming from the numerous parameters entering into the fabrication procedure (e.g. spin coating [6]) as well as the synthesis of the materials composing the device. These variations are, in a sense, hidden variables due to a systematic neglect of statistics when presenting OPV efficiency data, as the current habit is that only the “hero” device is presented. The extent of the spread, however, becomes quite obvious when large PV data sets of similarly prepared devices are studied (eg. ref [7,8] and SI of [9]). As ‘batch’ variations has been shown to be much smaller when using R2R methods [10] it is clear that these intrinsic variations can be mitigated by exchanging spin coating and evaporation with more scalable fabrication methods [11].

Another distinct factor which might be limiting OPV reproducibility can be said to be extrinsic. This extrinsic factor relates to the variations in the J-V characterization under AM1.5G STC. Influential parameters on the extrinsic variability includes effects related to masking and defining the device active area [13], and also the type of solar simulator used, especially if the spectral mismatch factor is disregarded. Such spectral variations might also have other unpredictable effects, depending on materials composition of interfacial layers and electrodes, such as the readily observed UV activation of ZnO [12–14]. While temporal variations in these extrinsic parameters might occur within each laboratory, the most significant variation must be inter-laboratory.

Perhaps the best way to investigate these inter-laboratory variations is through so-called round robin (RR) studies, where the same devices are measured in many laboratories. Previous to the work presented here, only one instance of a RR study with OPVs existed [15], while it is a technique often used within the field of inorganic PV [16–18].

This chapter presents two RR studies, performed in Europe and China respectively, the first one involving high efficiency relatively small area 'hero' devices fabricated on flexible substrate, but partially using spin coating and evaporation, while the latter RR involves a series of small modules and single cells fabricated using only R2R methods. Both studies involve ITO-free devices.

6.2. **Round Robin as a method for validating high efficiency OPV data**

In this study (ref. [19] and appendix 9), three different OPV devices were measured at four different laboratories in Europe: DTU in Denmark, FAU in Germany, INES in France and Merck in the UK. The devices A, B and C are shown in Figure 6.1(a-c). Devices A and B had an active area of 25 mm^2 and device C was 1 cm^2, where the active area was defined by the evaporated silver electrode with the layouts shown in Figure 6.1e.

Devices A and B were similar in all aspects but the front electrode, where A used an ITO-free front electrode consisting of slot-die coated highly conductive PEDOT:PSS (PH1000) (Figure 6.1e), while device B used the traditional PET/ITO substrate known from ProcessOne [13]. The devices were completed by fastening the substrate, either PET/PH1000 (A and C) or PET/ITO (B) to a bare glass slide using double sided tape, followed by spin coating of the ZnO-, active- and P5010 layer, and finally by evaporation of a silver electrode. The devices A and C were subdued to the switching procedure explained in section 5.2, before all the final devices were encapsulated using UV-curable adhesive (DELO LP655).

As the purpose of this study was to establish the RR method as a simple and robust way of obtaining consolidated PV data for the reporting of high efficiency OPV devices, the methodology was kept simple: The devices were transported between laboratories by an operator who also carried out all the J-V characterizations in collaboration with a local operator. Prior to the measurement, the solar simulator was calibrated to 100 mW cm^2 using the equipment and procedures customary to each laboratory. The measurement procedure was to make the J-V characterization as fast as possible, as to avoid heat-up of the device. The obtained J-V curves are presented in Figure 6.2(a-c) and the PV parameters summarized in

Table 6.1. The deviations in the PV parameters are illustrated in Figure 6.3 in terms of the relative deviation, δ, of measurement x, from the average μ: $\delta = {}^{x}/_{\mu} - 1$. As can be seen, there are severe variation in measurements between laboratories, up to ±15% relative to the mean, i.e. a disagreement of up to 30%. It is obvious that the deviations in PCE are largely due to variation of J_{sc} and thus the amount of incident light on the solar cells. The much lower disagreement in V_{oc} of <4% correlates well with a logarithmic light intensity dependence of V_{oc} [20]. The FF variation is somewhat in between with <13%, largest for the large device (C), likely due to the much higher series resistance in this device evident by the lower slope of the J-V curves in forward bias, causing an increased sensitivity to light intensity [21]. Despite the calibration procedures, the large variations in PCEs are thus mainly ascribed to spatial and temporal variations in the solar simulators with regards to spectrum, intensity and diffusivity (i.e. angular distribution). Factors which have all been found to influence greatly on PSC performance [22].

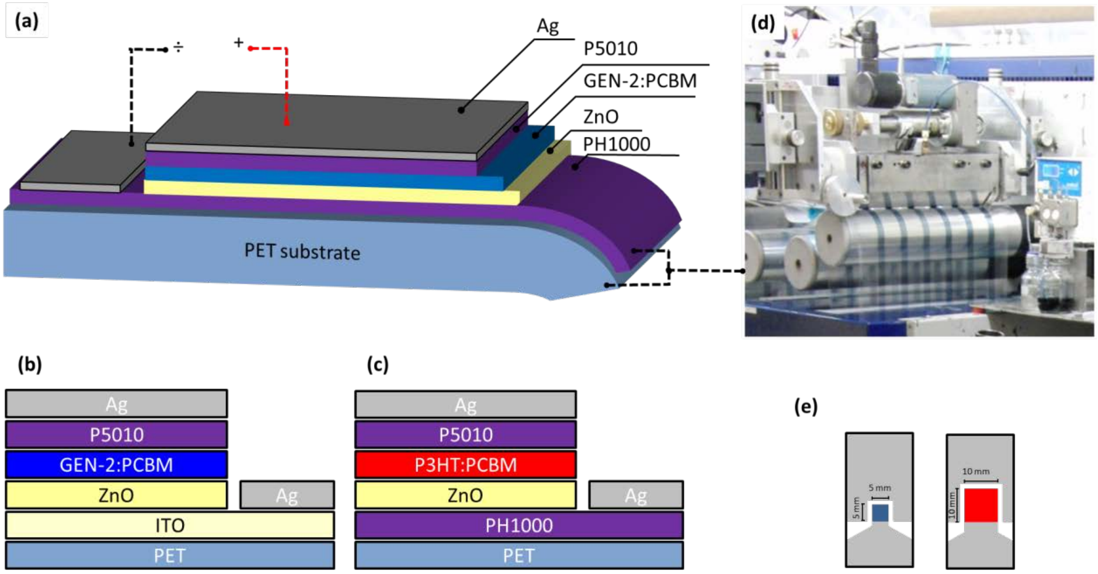

Figure 6.1: (a-c) show devices A,B and C respectively. (d) shows the slot-die coating of the PH1000 front PEDOT:PSS used for devices A and C. (e) shows the device layout, where device A and B are 5x5 mm^2 and device C is 10x10 mm^2.

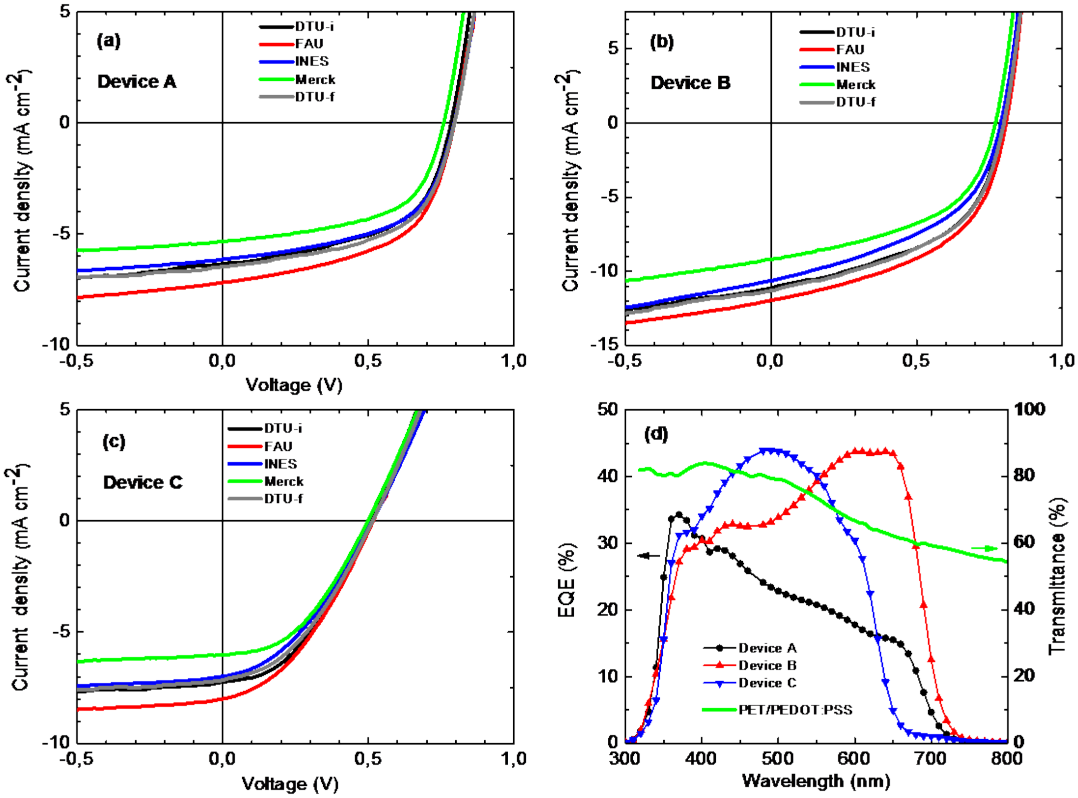

Figure 6.2: (a-c) J-V characteristics of the three devices A, B and C respectively as they were measured at the five different instances as indicated by the label, where '-i' and '-f' indicating initial and final measurement respectively.

Table 6.1: Summarized PV parameters of devices A / B /C as obtained at the different instances. where '-i' and '-f' indicating initial and final measurement respectively.

Lab / age	PCE (%)	Voc (V)	Jsc (mA cm^{-2})	FF (%)
(days)	A / B / C	A / B / C	A / B / C	A / B / C
DTU-i (3)	2.69 / 4.45 / 1.51	0.78 / 0.79 / 0.51	-6.33 / -11.1 / -7.24	54.2 / 50.3 / 40.9
FAU (6)	3.11 / 4.82 / 1.57	0.80 / 0.80 / 0.52	-7.17 / -12.0 / -7.99	54.2 / 50.3 / 37.7
INES (7)	2.69 / 3.86 / 1.34	0.80 / 0.79 / 0.51	-6.13 / -10.6 / -6.97	55.3 / 46.0 / 37.5
Merck (8)	2.29 / 3.52 / 1.28	0.76 / 0.77 / 0.50	-5.34 / -9.21 / -6.02	56.5 / 49.6 / 42.7
DTU-f (9)	2.83 / 4.47 / 1.44	0.80 / 0.80 / 0.51	-6.47 / -11.3 / -7.16	55.1 / 49.4 / 39.0
Average	2.70 / 4.22 / 1.42	0.79 / 0.79 / 0.51	-6.29 / -10.8 / -7.08	55.0 / 49.1 / 39.5
Rel.Std. dev. (%)[a]	9.73 / 11.1 / 7.46	1.93 / 1.38 / 1.46	9.36 / 8.53 / 8.97	1.60 / 3.26 / 5.00

[a] **Standard deviation relative to the average in [%].**

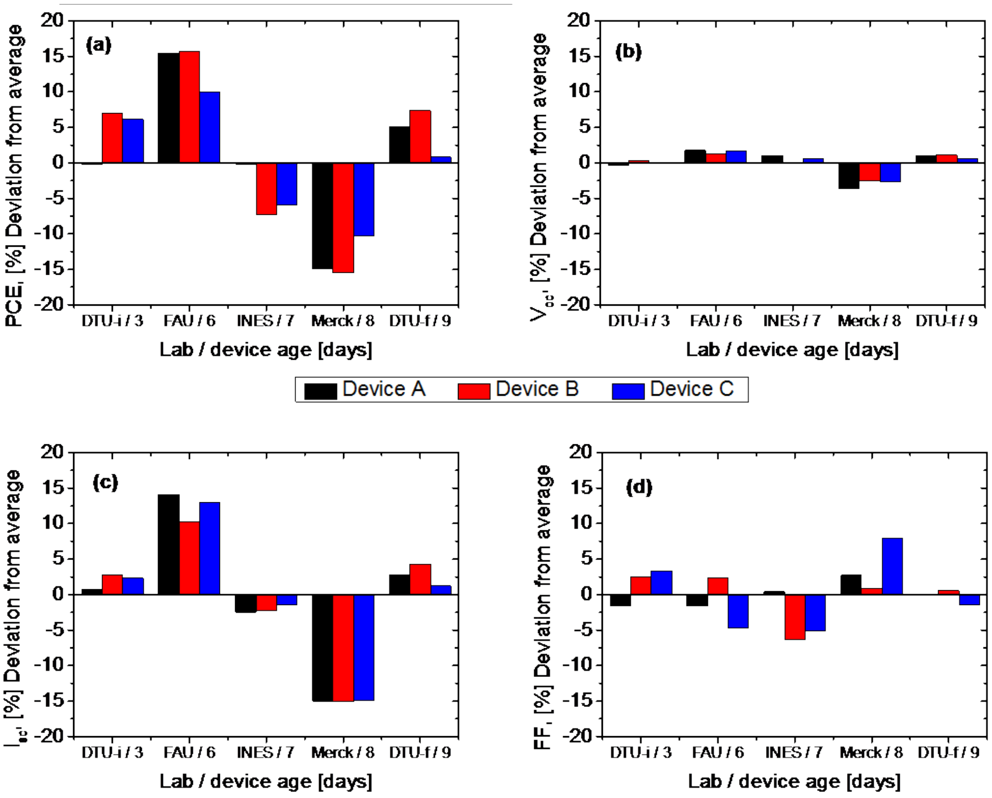

Figure 6.3: (a-d) Relative deviations from the average of the PV parameters PCE, V_{oc}, I_{sc} and FF respectively.

6.3. **A round robin across China**

To corroborate the findings in the previous section, a second, and larger, study was conducted (ref. [23] appendix 10) which employed the RR methodology to investigate the inter-laboratory variations among 14 laboratories in China, alongside DTU in Denmark where the devices, a set of all roll-to-roll (R2R) -coated and -printed ITO-free PSCs, were fabricated. As the number of publications on OPV coming from China today is among the highest for any country [5], this geographical boundary condition was an obvious choice as the high density of OPV laboratories enabled one operator to travel between each of the participating labs, ensuring that the measurements were conducted as similarly as possible, while keeping the total time of the experiment as low as possible, in order to minimize the effects of device degradation and failure.

6.3.1. The RR devices

The devices studied here were similar to the devices studied in section 5.4.2, fabricated according to the iOne procedure using the flextrode front electrode, with the solar cell module stack shown in Figure 6.4a. Three types of devices were cut out of the main roll of solar cells (Figure 6.4(b-g)), following the parameters listed in Table 6.2: RR devices physical data and definitions..

The devices were encapsulated between two sheets of flexible Amcor barrier foil applied with a UV-curable adhesive (DELO LP655), then passing each device through the nip of a R2R machine (<0.5 m min^{-1}) enabling a homogeneous adhesive layer, and finally curing the devices under a UV-intense solar simulator for 5 min on each side. Electrical contacting through the encapsulation was made using nickel free button contacts [24].

Table 6.2: RR devices physical data and definitions.

Device type	No. of stripes	Nom. Active area (cm^2)	Cell outline	No. of devices in RR
RR1	4	20	5-by-5 cm	3
RR2	4	24	5-by-6 cm	3
RR3	1	1	1-by-1 cm	5

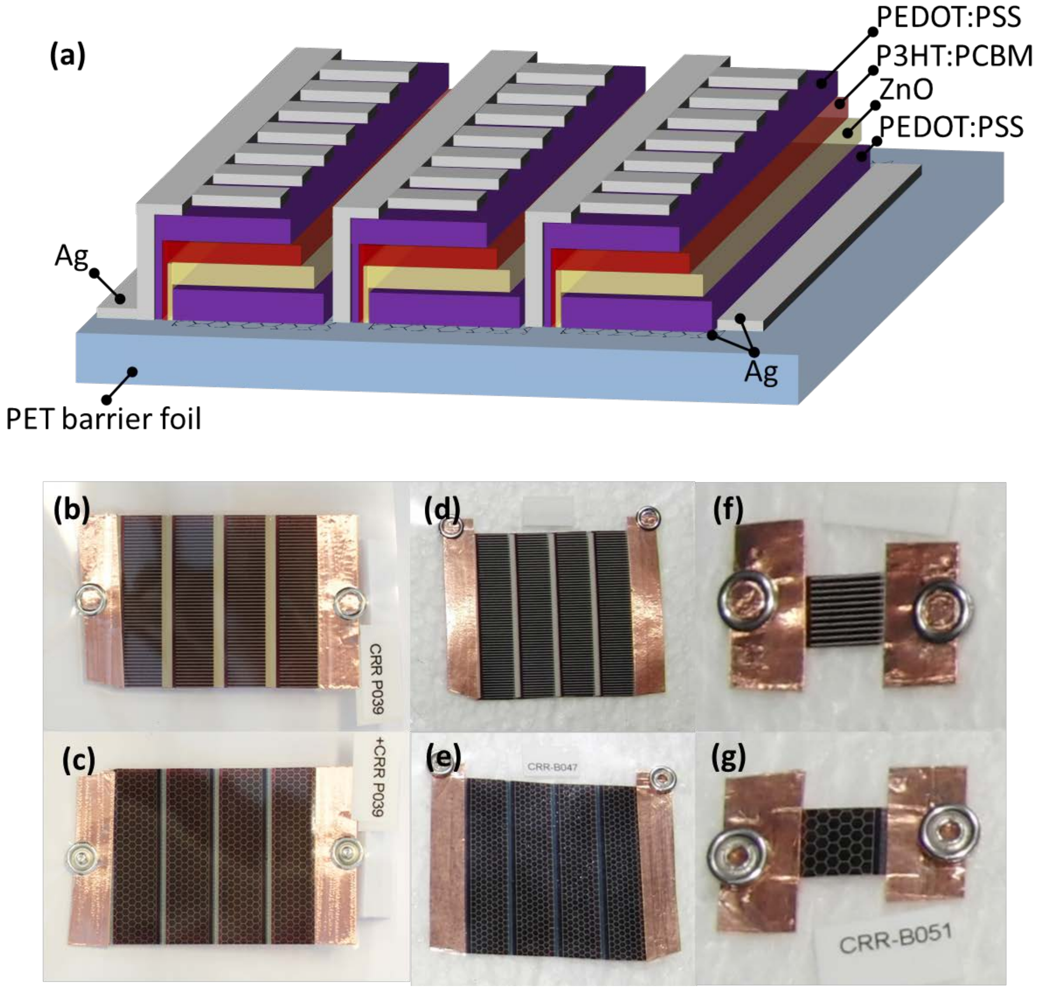

Figure 6.4: (a) Schematic drawing of the PV module stack used in this study, showing three stripes in series. (b-g) The RR devices under study, where b, d and f, shows the back side of devices of type RR1, RR2 and RR3 respectively. While c, e and g shows the flextrode (illuminated) side of type RR1, RR2 and RR3 respectively.

6.3.2. The RR laboratories and procedure

The RR included 15 laboratories 13 in mainland China, one in Hong Kong and DTU in Denmark. Acronyms and names of the laboratory responsible professor are listed in Table 6.3, with further details found in ref. [23].

Table 6.3: List of all contributing laboratories, listed alphabetically by Location. Highlighted laboratories also contributed to the lifetime round robin study.

Laboratory Name	Location	Laboratory leader
BNU	Beijing, China	Prof. Zhishan Bo
ICCAS 1	Beijing, China	Prof. Yongfang Li
ICCAS 2	Beijing, China	Prof. Jizheng Wang
ICCAS 3	Beijing, China	Prof. Jianhui Hou
NCNST	Beijing, China	Prof. Liming Ding
CIAC CAS	Changchun, China	Prof. Zhiyuan Xie
JLU	Changchun, China	Prof. Wenjing Tian
SCUT	Guanzhou, China	Prof. Hongbin Wu
ZJU	Hangzhou, China	Prof. Hongzhen Chen
IPP CAS	Hefei, China	Prof. Songyuan Dai
NCU	Nanchang, China	Prof. Yiwang Chen
FUNSOM	Suzhou, China	Prof. Wanli Ma
SINANO 1	Suzhou, China	Prof. Liwei Chen
SINANO 2	Suzhou, China	Prof. Liwei Chen
NKU	Tianjin, China	Prof. Yongsheng Chen
CUHK	Hong Kong, Hong Kong SAR	Prof. Ni Zhao
CLOP DTU	Roskilde, Denmark	Prof. Frederik C. Krebs

The RR procedure was as follows: The freshly prepared devices were initially J-V characterized at the OPV characterization lab (CLOP) at DTU. Next they were transported to China, where the operator (TTLO) brought them between laboratories by means of both land and air travel. Upon return to DTU, the devices were given a final characterization. At each laboratory, all the RR devices were tested according to a simple measurement protocol:

1. Each device is J-V characterized initially, keeping the illuminated time before measuring to a minimum (indicated as the 'initial' measurement in the following).
2. A dark J-V measurement is then performed.
3. The device is left under illumination for 5 min, and then a second J-V measurement is performed (indicated as the 'soaked' measurement in the following).
4. Followed by a final dark J-V measurement.

The protocol thus differs substantially from that used previously (section 6.2), building on the obtained experience and accommodating for a wish to further study temporal and spectral effects. To this end, the spectrum of each solar simulator was also recorded using a spectrometer (Avantes AvaSpec-3648).

The RR cycle is listed in Table 6.4, where the laboratories are listed anonymously due to the nature of the study. The table also lists the date of test and the types of devices tested; and as shown, some laboratories had small solar simulators which did not permit measurement of the larger **RR1-** and **RR2**-type devices. Furthermore, the first two labs in China only measured the **RR1** devices, as the other types did not arrive until later.

Table 6.4:The RR cycle, with the anonymous laboratory number and a corresponding date of the measurement. Circulation of devices of type a started a month earlier than the b and c type.

Laboratory #	Data of measurement	Device types measured
1 (DTU)	05-09-2012	RR1
2	21-09-2012	RR1
3	29-09-2012	RR1
4 (DTU)	05-10-2012	RR2, RR3
5	14-10-2012	RR1-3
6	16-10-2012	RR3
7	20-10-2012	RR1-3
8	22-10-2012	RR3
9	25-10-2012	RR1-3
10	26-10-2012	RR1-3
11	26-10-2012	RR3
12	29-10-2012	RR1-3
13	29-10-2012	RR1-3
14	05-11-2012	RR3
15	26-11-2012	RR1-3
16	28-11-2012	RR1-3
17	30-11-2012	RR1-3
18	30-11-2012	RR1-3
19	03-12-2012	RR3
20	03-12-2012	RR1-3
21 (DTU)	13-12-2012	RR1-3

To accommodate for long study period (3 months), an additional sub-study was carried out, designed to ascertain the long-term stability of the RR device types. A few laboratories chose to participate in this part as well, and have been highlighted in Table 6.3. In these long-term experiments, one device was kept outdoors without exposure to direct sunlight (i.e. in the shade), while a control device was kept indoor in the dark. The cells where routinely measured according to the same measurement protocol used in the RR.

6.3.3. Data treatment scheme

The large amounts of J-V data were handled by a number of Matlab® scripts. For each type of device, before and after light soaking, the following steps were carried out:

1. PV parameters were extracted for all J-V curves using two methods.
2. The two sets of PV data were compared and filtered for unphysical anomalies (e.g. spikes and abrupt jumps in J-V curves), while other non-converging data was manually evaluated.
3. The mean (μ_T) of all PV parameters was calculated, from which the relative deviation (δ_i) of each measurement (x_i) was calculated as: $\delta_i = {x_i}/{\mu_T} - 1$
4. Then, a new mean was calculated (μ_{10}) based ONLY on data which deviated ≤ 10% from μ_T. Thus avoiding biasing of the mean by a few outliers. Finally, using μ_{10}, the deviation of each measurement was calculated again: $\delta_i^{10} = {x_i}/{\mu_{10}} - 1$.

6.3.4. Evaluating the stability of the RR devices

An important factor for the success of the RR is to be able to rule out, or at least understand, possible device degradation, so as to be able to distinguish this from the ‘extrinsic’ deviations in PV performance. Therefore the stability of the RR devices was evaluated before further data treatment.

Figure 6.5a plot the difference in measured J_{sc} of the RR devices, from the initial measurement to the final one, meaning that negative current indicates degradation. As all **RR2**- and **RR2**-type devices show small, positive and similar current differences, we exclude degradation of these devices, while all **RR1**-type devices show significant degradation. This is also seen from the plot in Figure 6.5b, where the I_{sc} values have been normalized, both to the initial DTU measurement, and then to a combined average for the **RR2** and **RR3** devices for each laboratory, so as to average out the extrinsic inter-laboratory deviations. From this, it is clearly seen that the **RR1** devices fall much under the Y=1 line (black outlined symbols in Figure 6.5b). This, all in all, leads to the exclusion of the **RR1**-type devices from the final evaluation of the deviations in PV parameters as presented in the next section.

It is likely that the failure of **RR1**-type device is linked to the encapsulation procedure, which was done slightly different for the **RR1**-type, where the allowance of small air pockets between the barrier and solar cell gave rise to delamination in the device over time.

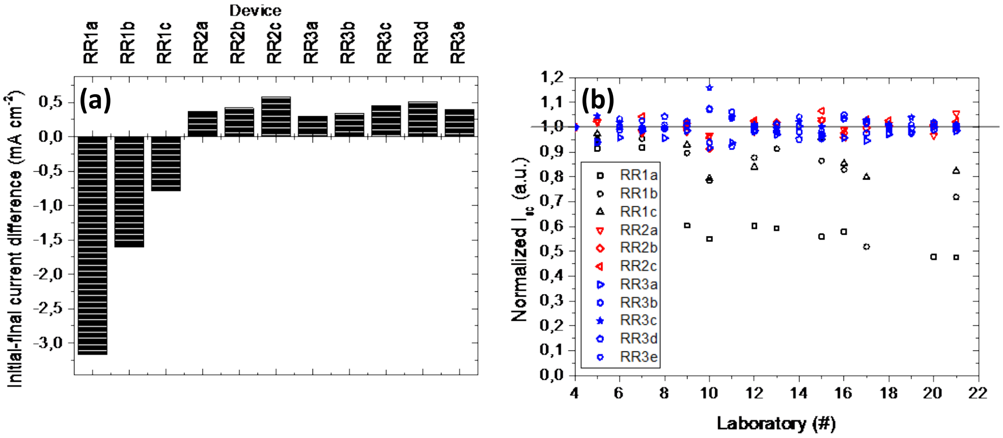

Figure 6.5:(a) The difference in J_{sc} between the initial and final characterization at CLOP (DTU) for all devices. (b) The normalized I_{sc} of all devices and all laboratories (lab # is proportional with time, c.f. Table 6.4), furthermore the data has been normalized to the combined average of the RR2- and RR3-type devices at each laboratory, to reveal the deviating behavior of the RR1 devices (black outlined symbols).

6.3.5. Deviations in 'initial' PV parameters

To best evaluate the inter-laboratory deviations, the 'initial' measurement is chosen (c.f. the RR protocol in section 0), as it is arguably the most comparable measurement, best avoiding effects from device temperature build-up and light-soaking.

In Figure 6.6 the relative deviations for all **RR2** and **RR3** devices are shown for the different laboratories, and the data shows obvious large variations. The two highlighted areas indicate laboratories using less than 1 sun intensity, 0.5 and 0.9 suns respectively. Although the deviations seen in both laboratories using lower intensity are significant and likely partially due to a nonlinear light intensity dependence of the I_{sc} [25], they are not outliers as such, and are not disregarded. Furthermore these measurements represent a not uncommon practice in OPV performance reporting. An important observation from Figure 6.6, is that the inter-laboratory variations are generally much larger than the intra-laboratory variations, meaning both that the devices are behaving comparably and that the observed variations are mostly effects of differences between measurement setups rather than operator-caused variations.

The maximum and overall standard deviations, with regards to the data shown in Figure 6.6, are summarized in Table 6.5. As can be seen, the RR experiment reveals up to 30 % deviation in PCE, mostly due deviations in I_{sc}. Also the FFs show large deviations up to 15 %, while the V_{oc} deviates the least. Both the trends and the significant deviations are on par with what was found in the smaller RR study presented in section 6.2, where also the I_{sc} was found to deviate the most.

The relative (absolute) standard deviations from the 'initial' measurements, for each device of type **RR2** and **RR3**, are plotted in Figure 6.7a. It is interesting to see that the magnitude of the standard deviations are very similar across all devices, considering the very different active area outline of the **RR2** and **RR3** types (5-by-6 cm module vs. 1-by-1 cm cell respectively), as one would expect spatial inhomogeneity in the measurement plane of the light sources [22] to impact PV variability of the larger module much more, as different serially connected stripes would be exposed to different intensities thus effecting the current output of the whole module.

In Figure 6.7b the relative deviation in PCE of all initial measurements are plotted in a histogram for device types **RR2** and **RR3** respectively, showing that deviations approach a normal distribution around the μ_{10} mean. This was not observed in the much smaller data set of section 6.2, and in this case validates the use of the derived standard deviations shown in Table 6.5.

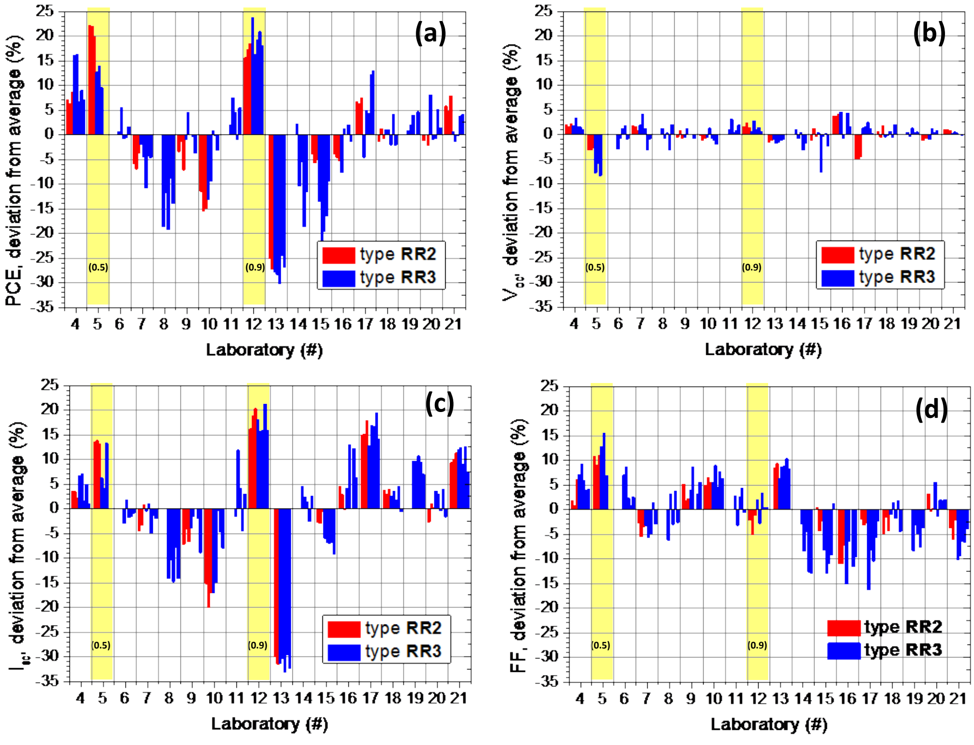

Figure 6.6: (a-d) Deviations in PV parameters (PCE, V_{oc}, I_{sc} and FF respectively) from the 'initial' measurements of all devices of type RR2 and RR3 among the different labs, relative to μ_{10}. For each lab, the devices are shown as columns in the order; first the three RR2 devices, then the five RR3 devices. The yellow markings indicate the two labs which used less than 1 sun intensity (fraction of suns indicated in the parenthesis, and I_{sc} data has been normalized to 1 sun).

Table 6.5: Summarized values of deviations in PV data from 'initial' measurements relative to μ_{10} also plotted in Figure 6.6.

Device type	Max deviation (+/- %)	Standard deviation (%)
	I_{sc} | V_{oc} | FF | PCE	I_{sc} | V_{oc} | FF | PCE
Type b	20/-31 | 4/-5 | 11/-11 | 22/-27	12 | 2 | 6 | 12
Type c	21/-33 | 5/-8 | 15/-16 | 24/-30	12 | 2 | 7 | 12

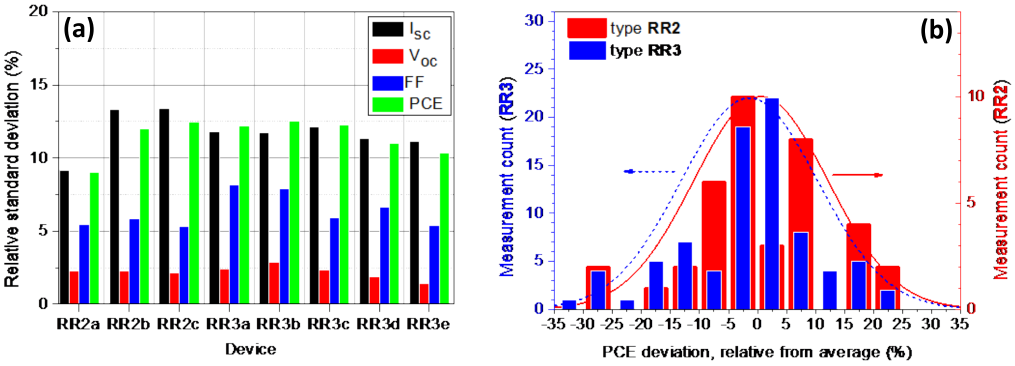

Figure 6.7: (a) Relative standard deviations for each of the RR2 and RR3 devices. (b) Histogram of all measurements, as deviations from μ_{10}, before light soaking ('initial') for device types RR2 and RR3.

6.3.6. Spectral effect: Light soaking and UV content

In an effort to partially deconvolute the effects leading to the inter-laboratory variation, the RR protocol included an additional J-V characterization following a 5 min light soaking step as well as the recording of the light source spectrum, so as to probe some spectral effects. In Figure 6.8 the correlation between measurements performed before and after light soaking is plotted for the different PV parameters. No light soaking effect would mean random distribution around the solid line, as is seen for the I_{sc}, while a small negative effect is seen for the V_{oc} (< 2 %), likely due to the increase in temperature. The FF on the other hand is positively affected by the light soaking with an average relative increase of 3 %, an increase which is likely also linked to the increased temperature as this will increase the conductivity of PEDOT:PSS and thus lower the series resistance in the device[26]. All-in-all this gives a slight positive effect of the light soaking on the PCE (Figure 6.8a).

Apart from the effect of temperature, the light soaking might have influence on the device performance through the known UV activation of the ZnO hole-blocking layer [12]. This was investigated through analysis of the recorded light source spectra seen in Figure 6.9a. This was done by calculating the relative amount of UV content, through integration of the normalized spectra from 280 nm to 380 nm. This defined UV-region of interest is plotted in Figure 6.9b from which a significant difference in UV content among the different solar simulators can clearly be seen.

However, no significant correlation was found between UV content and the effect of light soaking on the PV parameters.

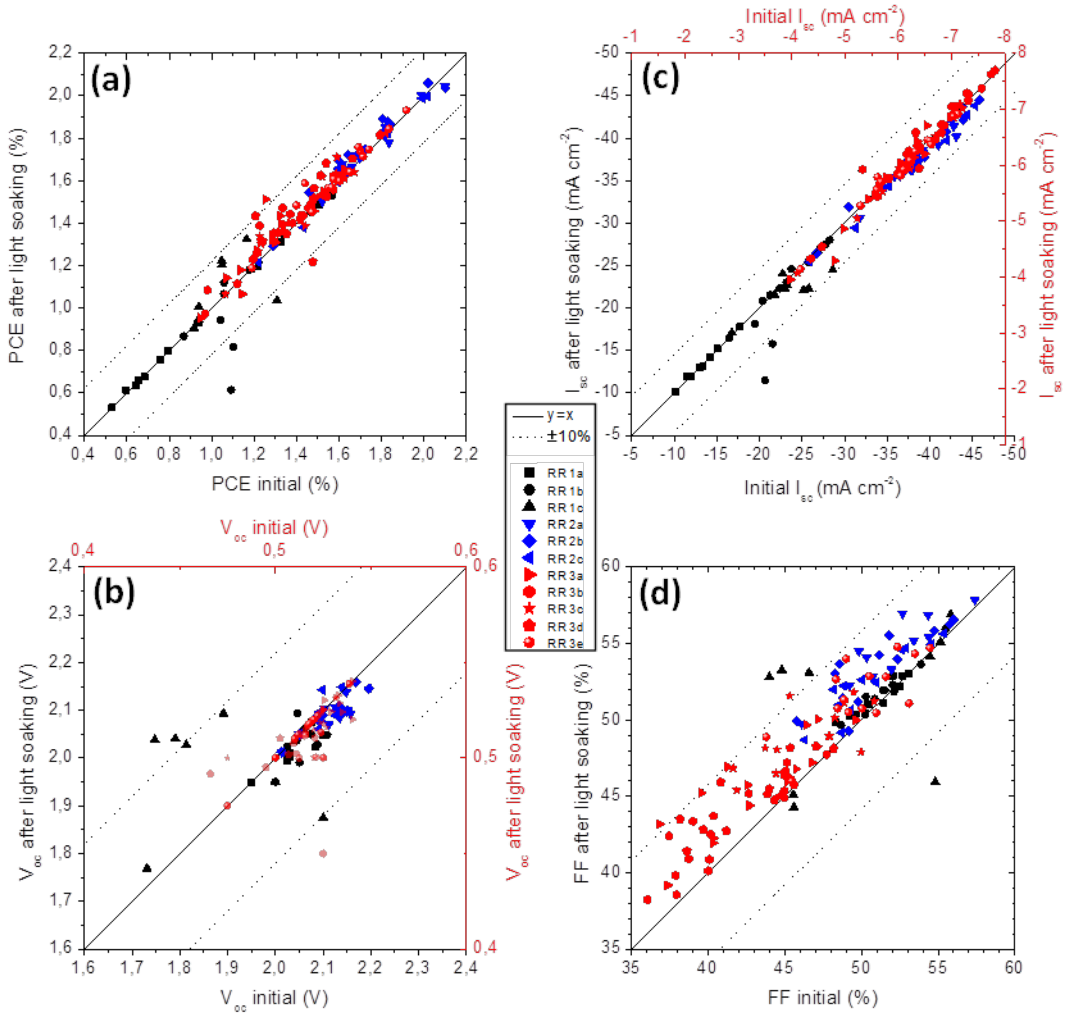

Figure 6.8: Correlation plots of PV parameters before and after light 5 min soaking for all laboratories. Each symbol represents a device of either type, where type is shown by color. In the case of I_{sc} and V_{oc} the top+right scale refers to the c-type devices as indicated by the color. The solid line indicates no difference between the initial and soaked measurements, while the dotted lines indicate ± 10 % of the (absolute) maximum value in the plot.

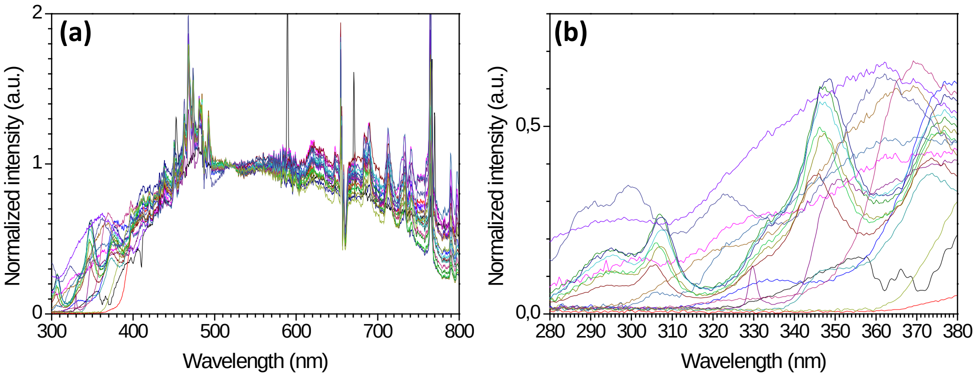

Figure 6.9: (a) Light source spectra from all the solar simulators used in the study, normalized to the intensity at 520 nm, where (b) is a zoom-in on the UV relevant range used to extract the relative UV content of the different light sources.

6.3.7. Long term stability study

As earlier mentioned, this RR study also included a parallel inter-laboratory study (ILS) of the long-term stability of the RR-type devices, along the lines of the much larger ILS-studies done in recent years [27,28]. This mini-ILS served the purpose of investigating what device stabilities could be expected during the RR, and included four laboratories performing outdoor shelf-life tests on the device types used in the RR in a range of climatic conditions representative for the RR route (climate details are listed in Table 6.6.). Figure 6.10 shows the PV parameters recorded at the four laboratories. Four of the five devices show less than 20 % degradation in PCE during the >90 days experiment, with the degrading parameter being the I_{sc}. One device shows complete failure after 100 days, possibly due to a failure of either a contact or the encapsulation. An interesting observation was that the one type-**RR1** device tested (LT4 at ZJU) does not show more degradation than the **RR2** devices.

As the actual RR devices were only exposed to extreme temperatures (outdoor conditions) for shorter periods of time during travel, and always kept in stabilizing packaging, these outdoor tests represent the worst possible scenario for the RR cells. So on the basis of this mini-ILS alone, it seems that these types of devices are relatively stable in a range of climatic conditions, and thus it can be assumed that degradation played a minor role in the PV parameter variations observed during the RR study.

Table 6.6: Details of the stability studies, including minimum, maximum, average temperature and average humidity, recorded in the study period. Data is taken from publically available weather sources.

Device ID (type)	Laboratory	T_{min} (°C)	T_{max} (°C)	T_{avg} (°C)	Avg. RH (%)
LT1 (RR2)	CIAC	-32	8	-14	72
LT2 (RR2)	CIAC	-32	8	-14	72
LT3 (RR2)	NCNST	-18	11	-4	54
LT4 (RR1)	ZJU	-5	31	10	65
LT5 (RR2)	NCU	-3	21	7	81

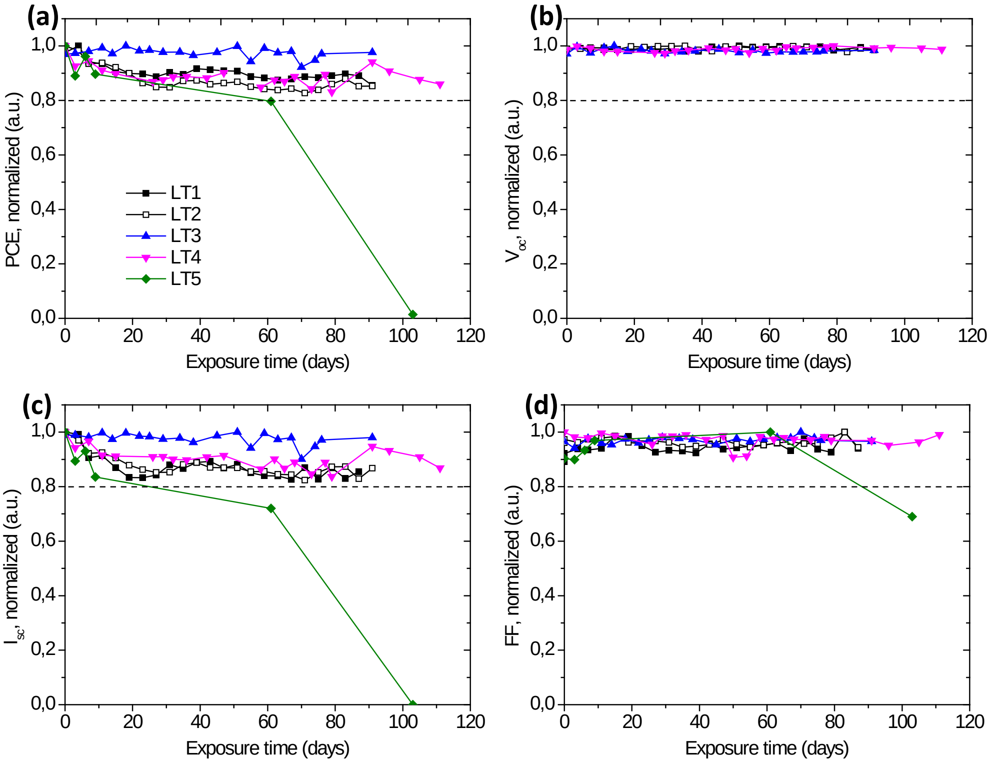

Figure 6.10: Data from 3-month long outdoor stability studies at four different locations, where the legend refers to the names defined in

Table 6.6.

6.4. Observations and recommendations

From the results from both RR studies it is clear that the I_{sc} is the prime contributor to the inter-laboratory variations. This is indeed regardless of the fact that a reference Si-device from the solar simulator manufacture was used regularly by all participating laboratories, and most often just prior to the measurements presented here. In several instances it seemed that some error had rooted itself in the calibration procedure at the given laboratory. Such phenomena would be avoidable, if laboratories routinely would share and exchange their reference devices as well as experimental devices in miniature round robins, such as the first study presented in this chapter.

Further improvements in accuracy would be given by a future convergence of measurement procedures [13], which might be led by strengthened editorial procedures regarding the reporting of solar cell efficiencies [29]. However, due to the unavoidable parameter variety among laboratories, in regards to device materials, device layouts, measurement temperature, IV sweep time etc., much of the observed deviation presumably cannot be avoided, and thus must be considered a standard measurement uncertainty. This would infer a PCE standard deviation of 10-12%, which using a standard 95% confidence interval will lead to a measurement uncertainty of up to ±24%. This would mean several percentage points in uncertainty for high performance devices.

6.5. **Conclusion**

Two RR studies were preseted. The first was a smaller studie of a set of high efficiency 'hero' devices, both ITO-free and ITO-based. By sharing these devices among 4 laboratories in Europe, which all conducted standard J-V characterization, the study showed up to 30% inter-laboratory disagreement in PCE, and an overall standard deviation around 10% with most of the variation found in the I_{sc}. For the highest performing device, this study resulted in a consensus (average) PCE of 4.2±0.5%, where the uncertainty is given by the standard deviation.

The second study was an elaborated version of the first, conducted as a combined Chinese-Danish collaboration between 14 Chinese laboratories (one in Hong Kong) and DTU in Denmark. The study included a series of ITO- and vacuum free all R2R coated and printed polymer solar cells and small modules of different sizes, all prepared at DTU. The results reconfirmed the previous study, revealing large inter-laboratory variations in photovoltaic parameters obtained in the STC J-V characterizations. Largest were the variations in I_{sc} (up to 33%) thus accounting for the largest source of observed variations in the PCE (up to 30%). Due to the much larger data set, the observed deviations now approached a normal distribution, with resulting average standard deviations for the RR devices of 12% for PCE and I_{sc}, 6% for FF and only 2% for V_{oc}. In further effort to deconvolute the responsible effects, the effects of light soaking and spectral UV content were investigated. Light soaking showed only a small effect on the FF and consequently the PCE, while the spectral proportion of UV-light was not seen to influence the performance significantly.

Based on the combined results of the two RR studies, a set of recommendations for future improvement of measurement accuracy and mutual agreement of results were given. Central to these is the promotion of inter-laboratory exchange of devices and measurement data. It is of significant interest and importance to conclude that there agreement between the spread in data as obtained for all OPV round robins so far, be it in EU/US [15] or as in this case EU and China. Thus the observable spread is general for OPV and independent of geographic/cultural region. Furthermore, the variation seems to be independent of the nominal performance and should therefore apply equally to all reported data, past or present.

A final conclusion of these combined results is the suggestion that any OPV report putting forth claims of high efficiencies should take these measures of uncertainty into consideration, and complement the independent report with certified data or consensus values obtained through miniature RR studies as exemplified here.

6.6. **References**

[1] J. You, C.-C. Chen, Z. Hong, K. Yoshimura, K. Ohya, R. Xu, et al., 10.2% power conversion efficiency polymer tandem solar cells consisting of two identical sub-cells., Advanced Materials (Deerfield Beach, Fla.). 25 (2013) 3973–8.

[2] J. You, L. Dou, K. Yoshimura, T. Kato, K. Ohya, T. Moriarty, et al., A polymer tandem solar cell with 10.6% power conversion efficiency., Nature Communications. 4 (2013) 1446.

[3] M.A. Green, K. Emery, Y. Hishikawa, W. Warta, E.D. Dunlop, Solar cell ef fi ciency tables (version 42), (2013) 827–837.

[4] Heliatek 12 % Efficiency record: www.heliatek.com, (2013).

[5] M. Jørgensen, J.E. Carlé, R.R. Søndergaard, M. Lauritzen, N. a. Dagnæs-Hansen, S.L. Byskov, et al., The state of organic solar cells—A meta analysis, Solar Energy Materials and Solar Cells. (2013) 1–10.

[6] L. Hou, E. Wang, J. Bergqvist, B.V. Andersson, Z. Wang, C. Müller, et al., Lateral Phase Separation Gradients in Spin-Coated Thin Films of High-Performance Polymer:Fullerene Photovoltaic Blends, Advanced Functional Materials. 21 (2011) 3169–3175.

[7] M.K. Riede, K.O. Sylvester-Hvid, M. Glatthaar, N. Keegan, T. Ziegler, B. Zimmermann, et al., High throughput testing platform for organic Solar Cells, Progress in Photovoltaics: Research and Applications. 16 (2008) 561–576.

[8] T. Tromholt, S.A. Gevorgyan, M. Jørgensen, F.C. Krebs, K.O. Sylvester-Hvid, Thermocleavable materials for polymer solar cells with high open circuit voltage-a comparative study., ACS Applied Materials & Interfaces. 1 (2009) 2768–77.

[9] E. Wang, L. Hou, Z. Wang, S. Hellström, F. Zhang, O. Inganäs, et al., An Easily Synthesized Blue Polymer for High-Performance Polymer Solar Cells, Advanced Materials. 22 (2010) 5240–5244.

[10] J. Alstrup, M. Jørgensen, A.J. Medford, F.C. Krebs, Ultra Fast and Parsimonious Materials Screening for Polymer Solar Cells Using Differentially Pumped Slot-Die Coating, ACS Applied Materials & Interfaces. 2 (2010) 2819–2827.

[11] J.E. Carlé, T.R. Andersen, M. Helgesen, E. Bundgaard, M. Jørgensen, F.C. Krebs, A laboratory scale approach to polymer solar cells using one coating/printing machine, flexible substrates, no ITO, no vacuum and no spincoating, Solar Energy Materials and Solar Cells. 108 (2013) 126–128.

[12] M.R. Lilliedal, A.J. Medford, M. V. Madsen, K. Norrman, F.C. Krebs, The effect of post-processing treatments on inflection points in current–voltage curves of roll-to-roll processed polymer photovoltaics, Solar Energy Materials and Solar Cells. 94 (2010) 2018–2031.

[13] F.C. Krebs, S. a. Gevorgyan, J. Alstrup, A roll-to-roll process to flexible polymer solar cells: model studies, manufacture and operational stability studies, Journal of Materials Chemistry. 19 (2009) 5442.

[14] J. Gilot, M.M. Wienk, R. a. J. Janssen, Double and triple junction polymer solar cells processed from solution, Applied Physics Letters. 90 (2007) 143512.

[15] F.C. Krebs, S.A. Gevorgyan, B. Gholamkhass, S. Holdcroft, C. Schlenker, M.E. Thompson, et al., A round robin study of flexible large-area roll-to-roll processed polymer solar cell modules, Solar Energy Materials and Solar Cells. 93 (2009) 1968–1977.

[16] H. Ossenbrink, K.. Krebs, R. V. Steenwinckel, Results of the 1984/1985 international round robin calibration summit working group on technology, growth and employment, IEEE. (1985) 943–944.

[17] J. Metzdorf, T. Wittchen, K. Heidler, K. Dehne, R. Shimokawa, F. Nagamine, et al., The results of the PEP'87 Round-Robin Calibration of reference cells and modules, Final Report, PTB Technical Report PTB-Opt-31, Braunschweig, Germany, 1990.

[18] T.R. Bets, R. Gottschalg, D.G. Infield, W. Kolodenny, M. Prorok, T. Zdanowicz, et al., Round robin comparison of European outdoor measurement systems, Proceedings of the 21st European Photovoltaic Solar Energy Conference. (2006) 2447–2451.

[19] T.T. Larsen-Olsen, F. Machui, B. Lechene, S. Berny, D. Angmo, R. Søndergaard, et al., Round-Robin Studies as a Method for Testing and Validating High-Efficiency ITO-Free Polymer Solar Cells Based on Roll-to-Roll-Coated Highly Conductive and Transparent Flexible Substrates, Advanced Energy Materials. 2 (2012) 1091–1094.

[20] L.J.A. Koster, E. Smits, V.D. Mihailetchi, P.W.M. Blom, Device model for the operation of polymer/fullerene bulk heterojunction solar cells, Physical Review B. 72 (2005) 1–9.

[21] T. Tromholt, E. a. Katz, B. Hirsch, A. Vossier, F.C. Krebs, Effects of concentrated sunlight on organic photovoltaics, Applied Physics Letters. 96 (2010) 073501.

[22] S.A. Gevorgyan, J. Eggert Carlé, R.R. Søndergaard, T.T. Larsen-Olsen, M. Jørgensen, F.C. Krebs, Accurate characterization of OPVs: Device masking and different solar simulators, Solar Energy Materials and Solar Cells. 110 (2013) 24–35.

[23] T.T. Larsen-Olsen, S. a. Gevorgyan, R.R. Søndergaard, M. Hösel, Z. Gu, H. Chen, et al., A round robin study of polymer solar cells and small modules across China, Solar Energy Materials and Solar Cells. 117 (2013) 382–389.

[24] F.C. Krebs, T. Tromholt, M. Jørgensen, Upscaling of polymer solar cell fabrication using full roll-to-roll processing., Nanoscale. 2 (2010) 873–86.

[25] L.J.A. Koster, V.D. Mihailetchi, H. Xie, P.W.M. Blom, Origin of the light intensity dependence of the short-circuit current of polymer/fullerene solar cells, Applied Physics Letters. 87 (2005) 203502.

[26] J. Huang, P.F. Miller, J.S. Wilson, a. J. de Mello, J.C. de Mello, D.D.C. Bradley, Investigation of the Effects of Doping and Post-Deposition Treatments on the Conductivity, Morphology, and Work Function of Poly(3,4-ethylenedioxythiophene)/Poly(styrene sulfonate) Films, Advanced Functional Materials. 15 (2005) 290–296.

[27] S.A. Gevorgyan, A.J. Medford, E. Bundgaard, S.B. Sapkota, H.-F. Schleiermacher, B. Zimmermann, et al., An inter-laboratory stability study of roll-to-roll coated flexible polymer solar modules, Solar Energy Materials and Solar Cells. 95 (2011) 1398–1416.

[28] D.M. Tanenbaum, M. Hermenau, E. Voroshazi, M.T. Lloyd, Y. Galagan, B. Zimmermann, et al., The ISOS-3 inter-laboratory collaboration focused on the stability of a variety of organic photovoltaic devices, RSC Advances. 2 (2012) 882.

[29] G.P. Smestad, F.C. Krebs, C.M. Lampert, C.G. Granqvist, K.L. Chopra, X. Mathew, et al., Reporting solar cell efficiencies in Solar Energy Materials and Solar Cells, Solar Energy Materials and Solar Cells. 92 (2008) 371–373.

7 Conclusion and Outlook

This thesis has presented a broad range of results all related to the furtherance of polymer solar cell development towards the vision of R2R fabricated devices for large scale energy production.

The use of aqueous nanoparticle inks, as a substitution for harmful organic solvents, resulted in three novel reports: R2R processed PSCs with water-processed active layers of three low band-gap polymers, the simultaneous formation of two layers in the solar cell stack using double slot-die coating, and the successful upscaling of the tandem PSC concept to R2R fabrication by processing the two BHJs from orthogonal solvents.

Secondly, the development of a scalable ITO-free transparent electrode based on PEDOT:PSS was presented. Its successful application in PSCs involved the development of a R2R post-processing step, comprising a short puls of high voltage applied to each device. The working mechanism of the post-process was investigated and suggested to be the in-situ formation of a charge selective layer by electrically-induced de-doping of PEDOT:PSS. Furthermore, a series of R2R fabricated small modules which were free from both ITO and Ag were presented and showed similar performance to ITO-based counterparts. To obtain true scalability, the PEDOT:PSS electrode was finally incorporated with various Ag grid-types in fully R2R coated ITO-free PSCs, and a comparison was presented. It was shown that the best results in terms of overall performance and scalability was the combination of PEDOT:PSS and flexographic printed Ag grid in all R2R-processed transparent electrodes.

In the final part of the thesis, two round robin studies were presented. The results showed large variations in the standard J-V characterizations done at different laboratories. The variations were shown to be equally large in both Europe and China, and the results pointed towards a generally applicable relative standard deviation as high as 12% to be used when reporting power conversion efficiencies of polymer solar cells.

Many of the experiments describes the upscaling from small area devices fabricated on rigid glass substrates using spin-coating to large area R2R processed devices. A general observation is that processes are not easily transferred and the resulting devices do not perform equally well. An important lesson to be drawn is thus, that a more scalable approach to small laboratory devices is of great importance, such as has been demonstrated recently by our group both for single junction devices [1] and for tandem devices [2].

A further continuation of the work described in regards to the *iOne* process has already lead to the demonstration of a novel concept for grid-connected electricity production from polymer solar cells [3]. This demonstrates a clear step towards large scale energy production.

In light of the results obtained in this thesis in terms of lowering the overall cost of fabrication, attention should now be put on increasing the PCE, e.g. through a further development of the R2R fabrication of tandem cells. In this respect, and in the spirit of minimizing environmental impart, it would be of great interest to develop further on the aqueous processing methods, ultimately towards the all-combining water processed ITO-free tandem solar cell.

[1] J.E. Carlé, T.R. Andersen, M. Helgesen, E. Bundgaard, M. Jørgensen, F.C. Krebs, Solar Energy Materials and Solar Cells 108 (2013) 126.

[2] T.R. Andersen, H.F. Dam, B. Andreasen, M. Hösel, M. V. Madsen, S. a. Gevorgyan, R.R. Søndergaard, M. Jørgensen, F.C. Krebs, Solar Energy Materials and Solar Cells (2013) 1.

[3] P. Sommer-Larsen, M. Jørgensen, R.R. Søndergaard, M. Hösel, F.C. Krebs, Energy Technology 1 (2013) 15.

8 Appendices

8.1. Content

Appendix 1

List of publications

- **T. T. Larsen-Olsen**, E. Bundgaard, K. O. Sylvester-Hvid, and F. C. Krebs, “A solution process for inverted tandem solar cells,” *Organic Electronics*, vol. 12, no. 2, pp. 364–371, Feb. 2011. (**Not included**)

- T. R. Andersen, **T. T. Larsen-Olsen**, B. Andreasen, A. P. L. Böttiger, J. E. Carlé, M. Helgesen, E. Bundgaard, K. Norrman, J. W. Andreasen, M. Jørgensen, and F. C. Krebs, “Aqueous Processing of Low-Band-Gap Polymer Solar Cells Using Roll-to-Roll Methods.,” *ACS nano*, vol. 5, no. 5, pp. 4188–4196, May 2011. (**Appendix 2**)

- **T. T. Larsen-Olsen**, B. Andreasen, T. R. Andersen, A. P. L. Böttiger, E. Bundgaard, K. Norrman, J. W. Andreasen, M. Jørgensen, and F. C. Krebs, “Simultaneous multilayer formation of the polymer solar cell stack using roll-to-roll double slot-die coating from water,” *Solar Energy Materials and Solar Cells*, vol. 97, pp. 22–27, Feb. 2012. (**Appendix 3**)

- **T. T. Larsen-Olsen**, T. R. Andersen, B. Andreasen, A. P. L. Böttiger, E. Bundgaard, K. Norrman, J. W. Andreasen, M. Jørgensen, and F. C. Krebs, “Roll-to-roll processed polymer tandem solar cells partially processed from water,” *Solar Energy Materials and Solar Cells*, vol. 97, pp. 43–49, Sep. 2011. (**Appendix 4**)

- Y.-X. Nan, X.-L. Hu, **T. T. Larsen-Olsen**, B. Andreasen, T. Tromholt, J. W. Andreasen, D. M. Tanenbaum, H.-Z. Chen, and F. C. Krebs, “Generation of native polythiophene/PCBM composite nanoparticles via the combination of ultrasonic micronization of droplets and thermocleaving from aqueous dispersion,” *Nanotechnology*, vol. 22, no. 47, p. 475301, Nov. 2011. (**Not included**)

- R. R. Søndergaard, M. Hösel, D. Angmo, **T. T. Larsen-Olsen**, and F. C. Krebs, “Roll-to-roll fabrication of polymer solar cells,” *Materials Today*, vol. 15, no. 1–2, pp. 36–49, Jan. 2012. (**Not included**)

- **T. T. Larsen-Olsen**, F. Machui, B. Lechene, S. Berny, D. Angmo, R. Søndergaard, N. Blouin, W. Mitchell, S. Tierney, T. Cull, P. Tiwana, F. Meyer, M. Carrasco-Orozco, A. Scheel, W. Lövenich, R. de Bettignies, C. J. Brabec, and F. C. Krebs, “Round-Robin Studies as a Method for Testing and Validating High-Efficiency ITO-Free Polymer Solar Cells Based on Roll-to-Roll-Coated Highly Conductive and Transparent Flexible Substrates,” *Advanced Energy Materials*, vol. 2, no. 9, pp. 1091–1094, Sep. 2012. (**Appendix 9**)

- T. R. Andersen, Q. Yan, **T. T. Larsen-Olsen**, R. R. Søndergaard, Q. Li, B. Andreasen, K. Norrman, M. Jørgensen, W. Yue, D. Yu, F. C. Krebs, H. Chen, and E. Bundgaard, “A Nanoparticle Approach towards Morphology Controlled Organic Photovoltaics (OPV),” *Polymers*, vol. 4, pp. 1242–1258, 2012. (**Not included**)

- X. Hu, L. Zuo, W. Fu, **T. T. Larsen-Olsen**, M. Helgesen, E. Bundgaard, O. Hagemann, M. Shi, F. C. Krebs, and H. Chen, “Incorporation of ester groups into low band-gap diketopyrrolopyrrole containing polymers for solar cell applications,” *Journal of Materials Chemistry*, vol. 22, no. 31, p. 15710, 2012. (**Not included**)

- J.-S. Yu, I. Kim, J.-S. Kim, J. Jo, **T. T. Larsen-Olsen**, R. R. Søndergaard, M. Hösel, D. Angmo, M. Jørgensen, and F. C. Krebs, “Silver front electrode grids for ITO-free all printed polymer solar cells with embedded and raised topographies, prepared by thermal imprint, flexographic and inkjet roll-to-roll processes.,” *Nanoscale*, vol. 4, no. 19, pp. 6032–40, Sep. 2012. (**Appendix 6**)

Appendix 1

- **T. T. Larsen-Olsen**, R. R. Søndergaard, K. Norrman, M. Jørgensen, and F. C. Krebs, “All printed transparent electrodes through an electrical switching mechanism: A convincing alternative to indium-tin-oxide, silver and vacuum,” *Energy & Environmental Science*, vol. 5, no. 11, p. 9467, 2012. (**Appendix 5**)

- L. Fu, H. Pan, **T. T. Larsen-Olsen**, T. R. Andersen, E. Bundgaard, F. C. Krebs, and H.-Z. Chen, “Synthesis and characterization of new electron-withdrawing moiety thieno[2,3-c] pyrrole-4,6-dione-based molecules for small molecule solar cells,” *Dyes and Pigments*, vol. 97, pp. 141–147, Dec. 2013. (**Not included**)

- W. Yue, **T. T. Larsen-Olsen**, X. Hu, M. Shi, H. Chen, M. Hinge, P. Fojan, F. C. Krebs, and D. Yu, “Synthesis and photovoltaic properties from inverted geometry cells and roll-to-roll coated large area cells from dithienopyrrole-based donor–acceptor polymers,” *Journal of Materials Chemistry A*, vol. 1, no. 5, p. 1785, 2013. (**Not included**)

- D. Angmo, **T. T. Larsen-Olsen**, M. Jørgensen, R. R. Søndergaard, and F. C. Krebs, “Roll-to-Roll Inkjet Printing and Photonic Sintering of Electrodes for ITO Free Polymer Solar Cell Modules and Facile Product Integration,” *Advanced Energy Materials*, vol. 3, no. 2, pp. 172–175, Feb. 2013. (**Appendix 8**)

- S. A. Gevorgyan, J. Eggert Carlé, R. R. Søndergaard, **T. T. Larsen-Olsen**, M. Jørgensen, and F. C. Krebs, “Accurate characterization of OPVs: Device masking and different solar simulators,” *Solar Energy Materials and Solar Cells*, vol. 110, pp. 24–35, Mar. 2013. (**Not included**)

- D. Angmo, S. A. Gevorgyan, **T. T. Larsen-Olsen**, R. Søndergaard, M. Hösel, M. Jørgensen, R. Gupta, G. U. Kulkarni, and F. C. Krebs, “Scalability and stability of very thin, roll-to-roll processed, large area, indium-tin-oxide free polymer solar cell modules,” *Organic Electronics*, vol. 14, no. 3, pp. 984–994, Feb. 2013. (**Appendix 7**)

- Y. Liu, **T. T. Larsen-Olsen**, X. Zhao, B. Andreasen, R. R. Søndergaard, M. Helgesen, K. Norrman, M. Jørgensen, F. C. Krebs, and X. Zhan, “All polymer photovoltaics: From small inverted devices to large roll-to-roll coated and printed solar cells,” *Solar Energy Materials & Solar Cells*, vol. 112, no. null, pp. 157–162, May 2013. (**Not included**)

- **T. T. Larsen-Olsen**, S. a. Gevorgyan, R. R. Søndergaard, M. Hösel, Z. Gu, H. Chen, Y. Liu, P. Cheng, Y. Jing, H. Li, J. Wang, J. Hou, Y. Li, X. Zhan, J. Wu, J. Liu, Z. Xie, X. Du, L. Ding, C. Xie, R. Zeng, Y. Chen, W. Li, T. Xiao, N. Zhao, F. Chen, L. Chen, J. Peng, W. Ma, B. Xiao, H. Wu, X. Wan, Y. Chen, R. Chang, C. Li, Z. Bo, B. Ji, W. Tian, S. Chen, L. Hu, S. Dai, and F. C. Krebs, “A round robin study of polymer solar cells and small modules across China,” *Solar Energy Materials and Solar Cells*, vol. 117, pp. 382–389, Oct. 2013. (**Appendix 10**)

- M. Jørgensen, J. E. Carlé, R. R. Søndergaard, M. Lauritzen, N. a. Dagnæs-Hansen, S. L. Byskov, T. R. Andersen, **T. T. Larsen-Olsen**, A. P. L. Böttiger, B. Andreasen, L. Fu, L. Zuo, Y. Liu, E. Bundgaard, X. Zhan, H. Chen, and F. C. Krebs, “The state of organic solar cells—A meta analysis,” *Solar Energy Materials and Solar Cells*, pp. 1–10, Jun. 2013.

Book contributions:

- **T. T. Larsen-Olsen**, H. F. Dam, B. Andreasen, T. Tromholt, and F. C. Krebs, “Polymersolceller,” in *Aspekter af dansk kemi i det 20. og 21. århundrede*, 1st ed., København: Kemiforlaget, 2012, pp. 109–118. (**Not included**)

- **T. T. Larsen-Olsen** and F. C. Krebs, “Fabrication of flexible polymer solar cells R2R,” in *McGraw-Hill 2013 Yearbook of Science and Technology*, McGraw-Hill, 2013. (**Peer reviewed**, **Not included**)

Appendix 2

Aqueous Processing of Low-Band-Gap Polymer Solar Cells Using Roll-to-Roll Methods

Thomas R. Andersen, Thue T. Larsen-Olsen, Birgitta Andreasen, Arvid P. L. Böttiger, Jon E. Carlé, Martin Helgesen, Eva Bundgaard, Kion Norrman, Jens W. Andreasen, Mikkel Jørgensen, and Frederik C. Krebs*

Solar Energy Programme, Risø National Laboratory for Sustainable Energy, Technical University of Denmark, Frederiksborgvej 399, DK-4000 Roskilde, Denmark

ABSTRACT Aqueous nanoparticle dispersions of a series of three low-band-gap polymers poly[4,8-bis(2-ethylhexyloxy)benzo(1,2-b:4,5-b′)dithiophene-alt-5,6-bis(octyloxy)-4,7-di(thiophen-2-yl)(2,1,3-benzothiadiazole)-5,5′-diyl] (P1), poly[(4,4′-bis(2-ethylhexyl)dithieno[3,2-b:2′,3′-d]silole)-2,6-diyl-alt-(2,1,3-benzothiadiazole)-4,7-diyl] (P2), and poly[2,3-bis-(3-octyloxyphenyl)quinoxaline-5,8-diyl-alt-thiophene-2,5-diyl] (P3) were prepared using ultrasonic treatment of a chloroform solution of the polymer and [6,6]-phenyl-C_{61}-butyric acid methyl ester ([60]PCBM) mixed with an aqueous solution of sodium dodecylsulphate (SDS). The size of the nanoparticles was established using small-angle X-ray scattering (SAXS) of the aqueous dispersions and by both atomic force microscopy (AFM) and using both grazing incidence SAXS (GISAXS) and grazing incidence wide-angle X-ray scattering (GIWAXS) in the solid state as coated films. The aqueous dispersions were dialyzed to remove excess detergent and concentrated to a solid content of approximately 60 mg mL^{-1}. The formation of films for solar cells using the aqueous dispersion required the addition of the nonionic detergent FSO-100 at a concentration of 5 mg mL^{-1}. This enabled slot-die coating of high quality films with a dry thickness of 126 ± 19, 500 ± 25, and 612 ± 22 nm P1, P2, and P3, respectively for polymer solar cells. Large area inverted polymer solar cells were thus prepared based on the aqueous inks. The power conversion efficiency (PCE) reached for each of the materials was 0.07, 0.55, and 0.15% for P1, P2, and P3, respectively. The devices were prepared using coating and printing of all layers including the metal back electrodes. All steps were carried out using roll-to-roll (R2R) slot-die and screen printing methods on flexible substrates. All five layers were processed using environmentally friendly methods and solvents. Two of the layers were processed entirely from water (the electron transport layer and the active layer).

KEYWORDS: roll-to-roll coating polymer solar cells · organic solar cells · slot-die coating · aqueous inks · nanoparticle dispersions

Aqueous processing of polymer solar cells presents the ultimate challenge in terms of environmental friendliness and has only been reported in a few instances. The approaches to solubilization of the conjugated and active material in water fall in three categories: solubilization through (1) ionic side chains such as sulfonic acid, carboxylic acid, or ammonium, (2) nanoparticle dispersions of hydrophobic polymers in water, or (3) nonionic alcohol and glycol side chains. The latter approach is the most recent and most successful in terms of performance where PCEs of up to 0.7% have been reached on indium tin oxide (ITO) substrates with aqueous processing of the four subsequent layers in the solar cell stack (including the printed metal back electrode).[1] The approach employing ionic side chains is perhaps conceptually the most appealing as it opens up for layer-by-layer assembly of the films or interface layers[2] but has so far not been employed successfully for the active layer itself. The nanoparticle dispersion approach developed by Landfester *et al.*[3−7] is particularly appealing as it allows for control of the nanoparticle size and for processing using pure water as solvent for common hydrophobic conjugated polymers. In terms of development of the polymer and organic photovoltaic (OPV) technology, the latter point is of some significance since the large body of polymers available today has been developed for processing in organic solvents such as chlorobenzene, 1,2-dichlorobenzene, *etc.* One could envisage a complete redesign of the chemistry as described above[1] (method 3) but it will require a complete rediscovery of the solvent–material interaction and morphology relationships. While this may be necessary, in the end it is of interest to simply adapt the large body of materials at hand to an aqueous process. It is also of critical importance to replace the organic solvents if one has the ambition to manufacture polymer solar cells on a gigawatt scale.

There are several concerns associated with the use of chlorinated and aromatic solvents on a very large scale. Concern for the people working at the manufacturing machine is crucial both in terms of toxicity and, in the case of aromatic solvents,

* Address correspondence to frkr@risoe.dtu.dk.

Received for review March 11, 2011 and accepted April 14, 2011.

10.1021/nn200933r

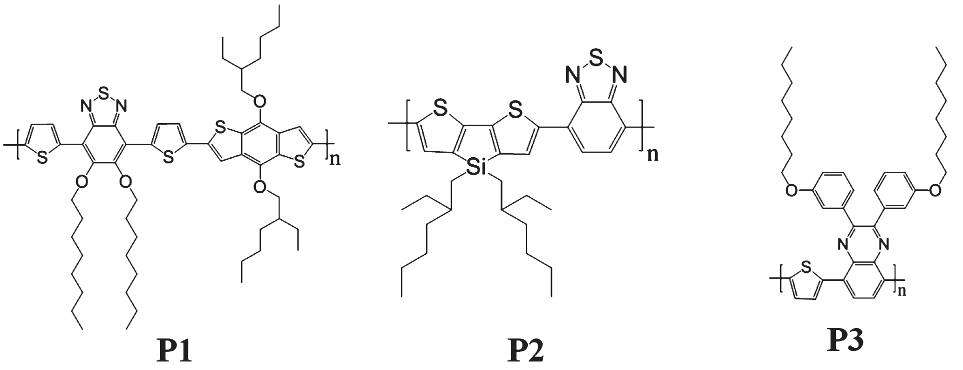

Figure 1. The structure for the three polymers used, P1, P2, and P3 (see text for the systematic names).

flammability. In the case of the chlorinated solvents the environmental concern is large, and it is unlikely that large scale manufacturing using such solvents is possible in a European setting. As an example, the current state of the art based on ProcessOne[8] would involve approximately 16 million liters of chlorobenzene for the production of 1 GW_p of polymer solar cell. An additional concern is the cumulative energy needed for raw materials production, where a poor choice of processing method and processing materials can severely affect the energy payback time (EPBT) of the solar cell. Life cycle analysis has confirmed that water is the solvent that is most beneficial to use, requiring only a small electrical energy input for production.[9] The cumulative thermal energy in materials production of chlorobenzene alone, as given in the example above, would be 880 TJ, adding 10 days to the EPBT. In contrast the use of water as the solvent would require only 17 TJ, adding only 4 h to the EPBT.

In terms of active materials the most successful approach so far has been the use of low-band-gap materials based on the donor–acceptor approach as shown in Figure 1. The UV–vis spectra of the three polymers **P1**, **P2**, and **P3** were recorded, and the optical band gaps were determined to be 1.8, 1.5, and 1.8 eV, respectively (Figure 2).

In this work we prepared aqueous nanoparticle dispersions of the known low-band-gap polymers poly[4,8-bis(2-ethylhexyloxy)benzo(1,2-b:4,5-b′)dithiophene-alt-5,6-bis(octyloxy)-4,7-di(thiophen-2-yl)(2,1,3-benzothiadiazole)-5,5′-diyl] (**P1**),[10] poly[(4,4′-bis(2-ethylhexyl)-dithieno[3,2-b:2′,3′-d]silole)-2,6-diyl-alt-(2,1,3-benzothiadiazole)-4,7-diyl] (**P2**),[11] and poly[2,3-bis-(3-octyloxyphenyl)-quinoxaline-5,8-diyl-alt-thiophene-2,5-diyl] (**P3**)[12] (Figure 1) in mixtures with [60]PCBM. We developed an aqueous R2R manufacturing process for flexible polymer solar cells through careful ink formulation and processing.

RESULTS AND DISCUSSION

Overview. The polymer solar cell has grown from a laboratory experiment to an emerging technology with great potential to significantly contribute to future energy production. Currently, polymer solar cells can be prepared using industrial roll-to-roll methods[8] and are sufficiently stable for demonstration products. They have for instance been employed as a low cost lighting solution for developing countries.[13] While upscaling has been described successfully their current potential should be viewed critically[14,15] and compared to existing thin film solar cell technologies such as CdTe and amorphous silicon. The polymer solar cell is currently the poorest performing PV technology (in existence) in terms of power conversion efficiency, while it has distinct advantages of high speed production, adaptability, and an abundance of raw materials. Recent work on the life cycle analysis from several groups[9] have highlighted the potential of the technology and in one case, where the source of data was fully public, revealed EPBTs in the range of 1.35–2.02 years.[9] As outlined in the introduction there is an urgent need for processes and processing materials that lower the embedded energy and the process energy, as this is a necessary method for lowering the EPBT. This should of course go in hand with an increase in efficiency. In this work where we aim at replacing the organic solvent for processing of the active area with water there is a direct gain at the site of manufacture but it should be emphasized that solvents and large amounts of

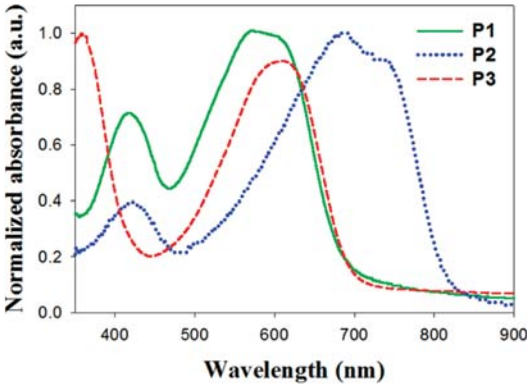

Figure 2. The UV–vis spectra of P1, P2, and P3. The optical band gap was determined to 1.8, 1.5, and 1.8 eV for P1, P2, and P3, respectively.

detergent are required for the manufacture of the nanoparticle dispersions. It is assumed that those can be recycled to fully benefit from the aqueous processing of hydrophobic materials that has already been developed. If this is not the case then there might not be any gain in the cumulative energy for raw materials production but there will still be a large gain in terms of human safety and lower emission of chlorinated or aromatic solvent into the environment because the preparation of the nanoparticle dispersions inherently allows for containment and reuse of solvents. A detailed life cycle analysis of the inks is thus warranted and until this has been carried out a complete comparison is not possible. At this point however the benefits of an aqueous ink are large enough to justify research in this direction.

Formation of Nanoparticle Dispersions. The generic method developed by Landfester *et al.* in a series of original research papers during the period from 1999 to 2004 was followed and found to be directly applicable with minor modifications.[3−7] A significantly larger amount of SDS was found to be needed than reported previously for a given nanoparticle size. The correlation between the size of the nanoparticles and the amounts of solvent, water, and SDS seem to be depending on the properties of the individual polymers. We found that a 100 mM SDS solution and a solid content in the organic phase of ∼40 mg mL^{-1} reproducibly gave nanoparticles with a size below 150 nm as established with SAXS measurements. We also found that the nanoparticles were conserved in the coated films (*vide supra*). The observed discrepancy in particle size as a function of SDS content could also be linked to the method of particle size determination where light scattering was employed previously. The reported method for the removal of the excess detergent comprises dialysis and centrifugal dialysis. These methods however allow for the preparation of only small quantities of ink. In our case large volumes (>100 mL) of inks with a high solid content was needed, and we initially attempted using a large basket centrifuge allowing for the continuous addition of water but finally settled on a Millipore filter system with a processing volume of 500 mL. Using this method, ink volumes of 100 mL with a solid content of 60 mg mL^{-1} could be prepared in a few hours. The inks were diluted 625 times corresponding to a final SDS concentration in the ink of 0.16 mM.

TABLE 1. The Average Particle Diameter in P1, P2, and P3 As Determined by SAXS and AFM. The Standard Deviation Is Given in the Brackets

polymer	SAXS (dispersions)	AFM (films)	GISAXS (films)
P1	130(38) nm	*a*	*a*
P2	32(10) nm	69(47) nm	32(22) nm
P3	87(21) nm	120(82) nm	107(72) nm

[a] Not possible to establish due to aggregation in the sample.

Particle Size and Crystalline Order. SAXS was employed on both the aqueous dispersions and on the solid films to determine particle sizes. AFM images of the films were analyzed to determine particle size distributions and gave similar results.

GIWAXS data showed poorly developed crystalline order of polymers **P2** and **P3**, with only weak first order reflections corresponding to lamellar spacings of 18.2 and 24.0 Å, respectively, and a broad peak at ∼1.34 Å^{-1} that we ascribe to packing of disordered side chains. **P1** showed very weak scattering, with no features that may be attributed to crystalline order of the polymer (the wide peak at high q values is the background signal from the glass substrate). All three films show a weak peak at ∼0.69 Å^{-1} that we ascribe to nanocrystalline [60]PCBM (Table 1 and Figures 3 and 4).

Inks and Roll-to-Roll Coating. The spin coating of thin films was possible, whereas large area films with the thickness/coverage required for making functional OPV devices was not possible. It was further found impossible to successfully coat these inks even with very fast web speeds and fast drying on a heated roller and a short distance (18 cm) between the coating head and the oven. Web speeds as high as 8 m min^{-1} were employed with a roller temperature of 80 °C. By heating the foil just after coating, quick drying was possible (within seconds), but significant dewetting was still observed (see Supporting Information).

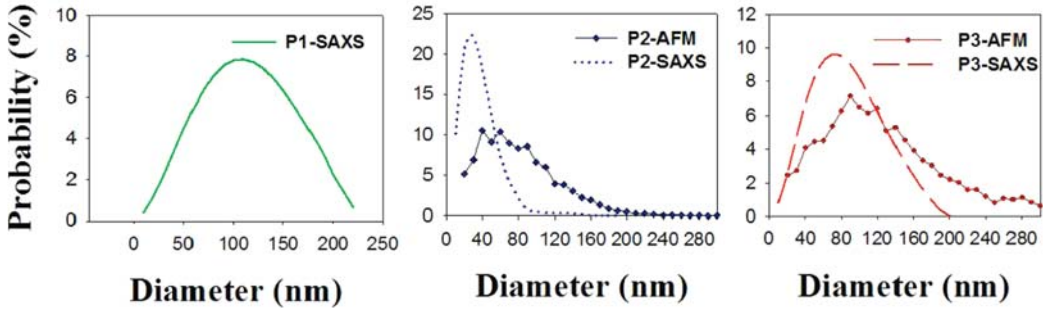

Figure 3. Size distributions of the particles P1 (left), P2 (middle), P3 (right) measured by AFM and SAXS. The SAXS measurements were performed with the particles in a water suspension, and the AFM was measured from spin-coated films. The distribution of P1 could not be determined by AFM due to aggregation of the particles.

Careful inspection of the wetting behavior revealed that the ink initially wets the surface and then dewets leaving a thin film (possibly comprising a single layer of nanoparticles). We ascribe this to the initial wetting and drying followed by lowering of the surface energy of the first layer and subsequent dewetting of the higher surface tension solution.

This phenomenon is quite well-known in the area of coating technology and is in essence a result of poisoning the otherwise wetable surface by the surface active properties of the ink itself. To solve this problem, the addition of a nonionic fluorosurfactant (FSO-100) was found to be necessary. The amount added was critical, and with too little material dewetting was still observed, whereas too much led to films with extremely poor adhesion. A concentration of 5 mg mL^{-1} was found to be the best compromise between coatability and adhesion. Films prepared in this manner passed the tape test.[16] The age of the meniscus was found to be of critical importance for efficient wetting and good adhesion of the dried film. This phenomenon is well-known in the area of coating technology, where shear induced in the ink as a result of the coating process itself leads to depletion of surfactant at the surface of the ink. In the case of water based inks this implies that the surface tension of the ink in the region of coating increases to a level where dewetting occurs. In such cases the speed of the coating process must be decreased to a level where the surfactant has time to diffuse to the surface and maintain the lower surface tension. Web speeds of 1 m min^{-1} were found to present the best conditions even though web speeds as high as 1.6 m min^{-1} could also be employed. A web speed of 0.6 m min^{-1} was used in all experiments to fabricate the devices presented in this work. Examples of dewetting during coating can be seen in the Supporting Information, and correct wettings are shown in Figure 5. The thickness of the dry active layers of **P1**, **P2**, and **P3** were measured by AFM profilometry and were found to be 126 ± 19, 500 ± 25, and 612 ± 22 nm, respectively.

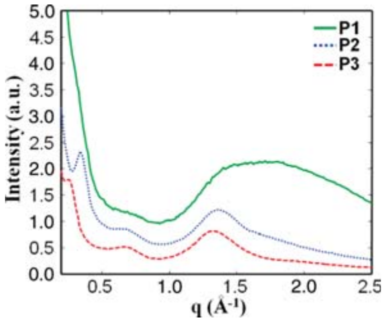

Figure 4. GIWAXS patterns of the three polymers, spin-coated on glass. No texture was observed, and the 2D patterns were thus azimuthally averaged as a function of *q*. The patterns are scaled for clarity.

The devices were completed by slot-die coating poly(3,4-ethylenedioxythiophene) poly(styrenesulfonate) (PEDOT:PSS) on top of the active layer and interestingly

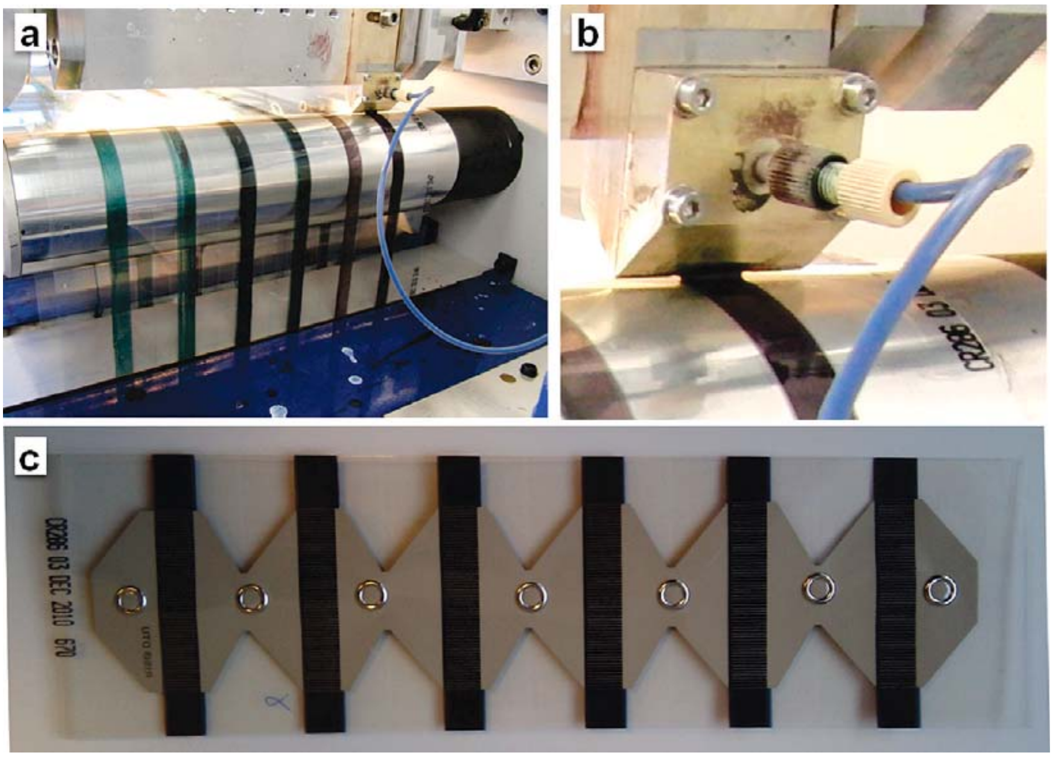

Figure 5. (a) Slot-die coating of the active layer using the aqueous nanoparticle dispersions and (b) an enlargement of the coating head, coating bead and wet film, and (c) showing a complete device with six individual solar cells.

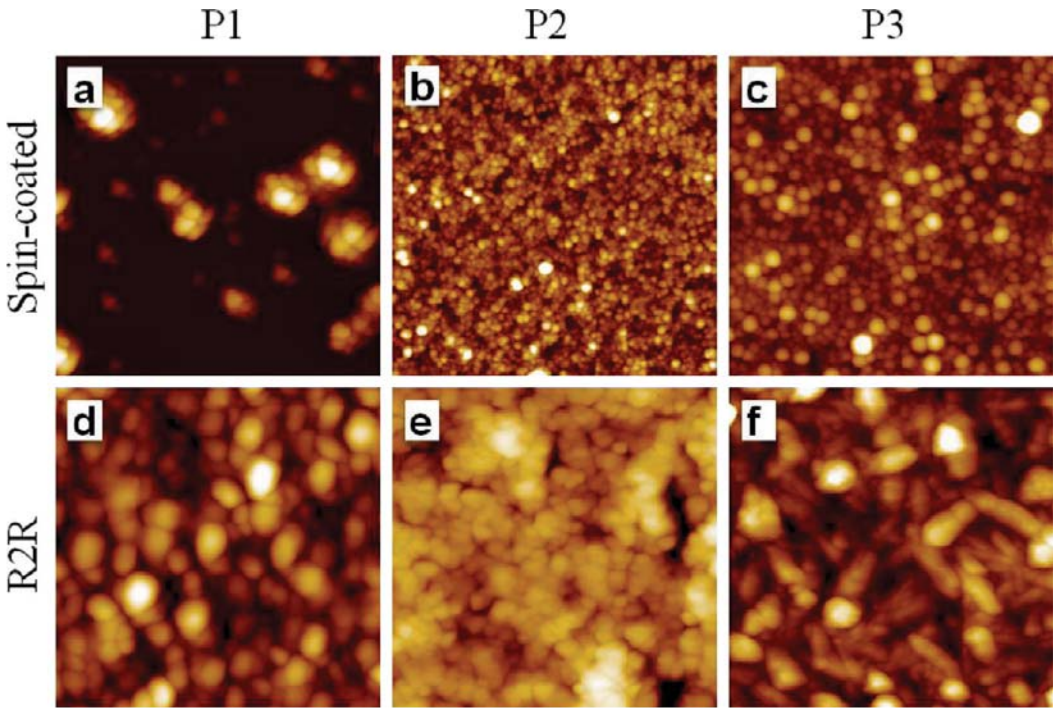

Figure 6. AFM topography images of spin-coated (a–c) and R2R (d–f) prepared samples of P1, P2, and P3. All the images were taken at 5 × 5 μm^2.

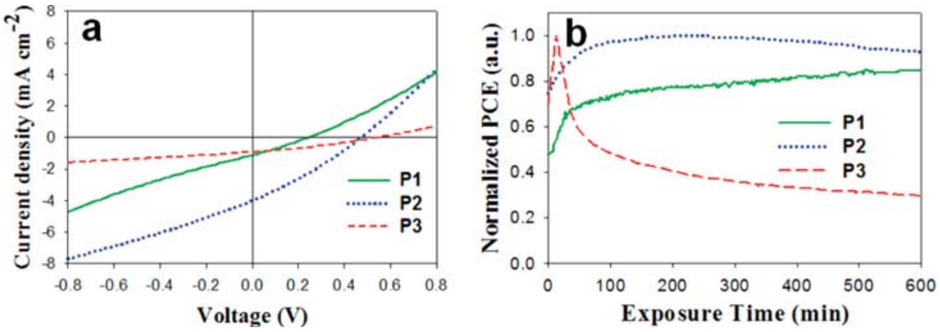

Figure 7. (a) *IV*-curves for the devices based on the three different polymers, at peak performance (AM1.5G, 1000 W m^{-2}, 85 ± 5 °C). (b) The development of the solar cell PCE during the initial 10 h of the exposure to 1 sun is shown for the three different polymers. Values are normalized to the corresponding peak value for each polymer (see Table 2).

no prewetting of the active layer with isopropyl alcohol was needed. We ascribe this to a fortuitous interaction between the fluorosurfactants in the PEDOT:PSS formulation and in the coated active layer. The devices were completed by screen printing a silver ink onto the PEDOT:PSS electrode. The devices were finally encapsulated using a simple barrier foil as described earlier and tested using an automated roll-to-roll IV-tester.[8,14,15]

Morphology. The morphology differences between spin-coated and R2R prepared samples and between the different sample materials can clearly be observed in the AFM images in Figure 6. On the spin-coated samples the individual nanoparticle shapes can be observed (with exception of **P1**, which looks like agglomerates made up of smaller particles). In the R2R samples the nanoparticles can no longer be clearly distinguished; instead it looks like the nanoparticles have merged in places. The different morphologies observed across the R2R samples could be caused by the "harsh" process conditions, where annealing at high temperatures is involved, and due to the different thermal properties of the polymers.

When the R2R coated samples in Figure 6 panels d, e, and f are compared, it looks like the particles are increasingly merged (d < f < e). This could be because these samples were prepared at slightly different conditions with the annealing time increasing (d < f < e). Each roll-to-roll experiment (a roll of foil) comprises six coated stripes as described earlier.[15] The first coated stripe will thus pass the oven a total of eight times, whereas that last coated stripe will pass the oven a total of three times (including the two passages when coating PEDOT:PSS and printing the silver back electrode).

Device Performance. The freshly prepared devices were put under a calibrated solar simulator (AM1.5G, 1000 W m^{-2}) and *IV*-scans were recorded every 1 min, for up to 36 h (according to the ISOS-L-1 procedure[26] using a temperature of 85 ± 5 °C). For all devices an initial steady increase in PCE during exposure to sunlight was generally observed.

However the optimum period of light exposure was significantly different for the three photoactive polymers, as can be seen in Figure 7. The PCE increase was caused by improvement of both the short circuit current and open circuit voltage, while the fill-factor was relatively constant. This behavior is not unique for these cells prepared from water-dispersed nanoparticles, but is readily observed for other polymer solar cells, having the same layer structure but an active layer processed from organic solvents such as chlorobenzene.[15] It is ascribed to a combination of effects such as photodoping of the zinc oxide layer by UV-light, accompanied by beneficial morphological changes in the active layer due to the relatively high temperature (85 ± 5 °C).[14]

The devices prepared from the aqueous dispersions show poorer performance compared to earlier reported efficiencies for devices based on **P1**, **P2**, and **P3**, prepared using chlorobenzene as solvent (Figure 7).[10−12] The source of this most likely shunts across the active layer. Because of the particle nature of the active layers (Figure 6), the film will be somewhat porous and thus susceptible to shunting by the subsequent processing of PEDOT:PSS. It is thus likely that the amount of shunts should be dependent on the layer thickness relative to the particle diameters. When the obtained PCEs for the different polymers are compared, it is observed that thicker layers and smaller particle size seem to give a higher performance. Apart from these suspected microscopic shunts, there are some larger shunts for some devices due to incomplete coverage evident from optical inspection of the film and even more so from the light beam induced current (LBIC) scan shown in Figure 8 where (blue) dots within the (red/green) active area reveal such shunts. Furthermore, effects from the significant amount of fluorosurfactant present in the ink along with the residual SDS bound to the surface of the nanoparticles have not been determined. This does however show that it is possible to prepare devices from water with a non-negligible performance, and worth noting that a large part of the relatively low performance of these devices prepared from water could be due to coating technicalities that are bound to become less pronounced as further experience is gained.

TABLE 2. The Photovoltaic Properties Obtained for the Devices When Processed from Water[a]

polymer	V_{oc} (V)	J_{sc} (mA cm^{-2})	FF (%)	PCE (%)
P1	0.24	1.10	27.5	0.07
P2	0.47	3.99	29.3	0.55
P3	0.54	0.92	30.8	0.15

[a] The device geometry was PET/ITO/ZnO/polymer-[60]PCBM/PEDOT:PSS/Ag-(printed), and the active area of the devices was 4 cm^2. The testing conditions were AM1.5G, 1000 W m^{-2}, 85 ± 5 °C.

Directions for Future Work. The possibility of achieving aqueous processing and operator safety and avoiding the emission of environmentally harmful solvents to the environment was demonstrated, and while this is a great step forward it was achieved at the expense of using a fluorinated surfactant. There is a well-documented concern over release of fluorinated surfactants to the environment where extremely harmful effects have been documented.[17] In our case the surfactant is not released directly to the environment but will follow the solar cell until the end of its life cycle, where it should be properly disposed. The identification of existing environmentally friendly surface active materials or the development of new ones for coating should be researched actively to avoid the use of fluorinated detergents while maintaining the advantages of aqueous processing of OPV.

The relationship between the chemical disposition of the polymer materials and nanoparticle size in the final ink will have to be established along with the relationship between the size of the nanoparticles and the performance of the solar cell printed from them. Since this requires quite large quantities of conjugated polymer material, the type of materials that perform best should be identified followed by replacement of the fluorinated surfactant. Once the truly environmentally friendly ink with the best performance has been identified the ink can be finally optimized with respect to nanoparticle size, solid content, drying time, *etc.*

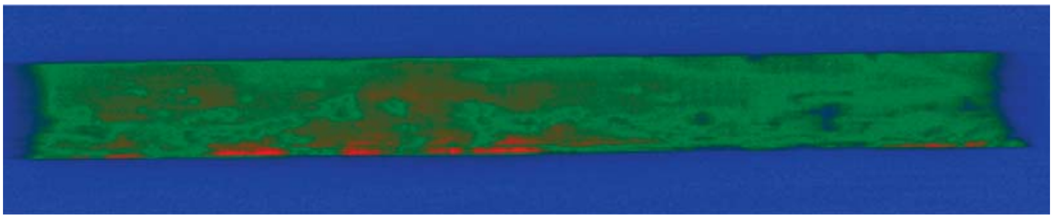

Figure 8. The LBIC image for a mapping of a P2 cell. The intensity scale is going from blue with no intensity over green to red with high intensity.

In our case **P2** proved to work best and further optimization using this class of materials should be pursued.

CONCLUSIONS

We have successfully prepared aqueous nanoparticle dispersions of three low-band-gap polymers and formulated inks for roll-to-roll processing into polymer solar cells on a flexible substrate which resulted in PCEs of 0.55, 0.15, and 0.07% for poly[(4,4′-bis(2-ethylhexyl)dithieno[3,2-b:2′,3′-d]silole)-2,6-diyl-alt-(2,1,3-benzothiadiazole)-4,7-diyl], poly[2,3-bis-(3-octyloxyphenyl)-quinoxaline-5,8-diyl-alt-thiophene-2,5-diyl], and poly[4,8-bis(2-ethylhexyloxy)benzo(1,2-b:4,5-b′)dithiophene-alt-5,6-bis(octyloxy)-4,7-di(thiophen-2-yl)(2,1,3-benzothiadiazole)-5,5′-diyl], respectively. We analyzed the nanoparticles in aqueous dispersion using SAXS and in solid film using GISAXS, GIWAXS, and AFM. The ink formulation and roll-to-roll processing was found to be challenging, however a reproducible method giving homogeneous films that adhered well to the surface of the zinc oxide based electron transport layer was obtained. The relatively poor device performance is ascribed to shunting and non-optimum morphology. Further work should be directed at improving coating condition and ink formulation as this has been successful in the case of organic solvent systems.

METHODS

Materials. The polymers were prepared as described in the literature.[10−12] They had values for M_n, M_w, and polydispersities of, respectively, 11.0 kDa, 28.7 kDa, and 2.6 for **P1**, 6.0 kDa, 10.9 kDa and 1.8 for **P2,** and 21.0 kDa, 89.0 kDa, and 4.2 for **P3**. [60]PCBM, SDS and chloroform were purchased in standard grade. An aqueous precursor solution for the zinc oxide was prepared as described in the literature.[1] PEDOT:PSS was based on EL-P 5010 from Agfa that was diluted with isopropyl alcohol to a viscosity of 200 mPa·s. The printable silver back electrode was PV410 from Dupont.

Nanoparticle Preparation. The typical recipe for small scale production, the polymer material (0.3 g) was together with [60]PCBM (0.3 g) dissolved in chloroform (15.5 mL) and mixed with an aqueous 100 mM SDS solution (50 mL) in a large beaker. The mixture was stirred vigorously for 1 h and then subjected to ultrasound (1 kW) for 5 min using an UIP 1000hd transducer from Hielscher ultrasound technology fitted with a booster head. The mixture was then stirred on a hot plate at 65 °C for 3 h until all the chloroform had evaporated. For small scale preparations, the aqueous dispersion was then dialyzed in dialysis tubing against 2 × 10 L pure water. In the final step the suspensions were concentrated to have a solid content of approximately 60 mg mL^{-1}.

For large scale preparations, the aqueous dispersion was dialyzed using a Millipore system with a capacity of 500 mL. The mixture was concentrated by dialysis from a volume of 500 mL to a volume of 100 mL with a forward pressure of 1.4 bar and a pressure gradient across the filter of 0.7 bar. Pure water (400 mL) was then added and the procedure was repeated 4 times corresponding to a dilution of the solution by a factor of 625. In the final step the suspensions were concentrated to have a solid content of 60 mg mL^{-1}.

X-ray Scattering. The SAXS and grazing incidence SAXS (GISAXS) experiments were performed at a laboratory setup using a rotating Cu-anode operating at 46 kV and 46 mA as X-ray source. The SAXS instrument was configured for a fully evacuated sample to detector distance of 4579 mm covering a q-range of $2.5 \times 10^{-3} < q < 0.12$ $Å^{-1}$, where the length of the scattering vector $q = 4\pi \sin(\theta)/\lambda$, with θ equal to half the scattering angle, and λ being the X-ray wavelength for Cu Kα (1.5418 Å). The X-rays are monochromated and collimated by two-dimensional multilayer optics and detected by a 2D "Gabriel"-type gas-proportional delay line detector.[18] The nanoparticle dispersions were measured in 1 mm borosilicate capillaries, sealed with epoxy glue for the SAXS experiments, and GISAXS of films spin-coated on glass were measured by orienting the substrate at an X-ray incidence angle of 0.5°. The 2D scattering images of the randomly oriented particles in dispersion were reduced to 1D cross sections by azimuthal averaging, whereas the GISAXS scattering were reduced to 1D curves by taking projections through the Yoneda peak[18] at constant q_z. The reduced 1D data were analyzed by using the Bayesian inverse Fourier transform (BIFT).[19]

GIWAXS of spin-coated films on glass were acquired by orienting the substrate surface just below the critical angle for total reflection with respect to the incoming X-ray beam (0.18°), maximizing scattering from the deposited film with respect to scattering from the substrate. In the wide scattering angle range (>5°), the X-ray scattering is sensitive to crystalline structure. For the experiment we used a camera comprising an evacuated sample chamber with an X-ray photosensitive image plate as detector and a rotating Cu-anode operating at 50 kV/200 mA as X-ray source, focused and monochromatized (Cu Kα, λ = 1.5418 Å) by a 1D multilayer.[19] The samples were mounted 120 mm from the detector. The GIWAXS data were analyzed by reducing the acquired 2D data by azimuthal averaging of intensity as a function of scattering vector length, q, to determine the characteristic d-spacings of the polymers, using the software SimDiffraction.[20]

Atomic Force Microscopy. AFM imaging was performed on an N8 NEOS (Bruker Nano GmbH, Herzogenrath, Germany) operating in an intermittent contact mode using PPP-NCLR cantilevers (NANOSENSORS, Neuchatel, Switzerland). Images were recorded at a scan speed of 0.8 lines min^{-1}. The images were analyzed using the image processing software package SPIP 5.1.5 (Image Metrology A/S, Hørsholm, Denmark).

The samples were first delaminated by ripping the plastic laminate off in a swift motion and thereafter placed on a glass slide using double sided tape.

It is well-known that AFM can at times overestimate particle sizes in the lateral plane and therefore the height z is often used as a measure for the diameter of spherical particles.[21−23] However, since the particles in the samples at hand are closely packed the height measurements of individual particles would be too time-consuming and inaccurate.[24] Therefore the best estimate to determine the particle size was to employ the Particle & Pore Analysis module included in the SPIP 5.1.5 software. The size was analyzed on at least two different positions of the sample analyzing a minimum of 2000 particles on each sample.

The thicknesses of the dry films were measured by AFM profilometry, see Figure 9. The thickness was measured at a minimum of three different positions on each film, with each position consisting of at least three individual measurements.

Light Beam Induced Current (LBIC) Mapping. The LBIC experiments were carried out using a custom-made setup with 410 nm laser diode (5 mW output power, 100 μm spot size (≈ 65 W/cm^{-2}), ThorLabs) mounted on a computer controlled XY-stage and focused to a spot size of <100 μm. The short circuit current from the device under study was measured using a computer

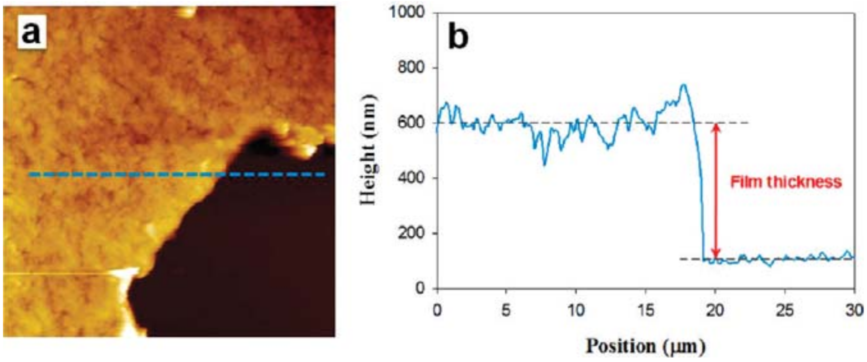

Figure 9. (a) $30 \times 30\ \mu m^2$ AFM topography image indicating where the thickness was measured. (b) line profile extracted from the AFM image (dashed line).

controlled source measure unit (Keithley 2400), and mapped by raster scanning across the device. Further details are available elsewhere.[25]

Ink Formulation. The nonionic fluorosurfactant (FSO-100) was added to the dialyzed aqueous suspension of the polymer/[60]PCBM nanoparticles. The concentration of fluorosurfactant was 5 mg mL^{-1} and the polymer/[60]PCBM concentration was 60 mg mL^{-1}. This solution was employed directly for slot-die coating

Roll-to-Roll Coating. A PET substrate with an ITO pattern was prepared and cleaned as described earlier.[13−15] The zinc oxide precursor solution was prepared as described earlier[1] and comprised $Zn(OAc)_2 \cdot 2H_2O$ (100 mg mL^{-1}), $Al(OH)(OAc)_2$ (2 mg mL^{-1}), and FSO-100 (2 mg mL^{-1}) in water. This solution was microfiltered immediately prior to use (0.45 μm) and then slot-die coated at a speed of 2 m min^{-1} with a wet thickness of 4.9 μm. After the initial drying of the precursor film it was converted into an insoluble film by passage through an oven at a temperature of 140 °C with a speed of 0.2 m min^{-1} (oven length = 4 m). This gave an insoluble doped zinc oxide film with a thickness of 25 ± 5 nm. The aqueous polymer/[60]PCBM nanoparticle dispersion was then slot-die coated at a speed of 1 m min^{-1} with a wet thickness of 30.4, 17.6, and 20.8 μm for **P1**, **P2**, and **P3**, respectively. The coating speed and the time between application of the wet film and the drying were critical for successful formation of a homogeneous film without dewetting. The slot-die coating head had a temperature of 60 °C, the coating roller had a temperature of 80 °C, and the temperature of the foil was kept at 80 °C until it reached the oven at 140 °C. The distance from the point of coating to the oven entry was 18 cm. PEDOT:PSS was then applied by slot-die coating at a speed of 0.2 m min^{-1} and dried at 140 °C (oven length = 2 m). It was found unnecessary to wet the film surface prior to coating the PEDOT:PSS and this might be due to the beneficial interaction between the fluorosurfactants in the active layer film and in the PEDOT:PSS. Finally the device was completed by roll-to-roll screen printing a silver grid electrode and drying at 140 °C. The devices were encapsulated using roll-to-roll lamination of a simple food packaging barrier with a pressure sensitive adhesive onto both sides of the foil.[13−15]

***IV*-Characterization.** In each coated stripe that represents one set of experiments a total of 150 solar cells were prepared (900 cells for each roll). The devices were light soaked with continuous sweeping of the *IV*-curve until a constant performance was reached. Typically the performance dropped rapidly during the first 10 min of light soaking followed by a slow improvement in performance over 4−6 h where a stable level of performance was reached. The data reported is for the stable regime. The devices were initially tested using a roll-to-roll tester and the functional devices were the recovered for further testing using a calibrated solar simulator (AM1.5G, 1000 W m^{-2}, 85 ± 5 °C). The prolonged testing was made according to the ISOS-L-1 procedure.[26]

Acknowledgment. This work was supported by the Danish National Research Foundation. We gratefully acknowledge the assistance of Steen Hansen with modifying the BIFT algorithm for use with polydisperse systems and Lasse Gorm Jensen for creating graphical illustrations.

Supporting Information Available: Details of the GISAXS analysis of solid films, with data and the description of the data reduction procedure; details of dewetting during coating. This material is available free of charge *via* the Internet at http://pubs.acs.org.

REFERENCES AND NOTES

1. Søndergaard, R.; Helgesen, M.; Jørgensen, M.; Krebs, F. C. Fabrication of Polymer Solar Cells Using Aqueous Processing for All Layers Including the Metal Back Electrode. *Adv. Eng. Mater.* **2011**, *1*, 68–71.
2. Rider, D. A.; Worfolk, B. J.; Harris, K. D.; Lalany, A.; Shahbazi, K.; Fleischauer, M. D.; Brett, M. J.; Buriak, J. M. Stable Inverted Polymer/Fullerene Solar Cells Using a Cationic Polythiophene Modified PEDOT:PSS Cathodic Interface. *Adv. Funct. Mater.* **2010**, *20*, 2404–2415.
3. Landfester, K. The Generation of Nanoparticles in Miniemulsions. *Adv. Mater.* **2001**, *13*, 765–768.
4. Kietzke, T.; Neher, D.; Landfester, K.; Montenegro, R.; Güntner, R.; Scherf, U. Novel Approaches to Polymer Blends Based on Polymer Nanoparticles. *Nat. Mater.* **2003**, *2*, 408–412.
5. Piok, T.; Gamerith, S.; Gadermaier, C.; Plank, H.; Wenzl, F. P.; Patil, S.; Montenegro, R.; Kietzke, T.; Neher, D.; Scherf, U.; *et al*. Organic Light-Emitting Devices Prepared from Semiconducting Nanospheres. *Adv. Mater.* **2003**, *15*, 800–804.
6. Kietzke, T.; Neher, D.; Kumke, M.; Montenegro, R.; Landfester, K.; Scherf, U. A Nanoparticle Approach to Control the Phase Separation in Polyfluorene Photovoltaic Devices. *Macromolecules* **2004**, *37*, 4882–4890.
7. Antonietti, M.; Landfester, K. Polyreactions in Miniemulsions. *Prog. Polym. Sci.* **2002**, *27*, 689–757.
8. Krebs, F. C.; Gevorgyan, S. A.; Alstrup, J. A Roll-to-Roll Process to Flexible Polymer Solar Cells: Model Studies, Manufacture, and Operational Stability Studies. *J. Mater. Chem.* **2009**, *19*, 5442–5442.
9. Espinosa, N.; García-Valverde, R.; Urbina, A.; Krebs, F. C. A Life Cycle Analysis of Polymer Solar Cell Modules Prepared Using Roll-to-Roll Methods Under Ambient Conditions. *Sol. Energy Mater. Sol. Cells* **2011**, *95*, 1293–1302.
10. Bundgaard, E.; Hagemann, O.; Jørgensen, M.; Krebs, F. C. Low-Band-Gap Polymers for Roll-to-Roll Coated Organic Photovoltaics Design, Synthesis and Characterization. *Green* **2011**, *1*, 55–64.
11. Hou, J.; Chen, H. Y.; Zhang, S.; Li, G.; Yang, Y. Synthesis, Characterization, and Photovoltaic Properties of a Low Band Gap Polymer Based on Silole-Containing Polythiophenes and 2,1,3-Benzothiadiazole. *J. Am. Chem. Soc.* **2008**, *130*, 16144–16145.
12. Wang, E.; Hou, L.; Wang, Z.; Hellström, S.; Zhang, F.; Inganäs, O.; Andersson, M. R. An Easily Synthesized Blue

Polymer for High-Performance Polymer Solar Cells. *Adv. Mater.* **2010**, *22*, 5240–5244.

13. Krebs, F. C.; Nielsen, T. D.; Fyenbo, J.; Wadstrøm, M.; Pedersen, M. S. Manufacture, Integration and Demonstration of Polymer Solar Cells in a Lamp for the "Lighting Africa" Initiative. *Energy Environ. Sci.* **2010**, *3*, 512–512.
14. Krebs, F. C.; Tromholt, T.; Jørgensen, M. Upscaling of Polymer Solar Cell Fabrication Using Full Roll-to-Roll Processing. *Nanoscale* **2010**, *2*, 873–886.
15. Alstrup, J.; Medford, A. J.; Jørgensen, M.; Krebs, F. C. Ultrafast and Parsimonious Materials Screening for Polymer Solar Cells Using Differentially Pumped Slot-Die Coating. *ACS Appl. Mater. Interfaces* **2010**, *2*, 2819–2827.
16. ASTM INTERNATIONAL Standards Worldwide. Standard Test Methods for Measuring Adhesion by Tape Test. p. 8.
17. Renner, R. Growing Concern over Perfluorinated Materials. *Environ. Sci. Technol.* **2001**, *35*, 154A–160A.
18. Yoneda, Y. Anomalous Surface Reflection of X-Rays. *Phys. Rev.* **1963**, *131*, 2010–2013.
19. Apitz, D.; Bertram, R.; Benter, N.; Hieringer, W.; Andreasen, J.; Nielsen, M.; Johansen, P.; Buse, K. Investigation of Chromophore-Chromophore Interaction by Electro-optic Measurements, Linear Dichroism, X-ray Scattering, and Density-Functional Calculations. *Phys. Rev. E* **2005**, *72*, 036610-1–036610-10.
20. Breiby, D. W.; Bunk, O.; Andreasen, J. W.; Lemke, H. T.; Nielsen, M. M. Simulating X-ray Diffraction of Textured Films. *J. Appl. Crystallogr.* **2008**, *41*, 262–271.
21. Villarrubia, J. Algorithm for Scanned Probe Microscope Image Simulation, Surface Reconstruction, and Tip Estimation. *J. Res. Natl. Inst. Stand. Technol.* **1997**, *102*, 425–454.
22. Hoo, C. M.; Starostin, N.; West, P.; Mecartney, M. L. A Comparison of Atomic Force Microscopy (AFM) and Dynamic Light Scattering (DLS) Methods to Characterize Nanoparticle Size Distributions. *J. Nanopart. Res.* **2008**, *10*, 89–96.
23. Boyd, R. D.; Cuenat, A. New Analysis Procedure for Fast and Reliable Size Measurement of Nanoparticles from Atomic Force Microscopy Images. *J. Nanopart. Res.* **2011**, *13*, 105–113.
24. Dias, A.; Buono, V. T. L.; Vilela, J. M. C.; Andrade, M. S.; Lima, T. M. Particle Size and Morphology of Hydrothermally Processed MnZn Ferrites Observed by Atomic Force Microscopy. *J. Mater. Sci.: Mater. Med.* **1997**, *32*, 4715–4718.
25. Krebs, F. C.; Søndergaard, R.; Jørgensen, M. Printed Metal Back Electrodes for R2R Fabricated Polymer Solar Cells Studied Using the LBIC Technique. *Sol. Energy Mater. Sol. Cells* **2011**, *95*, 1348–1353.
26. Reese, M. O.; Gevorgyan, S. A.; Jørgensen, M.; Bundgaard, E.; Kurtz, S. R.; Ginley, D. S.; Olson, D. C.; Lloyd, M. T.; Morvillo, P.; Katz, E. A.; *et al.* Consensus Stability Testing Protocols for Organic Photovoltaic Materials and Devices. *Sol. Energy Mater. Sol. Cells* **2011**, *95*, 1253–1267.

Appendix 3

Solar Energy Materials & Solar Cells 97 (2012) 22–27

Contents lists available at SciVerse ScienceDirect

Solar Energy Materials & Solar Cells

journal homepage: www.elsevier.com/locate/solmat

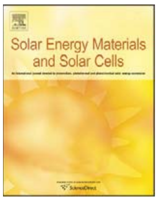

Simultaneous multilayer formation of the polymer solar cell stack using roll-to-roll double slot-die coating from water

Thue T. Larsen-Olsen, Birgitta Andreasen, Thomas R. Andersen, Arvid P.L. Böttiger, Eva Bundgaard, Kion Norrman, Jens W. Andreasen, Mikkel Jørgensen, Frederik C. Krebs*

Risø National Laboratory for Sustainable Energy, Technical University of Denmark, Frederiksborgvej 399, DK-4000 Roskilde, Denmark

ARTICLE INFO

Available online 23 September 2011

Keywords:
Double slot-die coating
Organic solar cells
Roll-to-roll coating polymer solar cells
Simultaneous multilayer formation
Slot-die coating

ABSTRACT

Double slot-die coating using aqueous inks was employed for the simultaneous coating of the active layer and the hole transport layer (HTL) in fully roll-to-roll (R2R) processed polymer solar cells. The double layer film was coated directly onto an electron transport layer (ETL) comprising doped zinc oxide that was processed by single slot-die coating from water. The active layer comprised poly-3-hexylthiophene:Phenyl-C_{61}-butyric acid methyl ester (P3HT:PCBM) as a dispersion of nanoparticles with a radius of 46 nm in water characterized using small-angle X-ray scattering (SAXS), transmission electron microscopy (TEM), and atomic force microscopy (AFM). The HTL was a dispersion of poly(3,4-ethylenedioxythiophene) poly(styrenesulfonate) (PEDOT:PSS) in water. The films were analyzed using time-of-flight secondary ion mass spectrometry (TOF-SIMS) as chemical probe and X-ray reflectometry as physical probe, confirming the identity of the layered structure. The devices were completed with a back electrode of either Cu tape or evaporated Ag. Under standard solar spectrum irradiation (AM1.5G), current–voltage characterization (J–V) yielded an open-circuit voltage (V_{oc}), short-circuit current (J_{sc}), fill factor (FF), and power conversion efficiency (PCE) of 0.24 V, 0.5 mA cm^{-2}, 25%, and 0.03%, respectively, for the best double slot-die coated cell. A single slot-die coated cell using the same aqueous inks and device architecture yielded a V_{oc}, J_{sc}, FF, and PCE of 0.45 V, 1.95 mA cm^{-2}, 33.1%, and 0.29%, respectively.

1. Introduction

Flexible polymer solar cells can be manufactured by roll-to-roll (R2R) processes, which are inherently faster than batch processing of solar cells [1]. The manufacture of polymer solar cells using R2R processing has been reported demonstrating high speed of manufacture even on a small scale [2–4]. Thus, polymer solar cell modules with the size of an A4 sheet of paper have total processing times in the range of one minute (45–90 s) [3]. This period of time is from the moment the fresh carrier substrate enters the process until the completed, encapsulated, and tested polymer solar cell module exits the process as a finished product. It is impossible to envisage such throughput speeds with any process that handles the solar cell as a discrete unit. The above example employed relatively simple R2R processing equipment and low web speeds in the range of 0.3–2 m min^{-1} processing one layer at a time by subsequent single passes through the machinery. In order to improve throughput speed there are a few routes, which can be followed. One obvious route is to increase the processing speed, which puts significant requirements on the drying equipment. The faster the web speed, the larger and more complex the ovens and driers become. Another option is to make an inline printing and coating machine where the same web passes through several printing stations with each station representing each layer in the solar cell stack. This method has the advantage of minimizing handling damage of the web. The method does put some constraints on the chosen printing and coating methods as they all have to operate in the same window of web speed and the final web speed will be determined by the slowest process. A final route is the simultaneous formation of several layers of the solar cells stack. This method is in many ways ideal as it lowers the number of passages through the processing equipment thus lowering the handling damage, increases the processing speed significantly without increasing the web speed and thus does not necessarily require more complex drying technology. In addition, there are advantages in the context of life cycle analysis and the method provides a path to a reduction of the energy payback time (EPBT) by significantly reducing the direct process energy involved in the manufacture [5]. The approach also introduces a massive challenge in

---

* Corresponding author. Tel.: +45 46 77 47 99.
E-mail address: frkr@risoe.dtu.dk (F.C. Krebs).

0927-0248/$ - see front matter © 2011 Elsevier B.V. All rights reserved.
doi:10.1016/j.solmat.2011.08.026

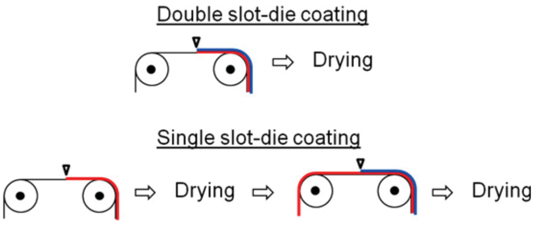

Fig. 1. Illustration of the double slot-die coating of the active layer (red) and the HTL (blue) in a R2R process, compared to the equivalent process using single slot-die coating. (For interpretation of the references to color in this figure legend, the reader is referred to the web version of this article).

the ink formulation for the layers that are coated simultaneously as the formation and drying of a wet multilayer film is highly complex. The successful application of the technique is however rewarding in terms of processing speed and simplicity, see Fig. 1.

In this work we demonstrate the simultaneous formation of two of the layers in the polymer solar cell stack by double slot-die coating of the active layer and the hole transporting layer (HTL) from aqueous dispersions. We describe the ink formulation and the required steps to efficiently design inks that give stable bilayer structures in the wet film and during drying.

2. Experimental

2.1. Materials

P3HT (Sepiolid P-200 from BASF) was employed as the donor polymer and technical grade PCBM was employed as the acceptor material (Solenne BV). An aqueous precursor solution for the ZnO was prepared as described earlier [6] and comprised $Zn(OAc)_2.2H_2O$ (100 mg mL^{-1}), $Al(OH)(OAc)_2$ (2 mg mL^{-1}), and the non- ionic fluorosurfactant (FSO-100) (2 mg mL^{-1}) in water. PEDOT:PSS was based on an aqueous dispersion (2:1 w/w) of Orgacon EL-P 5010 from Agfa that was used directly as received. The electrode material was either Cu tape or evaporated silver. The substrate was a 130 μm poly(ethylene terephthalate) (PET) substrate with a patterned ITO layer (nominally 60 Ω $square^{-1}$) (acquired from IST).

2.2. Nanoparticle preparation and ink

P3HT (4 g, Sepiolid P200, BASF) and PCBM (4 g, 99%, Solenne B.V.) were dissolved in chloroform (268 g, Spectrophotometric grade, Sigma-Aldrich) and mixed with an aqueous 100 mM sodium dodecyl sulfate (SDS) solution (480 mL) (99%, Sigma-Aldrich) in a large beaker. The mixture was stirred vigorously for one hour and then subjected to ultrasound (0.9 kW) for 6.5 min using an UIP 1000 hd transducer from Hielscher ultrasound technology fitted with a booster head. The mixture was then stirred on a hot plate at 65 °C for three hours until all the chloroform had evaporated. The aqueous dispersion was dialyzed to remove SDS using a Millipore system with a capacity of 500 mL. The mixture was concentrated by dialysis from a volume of 500 mL to a volume of 100 mL with a forward pressure of 1.4 bar and a pressure gradient across the filter of 0.7 bar. Pure water (400 mL) was then added and the procedure was repeated 4 times corresponding to a dilution of the solution by a factor of 625. In the final step the suspension were concentrated to have a solid content of 60 mg mL^{-1}. FSO-100 was added to the dialyzed aqueous suspension of the P3HT:PCBM nanoparticles. The concentration of fluorosurfactant was 5 mg mL^{-1} and the P3HT:PCBM concentration was 60 mg mL^{-1}. This solution was employed directly for slot-die coating.

2.3. TOF-SIMS

Depth profiling analysis was performed using a TOF-SIMS IV (ION-TOF GmbH, Münster, Germany). 25-ns pulses of 25-keV Bi^+ (primary ions) were bunched to form ion packets with a nominal temporal extent of <0.9 ns at a repetition rate of 10 kHz yielding a target current of 1 pA. Depth profiling was performed using an analysis area of $100 \times 100\ \mu m^2$ and a sputter area of $300 \times 300\ \mu m^2$. 30 nA of 3-keV Xe^+ was used as sputter ions. Electron bombardment (20 eV) was used to minimize charge build-up at the surface. Desorbed secondary ions were accelerated to 2 keV, mass analyzed in the flight tube, and post-accelerated to 10 keV before detection.

2.4. SAXS

The X-ray source for the SAXS measurements was a Cu rotating anode (Rigaku H3R), collimated and monochromatized by 2D multilayer optics (K_α radiation, $\lambda = 1.5418$ Å). The anode was operated in fine focus mode at 46 kV/46 mA and the beam diameter was collimated by 3 pinholes to 1.0 mm diameter at the sample position. An $18 \times 18\ cm^2$ 2D position sensitive gas detector was used for collecting the scattering data, and a 4 mm beamstop was placed in front of the gas detector, situated 4579 mm from the sample.

2.5. Reflectrometry

The reflectrometry measurement was made on setup with a rotating Cu-anode (Rigaku RU-200) operated at 50 kV/200 mA as X-ray source, focused and monochromatized by a 1D multilayer optic (K_α radiation, $\lambda = 1.5418$ Å).

2.6. AFM

The P3HT:PCBM nanoparticle dispersion was spin-coated on a glass substrate. The AFM imaging was performed on an N8 Neos (Bruker Nano GmbH, Herzogenrath, Germany) operating in an intermittent contact mode using PPP-NCLR cantilevers (NANOSENSORS, Neuchatel, Switzerland). The images were recorded at a scan speed of 0.8 lines s^{-1}.

2.7. Substrate preparation

A PET substrate with an ITO pattern was prepared and cleaned as described earlier [2]. The ZnO solution was microfiltered immediately prior to use (filter pore size of 0.45 μm) and then slot-die coated at a speed of 2 m min^{-1} with a wet thickness of 4.9 μm. After the initial drying of the precursor film it was converted into an insoluble film by passage through an oven at a temperature of 140 °C with a speed of 0.2 m min^{-1} (oven length = 4 m). This gave an insoluble doped zinc oxide film with a thickness of 25 ± 5 nm.

2.8. Double slot-die coating

The web was forwarded at a speed of 1 m min^{-1} when the aqueous P3HT:PCBM nanoparticle dispersion was pumped into the first chamber of a double slot-die coating head. The aqueous PEDOT:PSS dispersion was pumped into the second chamber of the double slot-die coating head. The double film was then slot-die coated at a nominal wet thickness of 23 μm for both the P3HT:PCBM film and the PEDOT:PSS dispersion. The slot-die coating head and the coating roller had temperatures of 60 °C and 80 °C, respectively. The temperature of the foil was kept at

80 °C until it reached the oven at 140 °C. The distance from the point of coating to the oven entry was 18 cm.

2.9. Device characterization

The devices were placed under simulated sunlight in a solar simulator with the following specifications: 1000 W m^{-2}, AM1.5G, 85 ± 2 °C, and $45 \pm 5\%$ relative humidity. The *J–V* curves were measured here were carried out at 85 °C by scanning both forwards and backwards in steps of 20 mV ensuring that no hysteresis was present. The scanning speed was 0.1 V s^{-1}.

3. Results and discussion

The simultaneous multilayer formation by roll coating methods has been achieved with only a few techniques such as curtain coating, slide coating, and slot-die coating [1]. The two former are only operational in the very high speed regime (typically $> 4\ \mathrm{m\ s^{-1}}$) and require relatively viscous solutions. In return, they offer the simultaneous formation of many layers. Slot-die coating has been explored for multilayer film formation with up to three layers (in triple slot-die coating) or in combination with the slide coating technique in slot-slide coating. In the context of polymer solar cells the simultaneous multilayer formation has not been reported so far.

There are many good reasons for double slot-die coating not having been employed for polymer solar cells. Firstly, the multilayer formation requires that the same solvent is used for the coated layers and that the layer coated first has the highest surface tension. Secondly, the drying has to be sufficiently fast to minimize diffusion of solutes between the layers. For a bilayer film with a total wet thickness of 100 μm, diffusion of solutes such as small molecules and ions are exceptionally fast unless the viscosity is high. In our case we employ water and the viscosity of the solutions are low (< 25 mPa s) implying that it would be difficult to prevent interlayer diffusion. The mean displacement for a molecule such as phenyl-C_{61}-butyric acid methyl ester (PCBM) is on the order of 30 μm s^{-1} and with wet thicknesses on the order of $\lll$ 100 μm this would imply that drying should be completed on timescales much faster than a second to avoid complete interlayer mixing by diffusion. We estimated the diffusion lengths using the Einstein equation [7] where we have the diffusion constant and mean displacement, as follows:

$$D = \frac{k_B T}{6\pi\eta r},\ \lambda_{1d} = \sqrt{2Dt}.$$

here k_B is boltzman's constant, T is absolute temperature, η is the viscosity (of the ink), r is the particle radius, and t is time. Eliminating D, we get the following mean displacement, during 1 s diffusion, for a C_{60} molecule (taken to be similar to PCBM) at 80 °C:

$$\lambda_{C_{60}} = \sqrt{\frac{k_B}{3\pi} \times \frac{1\,\mathrm{s} \times 353\,\mathrm{K}}{1\,\mathrm{mPa\,s} \times 0.5\,\mathrm{nm}}} = 3.22 \times 10^{-5}\,\mathrm{m}.$$

For $r = 50$ nm particle

$$\lambda_{np} = \sqrt{\frac{k_B}{3\pi} \times \frac{1\,\mathrm{s} \times 353\,\mathrm{K}}{1\,\mathrm{mPa\,s} \times 50\,\mathrm{nm}}} = 3.22 \times 10^{-6}\,\mathrm{m}.$$

here we have assumed a constant viscosity of 1 mPa s, which should be considered a conservative estimate, as it is likely to be higher and will increase as the drying proceeds. In our case, the inks P3HT:PCBM, and poly(3,4-ethylenedioxythiophene):poly (styrenesulfonate) (P3HT:PCBM and PEDOT:PSS) are both aqueous dispersions of large aggregates with average sizes 50–100 times larger than the PCBM molecule, hence interlayer mixing due to diffusion of the particles between the two layers would be 1–2 orders of magnitude slower, thus enabling drying without detrimental interlayer mixing. At the same time a limited amount of interdiffusion should be advantageous as it gives a diffusive interface between the coated layers with much higher adhesion, possibly lowering device degradation due to layer delamination. Experience gained from the actual coating experiments suggests that the process is very parameter sensitive. However, a stable operation regime was found and a very illustrative example of the simultaneous bilayer formation from the coating experiment is shown in Fig. 2, where it was possible to turn on and off the flow of one of the inks, thus revealing a sharp transition from single- to bilayer.

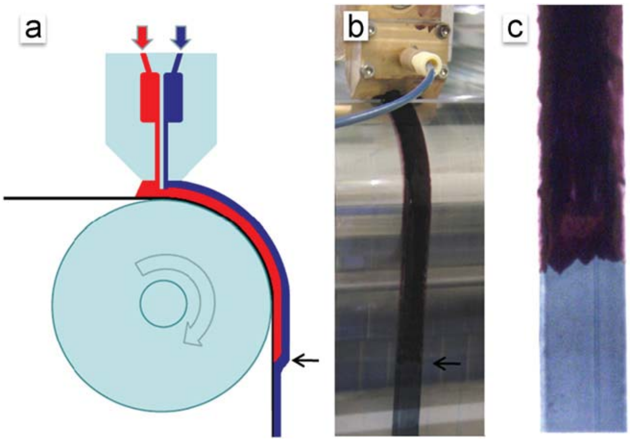

Fig. 2. Double slot-die coating experiment at an instance where the film changes appearance going from a single layer of PEDOT:PSS (blue) to a simultaneous coating of P3HT:PCBM (red) and PEDOT:PSS. The transition is marked by the arrows going from **(a)** a schematic of the experimental situation, to **(b)** a photograph of the experiment, and to **(c)** a close-up photograph of the same foil piece, taken after the coating experiment. (For interpretation of the references to color in this figure legend, the reader is referred to the web version of this article.)

3.1. Nanoparticle characterization

3.1.1. X-ray scattering

The aqueous ink was studied by small angle X-ray scattering (SAXS) in order to determine the size of the particles. The ink was placed in 1 mm capillaries and sealed with epoxy glue, and the data were analyzed using the Bayesian Indirect Fourier Transform [8]. The average particle radius was found to be 46 nm, see Fig. 3.

3.1.2. Microscopy

The drop-cast and spin-coated samples of the nanoparticles were imaged using transmission electron microscopy (TEM) (Fig. 3b) and atomic force microscopy (AFM) (Fig. 3c), respectively. The image documented that spherical nanoparticles had formed.

3.2. Bilayer characterization

3.2.1. Time-of-flight secondary ion mass spectrometry (TOF-SIMS) depth profiling analysis

The obvious concern when performing double slot-die coating is whether the expected bilayer is formed, or whether complete mixing of the layers had occurred. An experiment was designed to resolve this issue. A piece of double slot-die coated sample was submerged in a sodium hydroxide solution in order to facilitate delamination (Fig. 4b). After a while a discrete PEDOT:PSS film simply floated off the top of the surface leaving a P3HT:PCBM film

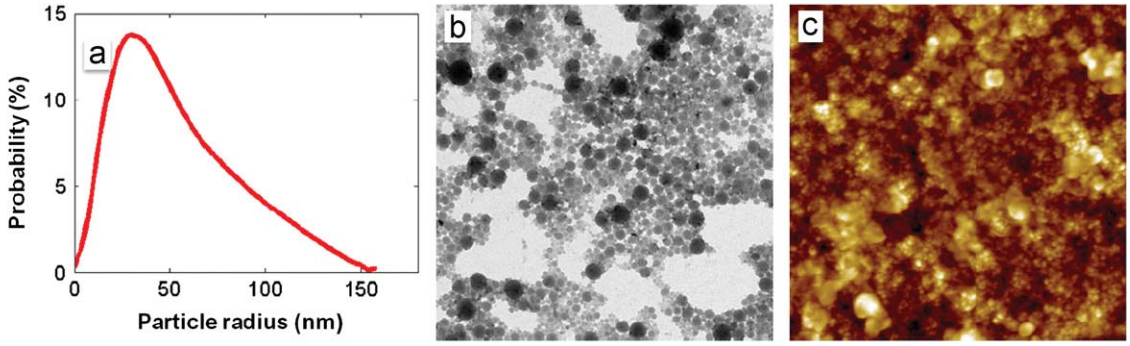

Fig. 3. **(a)** Volume weighted size distribution of the nanoparticles calculated from the SAXS measurement. **(b)** TEM image ($5 \times 5\ \mu m^2$) of a drop-cast sample. **(c)** AFM image ($5 \times 5\ \mu m^2$) of a spin-coated sample.

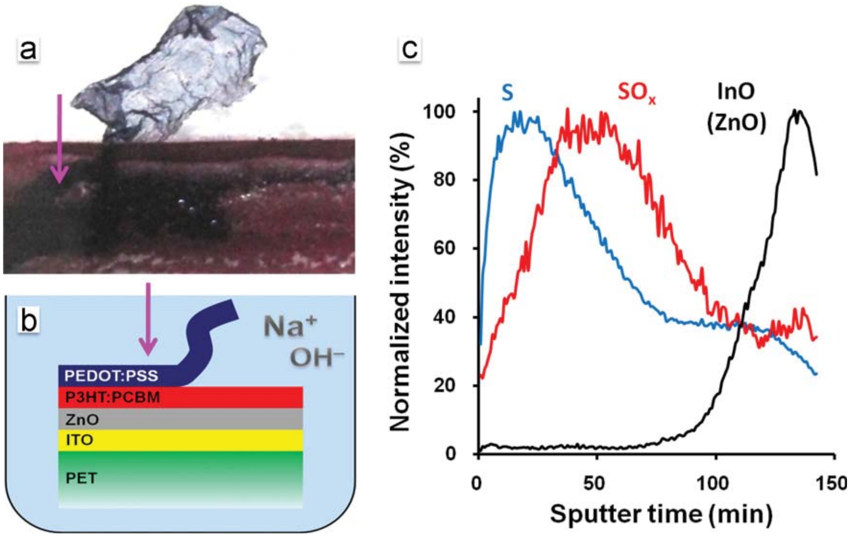

Fig. 4. **(a)** Photography showing a 18×7 mm^2 film section delaminated from the double slot-die coated film in NaOH (aq). **(b)** Schematic of the submerged sample showing the surface location (purple arrow) for the TOF-SIMS depth profiling analysis. **(c)** TOF-SIMS depth profiles in negative ion mode confirming that the double slot-die coated film has formed a bilayer. The ZnO layer was so thin that the resulting profile was too noisy, so it was left out for clarity. The noisy ZnO profile is superimposed (due to the thin nature of the film) on the InO$^-$ profile.

on the substrate surface (Fig. 4a). This is clear visual evidence that the double slot-die coating experiment yields a discrete bilayer film. The observations were confirmed by chemical analysis using TOF-SIMS.

TOF-SIMS depth profiling was in addition employed to support the observation and to further document that a bilayer had indeed formed during the double slot-die coating process. Fig. 4a–b shows the surface location where the depth profiling analysis was carried out. Several factors complicate the depth profiling analysis: (i) the sputter depth resolution (under the conditions in question) in soft materials is very poor (compared to hard materials, e.g. metals), and (ii) depth profiles are typically based on unique mass spectral markers that consist of molecular fragment ions or atomic ions, but no unique mass spectral markers are formed under the given experimental conditions. However, due to the fact that equivalent mass spectral markers originating from different molecular environments will produce a different signal response, the different materials may still be uniquely resolved. It turns out that the signal intensities for the S^- and SO_x^- fragment ions (formed in both layers) are extremely dependent on their origin. S^- is intense in PEDOT:PSS and relatively weak in P3HT:PCBM whereas SO_x^- exhibits the opposite behavior. Fig. 4c shows the depth profiles using S^- and SO_x^- as mass spectral markers. In spite of the complicated experimental conditions it was still possible to confirm that a bilayer was formed during the double slot-die coating process. In addition, a depth profile was acquired at a surface location where delamination had occurred that showed the presence of the expected one layer (see Fig. S1 in supporting information). Due to the aforementioned factors affecting the analysis it is not possible to conclude anything about the extent of interlayer mixing that was a consequence of the coating process. From the delamination experiment shown in Fig. 4 we however assume that the interface is discrete when viewed on the scale of the film thickness and probably resembles the roughness that an individual film of the P3HT:PCBM nanoparticles would.

3.2.2. *Reflectrometry*

The coated films were studied with reflectrometry in order to determine whether the two double slot-die coated liquids had mixed. Two samples were measured, a double slot-die coated PEDOT:PSS/P3HT:PCBM bilayer and a single slot-die coated PEDOT:PSS layer, both on a ZnO/ITO/PET substrate. The top layer of the two samples showed the critical angle for total reflection at the same position corresponding to the same electron density for the top layer in both preparations, see Fig. 5.

3.3. *Device performance*

The *J*–*V* characteristics of the freshly prepared solar cells are shown in Fig. 6 together with a reference device, also processed using the aqueous P3HT:PCBM nanoparticle ink as active layer

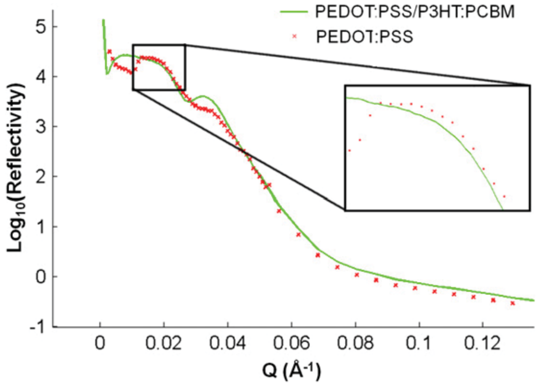

Fig. 5. Reflected intensity for two coated samples. One with PEDOT:PSS and one double slot-die coated PEDOT:PSS/P3HT:PCBM bilayer. The critical angle (θ_c) for total reflection is at 0.176° for both films corresponding to a scattering vector Q_c of 0.025 Å^{-1} ($Q = 4\pi\sin\theta/\lambda$, $\lambda = 1.5418$ Å).

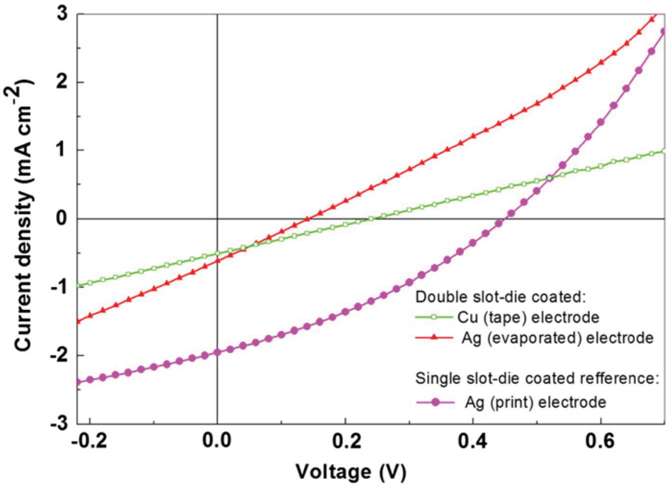

Fig. 6. *J–V* curves of the double slot-die coated devices shown in comparison with a device of similar layer structure processed by standard single slot-die coating.

Table 1
Summary of the *J-V* characterization.

Cell ID	*PCE* (%)	J_{sc} (mA cm^{-2})	V_{oc} (V)	FF (%)
Double slot-die (Cu tape)	0.03	0.5	0.24	25.0
(Ag evaporated)	0.02	0.61	0.14	25.6
Single slot-die	0.29	1.95	0.45	33.1

and PEDOT:PSS as HTL, but prepared by two sequential single slot-die coating steps (i.e. one layer at the time). The use of this nanoparticle ink constitutes a unique route for aqueous processing of large area low band gap polymer solar cells recently demonstrated by our group [9]. The extracted photovoltaic parameters are summarized in Table 1. As is evident the photovoltaic response is significantly lower for the double slot-die coated devices compared to the reference device with respect to all photovoltaic parameters. One notable feature is the linearity of the *J–V* curves within the active quadrant (FF of 25%), which suggests that the operation of the cells is dominated by the internal resistances in the devices, i.e. a low shunt resistance and a high series resistance. A low shunt resistance can be ascribed to two possible effects: (1) from the complex dynamic nature of the simultaneous bilayer formation, as it is likely that PEDOT:PSS forms percolation paths through the active layer during formation, which, in turn, will short the device. (2) It could also be linked to the known photoinduced defects in ZnO as reported recently [10].

Furthermore, the devices having the evaporated Ag electrode display the lowest shunt resistances and consequently lowest V_{oc}, probably due to shunts being formed during evaporation, while the Cu-tape avoids shunts by preferentially contacting the topmost part of the bilayer film, suggesting a somewhat inhomogeneous film. However, the higher series resistance for the devices utilizing a Cu-tape electrode hints to a large contact resistance at the PEDOT:PSS/Cu interface.

We also constructed the reference (blank) devices comprising ITO/ZnO/P3HT:PCBM/Cu-tape, and ITO/ZnO/PEDOT:PSS/Cu-tape, where ITO is indium tin oxide. The corresponding *J–V* curves under standard illumination conditions revealed no photovoltaic response thus documenting the photovoltaic properties of double slot-die coated films. The relatively poor performance of the double slot-die coated devices possibly also has its roots in the large areas we explore (several cm^2) compared to relative film inhomogeneity for the double slot-die coated films. Also the shunts might be located at the edges as is evident from the photograph in Fig. 4a where the PEDOT:PSS has the possibility to overspill the undercoat of P3HT:PCBM and thus short circuit the device. By further tuning the coating conditions, surface tensions for the inks and substrate surface energies it should be possible to minimize these effects.

4. Conclusions

We have successfully demonstrated double slot-die coated polymer solar cells processed roll-to-roll, using two aqueous inks for the simultaneous formation of both the active layer (P3HT:PCBM) and hole transporting layer (PEDOT:PSS). The devices performed relatively poor compared to similar devices processed by single slot-die coating. This is ascribed to far from perfect layer separation due to the complex nature of the bilayer formation process; resulting in shunts and low current extraction efficiencies. This convincingly demonstrates a possible route for lowering the energy payback time of polymer solar cells, which is an important factor in a possible future scenario of large scale energy production.

Acknowledgements

This work was supported by the Danish National Research Foundation. We also thank Dr. T. Kasama at DTU Center for Electron Nanoscopy for TEM measurements.

Appendix A. Supporting information

Supplementary data associated with this article can be found in the online version at doi:10.1016/j.solmat.2011.08.026.

References

[1] F.C. Krebs, Fabrication and processing of polymer solar cells. A review of printing and coating techniques, Solar Energy Materials and Solar Cells 93 (2009) 394–412.
[2] F.C. Krebs, T. Tromholt, M. Jørgensen, Upscaling of polymer solar cell fabrication using full roll-to-roll processing, Nanoscale 2 (2010) 873–886.
[3] F.C. Krebs, T.D. Nielsen, J. Fyenbo, M. Wadstrøm, M.S. Pedersen, Manufacture, integration and demonstration of polymer solar cells in a lamp for the Lighting Africa initiative, Energy & Environmental Science 3 (2010) 512–525.
[4] F.C. Krebs, J. Fyenbo, M. Jørgensen, Product integration of compact roll-to-roll processed polymer solar cell modules: methods and manufacture using flexographic printing, slot-die coating and rotary screen printing, Journal of Materials Chemistry 20 (2010) 8994–9001.

[5] N. Espinosa, R. García-Valverde, A. Urbina, F.C. Krebs, A life cycle analysis of polymer solar cell modules prepared using roll-to-roll methods under ambient conditions, Solar Energy Materials and Solar Cells 95 (2010) 1293–1302.
[6] R. Søndergaard, M. Helgesen, M. Jørgensen, F.C. Krebs, Fabrication of polymer solar cells using aqueous processing for all layers including the metal back electrode, Advanced Energy Materials 1 (2011) 68–71.
[7] A. Einstein, On the motion of small particles suspended in liquids at rest required by the molecular-kinetic theory of heat, Annalen Der Physik 17 (1905) 549–560.
[8] S. Hansen, Bayesian estimation of hyperparameters for indirect Fourier transformation in small-angle scattering, Journal of Applied Crystallography 33 (2000) 1415–1421.
[9] T.R. Andersen, T.T. Larsen-Olsen, B. Andreasen, A.P.L. Böttiger, J.E. Carle´, M. Helgesen, E. Bundgaard, K. Norrman, J.W. Andreasen, M. Jørgensen, F.C. Krebs, Aqueous processing of low-band-gap polymer solar cells using roll-to-roll methods, ACS Nano 5 (2011) 4188–4196.
[10] A. Manor, E.A. Katz, T. Tromholt, F.C. Krebs, Electrical and photo-induced degradation of ZnO layers in organic photovoltaics, Advanced Energy Materials (2011) 836–843.

Solar Energy Materials & Solar Cells 97 (2012) 43–49

Contents lists available at SciVerse ScienceDirect

Solar Energy Materials & Solar Cells

journal homepage: www.elsevier.com/locate/solmat

Roll-to-roll processed polymer tandem solar cells partially processed from water

Thue T. Larsen-Olsen, Thomas R. Andersen, Birgitta Andreasen, Arvid P.L. Böttiger, Eva Bundgaard, Kion Norrman, Jens W. Andreasen, Mikkel Jørgensen, Frederik C. Krebs*

Risø National Laboratory for Sustainable Energy, Technical University of Denmark, Frederiksborgvej 399, DK-4000 Roskilde, Denmark

ARTICLE INFO

Available online 21 September 2011

Keywords:
Roll-to-roll processing
Tandem solar cells
Polymer solar cells
Printing and coating
Aqueous processing

ABSTRACT

Large area polymer tandem solar cells completely processed using roll-to-roll (R2R) coating and printing techniques are demonstrated. A stable tandem structure was achieved by the use of orthogonal ink solvents for the coating of all layers, including both active layers. Processing solvents included water, alcohols and chlorobenzene. Open-circuit voltages close to the expected sum of sub cell voltages were achieved, while the overall efficiency of the tandem cells was found to be limited by the low yielding back cell, which was processed from water based ink. Many of the challenges associated with upscaling the multilayer tandem cells were identified giving valuable information for future experiments and development.

1. Introduction

The ultimate efficiency of polymer solar cells is inherently limited by the narrow absorption bands of the chromophores that constitute the photoactive layer of the solar cells. One obvious route to circumvent this is to stack several junctions having complementary absorption bands, thus increasing the spectral overlap of the solar cell and the terrestrial solar spectrum. The benefits of the tandem architecture over single junction cells have been thoroughly studied and reviewed [1–4], and within reasonable assumptions it has been found that a tandem architecture can increase the ultimate efficiency of polymer solar cells with 20–50%, where the highest increase is seen in the case where the single junction cells perform under their ultimate potential [1,2].

The most advantageous approach to polymer solar cell fabrication, with respect to application as an energy technology, is to allow for fast processing of all layers relying on as few coating/printing methods as possible using roll-to-roll (R2R) processing. With regards to tandem polymer solar cells the most obvious device is an all solution processed monolithic tandem cell where the sub cells are connected in series rather than parallel. This naturally presents some challenges in multilayer coating where the typical number of layers required in a tandem cell is around 6–8. All these layers (some of them very thin) have to be coated on top of each other without having subsequent coating steps adversely affecting already coated layers. The traditional laboratory approach to building up the stack is thus not expected to be easily scalable since it often employs vacuum deposition of many of the layers and a rational choice in the order of application. With the boundary condition that all layers have to be processed in air without vacuum, using only solution based printing and coating techniques, it becomes very challenging to realize functional tandem structures. So far only one report has documented vacuum free solution processing of all layers, including the printed metal back electrode [5], while large stacks by solution processing (and vacuum deposited back electrodes) have been reported [6]. Most tandem solar cell reports today employ one or more vacuum coating steps.

In this report we demonstrate R2R processing of tandem polymer solar cells on flexible substrates and show that there are many challenges associated not only with solution processing of entire tandem solar cell stacks, but also with the transfer from laboratory scale batch processing on rigid substrates to a full R2R only process on flexible films.

2. Experimental section

2.1. Materials

Poly-3-hexylthiophene (P3HT) was commercially available and had an M_n of ~20000 Da and an M_w ~40000 Da. Phenyl-C_{61}-butyric acid methyl ester (PC[60]BM) had a purity of 99%. Poly-[thiophene-2,5-diyl-*alt*-(2,3-bis(3-octyloxyphenyl)quinoxaline-5,8-diyl] (TQ-1) was synthesized according to the method described in the literature [7] and had an M_n of ~29000 Da and an M_w ~89000 Da.

The ink used for the front bulk heterojunction (BHJ) active layer comprised PC[60]BM as the acceptor material (18 mg mL^{-1}) and

---

* Corresponding author. Tel.: +45 46 77 47 99.
E-mail address: frkr@risoe.dtu.dk (F.C. Krebs).

0927-0248/$ - see front matter © 2011 Elsevier B.V. All rights reserved.
doi:10.1016/j.solmat.2011.08.025

P3HT as the donor polymer (22 mg mL^{-1}) dissolved in chlorobenzene. For the back BHJ active layer an aqueous ink [8] comprising an aqueous dispersion of nanoparticles consisting of the low band gap polymer TQ-1 (Fig. 1) and PC[60]BM prepared as described earlier [8]. An aqueous precursor solution for the zinc oxide (ZnO) used as electron transporting layer (ETL) was prepared as described earlier [9] and comprised $Zn(OAc)_2$ $2H_2O$ (100 mg mL^{-1}), $Al(OH)(OAc)_2$ (2 mg mL^{-1}) and FSO-100 (2 mg mL^{-1}) in water. Vanadium(V)oxide (V_2O_5) employed as hole transporting layer (HTL) was prepared by diluting a base solution of vanadium(V)-oxiisopropoxide with isopropanol to a concentration of 25 mg mL^{-1}, following recommendations of earlier studies [10,11]. Poly(3,4-ethylenedioxythiophene) poly(styrenesulfonate) (PEDOT:PSS) was based on Orgacon EL-P 5010 from Agfa diluted 2:1 (w:w) with isopropanol. The printable silver back electrode was PV410 from Dupont. The substrate was a 130 micron PET substrate with a patterned ITO layer (nominally 60 Ω $square^{-1}$).

2.2. *Slot-die coating*

The bottom electron contact was prepared directly on the PET/ITO substrate, prepared and cleaned as described earlier [12]. The zinc oxide precursor solution was microfiltered immediately prior to use (filter pore size of 0.45 μm) and then slot-die coated at a speed of 2 m min^{-1} with a wet thickness of 4.9 μm. After the initial drying of the precursor film it was converted into an insoluble film by passage through an oven at a temperature of 140 °C with a speed of 0.2 m min^{-1} (oven length = 4 m). This gave an insoluble doped zinc oxide film with a thickness of 25 ± 5 nm. The P3HT:PC[60]BM ink described above was microfiltered and slot die-coated with at a web speed of 1.6 m min^{-1} and a wet thickness of 11.2 μm. The film was dried by passage through an oven (2 m) at 140 °C. The recombination layer comprised a V_2O_5/ZnO stack that was slot-die coated in two steps. The V_2O_5 layer was slot-die coated directly on top of the dried P3HT:PC[60]BM layer, with a web speed of 2 ml min^{-1} and a wet thickness of 8 μm. The film was dried by passage through an oven (2 m) at 140 °C. The second zinc oxide layer was prepared exactly as the first (anode) layer, directly on the V_2O_5 layer. The back cell was prepared by slot-die coating an aqueous TQ-1:PC[60]BM nanoparticle dispersion (Fig. 2) at a web speed of 0.2 m min^{-1} and a wet thickness of 30 μm. The wet film was dried at 140 °C (oven length = 2 m) as described earlier [8]. The back electrode was prepared by applying PEDOT:PSS by slot-die coating at a speed of 0.2 m min^{-1} with drying at 140 °C (oven length = 2 m). It was found unnecessary to wet the film surface prior to coating the PEDOT:PSS and this might be due to the beneficial interaction between the fluorosurfactants in the aqueous nanoparticle dispersion and in the PEDOT:PSS. Finally, the device was completed by R2R screen printing a silver grid electrode and drying at 140 °C. The devices were encapsulated using R2R lamination of a simple food packaging barrier with a pressure sensitive adhesive onto both sides of the foil [12b].

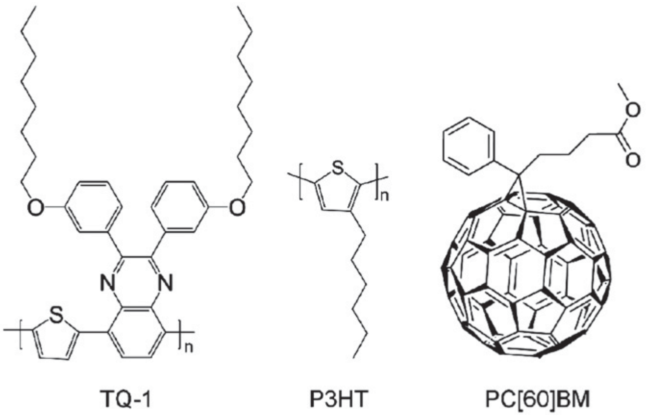

Fig. 1. Structure of poly-[thiophene-2,5-diyl-*alt*-(2,3-bis(3-octyloxyphenyl)quinoxaline-5,8-diyl] (TQ-1), poly-3-hexylthiophene (P3HT), and phenyl-C_{61}-butyric acid methyl ester (PC[60]BM).

2.3. *TOF-SIMS depth profiling analysis*

Time-of-flight secondary ion mass spectrometry (TOF-SIMS) was employed to perform a depth profiling analysis. The experiments were conducted using a TOF-SIMS IV (ION-TOF GmbH, Münster, Germany). 25-ns pulses of 25-keV Bi^+ (primary ions) were bunched to form ion packets with a nominal temporal extent of <0.9 ns at a repetition rate of 10 kHz yielding a target current of 1 pA. These primary ion conditions were used to obtain depth profiles in both negative and positive ion mode. Depth profiling was performed using an analysis area of $100 \times 100\ \mu m^2$

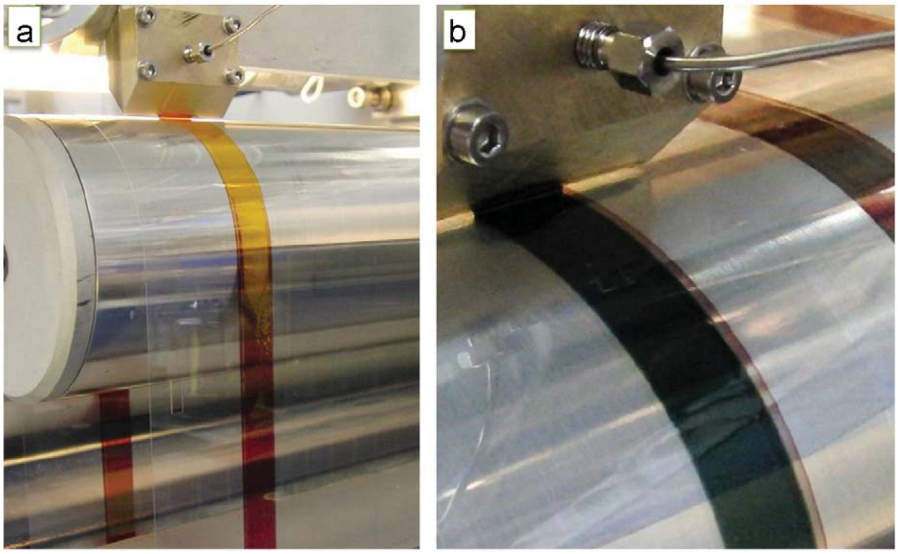

Fig. 2. Photographs of the actual R2R coating experiment in progress. (a) Coating of the front BHJ material (the drying process of the film is visible). (b) Coating of the back BHJ material.

and a sputter area of 300 × 300 μm^2. 30 nA of 3-keV Xe^+ were used as sputter ions. Electron bombardment (20 eV) was used to minimize charge build-up at the surface. Desorbed secondary ions were accelerated to 2 keV, mass analyzed in the flight tube, and post-accelerated to 10 keV before detection.

2.4. *J–V characterization*

The final devices were put under simulated sunlight at 1000 $W\,m^{-2}$, 85 ± 5 °C, 40 ± 10% relative humidity (rh) (AM1.5G). *J–V* curves were recorded by sweeping from −1 V to +1 V in steps of 20 mV and a rate of 0.1 $V\,s^{-1}$ to ensure that no dynamic effects resulted in over/under estimation of J_{sc} and V_{oc}. The time evolution of the photovoltaic performance was recorded by continuously illuminating the device under the above conditions while recording complete IV data every one minute according to ISOS-L-1 [13].

3. Results and discussion

3.1. *The tandem cell*

This study describes the transfer of a laboratory scale tandem solar cell process on rigid glass substrates to a R2R process on flexible plastic substrates. The laboratory process was described previously [11] and was developed with an aim of being compatible with R2R processing. The tandem solar cell structure comprised a multilayer stack with the composition PET/ITO/ZnO/front-BHJ/V_2O_5/ZnO/back-BHJ/PEDOT:PSS/Ag, where PET is poly(ethylene terephthalate) (substrate), ITO is indium tin oxide (transparent front electrode), ZnO is the electron transport layer, front-BHJ is the front bulk heterojunction consisting of P3HT:PC[60]BM (active layer 1), V_2O_5/ZnO is the recombination layer, back-BHJ consists of TQ-1:PC[60]BM (active layer 2), PEDOT:PSS is the hole transport layer, and Ag is the back electrode. Illustrative photographs of the coating process are shown in Fig. 2.

The first attempts resulted in very poorly performing devices typically showing open-circuit voltages around what is expected for single junction devices. Optical inspection of the completed devices revealed the possible origin of this malfunction to be cracks in the V_2O_5 part of the recombination layer (Fig. 3). It was found that these cracks form at some point during the processing of the V_2O_5 layer, possibly due to the heat treatment and/or bending of the substrate as it passes through the R2R equipment. As is also hinted in Fig. 3 these cracks persist after processing of the ZnO layer thus rendering the recombination layer penetrable to the solute of the back BHJ as this is coated. This would most likely solubilize the front BHJ and thus seriously compromise the integrity of the serial connection of the two sub cells. This situation is schematically described in Fig. 4a. Such a short-circuiting of the recombination layer would make the two active layers effectively function as one poorly performing active layer, in turn, explaining the single junction-like low open-circuit voltage observed for these devices.

However, it was possible to work around this issue by utilizing an aqueous ink for the processing of the back BHJ using a method recently described by Andersen et al. [8]. This presented a unique opportunity for orthogonal processing since water cannot solubilize the front BHJ. From the photomicrographs shown in Fig. 4 it is evident that the back cell looks less affected by the cracks in the recombination layer when water based processing is employed (Fig. 4b compared to Fig. 4a).

3.2. *TOF-SIMS depth profiling analysis*

TOF-SIMS depth profiling analysis was employed in both negative and positive ion mode in order to document the layer stack order. The encapsulation film is too thick for a depth profiling analysis, so it was necessary to delaminate the tandem solar cell. TOF-SIMS mass spectra of the exposed surfaces revealed that delamination took place at the PEDOT:PSS/back BHJ interface.

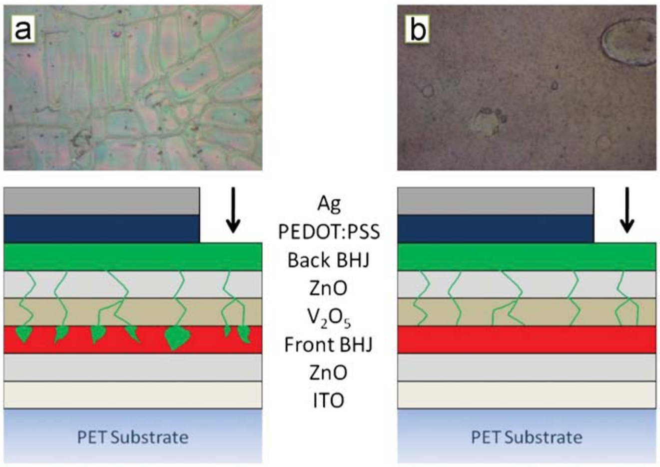

Fig. 4. Schematics of the tandem solar cell under study and photomicrographs (230 × 150 μm^2) obtained at the indicated positions (black arrows), which illustrates the proposed consequence of the observed cracks in the recombination layer when using (a) a non-orthogonal solvent (chloroform) and (b) an orthogonal solvent (water), for the processing of the back BHJ.

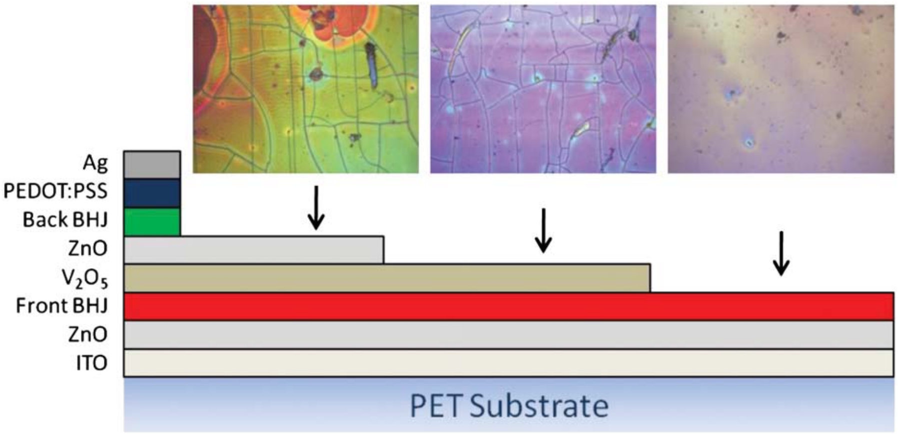

Fig. 3. Schematic of the tandem solar cell under study and photomicrographs (260 × 195 μm^2) revealing cracks in the V_2O_5 layer, which persist through the ZnO layer.

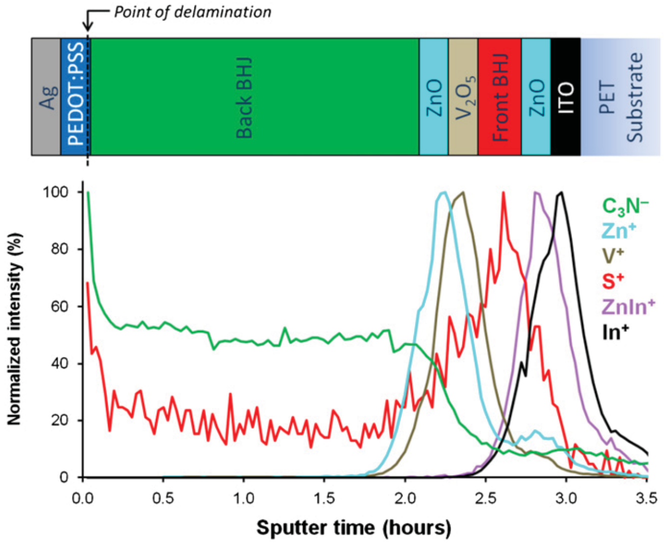

Fig. 5. TOF-SIMS depth profiles through the delaminated tandem solar cell. C_3N^- is a marker for the back BHJ obtained from a depth profile run in negative mode, Zn^+ is a marker for the ZnO, V^+ is a marker V_2O_5, S^+ is a marker for both front and back BHJ, and $ZnIn^+$ (formed during the ionization step of the analysis) is a marker for the front ZnO and In^+ is a marker for ITO.

Fig. 5 shows the results of the depth profile analysis. Various factors complicated the analysis, such as interface roughness, which is well known phenomenon in R2R processing (e.g. compared to spin coating). Furthermore, depth profiling in soft materials is associated with an inferior depth resolution (under the given sputter conditions), compared to hard materials (e.g. metals). These conditions constitute a challenge especially when it comes to performing depth profiling on very thin layers such as the ZnO (~25 nm) and V_2O_5 (~15 nm) layers present in this device. However, as is evident from Fig. 5 it was quite possible, in spite of the conditions, to document the multilayer stack composition in the tandem solar cell device. Residual PEDOT:PSS was present in the PEDOT:PSS/back BHJ interface after the delamination process presumably due to a small degree of interlayer mixing that resulted in presumably a matrix effect, which is observed as initially elevated signals from the back BHJ material (i.e. at the beginning of the sputter time window). During the ionization process the Zn^+ signal is discriminated due to the formation of the $ZnIn^+$ cluster ion caused by the close vicinity of the ITO (i.e. an ionization phenomenon). Finally, a significantly long sputter time window is observed for the back BHJ compared to the front BHJ, which suggests that the back BHJ is significantly thicker (assuming similar sputter rates) than the front BHJ consistent with an expected layer thickness of ~600 nm [8] for the back BHJ as compared to the thickness of the front BHJ ~200 nm.

3.3. Electrical characterization

J–V characteristics for the best performing tandem device are shown in Fig. 6, (blue triangles) together with representative J–V curves for both tandem and back cell reference devices with and without photo-annealing (800 min). The key photovoltaic parameters are summarized in Table 1, while the dynamic evolutions of the short circuit current (I_{sc}) and open-circuit voltage (V_{oc}) are shown in Fig. 7. By summing the V_{oc} values from the sub cell reference devices (Table 1) it is possible to estimate that the perfect tandem device would have an open-circuit voltage close to 1 V. As is clear from the presented data in Table 1, the actual tandem devices gave, at best, a V_{oc} around 0.9 V while V_{oc} values around 0.75 V were readily measured, hence between 0.1 and 0.25 V less than the expected ideal value.

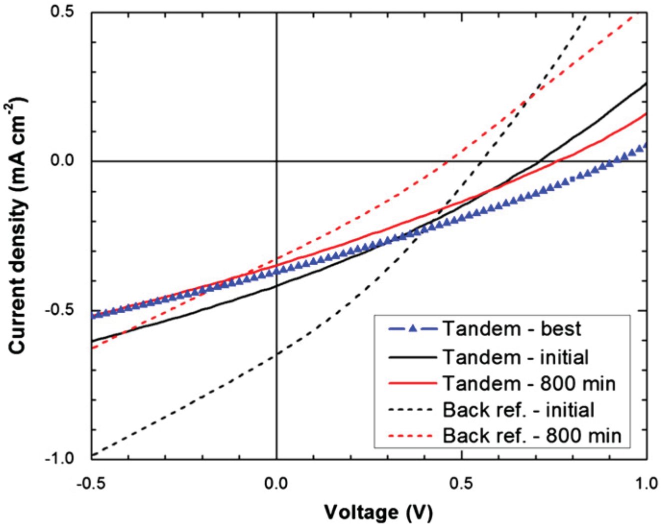

Fig. 6. J–V characteristics (AM1.5G 1000 W m^{-2}) for the best performing tandem cells. Also shown is a more average cell, before (initial) and after (800 min) photo-annealing.

Table 1
Summary of the J–V characterization.

Cell	PCE (%)	J_{sc} (mA cm^{-2})	V_{oc} (V)	FF (%)
Tandem ([a])				
(Initial)	0.09	−0.42	0.71	28.8
(800 min)	0.07	−0.35	0.76	27.5
(Best)	0.10	−0.37	0.91	28.2
Back cell ([a])				
(Initial)	0.11	−0.65	0.55	30.2
(800 min)	0.04	−0.33	0.46	27.7
Front cell (Ref. [11])	1.32	−7.17	0.50	36.9

[a] Cell active area of 4 cm^2.

Various loss mechanisms can influence the tandem voltage, of which most are related to the nature of the sub cell interconnection, i.e. the recombination layer. In this case it is highly probable that the before mentioned observed defects (Fig. 3) are likely to have a negative influence on V_{oc} if the mechanism schematically shown in Fig. 4b is considered, i.e. shunts across the recombination layer would lower the tandem V_{oc}. Furthermore, the results show that the front and back reference cells both exhibit a decreasing V_{oc} during the dynamic evolution J–V experiment as observed in Fig. 7 and S7 (see e-component). For the tandem devices the trend is opposite, i.e. increasing V_{oc} over time. Both reference cells display saturation at around 0.45 V, which fits well with the peak value of the best tandem cell.

It appears that the sub cell interconnection improves over time, possibly due to burning of shunts across the recombination layer, originally formed as a consequence of the defects. With respect to the I_{sc} it is noticeable that the tandem device and the back cell reference device have rather similar I_{sc} values. This should be compared to the front cell I_{sc}, which is a factor of 10 to 20 times larger. Thus the tandem device is severely current limited by the poor performing back cell.

This significant current mismatch is likely to influence the current–voltage characteristics of the tandem cell. Hadipour et al. [14] found that the excess current will cause the surplus of free holes to pile up at the middle electrode (recombination layer), which will result in a lowering of the effective internal field in the

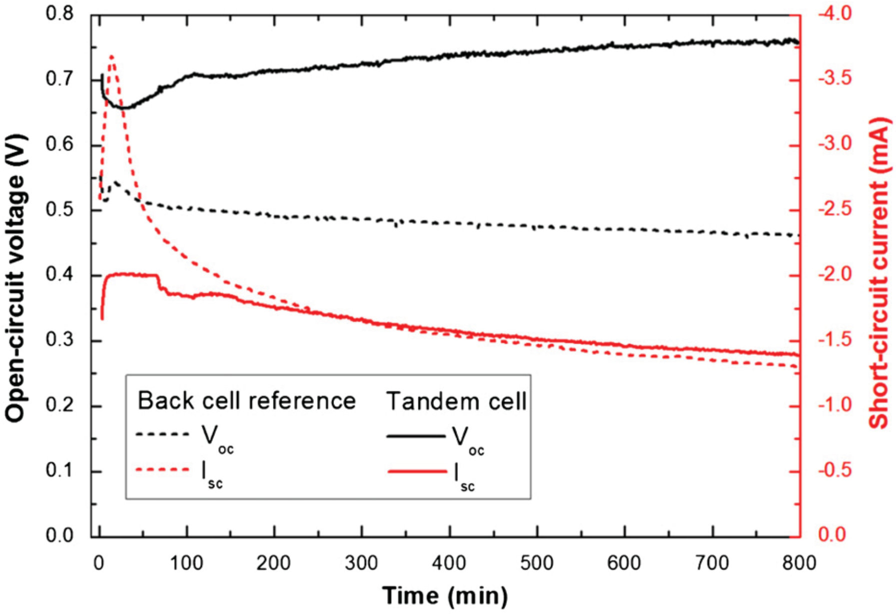

Fig. 7. Time evolution of the open-circuit voltage and short-circuit current during the 800 min of photo-annealing (AM1.5G 1000 W m^{-2}) of the tandem cell, and a corresponding single junction reference cell mimicking the current-limiting back cell.

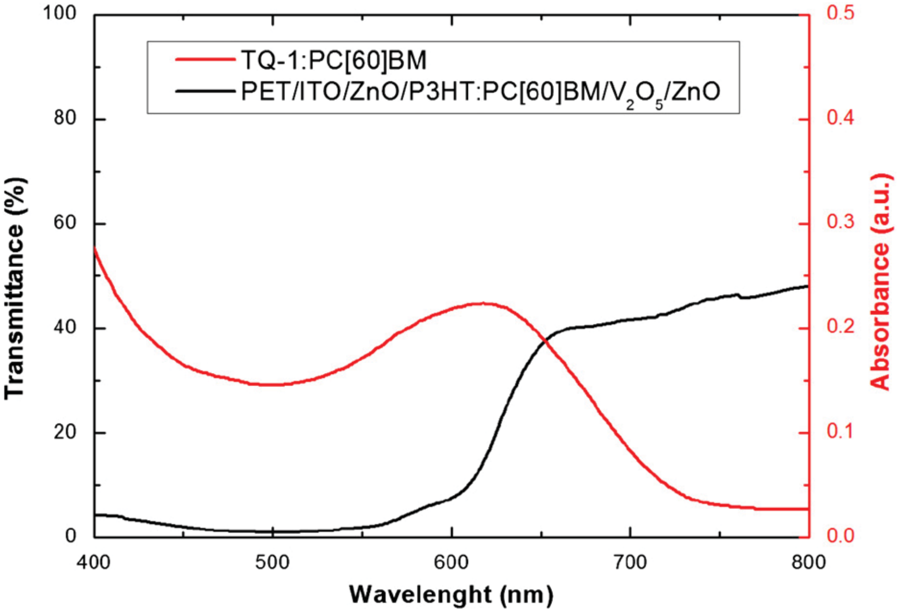

Fig. 8. Transmittance of the front cell and the recombination layer relative to the absorbance of the back cell active layer.

front sub cell, while for the back sub cell the opposite will be the case and the internal field will increase.

Hence the sub cell currents will equilibrate at some intermediate value, resulting in a higher I_{sc} value for the tandem device compared to the expected current of the limiting sub cell reference device. How the tandem current equilibrates is very much dependent on the slope of the *J–V* curves of the sub cells around short-circuit as well as the degree of current mismatch, as recently pointed out by Braun et al. [15] for the case of an inorganic tandem cell. This can be easily understood, e.g. in the case of the current limiting sub cell; as the reverse biasing caused by the current mismatch will only result in a significant increase in current if the *J–V* curve of the sub cell has a non zero slope in reverse bias, which is the case for the cells under study here. Furthermore, according to Fig. 8 the tandem back cell will suffer from an obvious poor spectral matching with the front cell transmission spectrum, and thus receive a significantly lower photon flux than the reference cell. From this, a significant lowering of the back cell current would be expected. However, as the *J–V* data shows that the I_{sc} of the tandem is not lower but rather comparable to that of the current limiting back cell reference device this would in fact imply a combination of the spectral mismatch and the increased quantum efficiency of the tandem back cell due to current mismatch (the effect described in Refs. [14 and 15]). To support this, we construct the ideal tandem curve from the two reference sub cells by summing voltages at equal currents, as described in Ref. [14]. We take into account the spectral mismatch by a mismatch factor *S*, which is simply multiplied with the current of the back cell reference. These can be seen in Fig. 9, for the case of $S=1$ and $S=0.5$, together with the

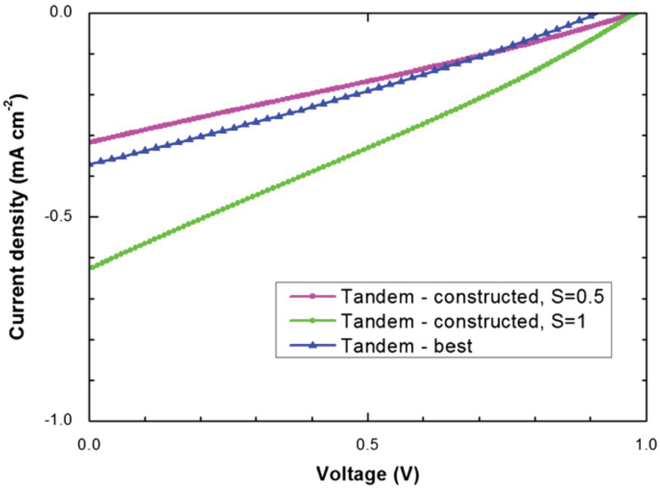

Fig. 9. Constructed tandem *J*–*V* characteristics with spectral mismatching ($S=0.5$) and without ($S=1$), compared with the best measured tandem device.

best tandem curve. As can be seen, it is likely that severe spectral mismatching is the cause of the low short-circuit current of the tandem cell, while the discrepancy between the model and the measurement can be explained by the somewhat crude model, such as negligence of V_{oc} dependence on light intensity [16], and the assumption of a perfect ohmic connection between the sub cells, e.g. a perfect recombination layer.

3.4. Future developments

The tandem approach within polymer photovoltaics has so far been utilized in an attempt to maximize efficiency, i.e. without constraints on materials and fabrication methods. The present work, however, demonstrates the fragility of the tandem device approach from a solution processing point of view, and in doing so, stresses the importance of having certain constraints in mind when assessing a given set of materials and processing methods. In this regard especially the recombination layer presents an all-determining weak-point of the tandem cell; a perfect recombination layer would be insoluble and solvent impenetrable, being either a pn-junction preferably a highly doped tunnel junction or alternatively having metal like characteristics. This has so far been achieved only for small area devices using rigid substrates [6,11,17–21]. Lee et al. [22] successfully demonstrated a small area tandem device on a flexible substrate but using vacuum deposition. However, as for upscaling of the fabrication, it is the view of the authors that a stable and highly reliable solution process for polymer tandem solar cells can only be ensured by a completely orthogonalized process in which none of the processing steps can seriously harm any of the previously processed layers. This has to do with the inherently rough nature of a high throughput R2R process, during which cracks and small coating imperfections would act as solvent paths leading to partial dissolution of underlying layers. The aqueous emulsion approach utilized in this work is one possible solution presenting both a stable and possibly environmentally friendly fabrication process. At the same time it allows for the use of the large amount of existing polymers. However, the success of this technique of course depends on whether significantly better device performance can be achieved. Another foreseeable solution would be a process where the layers by some in-line post process are rendered insoluble, for instance using thermal- or light-induced thermocleavage of the solubilizing groups as demonstrated earlier [5,23,24]. This would be very desirable as it ensures free choice of solvent for the subsequent layers, and also removes constraints on the recombination layer in terms of materials and layer thicknesses, thus opening for a wider range of tweakable parameters.

4. Conclusions

We have successfully demonstrated large area flexible polymer tandem solar cells with all layers processed entirely from solution, and partially from water. The multilayer stack on flexible PET substrate comprised a cathode of ITO/ZnO, a recombination layer of V_2O_5/ZnO, and a PEDOT:PSS/Ag (printed) anode. The two serially connected BHJs was comprised of a P3HT:PC[60]BM front cell processed from chlorobenzene and a back cell processed from an aqueous dispersion of poly[2,3-bis-(3-octyl oxyphenyl)-quinoxaline-5,8-diyl-alt-thiophene-2,5-diyl]:PC[60]BM nanoparticles. The composition and integrity of the multilayer stack was confirmed by TOF-SIMS depth profiling. The V_{oc} of the best tandem device was 0.9 V, while both the corresponding single junction reference devices had a V_{oc} around 0.5 V. This confirms a serial connection of the sub cells while the observed voltage losses are ascribed to visible defects in the recombination layer and a non-ohmic connection of the two sub cells.

Acknowledgment

This work was supported by the Danish National Research Foundation. We gratefully acknowledge Lasse Gorm Jensen for creating graphical illustrations and Jon E. Carlé and Martin Helgesen for preparing polymer materials.

Appendix A. Supplementary materials

Supplementary data associated with this article can be found in the online version at doi:10.1016/j.solmat.2011.08.025.

Details of GIWAXS measurements and time evolution for the back reference cell.

References

[1] T. Ameri, G. Dennler, C. Lungenschmied, C.J. Brabec, Organic tandem solar cells: a review, Energy & Environmental Science 2 (2009) 347–363.
[2] G. Dennler, M.C. Scharber, T. Ameri, P. Denk, K. Forberich, C. Waldauf, C.J. Brabec, Design rules for donors in bulk-heterojunction tandem solar cells. Towards 15% energy-conversion efficiency, Advanced Materials 20 (2008) 579–583.
[3] J.D. Kotlarski, P.W.M. Blom, Ultimate performance of polymer: fullerene bulk heterojunction tandem solar cells, Applied Physics Letters 98 (2011) 053301.
[4] Y.M. Nam, J. Huh, W.H. Jo, A computational study on optimal design for organic tandem solar cells, Solar Energy Materials and Solar Cells 95 (2011) 1095–1101.
[5] O. Hagemann, M. Bjerring, N.C. Nielsen, F.C. Krebs, All solution processed tandem polymer solar cells based on thermocleavable materials, Solar Energy Materials and Solar Cells 92 (2008) 1327–1335.
[6] J. Gilot, M.M. Wienk, R.A.J. Janssen, Double and triple junction polymer solar cells processed from solution, Applied Physics Letters 90 (2007) 143512.
[7] E. Wang, L. Hou, Z. Wang, S. Hellström, F. Zhang, O. Inganäs, M.R. Andersson, An easily synthesized blue polymer for high-performance polymer solar cells, Advanced Materials 22 (2010) 5240–5244.
[8] T.R. Andersen, T.T. Larsen-Olsen, B. Andreasen, A.P.L. Böttiger, J.E. Carle´, M. Helgesen, E. Bundgaard, K. Norrman, J.W. Andreasen, M. Jørgensen, F.C. Krebs, Aqueous processing of low-band-gap polymer solar cells using roll-to-roll methods, ACS Nano 5 (2011) 4188–4196.
[9] R. Søndergaard, M. Helgesen, M. Jørgensen, F.C. Krebs, Fabrication of polymer solar cells using aqueous processing for all layers including the metal back electrode, Advanced Energy Materials 1 (2011) 68–71.
[10] N. Espinosa, H.F. Dam, D.M. Tanenbaum, J.W. Andreasen, M. Jørgensen, F.C. Krebs, Roll-to-roll processing of inverted polymer solar cells using hydrated vanadium(V)oxide as a PEDOT:PSS replacement, Materials 4 (2011) 169–182.

[11] T.T. Larsen-Olsen, E. Bundgaard, K.O. Sylvester-Hvid, F.C. Krebs, A solution process for inverted tandem solar cells, Organic Electronics 12 (2011) 364–371.

[12] a) F.C. Krebs, T. Tromholt, M. Jørgensen, Upscaling of polymer solar cell fabrication using full roll-to-roll processing, Nanoscale 2 (2010) 873–886;
b) J. Alstrup, M. Jørgensen, A.J. Medford, F.C. Krebs, Ultra fast and parsimonious materials screening for polymer solar cells using differentially pumped slot-die coating, ACS Applied Materials & Interfaces 2 (2010) 2819–2827.

[13] M.O. Reese, S.A. Gevorgyan, M. Jørgensen, E. Bundgaard, S.R. Kurtz, D.S. Ginley, D.C. Olson, M.T. Lloyd, P. Morvillo, E.A. Katz, A. Elschner, O. Haillant, T.R. Currier, V. Shrotriya, M. Hermenau, M. Riede, K.R. Kirov, G. Trimmel, T. Rath, O. Inganäs, F. Zhang, M. Andersson, K. Tvingstedt, M. Lira-Cantu, D. Laird, C. McGuiness, S. Gowrisanker, M. Pannone, M. Xiao, J. Hauch, R. Steim, D.M. DeLongchamp, R. Rösch, H. Hoppe, N. Espinosa, A. Urbina, G. Yaman-Uzunoglu, J.-B. Bonekamp, A.J.J.M. van Breemen, C. Girotto, E. Voroshazi, F.C. Krebs, Consensus stability testing protocols for organic photovoltaic materials and devices, Solar Energy Materials and Solar Cells 95 (2011) 1253–1267.

[14] A. Hadipour, B. de Boer, P.W.M. Blom, Device operation of organic tandem solar cells, Organic Electronics 9 (2008) 617–624.

[15] A. Braun, N. Szabo´, K. Schwarzburg, T. Hannappel, E. Katz, J.M. Gordon, Current-limiting behavior in multijunction solar cells, Applied Physics Letters 98 (2011) 223506.

[16] T. Tromholt, E. Katz, B. Hirsch, A. Vossier, F.C. Krebs, Effects of concentrated sunlight on organic photovoltaics, Applied Physics Letters 96 (2010) 073501.

[17] A. Hadipour, B. de Boer, J. Wildeman, F.B. Kooistra, J.C. Hummelen, M.G.R. Turbiez, M.M. Wienk, R.A.J. Janssen, P.W.M. Blom, Solution-processed organic tandem solar cells, Advanced Functional Materials 16 (2006) 1897–1903.

[18] J.Y. Kim, K. Lee, N.E. Coates, D. Moses, T.–Q. Nguyen, M. Dante, A.J. Heeger, Efficient tandem polymer solar cells fabricated by all-solution processing, Science 317 (2007) 222–225.

[19] S. Sista, M.–H. Park, Z. Hong, Y. Wu, J. Hou, W.L. Kwan, G. Li, Y. Yang, Highly efficient tandem polymer photovoltaic cells, Advanced materials 22 (2010) 380–383.

[20] D.J.D. Moet, P. de Bruyn, P.W.M. Blom, High work function transparent middle electrode for organic tandem solar cells, Applied Physics Letters 96 (2010) 153504.

[21] C.–H. Chou, W.L. Kwan, Z. Hong, L.–M. Chen, Y. Yang, A. Metal-Oxide, Interconnection layer for polymer tandem solar cells with an inverted architecture, Advanced Materials 23 (2011) 1282–1286.

[22] B.J. Lee, H.J. Kim, W. -ik Jeong, J.–J. Kim, A transparent conducting oxide as an efficient middle electrode for flexible organic tandem solar cells, Solar Energy Materials and Solar Cells 94 (2010) 542–546.

[23] T. Tromholt, S.A. Gevorgyan, M. Jørgensen, F.C. Krebs, K.O. Sylvester-Hvid, Thermocleavable materials for polymer solar cells with high open circuit voltages – a comparative study, ACS applied materials & interfaces 1 (2009) 2768–2777.

[24] F.C. Krebs, K. Norrman, Using light induced thermocleavage in a roll-to-roll process for polymer solar cells, ACS applied materials & interfaces 2 (2010) 877–887.

Energy &
Environmental Science

Appendix 5

Cite this: DOI: 10.1039/c2ee23244h

www.rsc.org/ees

COMMUNICATION

All printed transparent electrodes through an electrical switching mechanism: A convincing alternative to indium-tin-oxide, silver and vacuum

Thue T. Larsen-Olsen, Roar R. Søndergaard, Kion Norrman, Mikkel Jørgensen and Frederik C. Krebs*

Received 22nd August 2012, Accepted 5th September 2012
DOI: 10.1039/c2ee23244h

Here we show polymer solar cells manufactured using only printing and coating of abundant materials directly on flexible plastic substrates or barrier foil using only roll-to-roll methods. Central to the development is a particular roll-to-roll compatible post-processing step that converts the pristine and non-functional multilayer-coated stack into a functional solar cell through formation of a charge selective interface, *in situ*, following a short electrical pulse with a high current density. After the fast post-processing step the device stack becomes active and all devices are functional with a technical yield and consistency that is compelling.

Although polymer and organic solar cells have been generally recognized for more than a decade and presented in a vision of low cost flexible solar panels with a thin outline and low cost, state-of-the art polymer solar cells are still handled in a glove box and employ rigid glass substrates, expensive indium-tin-oxide (ITO) and expensive or reactive metal electrodes evaporated under high vacuum. This reflects a developmental focus which has until now been mostly on increasing the solar cell efficiency[1] while neglecting the decisive issues of stability[2] and true scalability through the exclusive use of roll-to-roll processing and abundant materials with a low thermal budget.[3,4] The transition from single laboratory devices to mass produced modules has been slow and it has proven difficult to transfer the high performance reported for laboratory devices to a larger scale. Often results for laboratory devices are represented by a single (or a few) successful experiment(s) with the values for the "hero" device being quoted. Mass produced polymer solar cells, however, are represented by the average which in reality is what can become useful. In such a case the technical yield and consistency become critically important and the robustness of materials and processes is paramount. The few documented cases where many polymer solar cells have been reported are based on ProcessOne[5] which does fulfill the criteria of robustness and repeatability to an extent that many modules can be prepared with an even performance and integrated into demonstrators. In a recent example more than 10 000 small credit card sized OPV modules based on ProcessOne were manufactured and integrated into a small flashlamp.[6] ProcessOne comprise a PET-ITO-ZnO-P3HT:PCBM-PEDOT:PSS-silver stack and present performances in the range of 1.5–2% in an identical module layout.[6] In terms of materials usage however ProcessOne will never be competitive since it involves ITO that is arrived at by vacuum deposition followed by a time consuming lithographic process.[7] The overall processing speed of the patterned ITO electrode is unlikely to exceed 1 m min^{-1} even with large industrial machinery. Apart from the processing of ITO, the material involves the very rare metal indium and possesses some less critical attributes such as brittleness and poor thermomechanical properties.

There has been a significant research effort aimed at replacing ITO, and while there have been some successful laboratory reports[8–12] only few are directly compatible with large scale processing of

Department of Energy Conversion and Storage, Technical University of Denmark, Frederiksborgvej 399, DK-4000 Roskilde, Denmark. E-mail: frkr@dtu.dk

Broader context

The vision of polymer solar cells is a scalable, efficient and stable technology that can be prepared in large areas with a thin outline using ultrafast printing and coating methods that require little energy in the process and only abundant materials. State-of-the-art polymer and organic solar cells are far removed from this ideal situation and typically employ tiny areas processed through slow and time consuming vacuum steps on rigid substrates employing toxic processing conditions and elements with low abundance such as indium and silver. We present a simple solar cell stack that comprises only four printed and coated layers representing significant progress at all levels. We have thus moved from single cells to modules, from rigidity to flexibility, from spin coating to full roll-to-roll processing in all steps, from glove box to ambient processing, thousands of units and have eliminated the use of indium, silver and vacuum while achieving comparable performance. We introduce a method whereby functionality is arrived at through *in situ* formation of a rectifying interface inside the finished stack. We demonstrate how this switching mechanism is fully scalable and we use it in a fully automated roll-to-roll process. We also elucidate the chemistry behind this generic mechanism as a new processing step.

interconnected modules. The first successful example[8] involved a non-transparent first electrode based on coated silver nanoparticles. Even if the performance was quite poor compared to ProcessOne it did show that an ITO-free future could be anticipated pending the right developments.

To rationalize our efforts towards replacing ITO, one must logically also consider the relatively low abundance and high thermal budget of silver which make its use just as critical as the use of indium.[7] Silver, however, has the advantage over ITO of an exceptionally high conductivity enabling the use of much less material, if applied correctly as a very thin layer or a grid. In the ultimate case, however, even silver cannot be anticipated as being on the materials list unless it can be recycled efficiently.

When focusing on the functional part of the solar cell stack it comprises the active layer sandwiched between an electron and a hole selective layer where one or both of the charge selective layers may serve as electrode.

For the purpose of this study we introduce the generalized stack shown as the center piece in Fig. 1, comprising first-electrode/ZnO/active layer/PEDOT:PSS/second-electrode, forming the functional basis for the solar cell module, as succeeding stacks can be serially connected by overlapping of their first- and second-electrode. In the ideal case the two electrodes are based on abundant materials. Here we utilize a compact module comprised of 16 serially connected solar cells which enables us to alleviate the use of both ITO and Ag, thus in essence presenting a metal electrode-free solar cell module. The chosen device structures were thus simply PEDOT:PSS/ZnO/active layer/PEDOT:PSS/graphite, while a series of modules using Ag instead of graphite as the second-electrode were also fabricated for comparison.

Returning to the scalability and processability of this device stack it is highly compatible with high speed printing at all levels, especially the front electrode including the ZnO layer could be processed at very high speed even under simple pilot line conditions as shown in Fig. 1. We were thus able to process the entire front electrode structure with the front PEDOT:PSS electrode being formulated for rotary screen printing enabling printing speeds with high accuracy at >10 m min^{-1} (speed limited by the drier length of 2 m). The slot-die coating of the ZnO nanoparticle ink could easily be coated at 10 m min^{-1} also with high accuracy (48 cell lines coated simultaneously, 3 mm wide and spaced by 1 mm). The sheet resistivity of the pure PEDOT:PSS was 60 ohm per square and sufficient for transport over the 2 mm wide active area with part of the 4 mm repeat covered by the thick printed interconnection (Fig. 2e). The electrode structure thus presents a significant alternative to ITO at all levels by being comparable in performance, while being abundant and processable in air without vacuum. The active layer was like the ZnO layer slot-die coated and the back PEDOT:PSS electrode was rotary screen printed in registry with the underlying layer structure (for modules the interconnects or grids were also rotary screen printed in registry). It is of significant importance to underline that the realization of the patterned multilayer stack was readily achievable using standard coating and printing techniques (pending an appreciable effort in ink formulation, printing/coating methodology and machine design) and as such it did not present inventive steps (only skill).

The testing of the multilayer stack as a solar cell however presented a non-functional device with a very low parallel resistance as shown in Fig. 2b (essentially a short circuit). At first this was ascribed to coating or printing irregularities that bridge the two electrodes through the thin active part of the solar cell thus creating a short circuit. However, the process is in essence identical to ProcessOne where large numbers of similar solar cell modules can be made reliably, and careful analysis revealed that processing faults were not the cause.

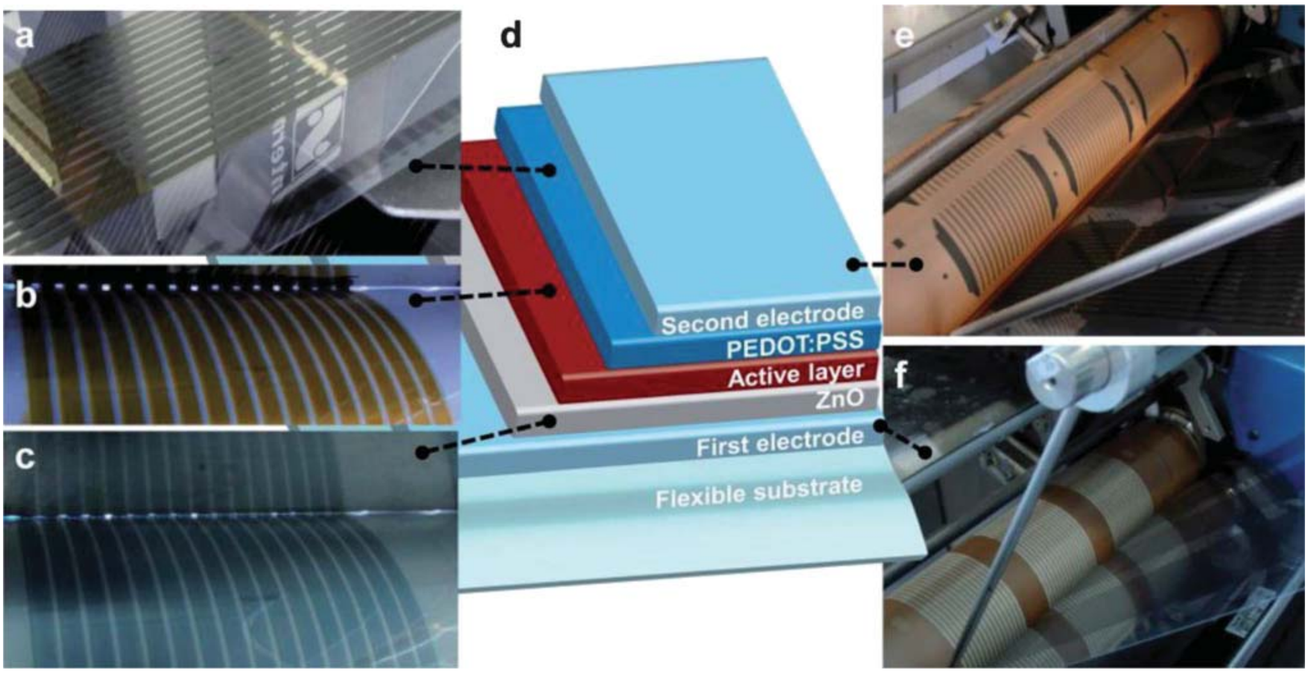

Fig. 1 The device structure (d) centrally surrounded by photographs of the R2R coating and printing, with (a) and (f) showing the rotary screen printing of the top and bottom PEDOT:PSS layers, respectively. (c) and (b) showing the slot-die coating of ZnO and P3HT:PCBM, respectively, while (e) shows the rotary screen printing of the graphite second-electrode.

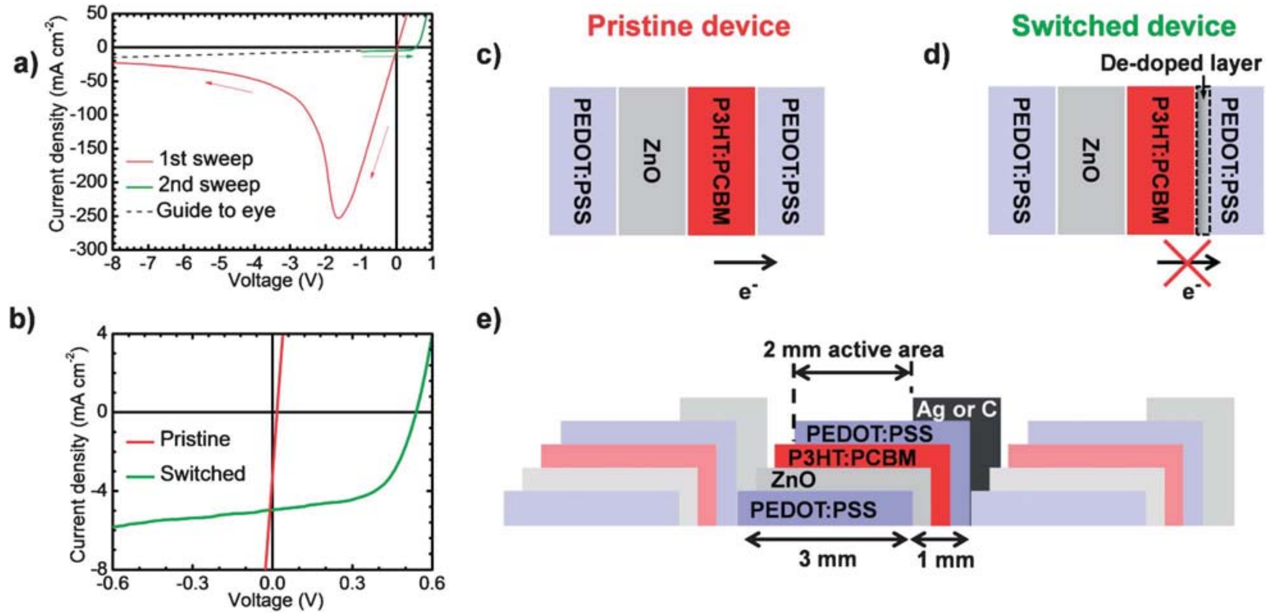

Fig. 2 Electrical characterization. (a) The *I–V* characterization under simulated solar light, showing the initial bias sweep (red) going from 1 V to −8 V, followed by a forward sweep from −1 V to 1 V (green). (b) A zoom-in on the active quadrant, showing the change in device performance. (c and d) show the layer stack before and after the de-doping has occurred. (e) shows a cross section of the device highlighting the active region and in the printed interconnection.

ZnO as a semi conductor is known to present interaction with atmospheric oxygen[13] and can also be subject to proton doping.[14] Both effects alter the transport properties of ZnO and can also be expected to be present in the stack we explore here. We found by studying very small area devices (≤25 mm^2) that a high current density at a significant applied field presented an irreversible response vis-à-vis a report on the use of PEDOT:PSS as a write-once-read-many-times (WORM) memory material[15–20] and ZnO as a reversible memory element.[13,21,22]

Fortunately, the device works exceptionally well after the short high current density-high electric field treatment as shown in Fig. 2b and it was thus a matter of characterizing the effect in order to make proper use of it in solar cell devices. The observation that a high negative bias dramatically alters the electrical performance is ascribed to the known permanent conductivity change in PEDOT:PSS films.

A switching mechanism was first demonstrated by Möller *et al.*[15,16] and later adopted by others,[17–20] in all cases for WORM devices. The exact nature of this bias induced phenomenon is still debated, but apart from de Brito *et al.*[18] who ascribed the conductivity loss to a delamination caused by gases produced by hydrolysis, it is believed to be caused by de-doping of the PEDOT ($\mathrm{PEDOT^+} \rightarrow \mathrm{PEDOT^0}$) molecules induced by charge injection, while the dedoped state is stabilized by the neutralization of the PSS counter-ions ($\mathrm{PSS^-} \rightarrow$ PSS-H).[16,19,23] Here we report for the first time that the de-doped PEDOT:PSS layer functions as a very efficient hole selective layer for solar cells. The proposed mechanism is, as illustrated in Fig. 2c and d, blocking of electron transport by the formation of a sufficiently thick de-doped PEDOT:PSS layer. The layer thus constitutes a thin region where the polythiophene is reduced and it thus behaves like an intrinsic semiconductor. The mechanism is in nature self-contained as the de-doping is electron injection induced, thus hindering "over-growth" of the de-doped layer. In the following we shed further light on this by providing chemical proof of the de-doping mechanism. As the devices have two distinct PEDOT:PSS layers and a ZnO layer there are several different junctions at which the switching phenomenon could take place. Initially we believed that the switch took place at the PEDOT:PSS/ZnO junction since this was the only variation with respect to the traditional ProcessOne device structure. The solar cell stack was taken apart and built again in order to prove that the active-layer–PEDOT:PSS interface is indeed responsible for the effect. Fortunately it is facile to delaminate the solar cell exactly at the P3HT:PCBM–PEDOT:PSS interface.[24] We could thus prepare devices and switch them to their functional form. Delamination and removal of the PEDOT:PSS-Ag electrode followed by application of the PEDOT:PSS layer and Ag electrode, again presented a non-functional device, displaying the initial ohmic shunting. More importantly it could be switched anew thus unequivocally proving that the active-layer–PEDOT:PSS interface is responsible for the effect (with a series of control experiments, it was deduced that the switching was not reversed by either the exposure to vacuum or solvents). To shed further light on the de-doping mechanism in the context of the active-layer–PEDOT:PSS interface, explored here as a solar cell junction, we systematically analyzed the interfaces using chemical probe time-of-flight secondary ion mass spectrometry (TOF-SIMS). It was clear that the effect should be small if the proposed mechanism was correct since it involves only the reduction of PEDOT:PSS to the neutral semiconducting $\mathrm{PEDOT^0}$ and PSS-H involving water and electrons for the reduction.[16,19] In terms of chemical composition, the changes at the interface are marginal and it is essentially only a redox reaction. What does change however is the polarity/ionic strength of the medium since the polythiophene cation becomes neutralized and ions are thus expected to diffuse away from the interface and towards the more ionic bulk PEDOT:PSS.

We thus analyzed the PEDOT:PSS interface through depth profiling from the surface and found a decreased sodium content at the interface for the switched device (we use sodium ions as a marker for the ion content). As expected the sodium content was identical in the two cases further in the bulk of the PEDOT:PSS layer. The experiment and results are shown in Fig. 3.

In order to gain appreciation for the implications and usefulness of this general approach we designed and built a machine that could usefully switch devices and modules in a full roll-to-roll process at a reasonable speed. The large current density at high fields does imply that the charge transporting layers and conductors have to dissipate heat. Whereas it is readily possible to dissipate heat when the devices are small (on the order of a few mm^2) it is a different matter for large area devices and modules, and we found that a large drum as shown in Fig. 4d was the most rational way to cool the foil during switching.

The switched modules performed as shown in Fig. 4a and Table 1, with only a minor difference in performance between the silver and carbon based devices (depicted in Fig. 4b). This performance is comparable or better than ITO containing ProcessOne cells (ref. 6).

The switching itself is fast and takes place in a matter of milliseconds and the largest challenge for an automated setup was to ensure that all devices achieve switching simultaneously. We demonstrated that three modules, each comprising sixteen serially connected cells, could be switched in parallel (see Fig. 4c and d). In terms of processing speed every extra step does reduce the throughput speed. To illustrate the delay that this new process incurs, it can be rationally compared to the processing speed of the module. The complete manufacture of a single module comprising 16 serially connected stripes with the same size as a credit card takes a total of 1.2–1.7 seconds in these experiments (limited only by the length of the driers). The switching of a single module was typically achieved in <2 seconds (not including automated measurements of whether the switching had taken place) which is comparable to the manufacturing speed. The switching pulse duration was optimized for each roll of solar cell modules (approx. 4900 modules for a typical run) and was typically 10 ms. This implies that the actual speed of switching could easily reach 50 ms (when switching 3 modules in parallel).

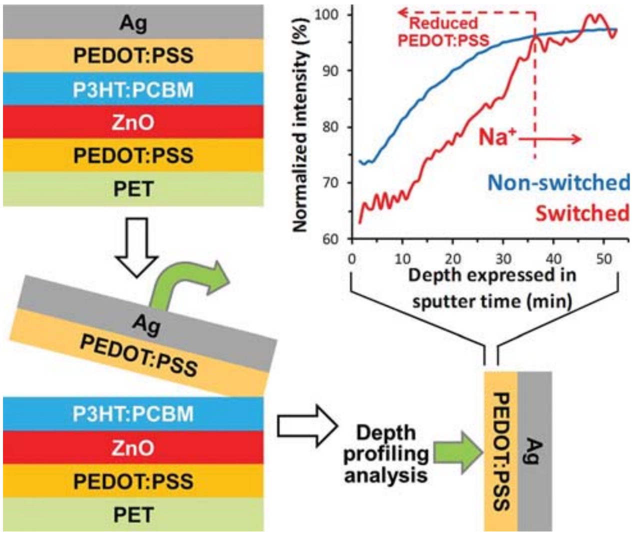

Fig. 3 Schematic OPV device illustrating where delamination occurs (confirmed from mass spectral data) that enables the exposed PEDOT:PSS surface to be analyzed. The resulting sodium ion depth profiles show a decreased content of sodium ions for the switched device in the PEDOT:PSS material facing the P3HT:PCBM–PEDOT:PSS interface.

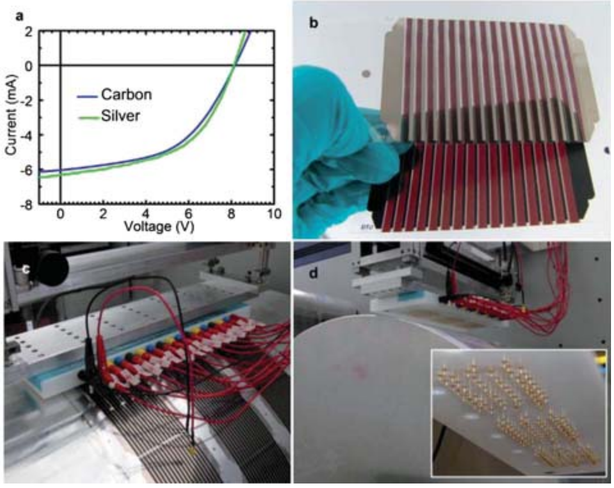

Fig. 4 (a) Current–voltage characteristics of small area modules having either a graphite or silver electrode, which are shown in the photo in (b). (c) Displays the switching setup in progress, switching 3 modules in parallel. (d) Photograph of a cooling drum and inset with close-up of gold pin array used for switching.

Table 1 Photovoltaic parameters

Device type	PCE (%)^a	J_{sc} (mA cm^{-2})	V_{oc} (V)	FF (%)
Carbon CC	1.6	−6.2^b	8.2	51
Silver CC	1.9	−6.5^c	8.1	52

^{a} Active area of the 16 striped device is 15.4 cm^{-2}. ^{b} Measured at 100 mW cm^{-2}. ^{c} Measured at 90 mW cm^{-2}.

In terms of applicability, we have tested this type of substrate extensively and found that it is robust in manufacture, and the switching is very consistent. It should be added that while automatic switching is a requirement for processing many modules, it is very easy to apply this principle on the laboratory scale (*i.e.* manual switching) and we easily foresee the use of this substrate in small research labs or even in a school classroom.

An operator can simply apply a short negative pulse by crossing two wires connected to the device. We have employed this method extensively, and it implies that the substrate described here works at all levels in terms of scale, from the student wishing to switch a small device to the professional that wish to switch multitudes of large modules in a fast and automated fashion.

Conclusions

We have described the underlying generic mechanism for this *in situ* formation of a charge selective interface through both chemical and physical analyses and believe that this new disruptive approach will radically change the field of polymer solar cells and finally eliminate the broad use of ITO in both research laboratories and industry. We also found that it was possible to replace silver electrodes by carbon and our modules thus represent a technology that is free from the three ingredients that hinder the wide dissemination of polymer solar cells, namely indium, silver and vacuum. The performance of the modules is qualitatively similar to ITO based devices with a cost reduction by a factor of >10 and an increase in processing speed by a factor of >10 under simple pilot scale conditions. In order to further the general alleviation of ITO this substrate material is made available freely by DTU to anyone with an academic interest†.

Notes and references

† Complete solar cell modules and front electrode samples comprising PET-PEDOT:PSS-ZnO are available freely for academic purposes. The authors declare no competing financial interests. Correspondence and requests for materials should be addressed to FCK.

1 L. Dou, J. You, J. Yang, C. Chen, Y. He, S. Murase, T. Moriarty, K. Emery, G. Li and Y. Yang, *Nat. Photonics*, 2012, **6**, 180–185.
2 M. Jørgensen, K. Norrman, S. A. Gevorgyan, T. Tromholt, B. Andreasen and F. C. Krebs, *Adv. Mater.*, 2012, **24**, 580–612.
3 N. Espinosa, M. Hösel, D. Angmo and F. C. Krebs, *Energy Environ. Sci.*, 2012, **5**, 5117.
4 R. Søndergaard, M. Hösel, D. Angmo, T. T. Larsen-Olsen and F. C. Krebs, *Mater. Today*, 2012, **15**, 36–49.
5 F. C. Krebs, S. A. Gevorgyan and J. Alstrup, *J. Mater. Chem.*, 2009, **19**, 5442.
6 F. C. Krebs, J. Fyenbo, D. M. Tanenbaum, S. A. Gevorgyan, R. Andriessen, B. van Remoortere, Y. Galagan and M. Jørgensen, *Energy Environ. Sci.*, 2011, **4**, 4116.
7 C. J. M. Emmott, A. Urbina and J. Nelson, *Sol. Energy Mater. Sol. Cells*, 2011, **97**, 14–21.
8 F. C. Krebs, *Org. Electron.*, 2009, **10**, 761–768.
9 S. K. Hau, H.-L. Yip, J. Zou and A. K.-Y. Jen, *Org. Electron.*, 2009, **10**, 1401–1407.
10 Y. Zhou, H. Cheun, S. Choi, W. J. Potscavage, C. Fuentes-Hernandez and B. Kippelen, *Appl. Phys. Lett.*, 2010, **97**, 153304.
11 Y. Zhou, C. Fuentes-Hernandez, J. Shim, J. Meyer, A. J. Giordano, H. Li, P. Winget, T. Papadopoulos, H. Cheun, J. Kim, M. Fenoll, A. Dindar, W. Haske, E. Najafabadi, T. M. Khan, H. Sojoudi, S. Barlow, S. Graham, J.-L. Brédas, S. R. Marder, A. Kahn and B. Kippelen, *Science*, 2012, **336**, 327–332.
12 R. Po, C. Carbonera, A. Bernardi, F. Tinti and N. Camaioni, *Sol. Energy Mater. Sol. Cells*, 2012, **100**, 97–114.
13 F. Verbakel, S. C. J. Meskers and R. A. J. Janssen, *Appl. Phys. Lett.*, 2006, **89**, 102103.
14 U. Özgür, Y. I. Alivov, C. Liu, A. Teke, M. A. Reshchikov, S. Doğan, V. Avrutin, S.-J. Cho and H. Morkoç, *J. Appl. Phys.*, 2005, **98**, 041301.
15 S. Möller, C. Perlov, W. Jackson, C. Taussig and S. R. Forrest, *Nature*, 2003, **426**, 166–169.
16 S. Möller, S. R. Forrest, C. Perlov, W. Jackson and C. Taussig, *J. Appl. Phys.*, 2003, **94**, 7811.
17 S. Smith and S. R. Forrest, *Appl. Phys. Lett.*, 2004, **84**, 5019.
18 B. C. de Brito, E. C. P. Smits, P. A. van Hal, T. C. T. Geuns, B. de Boer, C. J. M. Lasance, H. L. Gomes and D. M. de Leeuw, *Adv. Mater.*, 2008, **20**, 3750–3753.
19 J. Wang, F. Gao and N. C. Greenham, *Appl. Phys. Lett.*, 2010, **97**, 053301.
20 J. Wang, X. Cheng, M. Caironi, F. Gao, X. Yang and N. C. Greenham, *Org. Electron.*, 2011, **12**, 1271–1274.
21 A. Manor, E. A. Katz, T. Tromholt and F. C. Krebs, *Adv. Energy Mater.*, 2011, **1**, 836–843.
22 A. Manor, E. A. Katz, T. Tromholt and F. C. Krebs, *Sol. Energy Mater. Sol. Cells*, 2012, **98**, 491–493.
23 P.-J. Chia, L.-L. Chua, S. Sivaramakrishnan, J.-M. Zhuo, L.-H. Zhao, W.-S. Sim, Y.-C. Yeo and P. K.-H. Ho, *Adv. Mater.*, 2007, **19**, 4202–4207.
24 S. R. Dupont, M. Oliver, F. C. Krebs and R. H. Dauskardt, *Sol. Energy Mater. Sol. Cells*, 2012, **97**, 171–175.

View Article Online / Journal Homepage / Table of Contents for this issue
Nanoscale
Dynamic Article Links

Appendix 6

Cite this: *Nanoscale*, 2012, **4**, 6032
www.rsc.org/nanoscale

PAPER

Silver front electrode grids for ITO-free all printed polymer solar cells with embedded and raised topographies, prepared by thermal imprint, flexographic and inkjet roll-to-roll processes†

Jong-Su Yu,[a] Inyoung Kim,[a] Jung-Su Kim,[a] Jeongdai Jo,[a] Thue T. Larsen-Olsen,[b] Roar R. Søndergaard,[b] Markus Hösel,[b] Dechan Angmo,[b] Mikkel Jørgensen[b] and Frederik C. Krebs*[b]

Received 15th June 2012, Accepted 11th July 2012
DOI: 10.1039/c2nr31508d

Semitransparent front electrodes for polymer solar cells, that are printable and roll-to-roll processable under ambient conditions using different approaches, are explored in this report. The excellent smoothness of indium-tin-oxide (ITO) electrodes has traditionally been believed to be difficult to achieve using printed front grids, as surface topographies accumulate when processing subsequent layers, leading to shunts between the top and bottom printed metallic electrodes. Here we demonstrate how aqueous nanoparticle based silver inks can be employed as printed front electrodes using several different roll-to-roll techniques. We thus compare hexagonal silver grids prepared using either roll-to-roll inkjet or roll-to-roll flexographic printing. Both inkjet and flexo grids present a raised topography and were found to perform differently due to only the conductivity of the obtained silver grid. The raised topographies were compared with a roll-to-roll thermally imprinted grid that was filled with silver in a roll-to-roll process, thus presenting an embedded topography. The embedded grid and the flexo grid were found to perform equally well, with the flexographic technique currently presenting the fastest processing and the lowest silver use, whereas the embedded grid presents the maximally achievable optical transparency and conductivity. Polymer solar cells were prepared in the same step, using roll-to-roll slot-die coating of zinc oxide as the electron transport layer, poly-3-hexylthiophene:phenyl-C_{61}–butyric acid methyl ester (P3HT:PCBM) as the active layer and poly(3,4-ethylenedioxythiophene):poly(styrenesulfonate) (PEDOT:PSS) as the top electrode, along with a flat bed screen printed silver grid. The power conversion efficiency (PCE) obtained for large area devices (6 cm^2) was 1.84%, 0.79% and 1.72%, respectively, for thermally imprinted, inkjet and flexographic silver grids, tested outside under the real sun. Central to all three approaches was that they employed environmentally friendly solvents, *i.e.* water based nanoparticle silver inks.

1. Introduction

Advantages of polymer solar cells over other solar cell technologies have been listed in numerous cases and include properties such as low temperature processing, flexible substrates, fast preparation using printing and coating techniques, low cost and simple requirements for manufacture.[1] The performances have presented a steady growth with an increase by roughly half a percent in power conversion efficiency annually since the year 2000.[2] Now the technology reportedly presents power conversion efficiencies in excess of 10%,[3] with best performances agreed upon through inter-laboratory or round robin studies, involving many independent laboratories studying the same devices or the same set of devices, being somewhat lower (in the 1–5% range).[4–7] It is of significant interest that the record polymer solar cells are with a tiny active area prepared on rigid substrates under inert conditions, employing several vacuum coating steps and scarce elements such as indium in the semitransparent front electrode, making them far from being a realization of the potential advantages that polymer solar cells have to offer. Most notably the polymer solar cell has evolved around one single semitransparent conductor as the front electrode, namely indium-tin-oxide (ITO). There have been very few successful efforts replacing ITO without introducing new limitations that are worse than all those that ITO brings along.[7–17] ITO has a very negative impact on the energy payback time for organic photovoltaics (OPVs), and it is unlikely that competitive products can be made using ITO, as concluded in several life cycle analysis studies.[18–21]

---

[a] *Department of Printed Electronics, Korea Institute of Machinery & Materials (KIMM), 104 Sinseongno, Yuseong-Gu, Daejeon 305-343, Korea*
[b] *Department of Energy Conversion and Storage, Technical University of Denmark, Frederiksborgvej 399, DK-4000 Roskilde, Denmark. E-mail: frkr@dtu.dk*

† This work was supported by the bilateral Danish-Korean grant no.: B551179-08-03-00.

Whereas ITO-free devices have a potential to become competitive at much lower efficiencies,[22] ITO is most successfully prepared through a vacuum deposition process and there is a dawning consensus that any ITO replacement should be a printable or coatable formulation of a semitransparent conductor.[21,22] The only available material that currently fulfills this goal is the well known poly(3,4-ethylenedioxythiophene):poly(styrenesulfonate) (PEDOT:PSS), which is remarkably transparent and a good hole conductor that in many ways fits the purpose very well, except for its conductivity which is too low to enable a large area electrode with high optical transmission. The generally accepted solution to this challenge is to employ PEDOT:PSS in conjunction with a printed highly conducting metallic grid, presenting a small shadow loss of preferably less than 20%.[14,23–25] The grid–PEDOT:PSS composite electrode thus represents an efficient and fully printable alternative to ITO electrodes, and aside from the need for two different steps (printing the grid and coating the PEDOT:PSS), it does not present any disadvantages. It has however been subject to some discussion as to whether it is possible to prepare a sufficiently thin printed grid that does not result in shunts.[14,23–25]

This has identified two possible solutions that comprise either embedding the grid structure into the substrate or printing sufficiently thin grid structures on the order of 100 nm, which is comparable or similar in height to the intended thickness of the PEDOT:PSS layer. The disadvantage of the printed grid with a raised topography is that a thin grid needs a certain width to gain conductivity leading to a shadow loss.[25] The advantage is of course that it only requires one printing step. The embedded grid has the distinct advantages of potentially enabling very smooth substrate topography and a high aspect ratio of the embedded silver (low width compared to height) thus enabling very high conductivity at low shadow loss. Disadvantages are a lower maximum processing speed and it requires at least two distinct processing steps (thermal imprinting and filling with silver).

In this work we compare embedded silver grids prepared at the Korean Institute for Machinery & Materials (KIMM) with printed silver grids prepared at the Technical University of Denmark (DTU). It is demonstrated that the embedded and raised topography works equally well, in conjunction with highly conducting PEDOT:PSS, as a semitransparent ITO free front electrode, for polymer solar cells prepared at DTU, using only printing and coating techniques under ambient conditions (solar cell stack shown in Fig. 1). We highlight the strengths of each of the methods and also identify areas of research where improvements would have a high impact, this being especially within the development of conducting metallic inks with high metal loading.

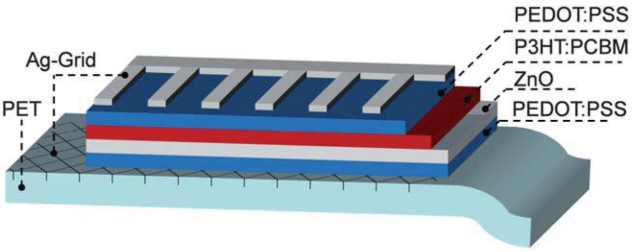

Fig. 1 A schematic illustration of the device architecture employed in this study. The only variation explored here is the nature of the front electrode grid which was either roll-to-roll inkjet printed, roll-to-roll flexographically printed or thermally imprinted and silver filled. The schematic shown here is for the embedded grid prepared by thermal imprinting and silver filling.

2. Experimental techniques

2.1 Materials and substrates

The silver inks were all aqueous based silver nanoparticle inks. For flexographic and thermal imprinting we employed PFI-722 (PChem Associates) and for inkjet printing we employed Suntronic U7089 (sun Chemical). The bottom PEDOT:PSS was PH1000 from Heraeus. The ZnO ink was a MEA (methoxyethoxy-acetic acid) stabilized nanoparticle suspension in acetone (56 mg ml^{-1}) with a particle size of 3–5 nm prepared at DTU. The active layer comprised a solution of poly-3-hexylthiophene (P3HT) (20 mg ml^{-1}, Sepiolid P200) and phenyl-C_{61}–butyric acid methyl ester (PCBM) (20 mg ml^{-1}, Solenne BV) dissolved in chlorobenzene and filtered through a 0.45 micron Teflon filter immediately prior to use. The top PEDOT:PSS was Agfa EL-P 5010 diluted with isopropanol (2 : 1 w/w). The top silver electrode ink was PV410 from Dupont. The adhesive for encapsulation of prototypes was UV-curing Delo LP655. The polyethyleneterephthalate (PET) substrate was Melinex ST506 from Dupont-Teijin with a thickness of 130 microns and a web width of 305 mm. The barrier substrate was an Amcor barrier with a thickness of 45 microns and a web width of 305 mm. The barrier had a WVTR (water vapor transmission rate) and an OTR (oxygen transmission rate) of respectively 0.04 g m^{-2} d^{-1} (38 °C, 90% RH), 0.01 cm^3 m^{-2} d^{-1} bar^{-1} (23 °C, 50% RH) as reported by Amcor. Contacts were made by application of Cu-tape (3M) to the silver electrodes before encapsulation followed by piercing metal contacts through the foil and Cu-tape once encapsulated. Devices were prepared with an edge seal having a rim of 1 cm.[26]

2.2 Embedded silver grid by roll-to-roll thermal imprinting and silver filling (at KIMM)

A nickel master grid having a raised topography was prepared by a photolithographic process. The grid lines had a nominal width of 15 microns and a height of 10 microns. The master was mounted on a heated steel imprinting roller giving a repeat length of 34 cm. The roller carrying the master was heated to 110 °C and the PET foil passed through the imprinting roller and the heated steel backing roller. The force applied was 100 kgf and the temperature of the rollers was 110 °C. The web speed was 0.96 m min^{-1}. After thermal imprinting, the pattern was inspected (shown in Fig. 2D) and then filled with the silver nanoparticle ink at a web speed of 0.96 m min^{-1}, by use of a squeegee, forcing the ink into the imprint. The silver filled film was then dried at 140 °C for 3 min. The pattern comprised 14 stripes with a length of 250 mm and width of 13 mm. These stripes were patterned with the diagonal print. The 14 lines were spaced by 2 mm. The repeat length was 340 mm. Please refer to Table 1 for further details.

2.3 Raised silver grid by roll-to-roll inkjet printing (at DTU)

A roll-to-roll inkjet printer with a maximum web width of 330 mm was employed comprising an unwinder, an edge guide, a double sided cleaner (Teknek), a corona treater (Vetaphone), an

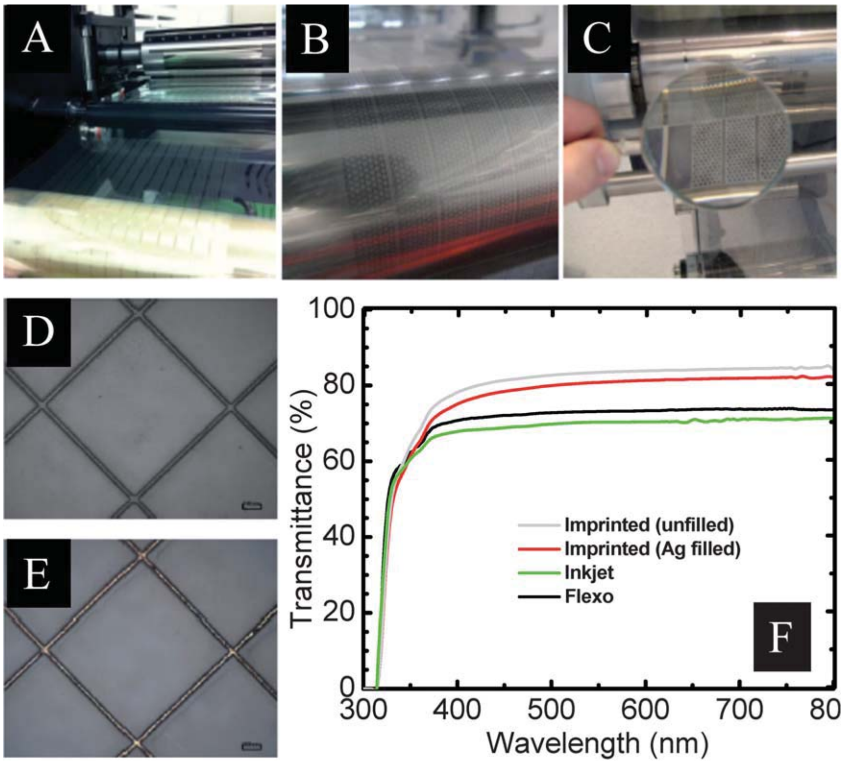

Fig. 2 (A) Thermal imprinting of PET using a nickel master roll. (B) Flexographically printed grid shown as the wet film with the red glow from the infrared drier. (C) The inkjet printed grid shown after hot air drying. (D) The thermally imprinted grid prior to silver filling. (E) The silver filled grid. In (D and E) the scale bar in the lower right hand corner is 100 μm. (F) Optical transmission of the PET films with the grid structures in place. The transmittance is not corrected for reflection losses and represents the optical transmission through the grid.

antistatic system, an inkjet printer, a hot-air oven (2 m oven length) operated at 140 °C, a nip and a rewinder. The inkjet printer is based on Kyocera inkjet printing heads and has a resolution of 600 DPI at right angles to the web direction and 1200 DPI in the direction of the web. The system has three heads and is capable of printing in the full width at speeds up to 75 m min^{-1}. In these experiments a web speed of 2 m min^{-1} was employed to ensure proper drying of aqueous ink and to reach a significant conductivity of the grid. A mild corona treatment of 300 W was employed at a web speed of 2 m min^{-1} which enabled good wetting of the PET substrate without excessive spreading of the ink droplets. The ink droplets were 14 pL and each grid line was nominally 2 dots wide. The pulseform for the droplet formation comprised 4 bursts and was terminated with a negative pulse sequence to reduce satellite droplet formation. Fig. 2C shows the inkjet printed grid after drying before the rewinder. A hexagonal pattern was chosen having a repeat of 2 mm and a nominal grid line width of 85 microns. Ink spreading led to an effective line width of $\sim$132 microns and a height of $\sim$300 nm, as shown in Fig. 4. The pattern comprised 16 stripes with a length of 303 mm and width of 13 mm. These stripes were patterned with the hexagonal print. The 16 lines were spaced by 2 mm. The repeat length was 305 mm. Please refer to Table 1 for further details.

2.4 Raised silver grid by roll-to-roll flexographic printing (at DTU)

A roll-to-roll flexographic printer comprising an unwinder, an edge guide, a double sided cleaner (Teknek), a corona treater (Vetaphone), a 4-roller flexographic printer, a drying system, a nip and a rewinder was employed. The drying system comprised 2 × 1.5 kW infrared dryers and 2 × 2 m ovens operated at 140 °C. The pattern was printed using a web speed of 25 m min^{-1}, an anilox roller with a nominal ink volume of 1.5 cm^3 m^{-2} and a laser engraved rubber printing roller with a hardness of 65 Shore. Full corona treatment (1500 W) was employed during printing that started at around 5 m min^{-1} with a minimum practical printing speed of 8 m min^{-1}. The pattern had reached full conductivity immediately after printing with little gain in conductivity upon further heating or sintering. The wet ink just before the first IR dryer is shown in Fig. 2B. A hexagonal pattern was chosen having a repeat of 2 mm and a nominal grid line width of 100 microns. Ink spreading led to an effective line width of $\sim$133 microns as shown in Fig. 4. The printed height was typically around 150 nm but due to viscous fingering (Saffman–Taylor instabilities[27,28]) the maximum observed thickness was up to 700 nm (see confocal micrograph in Fig. 4). The general observation was that the faster the printing, the lower the height of the viscous fingering. The pattern comprised 16 stripes with a length of 303 mm and a width of 13 mm. These stripes were printed with the hexagonal pattern. The 16 lines were spaced by 2 mm. The repeat length was 305 mm. Please refer to Table 1 for further details.

2.5 Roll-to-roll processing of the solar cell stack and encapsulation (at DTU)

The foils with inkjet printed, flexographically printed and thermally imprinted silver grids were spliced into one roll with a

Table 1 A comparison between conducting electrodes based on thermally imprinted and silver filled, inkjet printed, and flexographically printed grids using parameters covering cost, ease of processing and physical parameters. Confocal microscopy images are shown at the top of each table column for the corresponding grid structure (width-by-length of 280 μm × 230 μm)

	 Thermally imprinted	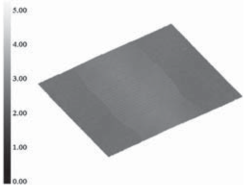 Inkjet printed	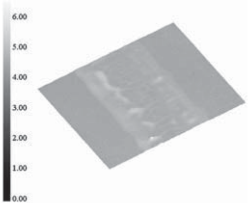 Flexo printed
Speed (m min^{-1})	0.48[a]	2	25
Maximum possible speed (m min^{-1})	6[a]	75	200
Number of steps	2	1	1
Ink type	Nanoparticles	Nanoparticles	Nanoparticles
Water as solvent	Yes	Yes	Yes
Cost of master	Medium	Free (digital)	Low
Optical transmission of substrate–grid[b]	82%	71%	73%
Resolution (micron)[c]	16 (8)	100 (42)	100 (32)
Printed height (nm)	0 ± 25	+200 ± 100	+200 ± 150[d]
Spikes (nm)	20	50	1000
Technical yield	High	High	High
Conductivity (Ω per square)	10	60	11

[a] The thermally imprinted grid is prepared in two consecutive steps. Firstly, the pattern is imprinted and secondly, it is filled with silver. The speed was 0.96 m min^{-1} in both steps. The maximum achievable speed is 12 m min^{-1} if carried out in an inline process. If the imprinting and silver filling is carried out in two discrete steps the maximum achievable speed is 6 m min^{-1}. [b] The optical transmission includes reflection losses and substrate absorption. [c] The value in brackets is the highest current resolution achievable, understood as the minimal width of a discretely printed line. [d] The flexoprinted grid lines presented spikes with a height of up to 400 microns.

length of 150 m. All subsequent processing was carried out on the same roll in the same processing step in order to keep variation as low as possible, limited to only the temporal difference between processing at the start and finish of the roll (see Section 2.1 for details on materials). PEDOT:PSS PH1000 was rotary screen printed on top of the grid structure with a printing speed of 10 m min^{-1} and dried using a 1.5 kW IR heater and a 2 meter oven at 140 °C. The remainder of the processing followed the well known ProcessOne[29] and comprised slot-die coating of a ZnO nanoparticle suspension in acetone with a web speed of 5 m min^{-1} and a wet thickness of 9.6 microns yielding a nominal dry thickness of ~96 nm of the ZnO layer. Drying took place through two ovens. The first oven (2 m long) was set to a temperature of 70 °C, and the second oven (2 m) was set to a temperature of 140 °C. The active layer was slot-die coated at a web speed of 2 m min^{-1} through a first oven (2 m) set to 90 °C and a second oven (2 m) set to 140 °C. The PEDOT:PSS EL-P 5010 was slot-die coated at a web speed of 0.6 m min^{-1} through a first oven (2 m) set to 120 °C and a 1.5 kW IR heater followed by a second oven (2 m) set to 140 °C. Finally the silver back electrode that comprised a bus bar and linear grid lines (comb structure) with a thickness of 0.2 mm and a repeat of 1 mm was screen printed at a web speed of 1 m min^{-1} and an oven temperature of 140 °C (oven length 1.2 m). Various electrode patterns were employed, and the most successful one was similar to a previously reported cell back electrode, except that it had a larger active area of 6 cm^2.[30] Devices were then placed on a large piece of barrier foil with some UV-curing adhesive, and Cu-tape was applied to each of the electrode bus bars. A little adhesive was then placed on the top followed by another large layer of barrier film. The unsealed laminate was passed through a laminator using a pressure of 150 kg over the width of the foil, thus forcing the adhesive to flow over the device on both sides, without bubbles. The adhesive was subsequently cured for 2 minutes under a solar simulator (1000 W m^{-2}, 85 °C), starting with the printed side (this is important). The final device was then contacted by piercing metal contacts through the barrier and the copper foil.

2.6 Characterisation of grids, films and devices using optical microscopy, FESEM, *I–V* curves solar simulation, real sunlight and LBIC

The grids were initially characterized for quality by optical microscopy using a microscope from Lab Engineering Instruments, India. The metal grids were then subjected to scanning electron microscopy in the regions of the metal ink to highlight the nanoparticle nature of the ink, and establish the size and the degree of fusion between the nanoparticles (Fig. 3), using a field emission scanning electron microscope (FE-SEM, FEI Nova NanoSEM 600). The nanoparticle sizes after filling/printing and curing were respectively for thermally imprinted grids and inkjet printed grids: 216 ± 37 nm, 45 ± 9 nm, as determined from SEM analysis. It was difficult to establish a size and average for flexo printed silver as the particles have fused to a large degree, as is readily seen in Fig. 3, but we estimate that the particles are in the 25–50 nm range. The solar cells were characterized using custom made software for the Keithley 2400 series source meters. All *I–V* characterization was carried out using full size devices with an

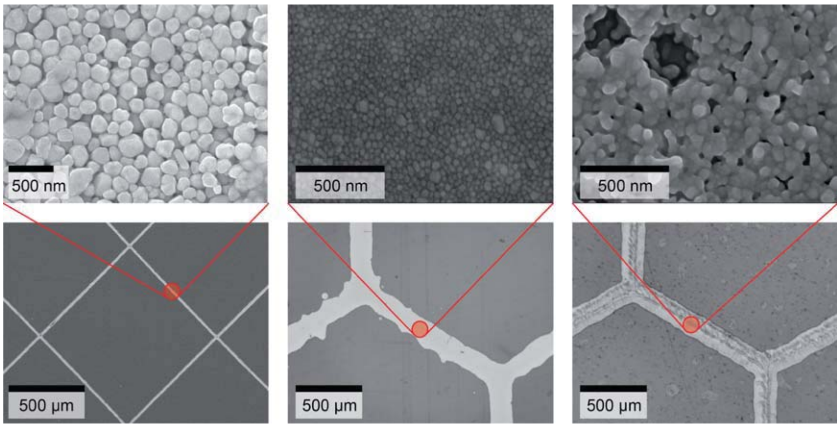

Fig. 3 SEM images of the nanoparticles for the three different silver electrodes (top) with corresponding optical images below. The grids prepared by thermal imprinting and silver filling are shown with a low degree of magnification due to larger particle sizes (left). The inkjet printed (middle) and flexographically printed grids (right) are shown with the same magnification.

active area of approx. 6 cm^2. In each case the active area was established carefully using light beam induced current (LBIC, Fig. 5).[31] Solar simulation employed a metal–halide lamp that approaches AM1.5G quite well and all measurements were performed at 1000 W m^{-2}, 85 °C. To establish a good accuracy of our reported efficiency, reference devices were also characterized under the real sun on 23rd of May 2012 starting at 12:00 (GMT + 1). The geographic position of the measurements were at DTU in Roskilde, with latitude/longitude 55°69′N/12°10′E with the solar cells mounted on a solar tracker thus having the sun at normal incidence. The incident sunlight was measured using an AM1.5G and an AM1.5D bolometer from Eppley Laboratories. The former was employed to establish the total incident intensity from the half space surrounding the solar cell and the latter to establish the degree of haze in the atmosphere. The day of the measurement presented a clear blue sky with some haze. The incident intensity was around 900 W m^{-2}, and the outside temperature was 22 °C. The temperature of the solar cells was 35 °C during the measurements. The exact intensity was recorded just before and just after the recording of each *I–V* curve. LBIC images were recorded using a custom made setup using a semiconductor laser with an optical output of 10 mW and a wavelength of 406 nm. The spot size was around 50 microns and the practical resolution due to scattering in the barrier film, adhesive and substrate layers was 100 microns.

3. Results and discussion

3.1 Water based silver inks as an ITO alternative

Critical to the fulfillment of the acclaimed environmental friendliness of polymer solar cells is the use of environmentally friendly processing steps. The solvents commonly employed when processing polymer solar cells on a laboratory or pilot scale[32] are most often chlorinated aromatic solvents. Only PEDOT:PSS and the commonly employed ZnO layer have been developed for aqueous processing. A few reports have demonstrated aqueous processing of all the layers including the metal back electrode[33] and the active layer using emulsions.[34] In this study only water based nanoparticle silver inks were employed which from this point of view fully address objectives of environmentally friendly processing in the desired manner with no drawbacks, while the choice of method would depend on other parameters for selection which might be specific to a particular application. Some parameters that allow for comparison between the methods are highlighted in Table 1.

It should be stressed that in addition to the environmental friendliness being a necessity for large scale production of OPV as a technology, the environment for the operator that manufactures the OPV is significantly improved, and in terms of health and safety water as a solvent does present the pinnacle of ink technology at all levels.

3.2 The roll-to-roll processing methods

To date almost all polymer solar cells reported in the literature have been prepared using the combination of two techniques, spin coating and metal evaporation. It should be stressed that neither of these techniques are expected to share a future with widely disseminated polymer solar cells, where only processes that rely on flexible substrates and the absence of vacuum steps are expected. To fully exploit the potential of the polymer solar cell, high speed and low temperature processing using printing and coating techniques should be pursued, and the process development based on spin coating and metal evaporation can, in general, not be expected to be directly transferable. Additional points are that a myriad of different printing and coating techniques exist, and it is almost certain that each technique presents its own optimization challenges. Furthermore, it is likely that one or a few of the techniques will be better suited for each layer in a given polymer solar cell. It is thus naïve to believe that a particular material combination and layer stack, chosen based on spin coating and metal evaporation, can be transferred to a roll-to-roll coating setting.[1] It is of significant importance to develop the device structure from the bottom, using the intended techniques, in an as similar setting as possible. So far, the most successful roll-to-roll based techniques employed for the processing of OPV are slot-die coating and flat bed screen printing. Few other techniques have been employed in a full roll-to-roll setting while techniques such as inkjet,[23–25,35–37] gravure,[38] flexo[1,39] and spray coating[40–44] have been reported for batch processed samples. It can be assumed that these techniques can be scaled to

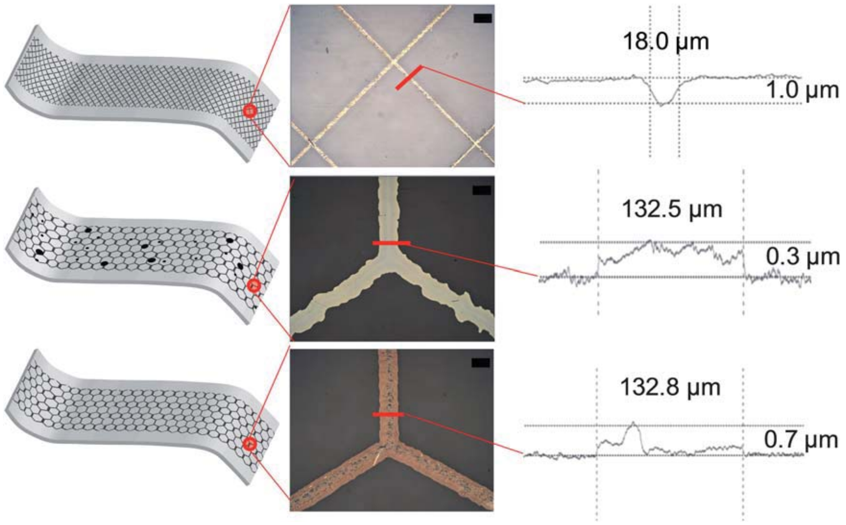

Fig. 4 Schematic illustrations of the different grid structures (~5 cm × 1 cm) along with optical confocal micrographs (scale bar is 100 µm) and traces across the grid lines showing the typical width and height (from confocal micrograph). The thermally imprinted grid with Ag filling (top). Inkjet is shown (middle) with an illustration of the occasional presence of misfired ink droplets and the irregular structure of the grid lines, as compared to the more regular flexographically printed grids (bottom).

full roll-to-roll processing with a relatively small effort, while some may be better suited than others. In this work we focused on the ITO free front electrode and demonstrate that three different techniques can be employed successfully.

3.3 Raised *versus* embedded grid topographies

A clear objective for any electrode structure for OPV, which is inherently a thin film multilayer technology, is that it is smooth and planar. This is especially critical since film roughness for thin film structures accumulates when processing subsequent layers, and it is practically impossible to erase a rough structure with a subsequent layer when the roughness is larger than the film thickness, especially when the solid content in the covered ink is low. An additional problem is that the function of the OPV relies on completely covered layers. If the first layer already presents a roughness that far exceeds the capacity of subsequently processed layers to cover it then it will not be possible to prepare functional polymer solar cells. Since the first processed layer in this case is the highly conducting silver electrode this would lead to shunted solar cells in cases where the silver transcends several of the layers. Here the nanoparticle based inks do seem to present some advantages as they give a certain roundness to protrusions in the printed grids. This seems to enable coverage of the structures even if the roughness is larger than the layer by a factor of 1–5. In this case the choice of printing method for the first PEDOT:PSS layer and the particular ink type seems to be especially important. Rotary screen printing is in many ways similar to flat bed screen printing but does differ in the much higher shear rates that are involved. Compared to spin coating, which has been viewed as an insufficient method to cover raised grid structures, rotary screen printing does present a difference here too, since the direction of shear is normal to the surface (and the roughness). This is in stark contrast to spin coating where the direction of shear is parallel to the surface. It is thus likely that rotary screen printing has a better capacity to print evenly around protrusions, enabling better coverage of rough structures. Common to all three grid types explored here is that they worked equally well, in the sense that all devices that were tested functioned, presenting no significant shunting (please see the next section for more details). In terms of transmittance (Fig. 2F) the thermally imprinted grid does have an edge over the other candidates, with the inkjet suffering the most due to irregularities in the grid structure (middle part of Fig. 4).

3.4 LBIC, *I–V* curves and performance

The devices were encapsulated and then tested using a solar simulator, while the best devices were also tested outside under the real sun on a clear day (see Fig. 6 and Table 2). A notable similarity between simulated and real sun measurements in terms of efficiency and photovoltaic parameters was generally observed. The small differences are ascribed to: the more direct light from the sun as compared to more diffuse light from the solar simulator; the slightly lower intensity of the real sun (specific to the day of measurement); and also a lower temperature for real sun measurement (see Section 2.6). Outdoor studies of polymer solar cells have been few,[4,5,45–47] but generally the field of polymer and organic solar cells would benefit greatly if this became customary. Even if sunlight in many regions of the world is not available every day, the sun does shine at regular intervals, and by recording the geographical location, the date and the time of measurement, it becomes much more consistent and easy to check against weather databases. We feel that such experiments should be encouraged.

Devices based on embedded grids and flexographically printed grids presented high fill factors between 51 and 56%, which is quite high considering that this is a large area device. The devices based on inkjet printed grids presented somewhat lower fill factors, which can be rationalized by the significantly higher resistivity of the inkjet printed grids (Table 1). In reverse bias, all device types performed similarly, presenting high shunt resistivity.

Table 2 *I–V* data comparison for the three device types, measured both under simulated light (lab) and under direct sunlight (outdoor)

	Imprint		Inkjet		Flexo	
	Lab[a]	Outdoor[b]	Lab[a]	Outdoor[c]	Lab[a]	Outdoor[d]
PCE (%)	1.92	1.84	0.75	0.79	1.82	1.72
J_{sc} (mA cm^{-2})	−7.06	−5.68	−4.27	−3.72	−7.02	−5.92
V_{oc} (V)	0.50	0.51	0.50	0.51	0.51	0.51
FF (%)	54.5	54.8	35.1	36.5	51.2	51.6

[a] AM1.5G, 1000 W m^{-2}. [b] 865 W m^{-2} (Global). [c] 876 W m^{-2} (Global). [d] 900 W m^{-2} (Global).

In terms of device manufacture and robustness of the solar cells, all types of printed grids performed equally well. The active areas of the devices were quite accurately established using LBIC measurements.[31] Even if the devices did not show any visual signs of defects it is clear that the active area was not as well defined along the edges as one would expect. Several non-active areas were also observed as shown in Fig. 5, where the yellow colour represents efficient light harvesting and conversion into an electrical current while a blue colour represents low or no light harvesting and conversion into an electrical current.

In the LBIC images (Fig. 5) the back electrode grid structure can be recognized as a slightly better performing area due to more efficient light harvesting. The front grid clearly shows up as nonactive areas due to the shadowing effect of the respective grids. In the case of the thermally imprinted grid, the resolution of the LBIC (∼100 microns) is too low to resolve the sub-resolution width of the grid lines but the structure is clearly visible. The performance of the devices is shown in Fig. 6 and Table 2 under both outdoor and indoor conditions. It is of interest to note that both the thermally imprinted and the flexographically printed grids exhibit a lower performance under outside conditions. We ascribe this to a larger shadow loss from the grid lines under a more direct light source (such as the sun). In the case of the inkjet grid based device, this effect is less pronounced, as it is likely countered by a non-linear light intensity dependence of the short circuit current due to the high series resistance in the device, which also gives the higher fill factor outdoor as compared to indoor.[48]

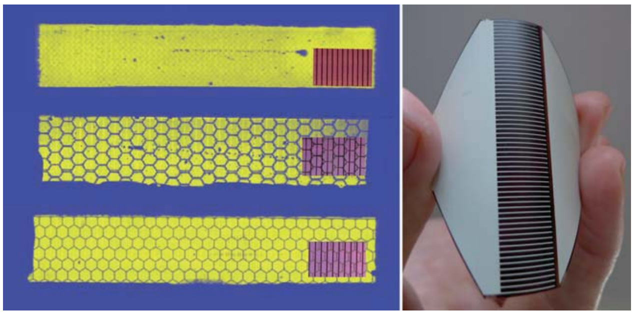

Fig. 5 LBIC images (left) of devices based on the thermally imprinted grid (top), inkjet (middle), and flexographic (bottom) respectively. The small insets show photos of the particular cell type with strong backlighting. (Right) Device seen from the back side, featuring the screen printed back electrode.

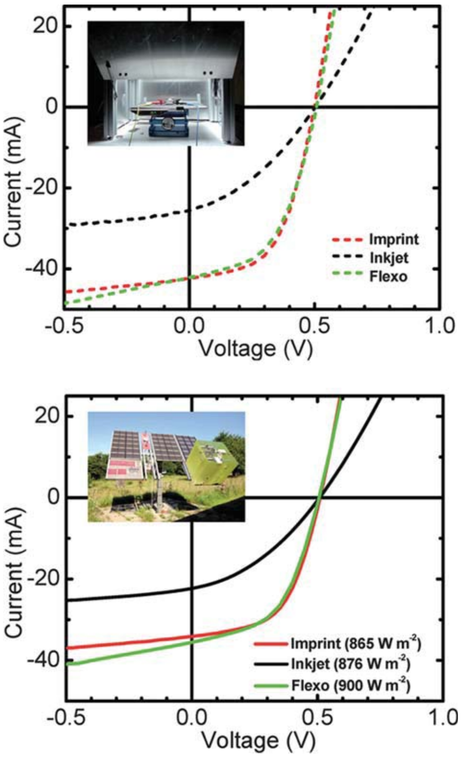

Fig. 6 *I–V* characteristics of the three types of devices, as measured in the lab (top) and under the real sun (bottom), where the number in parentheses indicates the incident light intensity.

3.5 Areas where further research would have an impact

Each of the grid structures presented here has its strengths and weaknesses. To identify the area where research could impact each of them the most we refer to Table 1 and also the results shown in Fig. 5 and 6. In terms of processing speed the flexographically printed grid is the most refined, as demonstrated by the significantly higher processing speeds achievable already in this laboratory experiment. Further refinement of this grid would be in achieving a higher resolution of the grid lines, which should be possible (30–50 microns should be within current technological capacity).

The embedded grid presents the highest fill factors and best performance in devices but suffers in processing speed. In this case, a significant gain could be reached if processing speed could be increased, while finer grids with perhaps line widths of 10 microns and repetitions of 500 microns would enable thinner front PEDOT:PSS layers to be used, leading to a higher optical transmission into the active layer.

The inkjet printed grid clearly suffers from poor conductivity and an effort here would bring about the fastest progress. For instance, roll-to-roll photonic sintering[49] could significantly improve the conductivity of the inkjet printed grid but would require an extra processing step. In terms of processing speed, the inkjet experiment here presented an intermediate speed. This is, however, not problematic to increase as the current system, employed in this experiment, can operate well in excess of 60 meters per minute, which represents the current research goal.[1] The curing time of the silver ink, however, significantly impacts the grid conductivity, and the speed chosen here was thus to fit the available oven length. Ink development would seem to be urgently needed to fully realize the advantages of the digital master and fast adaptability of the inkjet approach.

4. Conclusions

We successfully demonstrated that large area ITO free polymer solar cells can be prepared by only printing in the ambient atmosphere, with little compromise in performance compared to previously reported ITO-based devices with similar size and processing conditions. We found that the use of water based silver nanoparticle inks enable preparation of conductive grids for polymer solar cells. We demonstrate that embedded grids with a narrow line width extending deep into the substrate enable high conductivity electrodes with little shadow loss. The only limitation is in the processing speed, which overall is estimated to have an upper bound of around 6 m min^{-1} for a process comprising thermal imprinting, silver filling and drying (Table 1). For raised topographies we explored both inkjet and flexographic printing, where both methods provide inherently high speed processing, with inkjet currently having an upper limit of 75 m min^{-1}, and flexographic printing around 200 m min^{-1} and possibly higher. Limitations are that increased conductivity implies a large optical shadow loss. Flexographically printed grids and embedded grids were found to be qualitatively similar in this study, with flexographic printing providing the fastest processing of 25 m min^{-1} in this experiment, along with the lowest silver usage of around 200 mg per square metre of printed area. We conclude that the era of ITO is over, and that a new age can begin without reliance on indium and vacuum processes, since large area devices can be prepared with similar performance to ITO based devices.

Notes and references

1 R. Søndergaard, M. Hösel, D. Angmo, T. T. Larsen-Olsen and F. C. Krebs, *Mater. Today*, 2012, **15**, 36–49.
2 NREL PV Research efficiency overview, http://www.nrel.gov/ncpv/images/efficiency_chart.jpg, accessed June 2012.
3 Report from UCLA of 10.6 % efficiency, http://newsroom.ucla.edu/portal/ucla/ucla-engineers-create-tandem-polymer-228468.aspx, accessed June 2012.
4 F. C. Krebs, S. A. Gevorgyan, B. Gholamkhass, S. Holdcroft, C. Schlenker, M. E. Thompson, B. C. Thompson, D. Olson, D. S. Ginley, S. E. Shaheen, H. N. Alshareef, J. W. Murphy, W. J. Youngblood, N. C. Heston, J. R. Reynolds, S. Jia, D. Laird, S. M. Tuladhar, J. G. A. Dane, P. Atienzar, J. Nelson, J. M. Kroon, M. M. Wienk, R. A. J. Janssen, K. Tvingstedt, F. Zhang, M. Andersson, O. Inganäs, M. Lira-Cantu, R. de Bettignies, S. Guillerez, T. Aernouts, D. Cheyns, L. Lutsen, B. Zimmermann, U. Würfel, M. Niggemann, H. -F. Schleiermacher, P. Liska, M. Grätzel, P. Lianos, E. A. Katz, W. Lohwasser and B. Jannon, *Sol. Energy Mater. Sol. Cells*, 2009, **93**, 1968–1977.
5 S. A. Gevorgyan, A. J. Medford, E. Bundgaard, S. B. Sapkota, H.-F. Schleiermacher, B. Zimmermann, U. Würfel, A. Chafiq, M. Lira-Cantu, T. Swonke, M. Wagner, C. J. Brabec, O. Haillant, E. Voroshazi, T. Aernouts, R. Steim, J. A. Hauch, A. Elschner, M. Pannone, M. Xiao, A. Langzettel, D. Laird, M. T. Lloyd, T. Rath, E. Maier, G. Trimmel, M. Hermenau, T. Menke, K. Leo, R. Rösch, M. Seeland, H. Hoppe, T. J. Nagle, K. B. Burke, C. J. Fell, D. Vak, T. B. Singh, S. E. Watkins, Y. Galagan, A. Manor, E. A. Katz, T. Kim, K. Kim, P. M. Sommeling, W. J. H. Verhees, S. C. Veenstra, M. Riede, M. G. Christoforo, T. Currier, V. Shrotriya, G. Schwartz and F. C. Krebs, *Sol. Energy Mater. Sol. Cells*, 2011, **95**, 1398–1416.
6 D. M. Tanenbaum, M. Hermenau, E. Voroshazi, M. T. Lloyd, Y. Galagan, B. Zimmermann, M. Hösel, H. F. Dam, M. Jørgensen, S. A. Gevorgyan, S. Kudret, W. Maes, L. Lutsen, D. Vanderzande, U. Würfel, R. Andriessen, R. Rösch, H. Hoppe, G. Teran-Escobar, M. Lira-Cantu, A. Rivaton, G. Y. Uzunoğlu, D. Germack, B. Andreasen, M. V. Madsen, K. Norrman and F. C. Krebs, *RSC Adv.*, 2012, **2**, 882–893.
7 T. T. Larsen-Olsen, F. Machui, B. Lechene, S. Berny, D. Angmo, R. Søndergaard, N. Blouin, W. Mitchell, S. Tierney, T. Cull, P. Tiwana, F. Meyer, M. Carrasco-Orozco, A. Scheel, W. Lövenich, R. de Bettignies, C. J. Brabec and F. C. Krebs, *Adv. Energy Mater.*, 2012, **2**, http://dx.doi.org/10.1002/aenm.201200079.
8 F. C. Krebs, *Org. Electron.*, 2009, **10**, 761–768.
9 B. Zimmermann, H.-F. Schleiermacher, M. Niggemann and U. Würfel, *Sol. Energy Mater. Sol. Cells*, 2011, **95**, 1587–1589.
10 B. Zimmermann, M. Glatthaar, M. Niggemann, M. K. Riede, A. Hinsch and A. Gombert, *Sol. Energy Mater. Sol. Cells*, 2007, **91**, 374–378.
11 M. Manceau, D. Angmo, M. Jørgensen and F. C. Krebs, *Org. Electron.*, 2011, **12**, 566–574.
12 S. I. Na, B. K. Yu, S. S. Kim, D. Vak, T. S. Kim, J. S. Yeo and D. Y. Kim, *Sol. Energy Mater. Sol. Cells*, 2010, **94**, 1333–1337.
13 T. S. Kim, S. I. Na, S. H. Oh, R. Kang, B. K. Yu and J. S. Yeo, *Sol. Energy Mater. Sol. Cells*, 2012, **98**, 168–171.
14 Y. Galagan, B. Zimmermann, E. W. C. Coenen, M. Jørgensen, D. M. Tanenbaum, F. C. Krebs, H. Gorter, S. Sabik, L. H. Slooff, S. C. Veenstra, J. M. Kroon and R. Andriessen, *Adv. Energy Mater.*, 2012, **2**, 103–110.
15 K. Tvingstedt and O. Inganäs, *Adv. Mater.*, 2007, **19**, 2893–2897.
16 M.-G. Kang, M.-S. Kim, J. Kim and L. J. Guo, *Adv. Mater.*, 2008, **20**, 4408–4413.
17 R. Po, C. Carbonera, A. Bernardi, F. Tinti and N. Camaioni, *Sol. Energy Mater. Sol. Cells*, 2012, **100**, 97–114.
18 N. Espinosa, R. García-Valverde and F. C. Krebs, *Energy Environ. Sci.*, 2011, **4**, 1547.
19 N. Espinosa, R. García-Valverde, A. Urbina and F. C. Krebs, *Sol. Energy Mater. Sol. Cells*, 2010, **95**, 1293–1302.
20 N. Espinosa, R. García-Valverde, A. Urbina, F. Lenzmann, M. Manceau, D. Angmo and F. C. Krebs, *Sol. Energy Mater. Sol. Cells*, 2011, **97**, 3–13.
21 (*a*) C. J. M. Emmott, A. Urbina and J. Nelson, *Sol. Energy Mater. Sol. Cells*, 2011, **97**, 14–21; (*b*) B. Azzopardi, C. J. M. Emmott, A. Urbina, F. C. Krebs and J. Nelson, *Energy Environ. Sci.*, 2011, **4**, 3741–3753.
22 N. Espinosa, M. Hösel, D. Angmo and F. C. Krebs, *Energy Environ. Sci.*, 2012, **5**, 5117.
23 Y. Galagan, I. G. de Vries, A. P. Langen, R. Andriessen, W. J. H. Verhees, S. C. Veenstra and J. M. Kroon, *Chemical Engineering and Processing: Process Intensification*, 2011, **50**, 454–461.
24 Y. Galagan, J.-E. J. M. Rubingh, R. Andriessen, C.-C. Fan, P. W. M. Blom, S. C. Veenstra and J. M. Kroon, *Sol. Energy Mater. Sol. Cells*, 2011, **95**, 1339–1343.
25 Y. Galagan, E. W. C. Coenen, S. Sabik, H. H. Gorter, M. Barink, S. C. Veenstra, J. M. Kroon, R. Andriessen and P. W. M. Blom, *Sol. Energy Mater. Sol. Cells*, 2012, **104**, 32–38.
26 D. M. Tanenbaum, H. F. Dam, R. Rösch, M. Jørgensen, H. Hoppe and F. C. Krebs, *Sol. Energy Mater. Sol. Cells*, 2012, **97**, 157–163.
27 P. G. Saffman and G. Taylor, *Proc. R. Soc. London, Ser. A*, 1958, **245**, 312–329.
28 M. B. Amar and D. Bonn, *Phys. Nonlinear Phenom.*, 2005, **209**, 1–16.
29 F. C. Krebs, S. A. Gevorgyan and J. Alstrup, *J. Mater. Chem.*, 2009, **19**, 5442.
30 J. Alstrup, M. Jørgensen, A. J. Medford and F. C. Krebs, *ACS Appl. Mater. Interfaces*, 2010, **2**, 2819–2827.
31 F. C. Krebs, R. Søndergaard and M. Jørgensen, *Sol. Energy Mater. Sol. Cells*, 2011, **95**, 1–6.
32 F. C. Krebs, J. Fyenbo, D. M. Tanenbaum, S. A. Gevorgyan, R. Andriessen, B. van Remoortere, Y. Galagan and M. Jørgensen, *Energy Environ. Sci.*, 2011, **4**, 4116–4123.
33 R. Søndergaard, M. Helgesen, M. Jørgensen and F. C. Krebs, *Adv. Energy Mater.*, 2010, **1**, 68–71.
34 T. R. Andersen, T. T. Larsen-Olsen, B. Andreasen, A. P. L. Böttiger, J. E. Carlé, M. Helgesen, E. Bundgaard, K. Norrman, J. W. Andreasen, M. Jørgensen and F. C. Krebs, *ACS Nano*, 2011, **5**, 4188–4196.

35 A. Lange, M. Wegener, C. Boeffel, B. Fischer, A. Wedel and D. Neher, *Sol. Energy Mater. Sol. Cells*, 2010, **94**(10), 1816–1821.
36 C. N. Hoth, P. Schilinsky, S. A. Choulis and C. J. Brabec, *Nano Lett.*, 2008, **8**, 2806–2813.
37 T. Aernouts, T. Aleksandrov, C. Girotto, J. Genoe and J. Poortmans, *Appl. Phys. Lett.*, 2008, **92**(3), 033306.
38 A. Hübler, B. Trnovec, T. Zillger, M. Ali, N. Wetzold, M. Mingebach, A. Wagenpfahl, C. Deibel and V. Dyakonov, *Adv. Energy Mater.*, 2011, **1**(6), 1018–1012.
39 H. Yan, Z. Chen, Y. Zheng, C. Newman, J. R. Quinn, F. Dötz, M. Kastler and A. Facchetti, *Nature*, 2009, **457**, 679–686.
40 L.-M. Chen, Z. Hong, W. L. Kwan, C.-H. Lu, Y.-F. Lai, B. Lei, C.-P. Liu and Y. Yang, *ACS Nano*, 2010, **4**(8), 4744–4752.
41 C. Girotto, D. Moia, B. P. Rand and P. Heremans, *Adv. Funct. Mater.*, 2011, **21**, 64–72.
42 S.-Y. Park, Y.-J. Kang, S. Lee, D.-G. Kim, J.-K. Kim, J. H. Kim and J.-W. Kang, *Sol. Energy Mater. Sol. Cells*, 2011, **95**(3), 852.
43 G. Susanna, L. Salamandra, T. M. Brown, A. Di Carlo, F. Brunetti and A. Reale, *Sol. Energy Mater. Sol. Cells*, 2011, **95**(7), 1775.
44 J. E. Lewis, E. Lafalce, P. Toglia and X. Jiang, *Sol. Energy Mater. Sol. Cells*, 2011, **95**(10), 2816.
45 E. A. Katz, D. Faiman, S. M. Tuladhar, J. M. Kroon, M. M. Wienk, T. Fromherz, F. Padinger, C. J. Brabec and N. S. Sariciftci, *J. Appl. Phys.*, 2001, **90**, 5343.
46 E. A. Katz, S. A. Gevorgyan, M. S. Orynbayev and F. C. Krebs, *Eur. Phys. J.: Appl. Phys.*, 2007, **311**, 307–311.
47 R. R. Søndergaard, T. Makris, P. Lianos, A. Manor, E. A. Katz, W. Gong, S. M. Tuladhar, J. Nelson, R. Tuomi, P. Sommeling, S. C. Veenstra, A. Rivaton, A. Dupuis, G. Teran-Escobar, M. Lira-Cantu, S. B. Sapkota, B. Zimmermann, U. Würfel, A. Matzarakis and F. C. Krebs, *Sol. Energy Mater. Sol. Cells*, 2012, **99**, 292–300.
48 T. Tromholt, E. A. Katz, B. Hirsch, A. Vossier and F. C. Krebs, *Appl. Phys. Lett.*, 2010, **96**, 073501.
49 M. Hösel and F. C. Krebs, *J. Mater. Chem.*, 2012, **22**, 15683–15688.

Appendix 7

Organic Electronics 14 (2013) 984–994

Contents lists available at SciVerse ScienceDirect

Organic Electronics

journal homepage: www.elsevier.com/locate/orgel

Scalability and stability of very thin, roll-to-roll processed, large area, indium-tin-oxide free polymer solar cell modules

Dechan Angmo [a], Suren A. Gevorgyan [a], Thue. T. Larsen-Olsen [a], Roar R. Søndergaard [a], Markus Hösel [a], Mikkel Jørgensen [a], Ritu Gupta [b], Giridhar U. Kulkarni [b], Frederik C. Krebs [a,*]

[a] *Department of Energy Conversion and Storage, Technical University of Denmark, Frederiksborgvej 399, DK-4000 Roskilde, Denmark*

[b] *Chemistry and Physics of Materials Unit and DST Unit on Nanoscience, Jawaharlal Nehru Centre for Advanced Scientific Research, Jakkur P.O., Bangalore 560064, India*

ARTICLE INFO

Article history:
Received 3 September 2012
Received in revised form 17 December 2012
Accepted 21 December 2012
Available online 1 February 2013

Keywords:
ITO free
Roll-to-roll printing and coating
Flexible
Barrier
ICT
Thin foil

ABSTRACT

Polymer solar cell modules were prepared directly on thin flexible barrier polyethylene terephthalate foil. The performance of the modules was found to be scalable from a single cell with an area of 6 cm^2 to modules with a total area of up to 186 cm^2. The substrate thickness was also explored and the performance was found to be independent of thickness in the range of 20–130 µm. The thinner substrates were found to present some challenge regarding handling but were not limited in performance. Large area modules on a substrate thickness of 45 µm were finally prepared by full roll-to-roll processing employing P3HT:PCBM as the active material and were found to exhibit a total area efficiency of >1% (1000 W/m^{-2}; AM1.5G) with a typical active-area efficiency in the 1.5–1.6% for total module area of >110 cm^2 due to high fill factors in excess of 50%. The modules were also found to have an active-area efficiency of >1% under low light levels ($\sim$100 $W\,m^{-2}$). The modules were then subjected to extensive stability testing for a minimum of 1000 h employing several ISOS protocols. The modules presented higher than 80% of the initial performance (*T80*) in the dark (ISOS-D-1), in dark under elevated temperature of 65 °C (ISOS-D-2), under low light (ISOS-LL), under full sunlight (ISOS-L-2), and under outdoor testing (ISOS-O), which was conducted in two locations in India and Denmark. We estimate maximum *T80* for those tests to be 2800, 5000, 1300, 1000, and 3500 h respectively. The modules showed significant sensitivity to high humidity and had low values for *T80* for dark storage tests at 50 °C/85%RH (ISOS-D-3) and accelerated operation conditions with 0.7 sun/65 oC/50%RH (ISOS-L-3). We found the modules to be particularly suited for information and communications technology (ICT) and mobile applications where low humidity (<50%) and lower temperatures (<65 °C) can be anticipated and we estimate operational lifetimes in excess of 1 year.

1. Introduction

The possibility for application of polymer solar cells (PSCs) as a means for harvesting light and converting it into electricity has been subject to intense research with aims varying from bulk energy production to niche products and gadgets to academic studies. The vision of PSCs has however remained the same no matter what the purpose or intentions have been, and PSCs currently remain as the only photovoltaic technology that potentially presents flexible substrates, no abundance problems, no environmental concerns and full scalability through printing and coating technology.

The state-of-the-art of the laboratory PSCs is however still far removed from the vision of the widely disseminated low-cost solar cells as the concern for laboratory

---

[*] Corresponding author.
E-mail address: frkr@dtu.dk (F.C. Krebs).

1566-1199/$ - see front matter © 2013 Elsevier B.V. All rights reserved.
http://dx.doi.org/10.1016/j.orgel.2012.12.033

solar cells is focused on increasing the power conversion efficiency through materials design with little emphasis on operational stability and large-scale processing. It is for this reason that the few attempts at translating the record power conversion efficiencies of laboratory cells (now reaching 10% as claimed by Mitsubishi and others) to low-cost processing of PSCs through coating and printing remains largely futile. It is imperative for PSCs, if they are to be seen in real world applications, to demonstrate scalability of any new device concept, materials choices, and processing methods when brought forward while simultaneously maintaining the low cost objective of PSCs.

It has been repeatedly shown that the use of indium tin oxide (ITO) as a transparent conductor in PSCs is the major cost driving factor both from a material and processing perspective. ITO may account for as much as ~90% of the embedded energy in a PSC module [1]. Not only is indium expensive due to the scarcity, but the associated cost volatility due to its high demand from display industries is feared to create a bottleneck in the supply chain of indium in the future. Furthermore, the brittle nature of ITO limits the mechanical stability of flexible PSCs [2]. As a result, the future of low cost PSCs relies on a transparent conductor that is free of ITO and that preferably involves only solution processing under ambient conditions.

The operational stability of PSCs is yet another challenge that must be tackled in tandem with low-cost scalability and efficiency. Unlike inorganic solar cells, PSCs are far more sensitive to ambient conditions such as humidity, temperature, and radiation. Water, O_2, and UV radiation are the three well-known key factors that accelerate degradation of PSCs [3,4]. Apart from the choice of photoactive polymer and other materials and their processing, the choice of barrier material and encapsulation method is very critical for the stability of PSCs. An encapsulation with good barrier properties to water, oxygen and UV-light can significantly prolong the stability of PSCs.

In this paper, we comprehensively report ITO-free, large-area, polymer solar cell modules fabricated completely through an all-solution process using a combination of roll-to-roll (R2R) printing and coating methods. We further report on the operational stability of these modules under different simulated and real conditions following several ISOS protocols [5].

2. Materials and methods

2.1. General materials

The substrate was a packaging barrier foil of polyethylene terephthalate (PET) of thickness 45 μm purchased from Amcor and had web width of 305 mm. Ag for printing of Ag hexagonal grid was a commercial water-based silver ink PFI-722 purchased from PChem Associates and had 60 wt.% Ag content. Highly conductive poly(3,4-ethylenedioxythiophene) poly(styrenesulfonate) (PH1000) was purchased from Heraeus and used as received. A solution of ZnO nanoparticles in acetone with a concentration of 55 mg/ml was employed. Poly (3-hexylthiophene) was purchased as Sepiolid P200 from BASF and [C60] PCBM was purchased from Solenne BV (purity of 99%). The mixing ratio of P3HT:PCBM was 30 mg:30 mg per 1 ml of chlorobenzene. PEDOT:PSS (Orgacon EL-P 5010) was purchased from Agfa and was diluted with isopropanol in a 1:1 wt/wt ratio. Thermally curable Ag (PV410) was purchased from Dupont. Encapsulation was done by two methods. In the first method, the barrier material from Amcor (same as the one used for substrate as well) was used. It had a UV filter (cut-off at 390 nm) and a barrier performance of $0.01\ \mathrm{cm^3\ m^{-2}\ bar^{-1}\ day^{-1}}$ with respect to oxygen (measured according to ASTM D 3985-81) and $0.04\ \mathrm{g\ m^{-2}\ day^{-1}}$ with respect to water vapor (measured according to ASTM F 372-78). A UV curable adhesive from DELO® (DELO® – Katibobond LP 655) was used to laminate the modules between the barrier foils. For the second method, the barrier foil from Amcor pre-laminated with a pressure sensitive adhesive (467MPF) from 3M was used. The barrier foil with pre-laminated pressure sensitive adhesive had a thickness of 100 μm.

2.2. Roll-to-roll printing and coating

The processing of all layers were carried out using R2R printing and coating. Details on the equipment employed and module design could be found in Refs. [6,7]. Briefly, the final module comprised of varied number of cells, or stripes, separated by 2 mm gap. Each cell/stripe had an active-area width of 10 mm. Fig. 1 shows the schematics of a module comprising of three serially-interconnected cells. Shown also is a picture of a real module with seven interconnected cells. The length of the stripes were varied (6, 10.3, and 13.5 cm) to get modules with three different total areas of 38, 110, and 186 $\mathrm{cm^2}$ (including the area of the electrodes). In the following, the R2R processing of each layer is briefly described. The pictures of processing of each layer can be found in Fig. 2.

2.2.1. Flexographic printing of the Ag hexagonal grid (front electrode)

Flexographic printing was used for printing of Ag with a hexagonal grid structure on the barrier foil (Fig. 2a). The hexagonal pattern was printed to form several stripes (13 mm wide, 2 mm gap) with a repeat size of 10 mm along the print direction. With an anilox volume of $1.5\ \mathrm{ml\ m^{-2}}$ (0.97 BCM) and an elastomeric printing form (65 shore), the Ag grid was flexographic printed at a web speed of $10–25\ \mathrm{m\ min^{-1}}$ directly on the barrier foil and subsequently dried/annealed at 140 °C by passing through a hot-air oven of length 4 m. A bar code was inkjet printed on each module to enable identification of each motif for later analysis. Prior to printing, the barrier foil was corona treated (1.5 kW) to improve adhesion and print quality. The resulting hexagons had a nominal line width of 100 μm, a thickness of 200 nm, and the distance between two parallel sides in a hexagon of 2 mm.

2.2.2. Slot-die coating of highly conductive PEDOT:PSS, ZnO, P3HT:PCBM, and PEDOT:PSS

Highly conductive PEDOT:PSS (PH1000) was slot-die coated at a web speed of $10\ \mathrm{m\ min^{-1}}$ and dried using two

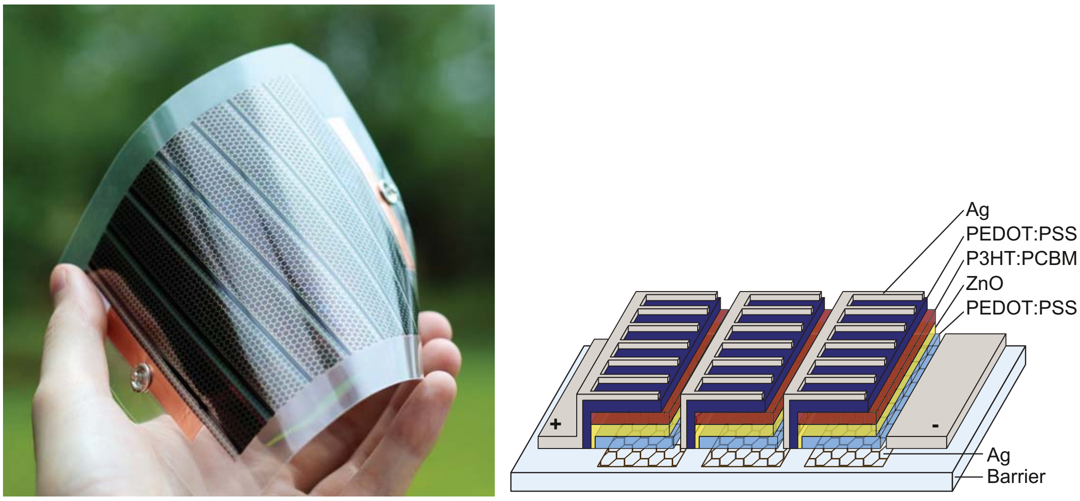

Fig. 1. An encapsulated ITO-free module (total area: 110 cm^2) processed on a 45 μm thick barrier substrate and comprising of seven interconnected cells (left); and schematics of a representative module with three interconnected cells. The number and length of cells were varied depending on the required module area.

infrared heaters (2 × 1.5 kW) and a 2 m hot-air drying oven at a temperature of 140 °C (Fig. 2b).

ZnO nanoparticle solution and P3HT:PCBM solutions were slot die coated at 5 m min^{-1} each (Fig. 2b–d). Every coating step was followed by drying by passing the web through the hot air oven of length 4 m set at 140 °C. The top PEDOT:PSS (EL-P 5010) was slot die coated at 1 m min^{-1} and dried by passage through firstly a 2 m hot air drying oven at a temperature of 140 °C then by passage under infrared heaters (2 × 1.5 kW) and finally a 2 m hot air drying oven at a temperature of 140 °C.

2.2.3. Screen printing of Ag paste (back electrode)

The silver back electrode was flat bed screen printed as a comb grid structure with a repeat of 1 mm and a line width of 200 μm (Fig. 2e–f). The silver grid electrodes also presented a bus-bar and serial interconnection between cells. The printing was carried out at a web speed of 1 m min^{-1}. Drying was carried out immediately after printing by passing the web through a hot air oven with temperature set at 140 °C and an oven length of 1.2 m. The web-speed is limited by the length of the oven.

2.3. Module encapsulation

Two different encapsulation techniques were evaluated. In the first method, the modules were manually encapsulated between two sheets of Amcor barrier foil using a UV curable adhesive from DELO®. The modules were then passed under nip pressure in a R2R machine with <1 m min^{-1} to achieve homogeneous distribution of the adhesive over and under the module and to eliminate any air bubbles. Finally, the device with the adhesive was placed under a solar simulator for 5 min to cure the adhesive from the UV present in the light. After UV curing, the final thickness of the encapsulated module was 200 μm. Note that the adhesive does not bear barrier properties at the same level as the barrier foil and hence it should be as thin as possible. In the second method, modules were laminated between the barrier foils pre-lined with pressure sensitive adhesive (PSA). The final thickness of the module using this encapsulation method was 320 μm. The results from the two lamination methods are discussed under Section 3.

2.4. Module testing

Full characterization of the modules was performed at CLOP (Characterization Laboratory for Organic Photovoltaics at Department of Energy Conversion and Storage, DTU, Roskilde, Denmark) including accurate *IV* testing under calibrated light sources and the real sun, which was followed by various ISOS stability tests [5].

2.4.1. IV characterization

The modules were *IV* characterized under calibrated light sources prior to subjecting to stability tests. A sulfur plasma lamp with *A* class spectrum in the absorption range of the active material was used for accurate *IV* characterization and a metal halide lamp with *B* class spectrum was used for stability tests (ISOS-L-2). Both simulators were calibrated to 1 sun using calibrated reference photodiode (taking into account the mismatch factor for each lamp). For calculation of the mismatch, an IPCE measurement of the samples was performed under bias light. Due to the sensitivity of the ZnO conductivity to the UV quantity of irradiation, the samples delivered lower IPCE values, since the bias light in the IPCE system was not rich in the UV region. The generally low IPCE was believed not to affect the mismatch factor however, as relative spectral values were used for calculations. When testing the modules under two different simulators, it was revealed that the modules delivered about 10% higher photocurrent under the metal halide lamp, which was ascribed to the richer UV content in the spectrum of the halide lamp. The measurement under real sun delivered a photocurrent close to the average of measurements under both simulators

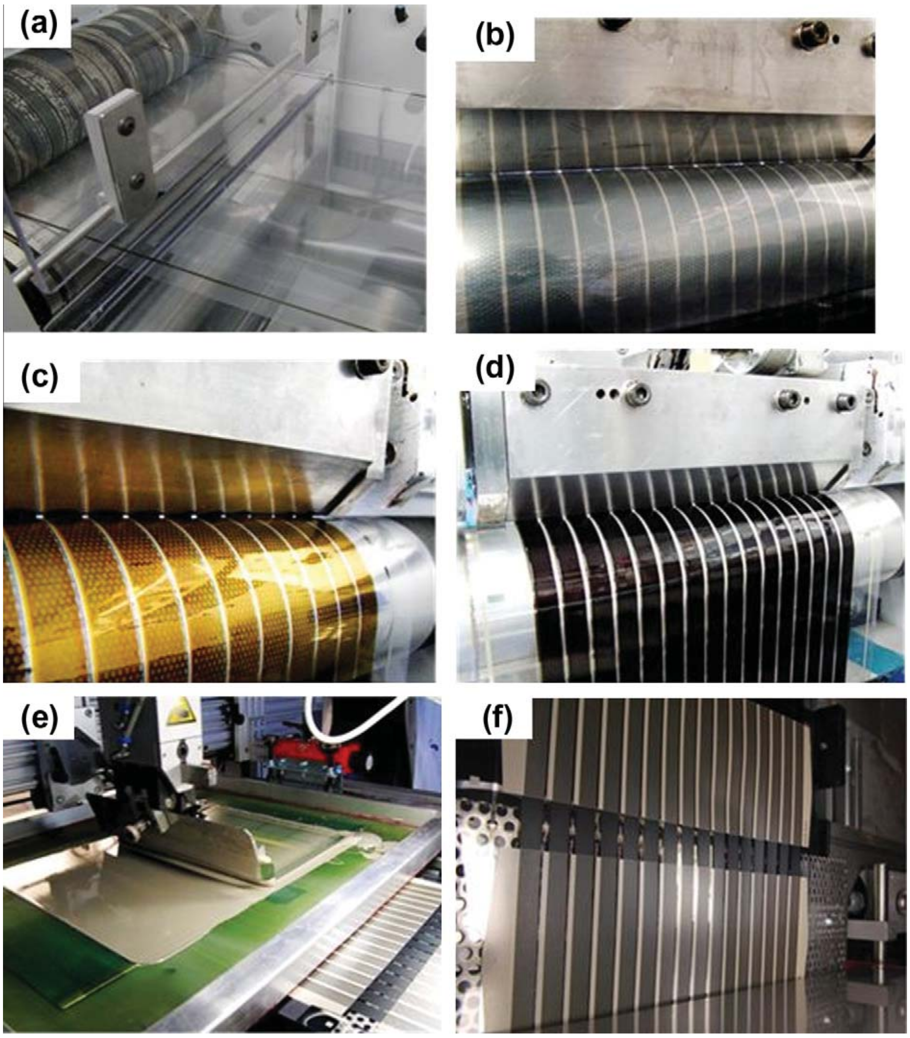

Fig. 2. Photographs of the stepwise R2R printing and coating processes in fabrication of the modules: (a) flexography printing of Ag grid; (b–d) slot die coating of hcPEDOT:PSS, P3HT:PCBM, and PEDOT:PSS respectively; (e) flat-bed screen printing of Ag paste; and (f) final module after step (e).

(bearing in mind however that outdoor measurement was performed at lower temperatures of 15 °C).

2.4.2. Lifetime and stability testing

The modules were subjected to lifetime testing according to the ISOS protocols [5]. A number of tests were performed including dark ISOS-D-1, 2 and 3; outdoor ISOS-O-2; and indoor ISOS-L-2, ISOS-L-3, ISOS-TC-3, and ISOS-LL tests. Table 2 in Section 3 gives an overview of the parameters involved in these tests as well as the minor deviations from the ISOS protocols. The modules were either placed under continuous exposure to light and continuously measured with an automated system (ISOS-L-2/-LL/-O) or periodically removed from their test systems and measured under calibrated sun simulator by recording three IV curves and taking the average values (ISOS-D-1/-D-2/-D-3/-L-3/-TC-3). Moduiles were stored in a drawer for ISOS-D-1 test. High temperature tests (ISOS-D-2) were performed in an oven, while a climate-control chamber (Q-SUN Xenon Test Chamber from Q-LAB) was used for the damp heat tests (ISOS-D-2/-D-3/-L-3). A thermal cycling chamber (Thermotron) was used to perform ISOS-TC-3. The modules were removed daily or weekly and characterized for photovoltaic performance under a solar simulator each time. For outdoor tests in Denmark, the modules were placed on a solar tracker and connected to an automated system for continuous monitoring (every 10 min). In India, modules were fixed on a roof-top at 5° inclination facing south and were measured intermittently. To perform ISOS-L-2 the modules were placed under a metal halide lamp based solar simulator (*B* class spectrum) with intensity close to 1 sun and continuously monitored. Additionally, modules were placed under fluorescent light with intensities close to 0.2 sun for ISOS-LL tests. Fig. 3 shows pictures of some of the instrumentation involved in the stability tests.

3. Results and discussion

Mobile and ICT applications are believed to be an area where polymer solar cells will find some application due

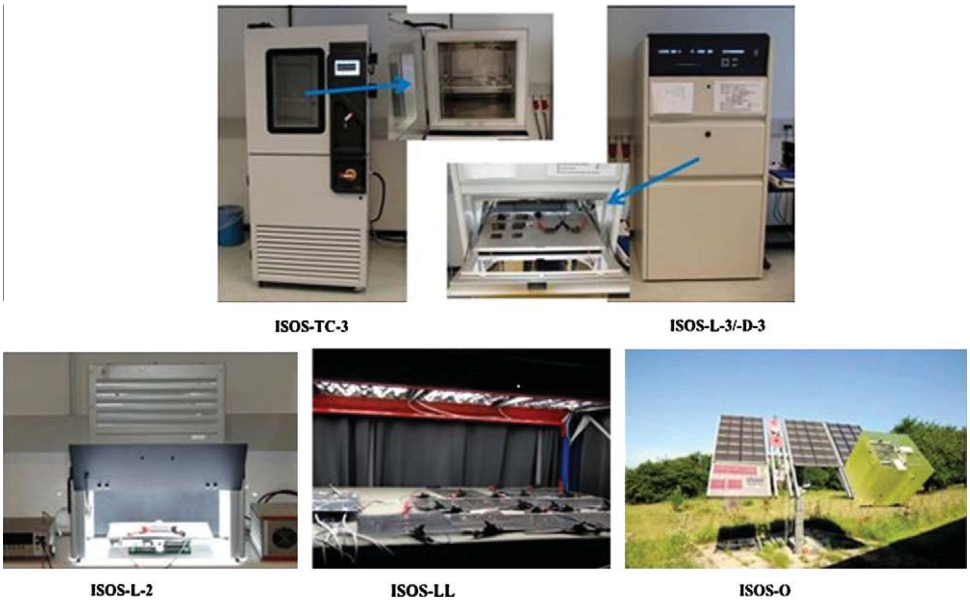

ISOS-TC-3 ISOS-L-3/-D-3

ISOS-L-2 ISOS-LL ISOS-O

Fig. 3. Photographs showing instrumentation for different stability tests.

to the possibility of low cost and fast adaption. PSCs can easily be made in a new shape or a new pattern at little extra cost, which is in stark contrast to all other PV technologies where the outline of the solar cell (i.e. a wafer) is fixed or too costly to change for low volume application. There are certain requirements for mobile and ICT applications that PSCs have to meet to be useful, and fortunately the weakest point for PSCs which is their operational stability is not very critical in the context of ICT applications as many of these products do not have a service life much beyond a few years. Of importance is the shelf life such that the modules can withstand the duration between manufacture and storage before integration into products without significant decline in performance. Encapsulation is therefore very crucial for maintaining the stability and prolonging the lifetime of PSCs. Barrier materials with UV cut-off and low transmission rate of water and oxygen can extend the lifetime of PSCs by several orders of magnitude. The barrier properties of the encapsulating material and the method of encapsulation introduces significant variability not only on the stability of the organic photovoltaic cells but also on the performance of the encapsulated cells/module. It is hence crucial to find a barrier material and an encapsulation technique that maximize both performance and stability of the PSCs.

3.1. Encapsulation method

In Fig. 4, the effect of the two encapsulation methods investigated in this study on the *IV* performance of the modules is shown. The modules were characterized prior to encapsulation and after encapsulation with the use of pressure sensitive adhesive (PSA) and a UV curable adhesive (DELO). Encapsulation with PSA introduces an ‘S’ shape inflection in the *IV* curve showing blockage of current collection and significant drop in V_{oc}. Upon prolonged exposure to light under the solar simulator, the S-shape evolves to the normal curve and the duration of this evolution is dependent on the UV content in the solar spectrum (Fig. 4, right). Such an inflection point is caused by the metastable conductivity of ZnO which is a result of oxygen adsorption on the surface of ZnO. UV exposure induces generation of holes in ZnO (band gap of 3.2 eV) causing release of oxygen from the surface and improving its conductivity [8,9]. On the other hand, no such inflection point is seen in the module encapsulated using the UV-curing adhesive. This indicates that the use of “liquid” adhesive enables better elimination of oxygen from the modules during the encapsulation process. Upon evaluation of the stability under accelerated conditions (ISOS-L-2) as described in Section 3.3, modules encapsulated with UV-curing adhesive were seen to perform significantly better than PSA-based encapsulation although the general trend of degradation was similar for both kinds of encapsulation. As a result, the remainder of the modules were manually encapsulated using UV-curing adhesive before further performance and stability characterization.

3.2. Performance

The all solution-based processing of the complete layer stack of PSC modules in our concept renders great flexibility in varying the dimensions of the modules on one roll of the substrate in a single R2R processing run. We exploited this possibility to evaluate scalability in the module dimensions by varying the length of the cells/strips in the module. Fig. 5 shows median *IV* curve of the modules in different sizes and Table 1 lists their key photovoltaic parameters.

All devices characterized showed an active-area power conversion efficiency (*PCE*) of >1%. Such an efficiency for an all-solution processed ITO-free PSC module of these

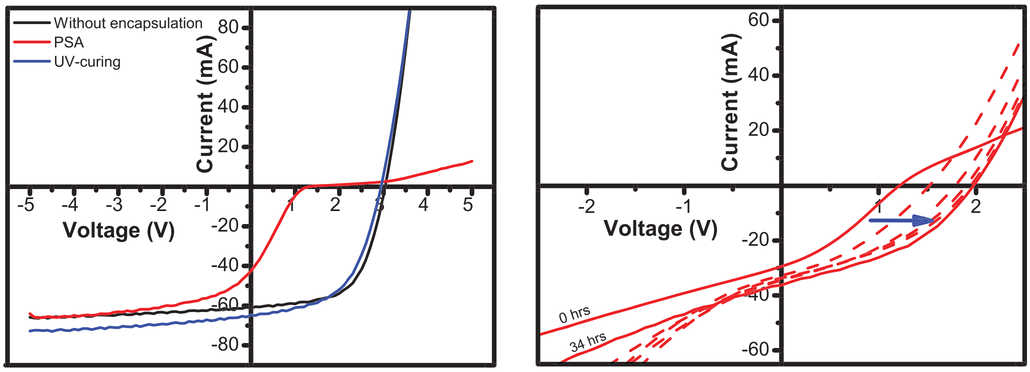

Fig. 4. Representative *IV* curves of modules showing the effect of encapsulation techniques (left). The evolution of the initial 'S' shaped curve of modules encapsulated with PSA upon constant exposure to light under solar simulator is shown (right). The active-area of the modules was 60 cm^2 and comprised of six interconnected cells.

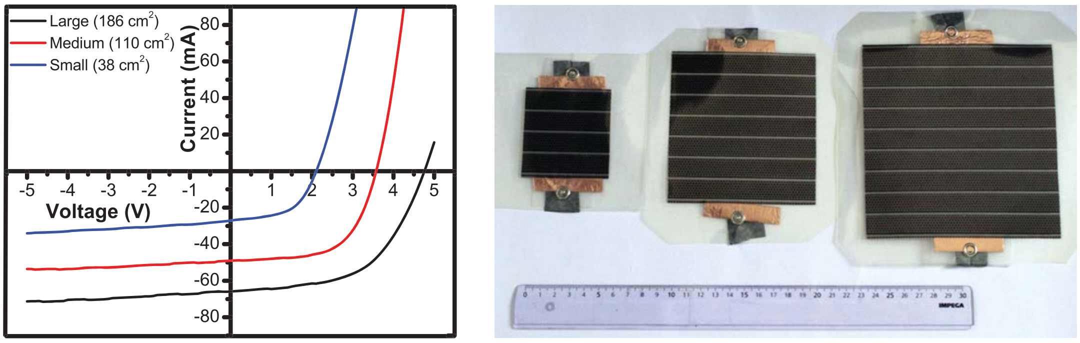

Fig. 5. *IV* curves of ITO-free modules of three different sizes prepared in this study (left) and the corresponding pictures (right).

dimensions and particularly for >100 cm^2 active-area, has not been reported so far. We have named this process as *IOne*. Previously, we have reported *IOne* process for a 6 cm^2 single cell that showed a *PCE*: 1.82%; V_{oc}: 0.51 V; J_{sc}: 7.02 mA cm^{-2}, and *FF*: 51.2% [10]. From Table 1, it is clear that *IOne* is scalable as the medium and large cells have the same active-area efficiency. Of particular significance is *FF* which is known to decrease with increasing area in PSC employing PEDOT:PSS as a replacement to ITO which has been interpreted as being due to the high sheet resistance of PEDOT:PSS [11]. In our case, however, the combination of metal grid and hcPEDOT:PSS has allowed us to maintain a high FF when scaling up from a single cell to modules of different sizes. Note that since the cells are interconnected in series, the J_{sc} given in Table 1 is that of the weakest performing cell in the module. It is unclear why J_{sc} of Large module is higher, although this could be due to a defect or other inhomogeneity caused during processing such as lower thickness of the highly conductive PEDOT:PSS in the front electrode that could cause increased transmittance of light to the photoactive layer. Regardless, such a photovoltaic performance on large area modules is comparable to ITO-based modules (*ProcessOne*) for which a mean *PCE* of 1.22% for a module of the total area of 160 cm^2 was previously reported by our group [6].

3.3. Stability measurements

Table 2 shows the ISOS stability tests performed for the modules and the corresponding *T80* of the modules estimated from the measurements. *T80* were estimated directly from data points when available since most measurements were performed for a minimum of 1000 h. For very stable modules having *T80* exceeding the testing period, it was estimated by linear extrapola-

Table 1
Key photovoltaic parameters of ITO-free modules studied. Total area includes area of the busbar for electrical contact of the module.

Module abbreviation	Total area (cm^2)	Active-area (cm^2)	No. of stripes or cells	Area of 1 cell (cm^2)	J_{sc} (mA cm^2)	V_{oc} (V)	*FF* (%)	*PCE* (active-area)	*PCE* (total area)
Small	38.28	24.00	4	6.00	4.84	2.11	53.60	1.36	0.86
Medium	110.47	70.00	7	10.30	4.85	3.59	61.30	1.60	1.10
Large	186.30	121.5	9	13.50	5.45	4.76	55.60	1.62	1.05

Table 2
T80 of the modules for each type of ISOS tests conducted.

Category	Light (sun)	Temperature (°C)	Relative humidity (%)	T_{80} (h)	Deviations from ISOS protocols
ISOS-D-1	0	25	20–35	~2800	–
ISOS-D-2	0	65	10–15	~5000	–
ISOS-D-3	0	50	85	100–200	Lower storage temperature by 15 °C
ISOS-L-2	1	70	10–15	500–1300	Testing was performed in room environment
ISOS-L-3	0.7	65	50	100–200	Modules were kept at open circuit
ISOS-LL	0.2	30	10–15	700–1000	–
ISOS-TC-3	0	−40 to 85	55	600–700	–
ISOS-O	0–1	10–25	20–50	~1500	–

tion of the decay curves. The reasons that a range of *T80* is given in some cases is because some of the modules measured under the same conditions had different values for *T80*, which is explained mainly by the fact that the encapsulation is performed manually and, therefore, defects during encapsulation such as variability in the thickness of the adhesive are inevitable. Although such defects during encapsulation (that cannot be observed by visual inspection of the device) introduces negligible difference in initial performance, it can result in a significant stability difference over time. An automated encapsulation approach would improve the consistency in such a case.

At first, the stability of the modules encapsulated using PSA and UV-curing adhesive were compared by performing accelerated aging tests. Fig. 6 demonstrates the photovoltaic parameters versus time for both types of modules. The graphs represent the most stable out of two measured modules pertaining to each type of encapsulation. The results showed that the modules encapsulated using PSA adhesive had lower stability due to decay in the V_{oc} (this is ascribed to faster ingress of oxygen). An oxidation pattern of the copper tape around the contact button was observed on all PSA-based modules after the end of the test (Fig. 7). No such effect was recorded on the devices encapsulated with UV-curing adhesive further confirming the

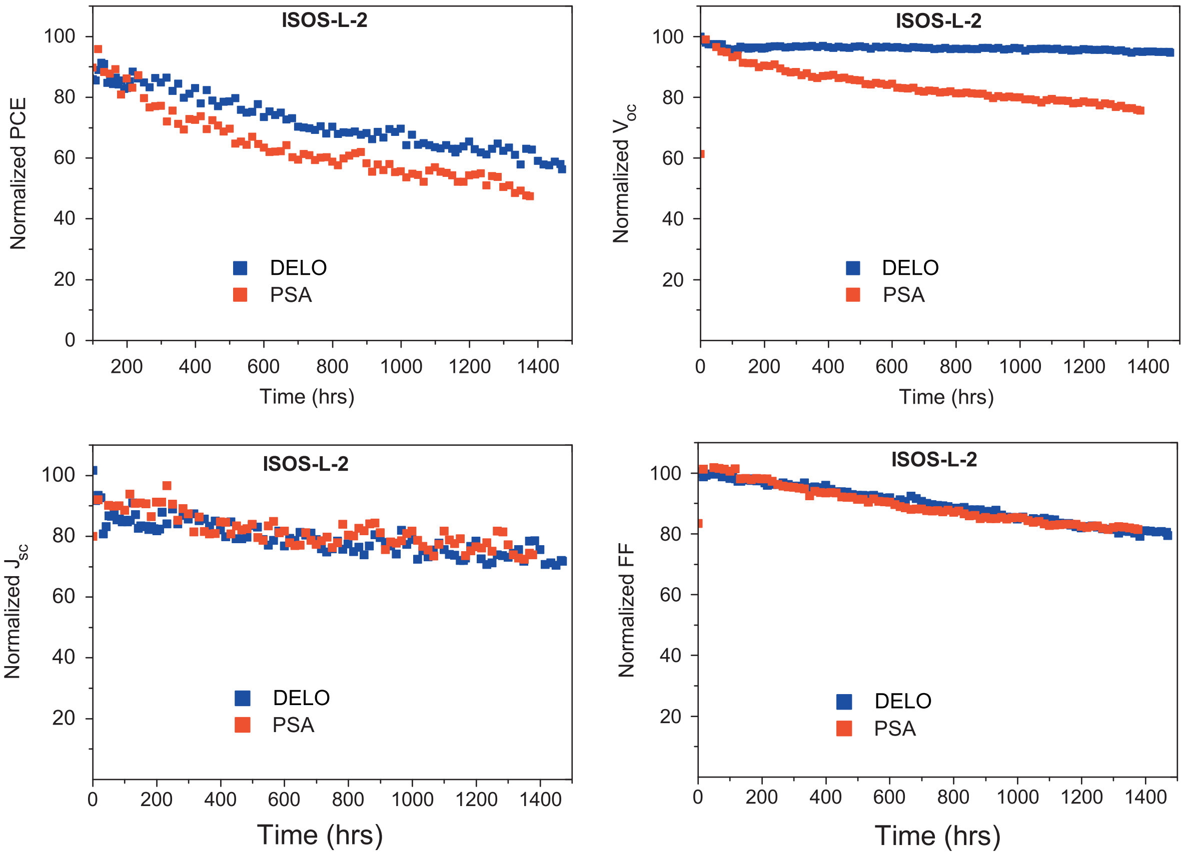

Fig. 6. Photovoltaic parameters versus time for modules encapsulated using pressure sensitive adhesive (PSA) and UV-curing adhesive (DELO).

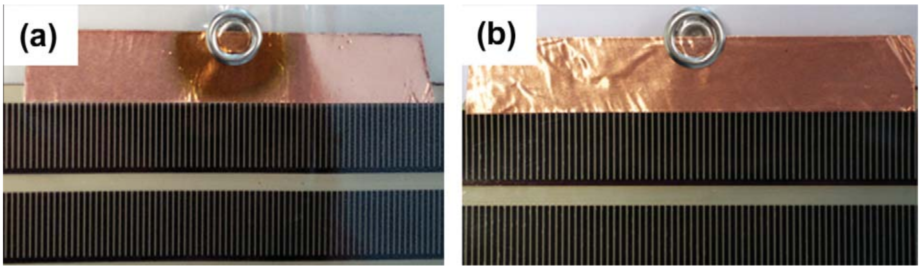

Fig. 7. Contacts of modules PSA-based encapsulation (a) and UV-curing encapsulation (b) after ISOS-L-2 test for >1500 h showing visible oxidation of the copper contacts in PSA-based encapsulated modules.

advantage of UV-curing encapsulation over PSA. It should be stressed however that PSA based adhesives have significant processing advantages over UV-curing adhesives and are more readily adaptable to integration into different applications.

Based on the obtained results, further analyses were performed using modules with UV-curing adhesive encapsulation. Fig. 8 presents the stability graphs of the most stable modules for each corresponding ISOS test. For most of the tests, *T80* of the modules was over 1000 h except in those cases where high humidity levels were involved (ISOS-D-3 and ISOS-L-3). The fast decline in performance in humid environment can possibly be explained as due to the low resistance of the encapsulation against moisture diffusion into the device, which affects all photovoltaic parameters. The highest stability was recorded for the modules stored in the dark in an oven at 65 °C (ISOS-D-2) with *T80* reaching up to 5000 h estimated by the linear extrapolation. Meanwhile, modules stored in dark simply on a shelf showed less stability reaching only 2800 h (ISOS-D1). This can be explained by the fact that the elevated temperature in the oven can reduce the moisture level easing the conditions the modules are exposed to. *T80* for the measurements under light in indoor conditions was

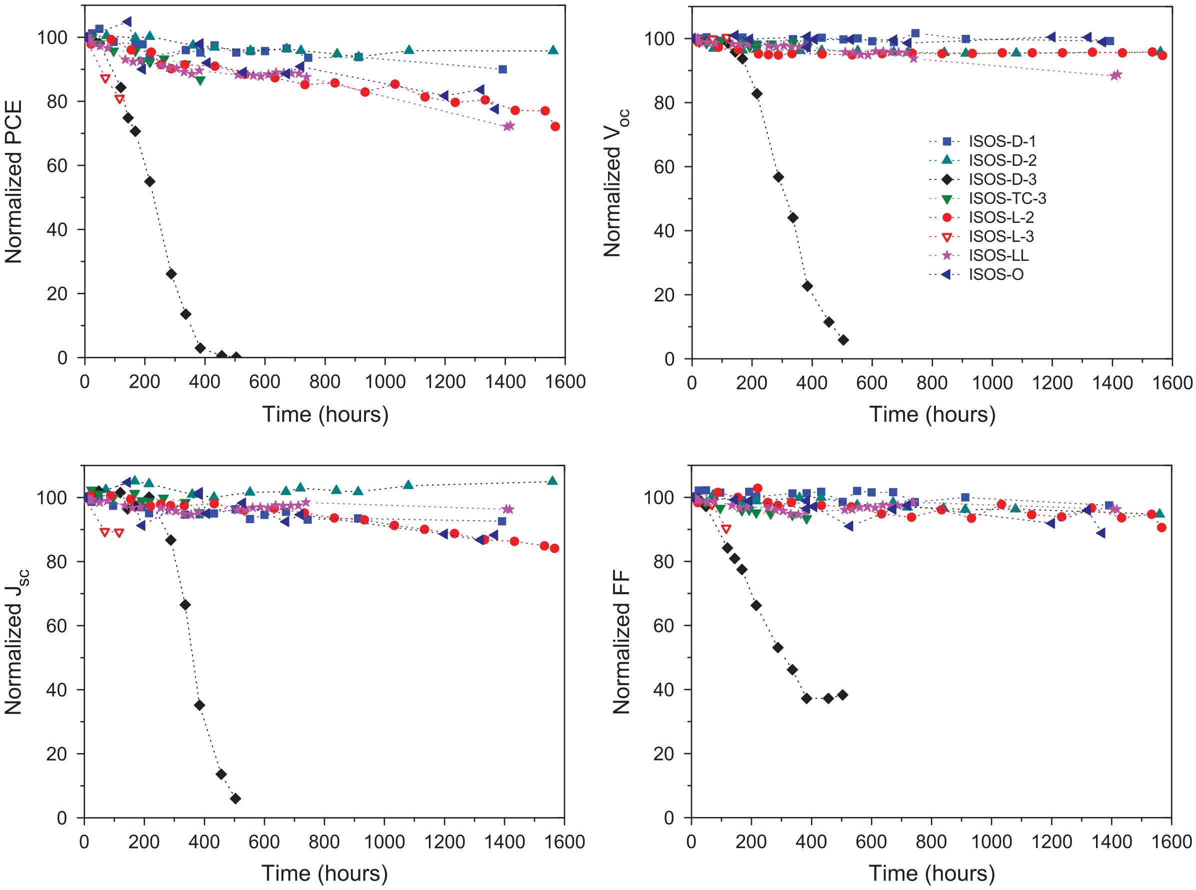

Fig. 8. *PCE* of the modules subjected to eight different ISOS tests shown in the legend.

in the range of 500–1300 h and the decline in performance was mainly due to the decrease of J_{sc}, suggesting degradation of photoactive polymer. This is mainly attributed to the fact that the light spectrum of the metal halide lamp has significantly higher UV content compared to AM1.5G. It is therefore expected that the stability of the modules measured in outdoor conditions would be significantly higher as confirmed by the outdoor tests detailed below.

The outdoor testing was performed at two locations, in India and Denmark. Table 3 shows the average conditions of testing in both locations. The main difference in testing conditions was that in Denmark the modules were placed on a solar tracker, while in India on a roof top with 5° inclination towards south. This resulted in a different amount of energy dose reaching the modules. Fig. 9 demonstrates the stability of modules measured in both locations. The graphs are representatives of several modules measured at each location. From the graphs, it is obvious that the degradation had identical rate at both locations.

Overall, the presented ITO-free generation of PSC modules with uv-curing based encapsulation has significantly higher stability compared to the older generation of ITO-based PSC modules produced according to the *ProcessOne* technique [6,12] as can be seen in Fig. 10 which demonstrates the *PCE* of most stable modules measured according to ISOS-L-2. The comparison is presented to demonstrate what has already been shown with ITO-based PSCs modules and what is now achieved on ITO-free modules by our study even-though these studies were performed independently and have many variables that could account for the difference in stability. Among the most important variables are the encapsulation techniques: *ProcessOne* devices were encapsulated using PSA and not edge sealed and in addition, the thick outline of PEDOT:PSS of *ProcessOne* modules is a well-known source of degradation in PSCs [13,14].

Further analyses of the modules in a humid environment revealed that the modules cannot withstand a relative humidity much above 65%. Typical decay profile of the graphs in a humid environment was characterized by an initial stable performance for a few days followed by a fast decline in the performance (Fig. 11). This can possibly be explained by a gradual absorption of humidity by PEDOT:PSS in the modules as was mentioned earlier, which results in expansion of the layer. This will stress the encapsulation due to expansion creating channels for accelerated passage of humidity inside the module forcing the degradation processes to go much faster. When a double encapsulation was applied to the modules, the performance was drastically improved with *T80* reaching around 800 h, as shown in Fig. 11. It is very likely that the Achilles heel in this whole process of rapid degradation of the modules at high humidity is in the use of the food packaging barrier having a water vapor transmission rate (WVTR) of 0.04 g $\mathrm{cm^{-2}}$ $\mathrm{day^{-1}}$ at 40%RH. Above this humidity level, the lag time of the barrier foil – that is, the initial transient state of water vapor permeation (characterized by a slower rate) before establishment of an equilibrium level (a faster rate), is likely to be much shorter [15]. As of result of this, a short duration of stability (~100 h) is observed for modules under high humidity conditions (ISOS-D-3) followed by a rapid decline. The use of a double encapsulation effectively increases the lag time and therefore the stable regime of the modules.

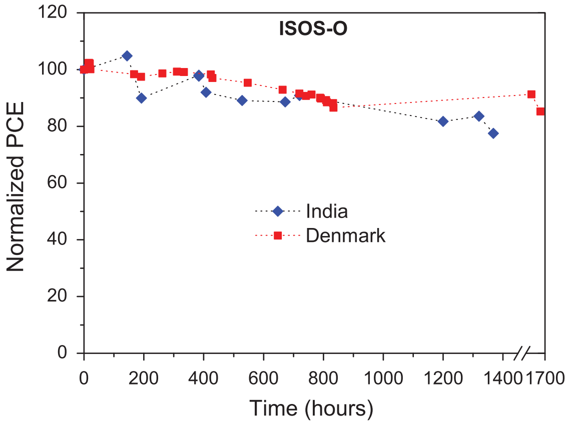

Fig. 9. *PCE* of the modules with an area of 100 $\mathrm{cm^2}$ measured in outdoor conditions in Jawaharlal Nehru Centre for Advanced Scientific Research, Bangalore, India and Technical University of Denmark, Roskilde, Denmark.

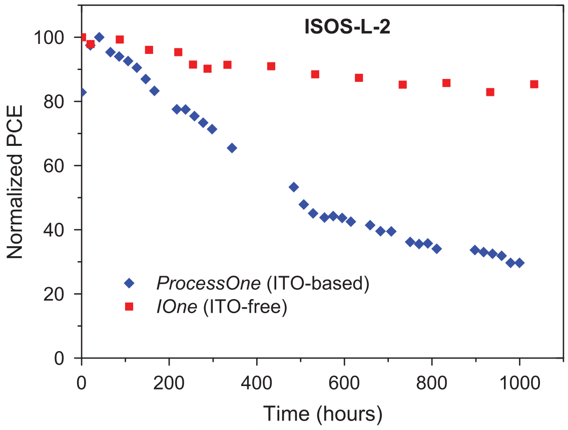

Fig. 10. Comparison of stability of the new generation ITO-free modules (*IOne*) with the older generation of *ProcessOne* based modules. The *PCE* in both cases was around 1.2%.

Table 3
Outdoor conditions of measurements in two locations Denmark and India. The temperature and relative humidity values are averaged over the entire testing period.

Location	Geographic coordinates	Platform	Temperature (°C)	Relative humidity
India	13°04′N, 77°36′E Elevation 897 m	Stand still, roof top Tilted at 5° towards south	20–32	72–96% Morning 38–88% Afternoon
Denmark	55°41′N, 12°6′E Elevation ~10 m	Solar tracker	7–27	65–95% Morning 43–73% Afternoon

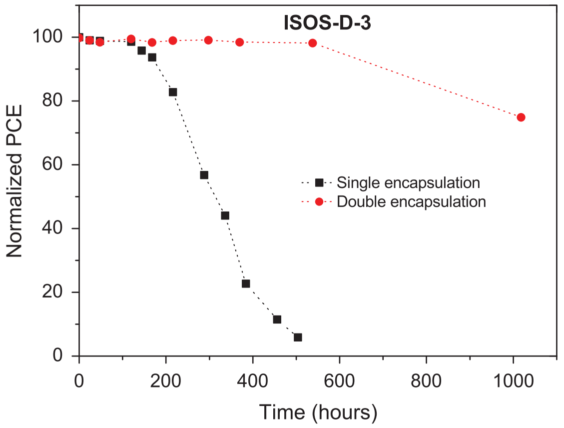

Fig. 11. Comparison of module performance in high relative humidity for modules with single and double encapsulation. The inset shows the initial *IV*s of the modules after the encapsulation.

Table 4
Initial and final photovoltaic parameters of ITO-free modules (active-area 70 cm^2 with 7 cells in each module) subjected to various aging conditions as measured under 1000 W m^{-2} (AM 1.5) solar irradiation at room temperature.

Tests		Duration of test (h)	V_{oc} (V)	I_{sc} (mA)	*FF* (%)	*PCE* on active-area (%)
ISOS-D-1	Initial	1392	3.11	51.59	58.23	1.34
	Final		3.08	47.86	56.39	1.19
ISOS-D-2[a]	Initial	1560	2.00	33.01	52.33	1.20
	Final		1.91	33.94	49.55	1.15
ISOS-D-3	Initial	504	3.56	51.04	55.41	1.44
	Final		0.98	3.34	17.85	0.00
ISOS-L-2	Initial	1442	3.56	51.37	59.36	1.55
	Final		3.36	28.18	48.15	0.65
ISOS-L-3[b]	Initial	116	1.99	28.57	53.93	1.38
	Final		1.99	23.77	48.74	1.04
ISOS-LL	Initial	1582	3.53	51.85	52.43	1.35
	Final		3.42	46.76	48.48	1.11
ISOS-TC-3	Initial	385	3.55	50.52	61.29	1.57
	Final		3.46	57.25	47.72	1.36
ISOS-O (Denmark)	Initial		3.57	56.14	56.15	1.43
	Final-1	1554	3.42	43.07	55.98	1.17

[a] Module area = 28.8 cm^2 with 4 cells/strips.
[b] Module area = 22 cm^2 with 4 cells/strips.

Overall the stability tests demonstrated that the new generation of roll-to-roll ITO-free coated modules have promising performance in terms of operational lifetime reaching *T80* values above 1000 h and significantly higher shelf-life stability with *T80* > 2800 h. It also demonstrated that further improvement in encapsulation can lead to rather stable modules with a stability reaching more than a year. A summary of the initial and final performance of modules tested in all the stability tests is given in Table 4.

4. Conclusion

In this work, we have successfully demonstrated all solution processed ITO-free polymer solar cell modules with a total area reaching 186 cm^2 and an active-area power conversion efficiency of 1.6%. The module structure Ag/PEDOT:PSS/ZnO/P3HT:PCBM/PEDOT:PSS/Ag is a cost effective alternative to ITO-based devices and is processed using a combination of roll-to-roll printing and coating methods for all layers. Modules based on this structure were found to be easily scalable. We have further shown the influence of the encapsulation technique on the stability of the modules despite the use of a food packaging barrier. Comprehensive stability tests using several ISOS protocols were performed and the modules displayed superior stability in all tests except under high humidity conditions. With the use of a two layers of encapsulation, the module stability under high humidity conditions were found to significantly improve. Particularly, these modules are found to be very stable for long-term storage for several months and significantly more stable if stored under elevated temperature conditions of 65 °C. Furthermore, these modules have good operational stability both under low light and 1 sun conditions. Note that we have used a food packaging barrier having significantly lower WVTR than sought for organic current generating devices (10^{-6} g cm^{-2} day^{-1}) and yet modules in most tests are rather stable. With improvement in barrier properties, the lifetime of the devices will be further improved.

Acknowledgements

This work has been supported by the European Commission as part of Framework 7 ICT 2009 collaborative project HIFLEX (Grant No. 248678) and by EUDP (J. No. 64011-0002). Partial contribution is received from the EU-India framework project "LargeCells" (FP7/2007-13, Grant Nos. 261936 and INT/IRMC/EC-SOLAR/OISC/LARGECELLS:1/261936/2010).

References

[1] N. Espinosa, R. García-Valverde, A. Urbina, F.C. Krebs, A life cycle analysis of polymer solar cell modules prepared using roll-to-roll methods under ambient conditions, Sol. Energy Mater. Sol. Cells 95 (2011) 1293–1302.
[2] S. Na, S. Kim, J. Jo, D. Kim, Efficient and flexible ITO-free organic solar cells using highly conductive polymer anodes, Adv. Mater. 20 (2008) 4061.
[3] M. Jørgensen, K. Norrman, F.C. Krebs, Stability/degradation of polymer solar cells, Sol. Energy Mater. Sol. Cells 92 (2008) 686–714.
[4] N. Grossiord, J.M. Kroon, R. Andriessen, P.W.M. Blom, Degradation mechanisms in organic photovoltaic devices, Org. Electron. 13 (2012) 432–456.
[5] M.O. Reese, S.A. Gevorgyan, M. Jørgensen, E. Bundgaard, S.R. Kurtz, D.S. Ginley, D.C. Olson, M.T. Lloyd, P. Morvillo, E.A. Katz, A. Elschner, O. Haillant, T.R. Currier, V. Shrotriya, M. Hermenau, M. Riede, K.R. Kirov, G. Trimmel, T. Rath, O. Inganäs, F. Zhang, M. Andersson, K. Tvingstedt, M. Lira-Cantu, D. Laird, C. McGuiness, S. Gowrisanker, M. Pannone, M. Xiao, J. Hauch, R. Steim, D.M. DeLongchamp, R. Rösch, H. Hoppe, N. Espinosa, A. Urbina, G. Yaman-Uzunoglu, J. Bonekamp, A.J.J.M. van Breemen, C. Girotto, E. Voroshazi, F.C. Krebs, Consensus stability testing protocols for organic photovoltaic materials and devices, Sol. Energy Mater. Sol. Cells 95 (2011) 1253–1267.
[6] F.C. Krebs, T. Tromholt, M. Jørgensen, Upscaling of polymer solar cell fabrication using full roll-to-roll processing, Nanoscale 2 (2010) 873–886.
[7] D. Angmo, M. Hösel, F.C. Krebs, All solution processing of ITO-free organic solar cell modules directly on barrier foil, Sol. Energy Mater. Sol. Cells 107 (2012) 329–336.
[8] H. Cheun, C. Fuentes-Hernandez, Y. Zhou, W.J. Potscavage Jr., S. Kim, J. Shim, A. Dindar, B. Kippelen, Electrical and optical properties of

ZnO processed by atomic layer deposition in inverted polymer solar cells, J. Phys. Chem. C 114 (2010) 20713.
[9] F. Verbakel, S.C.J. Meskers, R.A.J. Janssen, Electronic memory effects in diodes from a zinc oxide nanoparticle-polystyrene hybrid material, Appl. Phys. Lett. 89 (2006) 102103.
[10] J. Yu, I. Kim, J. Kim, J. Jo, T.T. Larsen-Olsen, R.R. Søndergaard, M. Hösel, D. Angmo, M. Jørgensen, F.C. Krebs, Silver front electrode grids for ITO-free all printed polymer solar cells with embedded and raised topographies, prepared by thermal imprint, flexographic and inkjet roll-to-roll processes, Nanoscale 4 (2012) 6032.
[11] Jun-Seok Yeo, Jin-Mun Yun, Seok-Soon Kim, Dong-Yu Kim, Junkyung Kim, Seok-In Na, Variations of cell performance in ITO-free organic solar cells with increasing cell areas, Semicond. Sci. Technol. 26 (2011) 034010.
[12] F.C. Krebs, S.A. Gevorgyan, J. Alstrup, A roll-to-roll process to flexible polymer solar cells: model studies, manufacture and operational stability studies, J. Mater. Chem. 19 (2009) 5442–5451.
[13] E. Voroshazi, B. Verreet, A. Buri, R. Müller, D. Di Nuzzo, P. Heremans, Influence of cathode oxidation via the hole extraction layer in polymer: fullerene solar cells, Org. Electron. 12 (2011) 736–744.
[14] K. Norrman, M.V. Madsen, S.A. Gevorgyan, F.C. Krebs, Degradation patterns in water and oxygen of an inverted polymer solar cell, J. Am. Chem. Soc. 132 (2010) 16883–16892.
[15] G.L. Graff, R.E. Williford, P.E. Burrows, Mechanisms of vapor permeation through multilayer barrier films: lag time versus equilibrium permeation, J. Appl. Phys. 96 (2004) 1840.

Materials Views
www.MaterialsViews.com
ADVANCED ENERGY MATERIALS
www.advenergymat.de

Roll-to-Roll Inkjet Printing and Photonic Sintering of Electrodes for ITO Free Polymer Solar Cell Modules and Facile Product Integration

*Dechan Angmo, Thue T. Larsen-Olsen, Mikkel Jørgensen, Roar R. Søndergaard, and Frederik C. Krebs**

The successful integration of printed polymer solar cells into complex electronic circuitry relies heavily on the adaptability of the processing methods thus enabling fast device design. Printing and coating methods[1,2] have been employed for some time for the large scale manufacture of OPV modules and have demonstrated the ease with which they can enter a more complex device through integration following routes commonly employed within the area of printed and flexible electronics.[3] All known OPV demonstrators to date have however employed indium-tin-oxide (ITO) as the semitransparent front electrode which brings along several disadvantages. The most important disadvantage is that ITO accounts for >80% of the cost and up to 90% of the embedded energy, a disadvantage that is likely to become more severe in the future, due to the scarcity of indium.[4] Secondary disadvantages are that the ITO is prepared by vacuum deposition and requires subsequent processing to arrive at the conducting pattern (photolithography or laser scribing), and finally that ITO is brittle and while it may be capable of handling some bending during manufacture, it is best integrated into a product that does not require further bending during operation i.e., bending is acceptable during roll-to-roll manufacture and product integration but the final product should be rigid. A fully printable alternative to ITO would thus be highly beneficial and while several reports exist[5–8] few of them have been corroborated between independent research laboratories[8] and none of them have been integrated into demonstrators. This could of course be indicative that the initial development is there but that it is not fully at the level required for completely replacing ITO in a real manufacturing setting or even within the academic research community.

Here we demonstrate how semitransparent silver grids can be directly printed onto flexible polyethyleneterphthalate (PET) foil followed by photonic sintering. Subsequent printing of PEDOT:PSS and slot-die coating of ZnO nanoparticles yields an electron accepting semitransparent front electrode, that can be applied directly in the manufacture of polymer solar cell modules comprising 16 serially connected solar cells. We further integrate these fully solution processed modules in credit card sized laser pointers enabling direct charging of lithium-polymer batteries and application in consumer electronics, following a similar approach to that of the OE-A demonstrator from 2011.[3]

Firstly, a diagonal grid electrode pattern was roll-to-roll inkjet printed using an aqueous silver ink onto flexible polyester foil with a resolution of 600 × 600 DPI. The inkjet drop formation was carefully studied to minimize satellite droplet formation which is critical for water based inks with a relatively high surface tension and a special pulse-form was developed using a pulse editor comprising 4 bursts with short trailing retention pulses and one final retention pulse. The dropsize for the optimized pulseform was approximately 14 pL. The web speed during printing was 2 m min^{-1} and a corona treatment of the foil (with antistatic control) was critically important for sufficient wetting and initial adhesion. The corona power was optimized to around 600 W with the applied web speed of 2 m min^{-1} and the relationship between corona power and web speed was found to be a function of the distance between the corona station and the printing head. We ascribe this to the fact that the surface energy of the substrate decreases rapidly immediately after corona treatment and then reaches a more stable level. The distance from the corona station to the printing head was 0.9 meters and the time lapse between the corona treatment and the inkjet printing was thus ~0.45 minute with the applied web speed. The chosen web speed was the fastest possible with the oven available (2 meter oven length). The width of the grid lines were nominally set to be 2 pixels wide (nominally 85 micron) but ink spread and drying led to an effective line width of the printed pattern of around 170 micron. The grid spacing was 2 mm. The solar cell module was designed to fit applications with the size of a standard credit card and comprise 16 serially connected cells. The grid electrode pattern consists of 16 stripes 3 mm wide and spaced by 1 mm. The web width was 305 mm and the length of the printed motif (along the web) was 305 mm. Each motif had 3 parallel sets of solar cell modules and each motif carried 15 individual modules (i.e., 240 individual solar cells for each motif). Inkjet printing, photonic sintering and the motif structure are shown in **Figure 1**. The silver grid had a sheet resistivity immediately after printing and drying of 40–50 ohm square^{-1} and was found to be improved by an extra drying step and significantly more by flash photonic sintering using a setup described earlier.[9] The photonic sintering was carried out with a constant flash rate of 1.8 Hz which is the fastest

---

Ms. D. Angmo, Mr. T. T. Larsen-Olsen, Dr. M. Jørgensen,
Dr. R. Søndergaard, Prof. F. C. Krebs,
Department of Energy Conversion and Storage
Technical University of Denmark
Frederiksborgvej 399, DK-4000 Roskilde, Denmark
E-mail: frkr@dtu.dk

DOI: 10.1002/aenm.201200520

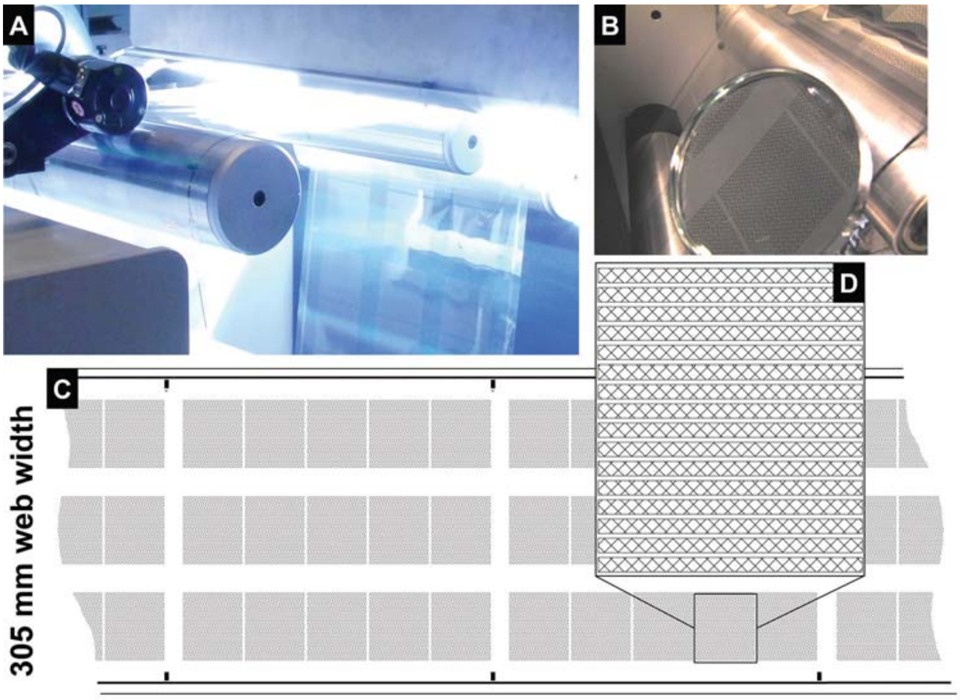

Figure 1. (A) A photograph of roll-to-roll photonic sintering of the inkjet printed silver grid structures taken during a flash. (B) A view of the roll-to-roll inkjet printed pattern after drying, through a magnifying glass. (C) Graphical illustration of the web showing the repeated motif comprising 15 individual modules. (D) Zoom-in on the silver electrode pattern corresponding to one module.

possible with the current setup ruled by the time required to recharge the pulse forming network after firing of each pulse. The flash dosage was thus ruled by the individual pulse energy and the web speed. The pulse energy was found experimentally and set to the highest level that did not lead to cracking of the printed grid lines with the chosen footprint of the flash (40 mm distance and 830 J per pulse). Once those settings had been made, the maximum web speed is fixed by the pulse frequency and the width of the footprint for the flash. Web speeds of 0.5, 1 and 2 m min^{-1} were employed for the flashing thus corresponding to 4, 2 and 1 flashes per area. The remainder of the solar cell stack was thus processed using a device geometry similar to the previously reported[5] but employed full roll-to-roll processing for all layers (the previous study employed spin coating and vacuum evaporation). The device stack was thus completed by rotary screen printing of PEDOT:PSS, slot-die coating of the electron transport layer (ZnO) and the active layer (P3HT:PCBM) and rotary screen printing of the hole transport layer (PEDOT:PSS) and water based silver nanoparticles for the busbars. All drying steps were carried out at 140 °C which is the maximum temperature that the PET substrate can endure without excessive shrinkage and deformation. The modules were finally packaged before testing and integration into the laser pointer following the same method employed for the OE-A demonstrator.[3] The results of the IV-characterization are shown in **Figure 2**A and summarized in **Table 1**. A general observation was that the fill factor (FF), reaching more than 52%, is significantly improved as compared to the previous ITO-based modules used in OE-A demonstrator.[3] The overall performance is comparable to (or slightly better) than the previously reported ITO based device, especially considering the relatively low transmittance (Supporting information, Figure S1), and the many advantages of facile processing nicely demonstrate that it is possible to successfully replace ITO. When correlating the device IV–performance with the degree of photonic sintering of the grid, the only significant difference in device performance is an increase in photocurrent for an increasing number of

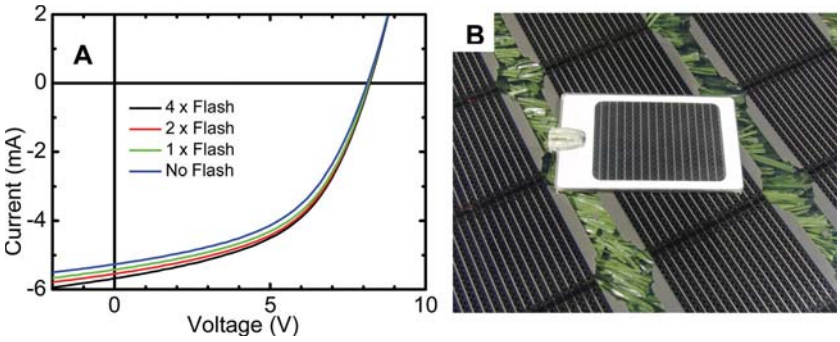

Figure 2. (A) IV-data for complete modules based on the roll-to-roll inkjet printed grids with varying degree of photonic sintering corresponding to 4, 2, 1 and 0 flashes. (B) A photograph of the demonstrator laser pointer on top of the printed modules as prepared on the roll.

Adv. Energy Mater. **2012**,
DOI: 10.1002/aenm.201200520

Table 1. Summary of IV-data of devices with varying degree of photonic sintering (number of flashes). The values are averaged over 6 modules with the standard deviation in parenthesis.

Number of flashes	PCE[a)] (%)	I_{sc} (mA)	V_{oc} (V)	FF (%)	R_{sh}[b)] ($\Omega_\square$)
No flash	1.5 (0.04)	−5.3 (0.2)	8.1 (0.04)	50 (0.6)	18–20
1 x flash	1.6 (0.03)	−5.4 (0.16)	8.2 (0.05)	51 (0.9)	16–17
2 x flash	1.7 (0.1)	−5.5 (0.3)	8.2 (0.03)	51 (0.7)	14–16
4 x flash	1.7 (0.1)	−5.7 (0.3)	8.2 (0.04)	51 (0.9)	9–12

[a)] Module active area of 15.4 cm^2 (i.e., not corrected for aperture loss caused by the front grid); [b)] Sheet resistance of the inkjet printed front grid.

flashes. The FF and V_{oc} are improved slightly as well, reaching significance when comparing 4 flashes with 0 flashes. Compared to the steady decrease in sheet resistivity of the grid with increasing photonic sintering (Table 1), the reason that we only observe a slight increase in FF is ascribed to the narrow width of the already high conductivity PEDOT:PSS lines for this module geometry. This is of course a requirement imposed by the small size of the demonstrator. An added advantage of the photonic sintering is a significant improvement in adhesion already after 1 flash. The freshly printed and dried inkjet printed grid did not pass the tape test whereas a single flash made the grid structure stick exceptionally well (it passes the tape test).

In conclusion we demonstrate how ITO can be replaced by an inkjet printed front grid electrode in conjunction with a rotary screen printed PEDOT:PSS electrode. This enabled complete manufacture of ITO-free credit card sized solar cell modules comprising 16 serially connected cells that were easily integrated into a demonstrator (here a laser pointer). Photonic sintering was found to improve not only the performance but also to improve the adhesion very significantly.

Experimental Section

Roll-to-roll inkjet printing: A water based ink with a 20% silver loading was employed (Suntronic U7089 from Sun Chemicals). Inkjet printing was carried out by printing directly on PET foil (Melinex ST506 from Dupont-Teijin) on a roll-to-roll inkjet printer comprising unwinder, web-cleaning (Teknek), corona treater (Vetaphone), double sided antistatic bars, ink jet printer (Kyocera), hot air oven, nip and rewinder. The web speed during printing was 2 m min^{-1} and the corona treatment was set to 600 W. The oven was set to 140 °C and had a length of 2 meters (1 minute drying time). After printing and first drying the sheet resistivity was 60–70 Ohm $Square^{-1}$. Repassage of the foil through the dryer at 1 m min^{-1} lowered the sheet resitivity to 18–20 Ohm $Square^{-1}$. The dried lines had a height of ~0.25 μm and a width of ~170 μm. The inkjet printing machine comprise and automated ink filling system and meniscus pressure/temperature control system. Three droplet on demand (DOD) print heads allow for printing in a full width of 315 mm with 600 DPI at a web speed of up to 72 m min^{-1}. In the web direction it is possible to increase the resolution to 1200 DPI. Registration marks were printed at the leading edge of every motif allowing for printing in 2-dimensional registry when rotary screen printing and a 2 mm wide pilot line was printed continuously on either side of the motif along the web for 1-dimensional registration of the slot die coating (see Figure 1).

Roll-to-roll photonic sintering: A commercial xenon flash lamp system (Sinteron 2000, Xenon Corp.) mounted on a roll-tol-roll system was employed for photonic sintering of the ink jet printed patterns. The pulse forming network delivers electrical pulse energies from 150 to 2000 Joules by changing the voltage setting. The pulse duration was set to 0.5 ms with maximum electrical pulse energy of 830 J and a flash frequency of 1.8 Hz. The 16” xenon flash lamp emits a broadband spectrum from 190 nm to 1000 nm (lamp C). The distance between the lamp housing and the unsupported substrate (it is important that the web is unsupported) was set to 40 mm to increase the foot print and defocus slightly. The number of flashes per area was determined by the web speed and the frequency of the flashes was kept constant at the maximum of 1.8 Hz.

Roll-to-roll rotary screen printing of front/back PEDOT:PSS and silver: An RSI compact printer (Stork Prints BV) was employed for both PEDOT:PSS electrodes and silver bus bars. The front PEDOT:PSS (PH1000 from Heraeus) was diluted with isopropanol in a ratio of 3:1 (w/w) and printed at a web speed of 10 m min^{-1} with IR drying (2 × 1.5 kW) and hot air drying (140 °C, 2 meter oven length) in registration with the inkjet printed silver grid, which gave a layer thickness of ~0.4 μm. The back PEDOT:PSS electrode (Orgacon EL-P 5010 from Agfa) was diluted with isopropanol in a ratio of 10:2 (w/w) and printed at a web speed of 2 m min^{-1} with IR drying (2 × 1.5 kW) and hot air drying (140 °C, 2 meter oven length). The resulting layer was somewhat coarse due to the coarse mesh of the screen printing mask, but with an average thickness of ~1.5 μm. The printing of silver bus bars employed water compatible silver nanoparticle ink (PS-004 from Paru) and was printed at a web speed of 2 m min^{-1} with IR drying (2 × 1.5 kW) and hot air drying (140 °C, 2 meter oven length). The printing was carried out in registry with the underlying inkjet printed silver grid.

Slot-die coating of electron transport layer/active layer: The required pattern comprised 48 stripes with a width of 3 mm spaced by 1 mm in 3 sets of 16 stripes (i.e. 3 modules were prepared simultaneously (see Figure 1). The mask for the pattern was a laser cut stainless steel mask (stainless steel 316) fitted with a meniscus guide. Slot-die coating of ZnO nanoparticles was carried out using MEA stabilized ZnO nanoparticles in acetone with a size of 3–5 nm and a concentration of 55 mg mL^{-1}. The web speed was 5 m min^{-1} and the film was dried through two ovens (each 2 meters long), yielding a calculated dry layer thickness of ~70 nm. The first oven had a temperature of 90 °C and the second oven had a temperature of 140 °C. The active layer comprised a solution of P3HT:PCBM (P3HT was Sepiolid P200 from BASF and PCBM was technical grade [60]PCBM from Solenne BV) in chlorobenzene (30 mg mL^{-1} for both P3HT and PCBM). The active layer was coated at a web speed of 5 m min^{-1}, and dried through two ovens set to 140 °C (each 2 meters long), giving a calculated dry layer thickness of ~500 nm. The slot-die coating was carried out using a camera system (from BST) tracking the inkjet printed pilot line to ensure that the fine slot-die coated lines (48 in total) were in registry with the inkjet printed silver grid structures.

Layer stack characterization: Layer thicknesses and line widths were measured on a Dektak profilometer.

Device testing: The final roll with solar cells was subjected to in-situ interface switching to achieve functional modules and testing using automated roll-to-roll testing equipment. The different devices with different degrees of flashing were all prepared along the same roll to minimize effects of process variation. JV-measurements for Figure 2 and Table 1 were acquired by point sampling 6 random modules for each flashing condition. They were cut out and tested carefully using a solar simulator (1000 W m^{-2}, AM1.5G, 85 °C). Each module had a geometric fill factor of 50% leading to an active area of 15.4 cm^2. The solar simulator was calibrated immediately before the measurements that were not corrected for differences in diffuse/direct light or mismatch.

Demonstrator integration: The roll was cut into sheets of 15 modules and integrated into the demonstrator using exactly the same procedure and materials as reported for the OE-A demonstrator[3] except that the white LED in the OE-A demonstrator had been replaced with a 1 mW red laserdiode (DRM104-001) and an injection molded polycarbonate case. The operating voltage for the laser diode was 3 V and the typical operating current was 10 mA.

Supporting Information

Supporting Information is available from the Wiley Online Library or from the author.

Acknowledgements

Financial support was received from the European Commission as part of the Framework 7 ICT 2009 collaborative project HIFLEX (grant no. 248678). We would like to thank Markus Hösel and Jan Fyenbo for assistance during prototype design and integration.

Received: July 12, 2012

---

[1] C. J. Brabec, J. A. Hauch, P. Schilinsky, C. Waldauf, *MRS Bull.* **2005**, *30*, 50.

[2] R. Søndergaard, M. Hösel, D. Angmo, T. T. Larsen-Olsen, F. C. Krebs, *Mater. Today* **2012**, *15*, 36.

[3] F. C. Krebs, J. Fyenbo, D. M. Tanenbaum, S. a. Gevorgyan, R. Andriessen, B. van Remoortere, Y. Galagan, M. Jørgensen, *Energy. Env. Sci.* **2011**, *4*, 4116.

[4] N. Espinosa, R. García-Valverde, A. Urbina, F. C. Krebs, *Sol. Energy Mater. Sol. Cells* **2011**, *95*, 1293.

[5] F. C. Krebs, *Org. Electron.* **2009**, *10*, 761–768.

[6] T. Kim, S. Na, S. Oh, R. Kang, B. Yu, J. Yeo, *Sol. Energy Mater. Sol. Cells* **2012**, *98*, 168–171.

[7] Y. Galagan, B. Zimmermann, E. W. C. Coenen, M. Jørgensen, D. M. Tanenbaum, F. C. Krebs, H. Gorter, S. Sabik, L. H. Slooff, S. C. Veenstra, J. M. Kroon, R. Andriessen, *Adv. Energy Mater.* **2012**, *2*, 103–110.

[8] T. T. Larsen-Olsen, F. Machui, B. Lechene, S. Berny, D. Angmo, R. Søndergaard, N. Blouin, W. Mitchell, S. Tierney, T. Cull, P. Tiwana, F. Meyer, M. Carrasco-Orozco, A. Scheel, W. Lövenich, R. de Bettignies, C. J. Brabec, F. C. Krebs, *Adv. Energy Mater.* **2012**, DOI: 10.1002/aenm.201200079.

[9] M. Hösel, F. C. Krebs, *J. Mater. Chem.* **2012**, *22*, 15683–15688.

[10] T. T. Larsen-Olsen, R. R. Søndergaard, K. Norrman, M. Jørgensen, F. C. Krebs, *Energy Environ. Sci*. **2012**, DOI: 10.1039/C2EE23244H.

Appendix 9

Materials Views
www.MaterialsViews.com

ADVANCED ENERGY MATERIALS
www.advenergymat.de

Round-Robin Studies as a Method for Testing and Validating High-Efficiency ITO-Free Polymer Solar Cells Based on Roll-to-Roll-Coated Highly Conductive and Transparent Flexible Substrates

*Thue T. Larsen-Olsen, Florian Machui, Balthazar Lechene, Stephane Berny, Dechan Angmo, Roar Søndergaard, Nicolas Blouin, William Mitchell, Steven Tierney, Tobias Cull, Priti Tiwana, Frank Meyer, Miguel Carrasco-Orozco, Arnulf Scheel, Wilfried Lövenich, Rémi de Bettignies, Christoph J. Brabec, and Frederik C. Krebs**

Photovoltaic cells[1] based on organic and polymer materials (OPVs) are celebrated as being a possible solution to the energy needs of the future,[1b] and, with record efficiencies having breached the 10% milestone accompanied by emerging involvement from the materials industry, expectations are rapidly approaching reality.[1c] However, in order to move OPVs beyond the individual laboratory and into a generally applied setting, scientists need to limit the gap between carefully prepared hero devices and the large-scale manufacture of thousands of devices. We propose that this is done by urgently attending to the challenges of scalability and reproducibility. In this communication, we demonstrate an approach using round-robin testing as a method to validate efficiency measurements of OPVs based on semitransparent electrodes on flexible substrates, with and without indium tin oxide (ITO). ITO-free substrates were roll-to-roll coated under ambient conditions and were truly scalable. Our results demonstrate inherent uncertainties in the device-efficiency data, with variations in the carefully measured efficiency data for the same device between highly qualified laboratories as high as 25%, depending on the substrate and its active area.

Thus the concrete needs of society impose a broadening of the scientific perspective, but also a requirement for the validation and verification of reports. The view should thus be that it is no longer enough to report very high efficiency unless several independent laboratories report it. In a few instances, laboratories have obtained certified efficiency data for record devices, but, in practical terms, this efficient solution represents a bottleneck, as very few laboratories have the capacity to offer certification, and it would not be possible to certify all efficiency reports with the currently available laboratories. Instead, concerns of the validity of efficiency data and reproducibility should be tackled by employing interlaboratory studies and round robins, in an effort to gain a consensus and gradually approach standardization.[2–4]

Regarding the important issue of scalability, the average efficiency of many devices prepared by large-scale methods is unlikely to rival current record efficiencies. It has been argued that it is no longer enough to present high efficiencies, focusing on the decimals of the reported numbers, without seriously addressing which processes and which materials can reasonably be included when fabricating polymer solar cells on what will eventually be a GW_p per day scale. To do this, considerations of both the economic and environmental impact should be made.[1b] In this regard, a systematic approach to such considerations as, for example, offered by life-cycle assessments is very important at this point.[1,5–7] Such studies reveal the favorite transparent electrode material, ITO, as being the most-critical bottleneck for state-of-the-art solar cells, in terms of embodied energy and cost, inherently bound to the scarcity of indium in the Earth's crust. This fact will without doubt prohibit large-scale dissemination of polymer and organic solar cells based on ITO, which is also a brittle material that does not allow for the desired flexibility of polymer solar cells. Due to these facts,

---

T. T. Larsen-Olsen, D. Angmo, Dr. R. Søndergaard, Prof. F. C. Krebs
Department of Energy Conversion and Storage
Technical University of Denmark
Frederiksborgvej 399, DK-4000 Roskilde, Denmark
E-mail: frkr@dtu.dk

F. Machui, Prof. C. J. Brabec
Friedrich-Alexander-Universität Erlangen-Nürnberg and Bayerisches Zentrum für Angewandte Energieforschung (ZAE Bayern)
Martensstrasse 7, D-91058 Erlangen, Germany

B. Lechene, Dr. R. de Bettignies
Institut National de l'Energie Solaire
INES-RDI – Laboratoire des Composants Solaires
CEA-DRT/LITEN/DTS/LCS
50 Avenue du Lac Léman BP 332, 73377 Le Bourget du Lac, France

Dr. S. Berny, Dr. N. Blouin, Dr. W. Mitchell, Dr. S. Tierney,
Dr. T. Cull, Dr. P. Tiwana, Dr. F. Meyer, Dr. M. Carrasco-Orozco
Merck Chemicals Ltd., Chilworth Technical Centre
University Parkway
Southampton, SO16 7QD, UK

Dr. A. Scheel, Dr. W. Lövenich
Heraeus Precious Metals GmbH & Co. KG
Conductive Polymer Division (Clevios)
Chempark Leverkusen
Bldg. B202, 51368 Leverkusen, Germany

DOI: 10.1002/aenm.201200079

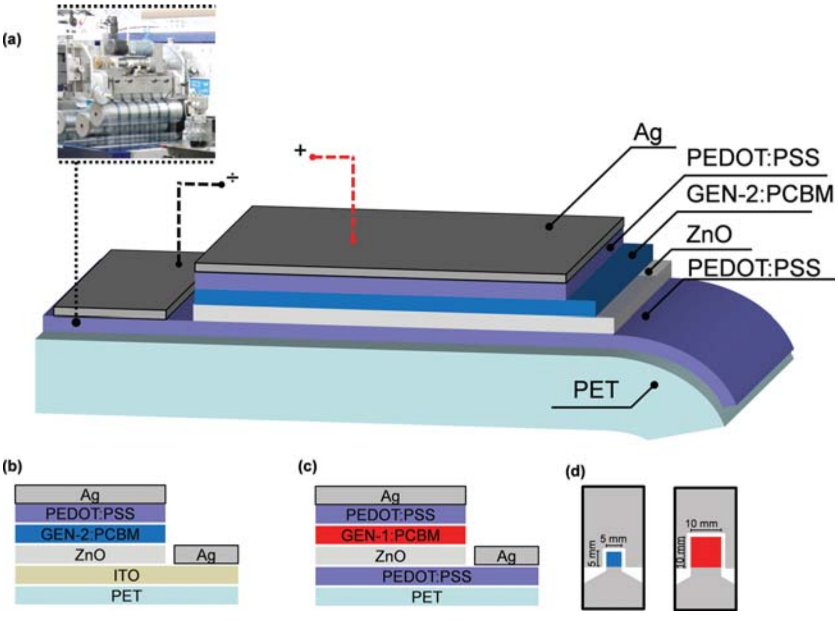

Figure 1. a–c) Graphical representation of devices A, B, and C respectively. d) Top view of the two different device layouts, of either 0.25 cm^2 or 1 cm^2.

increasing effort is being invested into finding alternatives to ITO.[8–20]

In order to contribute constructively, this communication presents how round-robin studies can be used as a simple and relatively fast tool to find consensus values of performance between several laboratories, and also to establish a good picture of how accurately reported data should be taken. We exemplify this by studying an inverted, ITO-free polymer solar cell (device A) with a layer structure shown in **Figure 1**a, based on a flexible poly(ethylene terephthalate) (PET) substrate employing a high-conductivity, high-transparency poly(3,4-ethylenedioxythiophene):poly(styrenesulfonate) (PEDOT:PSS) electrode prepared by roll-to-roll slot-die coating (Clevios PH 1000). A layer of ZnO functioned as an electron-transport (hole-blocking) layer, while the active layer is exemplified here as either a generation-1 material (i.e., a traditional material such as poly(3-hexylthiophene)) or a generation-2 material (i.e., a low-band-gap polymer such as poly(dithienodiethylhexylsilole-*co*-benzothiadiazole)) mixed with [60]PCBM. The hole-collecting electrode comprised a layer of PEDOT:PSS with evaporated Ag on top. The flexible solar cell was encapsulated between two glass slides using a UV-curable glue (DELO LP655) enabling transport between laboratories. The cell was measured at 4 different locations over a period of 7 d, which resulted in a power conversion efficiency (PCE) spanning from 2.3% to 3.1%, with no detectable degradation.

For comparison, a total of three cells were included in the round robin between the four institutions (DTU, FAU, INES and Merck), and the respective cell stacks can be seen in Figure 1a–c. Device B was the ITO-based equivalent of device A, while device C was based on the same substrate as device A, only using generation-1 material as a donor and having a larger active area (Figure 1c). In **Figure 2**a–c, we show the *J–V* curves obtained, and, as can observed, the spread is significant but consistent. Furthermore, as the “final” and “initial” Technical University of Denmark (DTU) measurements do not show significant deviation, one can rule out degradation of the cells during the round trip (**Table 1**, **Table 2**).

The standard error in the efficiency data was found to be largest with the ITO substrates (25%), smaller for ITO-free devices (13%), and smallest (5%) for the devices with a larger area (1 cm^2). The implications of this are quite significant, and unless scientists report data from many laboratories, reported efficiency values should be viewed as having a general standard error of as much as 25%, which makes comparison of the performance of next-generation materials difficult without measures such as the ones we have employed here. This implies that careful statistical analysis of many devices in a single laboratory report should be encouraged, but should by no means be considered as a validation or a qualification of an efficiency number. We ascribe the large spread in data to many factors, but most significantly to the solar simulator, which, in spite of careful calibration in each measurement, does vary with respect to the

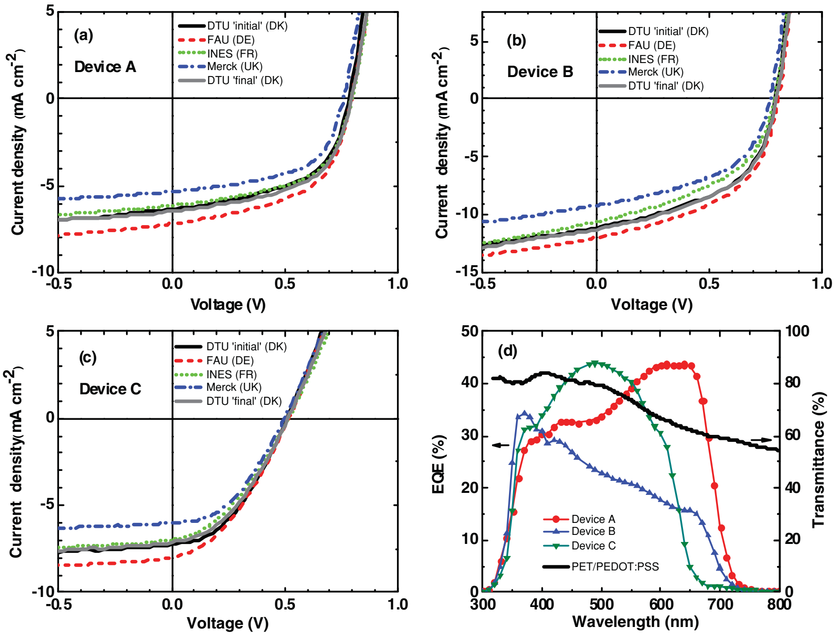

Figure 2. a–c) *J–V* curves of devices A–C respectively, obtained at 4 four different locations. d) The initial EQE of the devices, together with the transmittance of the PET/PEDOT:PSS substrate.

DOI: 10.1002/aenm.201200079

Table 1. PCE data comparison for the three devices at the four different locations.

Location/age [days after fabrication]	Device A PCE [%]	Device B PCE [%]	Device C PCE [%]
DTU "initial"/3 d	2.69	4.45	1.51
FAU/6 d	3.11	4.82	1.57
INES/7 d	2.69	3.86	1.34
Merck/8 d	2.29	3.52	1.28
DTU "final"/9 d	2.83	4.47	1.44

Table 2. Summary of the *J*–*V* data of device A.

Location/age [days after fabrication]	PCE [%]	V_{oc} [V]	J_{sc} [mA cm^{-2}]	FF [%]
DTU "initial"/3 d	2.69	0.78	− 6.33	54.2
FAU/6 d	3.11	0.80	− 7.17	54.2
INES/7 d	2.69	0.80	− 6.13	55.3
Merck/8 d	2.29	0.76	− 5.34	56.5
DTU "final"/9 d	2.83	0.80	− 6.47	55.1

diffusivity, spectral, and temporal quality of the light sources. This was done on purpose to expose additional and inherent variations in measurements of this kind. The error that can be expected from different operators was sought to be eliminated in this experiment by having an operator that travelled along with the samples, thus safeguarding them and ensuring some level of operator control from laboratory to laboratory. It should finally be emphasized that there is an urgent need for a solar simulator that can synthesize its own spectrum and calibrate itself such that comparisons of measurements and data between laboratories can be made more accurate. We estimate that an improvement by a factor of 10 in accuracy is required before independent reported data can be compared. Until we have devised light sources and equipment to achieve such accuracy, we believe that the round robin, as an experimental and low-cost tool, should be employed in general when presenting data where the efficiency or a novel device structure are the main claims of the work. Finally, we would suggest that data is reported for a large active area (≈1 cm^2 rather than ≈1 mm^2), as this was demonstrated to increase the accuracy.

Experimental Section

Slot-Die Coating: A PET substrate was slot-die coated with PEDOT:PSS (Clevios PH 1000 SCA 268-1) diluted with isopropyl alcohol in a ratio of 3:1 (v/v) at a web speed of 1 m min^{-1} with a wet thickness of 38 μm. The substrate was then passed through an oven at 140 °C for 2 min.

Device Fabrication: The final substrate, being either PET/PEDOT:PSS (device A and C) or PET/ITO (device B), was fastened to a glass substrate before being first spin-coated with 2 subsequent layers of ZnO solution[9] at a concentration of 50 mg ml^{-1} (device B: only one layer and a concentration of 25 mg ml^{-1}) at 1000 rpm for 10 s, followed by 2 min annealing at 140 °C. The active layer (generation-1 or generation-2 mixed with [60]PCBM, 15:15 mg ml^{-1}, in chlorobenzene) was then applied by spin coating at 600 rpm for 10 s. A final layer of PEDOT:PSS (Agfa Orgacon EL-P 5010, diluted with isopropyl alcohol, 2:1 w/w) was spin coated at 1000 rpm for 30 s, followed by annealing at 140 °C for 3 min. The final Ag electrode was evaporated through a shadow mask at a pressure of ≈5×10^{-6} mbar.

J–V Measurements: *J*–*V* measurements were carried out at 100 mW cm^{-2} AM1.5G equivalent conditions in four different labs. In each instance, the sun was calibrated immediately before measurement. The measurements were not corrected for differences in diffuse/direct light or mismatch.

Acknowledgements

Financial support was received from the European Commission as part of the Framework 7 ICT 2009 collaborative project ROTROT (grant no. 288565). TTLO also gratefully acknowledges financial support from the Danish National Research Foundation.

Received: February 3, 2012
Revised: March 14, 2012

[1] a) M. Jørgensen, K. Norrman, S. A. Gevorgyan, T. Tromholt, B. Andreasen, F. C. Krebs, *Adv. Mater.* **2012**, *24*, 580; b) N. Espinosa, M. Hösel, D. Angmo, F. C. Krebs, *Energy Environ. Sci.* **2012**, *5*, 5117; c) Report from UCLA/NREL: http://www.nrel.gov/news/press/2012/1801.html, accessed date: April, 2012.

[2] F. C. Krebs, S. A. Gevorgyan, B. Gholamkhass, S. Holdcroft, C. Schlenker, M. E. Thompson, B. C. Thompson, D. Olson, D. S. Ginley, S. E. Shaheen, H. N. Alshareef, J. W. Murphy, W. J. Youngblood, N. C. Heston, J. R. Reynolds, S. Jia, D. Laird, S. M. Tuladhar, J. G. A. Dane, P. Atienzar, J. Nelson, J. M. Kroon, M. M. Wienk, R. A. J. Janssen, K. Tvingstedt, F. Zhang, M. Andersson, O. Inganäs, M. Lira-Cantu, R. de Bettignies, S. Guillerez, T. Aernouts, D. Cheyns, L. Lutsen, B. Zimmermann, U. Würfel, M. Niggemann, H.-F. Schleiermacher, P. Liska, M. Grätzel, P. Lianos, E. A. Katz, W. Lohwasser, B. Jannon, *Sol. Energy Mater. Sol. Cells* **2009**, *93*, 1968.

[3] S. A. Gevorgyan, A. J. Medford, E. Bundgaard, S. B. Sapkota, H.-F. Schleiermacher, B. Zimmermann, U. Würfel, A. Chafiq, M. Lira-Cantu, T. Swonke, M. Wagner, C. J. Brabec, O. Haillant, E. Voroshazi, T. Aernouts, R. Steim, J. A. Hauch, A. Elschner, M. Pannone, M. Xiao, A. Langzettel, D. Laird, M. T. Lloyd, T. Rath, E. Maier, G. Trimmel, M. Hermenau, T. Menke, K. Leo, R. Rösch, M. Seeland, H. Hoppe, T. J. Nagle, K. B. Burke, C. J. Fell, D. Vak, T. B. Singh, S. E. Watkins, Y. Galagan, A. Manor, E. A. Katz, T. Kim, K. Kim, P. M. Sommeling, W. J. H. Verhees, S. C. Veenstra, M. Riede, M. Greyson Christoforo, T. Currier, V. Shrotriya, G. Schwartz, F. C. Krebs, *Sol. Energy Mater. Sol. Cells* **2011**, *95*, 1398.

[4] M. O. Reese, S. A. Gevorgyan, M. Jørgensen, E. Bundgaard, S. R. Kurtz, D. S. Ginley, D. C. Olson, M. T. Lloyd, P. Morvillo, E. A. Katz, A. Elschner, O. Haillant, T. R. Currier, V. Shrotriya, M. Hermenau, M. Riede, K. R. Kirov, G. Trimmel, T. Rath, O. Inganäs, F. Zhang, M. Andersson, K. Tvingstedt, M. Lira-Cantu, D. Laird, C. McGuiness, S. Gowrisanker, M. Pannone, M. Xiao, J. Hauch, R. Steim, D. M. DeLongchamp, R. Rösch, H. Hoppe, N. Espinosa, A. Urbina, G. Yaman-Uzunoglu, J.-B. Bonekamp, A. J. J. M. van Breemen, C. Girotto, E. Voroshazi, F. C. Krebs, *Sol. Energy Mater. Sol. Cells* **2011**, *95*, 1253.

[5] N. Espinosa, R. García-Valverde, A. Urbina, F. C. Krebs, *Sol. Energy Mater. Sol. Cells* **2010**, *95*, 1293.

[6] N. Espinosa, R. García-Valverde, F. C. Krebs, *Energy Environ. Sci.* **2011**, *4*, 1547.

[7] C. J. M. Emmott, A. Urbina, J. Nelson, *Sol. Energy Mater. Sol. Cells* **2011**, *97*, 14.
[8] S.-I. Na, S.-S. Kim, J. Jo, D.-Y. Kim, *Adv. Mater.* **2008**, *20*, 4061.
[9] F. C. Krebs, *Org. Electron.* **2009**, *10*, 761.
[10] S. K. Hau, H.-L. Yip, J. Zou, A. K.-Y. Jen, *Org. Electron.* **2009**, *10*, 1401.
[11] S.-I. Na, B.-K. Yu, S.-S. Kim, D. Vak, T.-S. Kim, J.-S. Yeo, D.-Y. Kim, *Sol. Energy Mater. Sol. Cells* **2010**, *94*, 1333.
[12] J.-R. Kim, J. M. Cho, W. S. Shin, W.-W. So, S.-J. Moon, *Mol. Cryst. Liq. Cryst.* **2010**, *519*, 245.
[13] B. Zimmermann, H.-F. Schleiermacher, M. Niggemann, U. Würfel, *Sol. Energy Mater. Sol. Cells* **2011**, *95*, 1587.
[14] M. Manceau, D. Angmo, M. Jørgensen, F. C. Krebs, *Org. Electron.* **2011**, *12*, 566.
[15] Y. H. Kim, C. Sachse, M. L. Machala, C. May, L. Müller-Meskamp, K. Leo, *Adv. Funct. Mater.* **2011**, *21*, 1076.
[16] Y. Galagan, J.-E. J. M. Rubingh, R. Andriessen, C.-C. Fan, P. W. M. Blom, S. C. Veenstra, J. M. Kroon, *Sol. Energy Mater. Sol. Cells* **2011**, *95*, 1339.
[17] J.-S. Yeo, J.-M. Yun, S.-S. Kim, D.-Y. Kim, J. Kim, S.-I. Na, *Semicond. Sci. Technol.* **2011**, *26*, 034010.
[18] S. Wilken, T. Hoffmann, E. von Hauff, H. Borchert, J. Parisi, *Sol. Energy Mater. Sol. Cells* **2012**, *96*, 141.
[19] R. Paetzold, K. Heuser, D. Henseler, S. Roeger, G. Wittmann, A. Winnacker, *Appl. Phys. Lett.* **2003**, *82*, 3342.
[20] J. Lewis, S. Grego, B. Chalamala, E. Vick, D. Temple, *Appl. Phys. Lett.* **2004**, *85*, 3450.

DOI: 10.1002/aenm.201200079

Appendix 10

Solar Energy Materials & Solar Cells 117 (2013) 382–389

Contents lists available at SciVerse ScienceDirect

Solar Energy Materials & Solar Cells

journal homepage: www.elsevier.com/locate/solmat

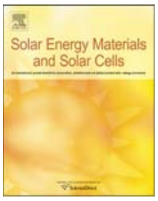

A round robin study of polymer solar cells and small modules across China

Thue T. Larsen-Olsen [a], Suren A. Gevorgyan [a], Roar R. Søndergaard [a], Markus Hösel [a], Zhouwei Gu [b], Hongzheng Chen [b], Yao Liu [c], Pei Cheng [c], Yan Jing [c], Hui Li [c], Jizheng Wang [c], Jianhui Hou [c], Yongfang Li [c], Xiaowei Zhan [c], Jiang Wu [d], Jian Liu [d], Zhiyuan Xie [d], Xiaoyan Du [e], Liming Ding [e], Chen Xie [f], Rong Zeng [f], Yiwang Chen [f], Wenwu Li [g], Ting Xiao [g], Ni Zhao [g], Fei Chen [h], Liwei Chen [h], Jun Peng [i], Wanli Ma [i], Biao Xiao [j], Hongbin Wu [j], Xiangjian Wan [k], Yongshen Chen [k], Ruibing Chang [l], Cuihong Li [l], Zhishan Bo [l], Bian Ji [m], Wenjing Tian [m], Shuanghong Chen [n], Linhua Hu [n], Sungyuan Dai [n], Frederik C. Krebs [a],*

[a] *Department of Energy Conversion and Storage, Technical University of Denmark, Frederiksborgvej 399, 4000 Roskilde, Denmark*
[b] *MOE Key Laboratory of Macromolecular Synthesis and Functionalization, State Key Lab of Silicon Materials, & Department of Polymer Science and Engineering, Zhejiang University, Hangzhou 310027, PR China*
[c] *Beijing National Laboratory for Molecular Sciences, Key Laboratory of Organic Solids, Institute of Chemistry, Chinese Academy of Sciences, Beijing 100190, PR China*
[d] *State Key Laboratory of Polymer Physics and Chemistry, Changchun Institute of Applied Chemistry, Chinese Academy of Sciences, Renmin Street 5625, Changchun 130022, PR China*
[e] *National Center for Nanoscience and Technology, Beijing 100190, PR China*
[f] *Department of Chemistry, Nanchang University, 999 Xuefu Avenue, Nanchang 330031, PR China*
[g] *Department of Electronic Engineering and Materials Science and Technology Research Centre, The Chinese University of Hong Kong, Shatin, Hong Kong SAR, PR China*
[h] *Suzhou Institute of Nano-Tech and Nano-Bionics Chinese Academy of Sciences 398 Ruoshui Road Suzhou Industrial Park Suzhou 215123, PR China*
[i] *Institute of Functional Nano & Soft Materials (FUNSOM), Soochow University, 199 Ren-Ai Road, Suzhou Industrial Park, Suzhou, Jiangsu 215123, PR China*
[j] *Institute of Polymer Optoelectronic Materials and Devices State Key Laboratory of Luminescent Materials and Devices South China University of Technology Guangzhou 510640, PR China*
[k] *Key Laboratory of Functional Polymer Materials and the Centre of Nanoscale Science and Technology, Institute of Polymer Chemistry, College of Chemistry, Nankai University, Tianjin 300071, PR China*
[l] *College of Chemistry, Beijing Normal University, Beijing 100875, PR China*
[m] *State Key Laboratory of Supramolecular Structure and Materials, Jilin University, Changchun 130012, PR China*
[n] *Key Lab of Novel Thin Film Solar Cells, Institute of Plasma Physics, Chinese Academy of Sciences, Hefei, Anhui 230031, PR China*

ARTICLE INFO

Article history:
Received 23 April 2013
Received in revised form
7 June 2013
Accepted 18 June 2013

Keywords:
Round robin
Polymer solar cells
15 Chinese laboratories
30% variation
Inherent variability

ABSTRACT

A round robin study across 15 laboratories in China was carried out using single junction devices with an active area of 1 cm^2 and differently sized small module with an active area of 20 and 24 cm^2 respectively. The devices represented the state of the art in terms of processing as they did not employ indium or vacuum and were prepared using only printing and coating techniques on flexible substrates. The devices were studied in their flexible form and thus approach the vision of what the polymer solar cell is. The main purpose of the work was to establish and chart geographic and cultural differences in what constitutes a competent *IV*-characterization procedure and also to establish the spread in measured data across the globe. The main finding is that efficiency data deviated up to 30% from the mean while an overall relative standard deviation of 12% was observed. Collating this spread with previous findings points toward a seemingly region-independent i.e. global observation of the uncertainty in the *IV*-characterization of a polymer solar cell. Finally, we highlight what might be done to improve the accuracy of the reported data.

1. Introduction

Organic photovoltaics (OPV), using either polymers [1] or oligomers [2] as light absorbing material, have now convincingly

---

* Corresponding author. Tel.: +45 46 77 47 99.
E-mail address: frkr@dtu.dk (F.C. Krebs).

0927-0248/$ - see front matter © 2013 Elsevier B.V. All rights reserved.
http://dx.doi.org/10.1016/j.solmat.2013.06.029

peaked beyond 10% power conversion efficiency (PCE) [3–5]. At the same time roll-to-roll (R2R) fabrication schemes have evolved toward encompassing true scalability, from gadgets to bulk energy production [6–9]. However, the average laboratory efficiencies, be it for either small area OPV prepared by spin coating or large area OPV prepared via R2R coating and printing methods, are still lacking significantly behind the record numbers. This has been shown neatly by Dang et al., taking a bird's eye view of selected data for the all-time favorite P3HT-PCBM blend system [10]. Thus it might seem a fact of life within the field of OPV that reproducibility is relatively poor. Two distinct factors can be said to contribute to this apparent reproducibility challenge: One is intrinsically inherent to the OPV device, coming from the myriad of parameters entering into the fabrication procedure as well as the synthesis of the materials composing the device. These variations are in a sense hidden variables due to a systematic neglect of statistics when presenting OPV efficiency data, as the current habit is that only the "hero" device is presented. The extent of the spread, however, becomes quite obvious when large PV data sets of similarly prepared devices are studied [11,12].

Another distinct factor which might be hampering the reproducibility can be said to be extrinsic. This extrinsic factor relates to the variations in the current–voltage (*IV*) characterization under simulated AM1.5G illumination conditions. Influential parameters on the extrinsic variability includes effects related to masking and defining the device active area [13], while also the type of solar simulator used, especially of course if the spectral mismatch factor is disregarded. But spectral variations might also have other unpredictable effects, depending on materials composition of interfacial layers and electrodes, such as the readily observed UV activation of ZnO [14–16]. While temporal variations in these extrinsic parameters might occur within each laboratory, the most significant variation must be inter-laboratory.

Perhaps the best way to investigate the inter-laboratory variations is through so-called round robin (RR) studies, where the same devices are measured in many laboratories. Where only a few exists for OPV [15,17], it is a technique often used within the field of inorganic PV [18–20].

In this study we employ the RR methodology to investigate the inter-laboratory variations among 14 laboratories in China and one laboratory in Denmark where the devices, a set of all roll-to-roll (R2R) -coated and -printed ITO-free devices, were fabricated [7,21]. As the number of publications on OPV coming from China today is among the highest for any country, this geographical boundary condition was an obvious choice as the high density of OPV laboratories enabled one operator to travel between each of the participating labs, ensuring that the measurements were conducted as similarly as possible, while keeping the total time of the experiment as low as possible, in order to minimize the effects of device degradation and failure.

2. Experimental

2.1. PV device preparation

The devices were prepared by R2R following the process earlier reported as "IOne" [7,21], and were based on a flexible ITO-free substrate (Flextrode [8]), upon which the inverted solar cell stack was completed, so that the entire stack was PET/Ag/PEDOT:PSS/ZnO/P3HT:PCBM/PEDOT:PSS/Ag. As shown in the schematic in Fig. 1, the devices consisted of serially connected stripes each with an active width of 1 cm. The devices were manually cut from the roll of solar cells, in three different sizes according to Table 1 and Fig. 2. Then each contact was reinforced by Cu tape. The devices were encapsulated; by manual placement of the device between two sheets of flexible Amcor® barrier foil applied with a UV-curable adhesive (DELO® LP655), then passing each device through the nip of a R2R machine ($<0.5\ \mathrm{m\ min^{-1}}$) enabling a homogeneous adhesive layer, and finally curing the devices under a UV-intense solar simulator for 5 min on each side. Electrical contacting through the encapsulation was made using nickel free button contacts [22]. Examples of the three types of final devices can be seen in Fig. 2.

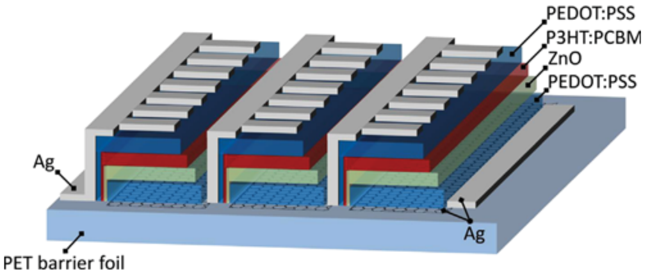

Fig. 1. A schematic drawing of the PV module stack used in this study. Three stripes in series are shown here.

Table 1
Relevant parameters of the three device types.

Device type	No. of stripes	Nom. active area (cm^2)	Cell outline
a	4	20	5-by-5 cm
b	4	24	5-by-6 cm
c	1	1	1-by-1 cm

2.2. Participating laboratories

The RR included 15 laboratories, 14 in China (one in Hong Kong), and DTU in Denmark. Details can be found in Table 2. Due to the nature of the study, all PV data will be presented anonymously.

2.3. The round robin procedure

The RR cycle was as follows: The devices were, once prepared, initially characterized at the OPV characterization lab (CLOP) at DTU. Next they were transported to China, where an operator brought them between laboratories by means of both land and air travel. At each laboratory, all the RR devices were tested according to a simple measurement protocol:

1. Each device is *IV* measured initially, keeping the illuminated time before measuring to a minimum.
2. A dark *IV* measurement is then performed.
3. The device is left under illumination for 5 min, and then a second *IV* measurement is performed
4. Followed by a final dark measurement.

Additionally, the spectrum of the solar simulator was recorded using a spectrometer (Avantes AvaSpec-3648).

At some laboratories, the size of the solar simulator only permitted correct measurement of the smaller sized **c-type** devices. The cycle was as shown in Table 3.

2.4. Long-term stability

At some laboratories a sub-study was carried out, designed to ascertain the long-term stability of the type of devices used in the RR. These laboratories have been highlighted in Table 2. In the experiments, one device was kept outdoors without exposure to

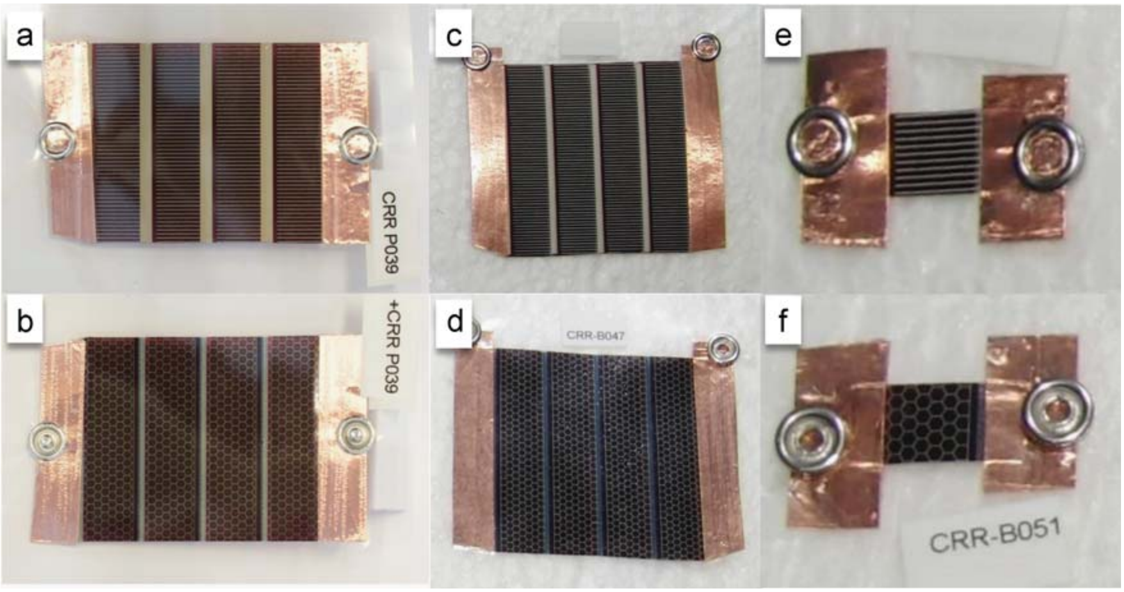

Fig. 2. The devices under study, where **a**, **c** and **e**, show the back side of devices of type **a**, **b** and **c** respectively. While **b**, **d** and **f** show the front (illuminated) side of type **a**, **b** and **c** respectively.

Table 2
List of all contributing laboratories, listed alphabetically by location. Highlighted laboratories also contributed to the lifetime round robin study.

Laboratory name	Location	Laboratory leader
BNU	Beijing, China	Prof. Zhishan Bo
ICCAS 1	Beijing, China	Prof. Yongfang Li
ICCAS 2	Beijing, China	Prof. Jizheng Wang
ICCAS 3	Beijing, China	Prof. Jianhui Hou
NCNST	Beijing, China	Prof. Liming Ding
CIAC CAS	Changchun, China	Prof. Zhiyuan Xie
JLU	Changchun, China	Prof. Wenjing Tian
SCUT	Guanzhou, China	Prof. Hongbin Wu
ZJU	Hangzhou, China	Prof. Hongzhen Chen
IPP CAS	Hefei, China	Prof. Songyuan Dai
NCU	Nanchang, China	Prof. Yiwang Chen
FUNSOM	Suzhou, China	Prof. Wanli Ma
SINANO 1	Suzhou, China	Prof. Liwei Chen
SINANO 2	Suzhou, China	Prof. Liwei Chen
NKU	Tianjin, China	Prof. Yongsheng Chen
CUHK	Hong Kong, Hong Kong SAR	Prof. Ni Zhao
CLOP DTU	Roskilde, Denmark	Prof. Frederik C. Krebs

direct sunlight (i.e. in the shade), while a control device was kept indoor in the dark. The cells where routinely measured according to the same measurement protocol used in the RR.

3. Results & discussion

3.1. *Deviations in the photovoltaic performance*

The data treatment to extract the deviations in PV performances for each device, before and after light soaking, was as follows: First the data was filtered for any unphysical anomalies. Then each PV parameter was averaged over all laboratories, from which a new average was calculated including only the data which deviated $<10\%$ from the original average. Now, the relative deviation of the raw data to this new average (μ_{10}) is calculated.

We first consider the initial measurement with respect to the RR protocol from Section 2.4, since this might be argued to be the most comparable measurement, as it best avoids effects from device temperature build-up and light-soaking.

Table 3
The RR cycle, with the anonymous laboratory number and a corresponding date of the measurement. Circulation of devices of type **a** started a month earlier than the **b** and **c** type.

Laboratory #	Data of measurement	Device types measured
1 (DTU)	05-09-2012	**a**
2	21-09-2012	**a**
3	29-09-2012	**a**
4 (DTU)	05-10-2012	**b,c**
5	14-10-2012	**a,b,c**
6	16-10-2012	**c**
7	20-10-2012	**a,b,c**
8	22-10-2012	**c**
9	25-10-2012	**a,b,c**
10	26-10-2012	**a,b,c**
11	26-10-2012	**c**
12	29-10-2012	**a,b,c**
13	29-10-2012	**a,b,c**
14	05-11-2012	**c**
15	26-11-2012	**a,b,c**
16	28-11-2012	**a,b,c**
17	30-11-2012	**a,b,c**
18	30-11-2012	**a,b,c**
19	03-12-2012	**c**
20	03-12-2012	**a,b,c**
21 (DTU)	13-12-2012	**a,b,c**

In Fig 3 the relative deviations for all devices of type **b** and **c** are shown for the different laboratories. The deviations of cell type **a** have been omitted from these plots as they showed significant signs of degradation, as shown in Section 3.3. The two highlighted laboratories in Fig. 3 used less than 1 sun intensity, 0.5 and 0.9 suns respectively. Although the deviations seen in both laboratories using lower intensity are significant and arguably at least partially due to a nonlinear light intensity dependence of the I_{sc} [23], they are not outliers as such, and are not disregarded.

The maximum and overall standard deviations are summarized in Table 4. As can be seen, the RR experiment reveals up to 30% deviation in PCE, mostly due to in the short-circuit currents (I_{sc}). Also the fill-factors (FF) show large deviations up to 15%, while the open-circuit voltages (V_{oc}) deviate the least. Such significant deviations are on par with what was found in a recent RR study [17], where also the I_{sc} was found to deviate the most. However,

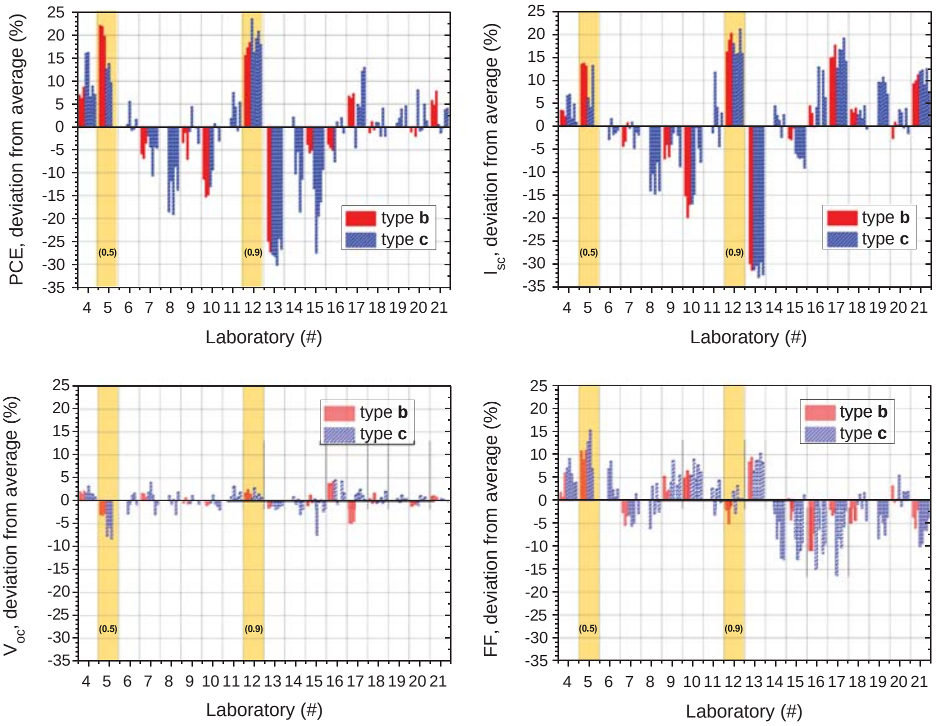

Fig. 3. Deviations in PV parameters of all devices of type **b** and **c** among the different labs, relative to the **p10** average. For each lab, the devices are shown as columns in the order; **b1**, **b2**, **b3**, **c1**, **c2**, **c3**, **c4**, **c5**. The yellow markings indicate the two labs which used less than 1 sun intensity (fraction of suns indicated in the parenthesis).

Table 4
Summarized values of deviations in PV data from 'initial' measurements relative to μ_{10} also plotted in Fig. 3, and the resulting standard deviations also plotted in Fig. 4.

Device type	Max deviation (+/− %) I_{sc} ∣ V_{oc} ∣ FF ∣ PCE	Standard deviation (%) I_{sc} ∣ V_{oc} ∣ FF ∣ PCE
Type b	20/−31 ∣ 4/−5 ∣ 11/−11 ∣ 22/−27	12 ∣ 2 ∣ 6 ∣ 12
Type c	21/−33 ∣ 5/−8 ∣ 15/−16 ∣ 24/−30	12 ∣ 2 ∣ 7 ∣ 12

from the work in Ref. [17] we anticipated that the 1 cm^2 active areas of the single cell devices used in this study would result in less deviation, but this was not found to be the case.

In Fig. 4 we plot the cumulative standard deviation across all laboratories, for each device of type **b** and **c**. It is interesting to see that the magnitude of the standard deviations are very similar across all devices, considering the very different active area outline of the **b** and **c** types (5-by-6 cm module vs. 1-by-1 cm cell respectively), as one would expect spatial inhomogeneity in the measurement plane of the light sources to impact PV variability of the larger module much more, as different stripes would be exposed to different intensities [13].

In Fig. 5 the relative deviation in PCE of all individual initial measurements are plotted in a histogram for device types **a** and **b**, showing that deviations are normally distributed around the μ_{10} mean. This confirms the validity of the standard deviations shown in Table 4 and Fig. 4.

3.2. *The effect of light soaking*

Next we consider the measurements performed after 5 min of light soaking, to ascertain its effect. In Fig. 6 the correlation between measurements performed before and after light soaking is plotted. No effect would mean random distribution around the solid line, as is seen for the I_{sc}, while a small negative effect is seen for the V_{oc} ($<2\%$). The FF on the other hand is positively affected by the light soaking with an average relative increase of 3%.

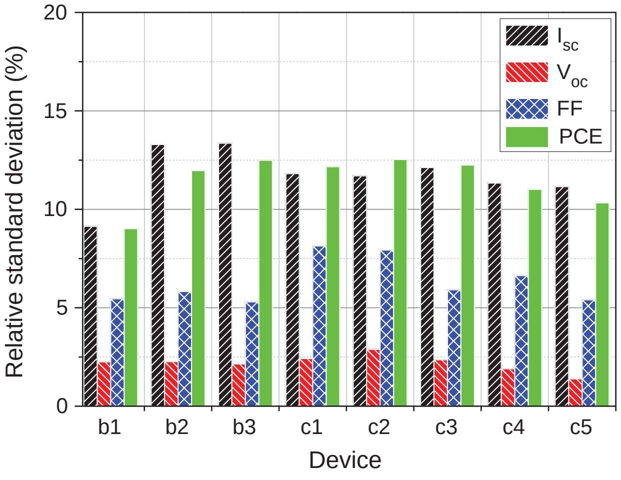

Fig. 4. The cumulative standard deviation of all PV parameters for each device.

This all-in-all gives a slight positive effect of the light soaking on the PCE, most likely linked to the increase in temperature. However, as the devices have a hole-blocking layer of ZnO, we try to investigate the possible effect of UV content of the light source.

3.2.1. *Effect of UV content*

At each laboratory the spectrum of the light source was recorded in a way that only allowed for relative comparison. The normalized spectra are plotted in Fig. 7.

From the normalized spectra shown in Fig. 7a, we calculated the relative amount of UV content (integration from 280 nm to 380 nm). From Fig. 7b it is clear that there is a significant difference in UV content among the different solar simulators, however no significant correlation was found between UV content and the effect of light soaking on the PV parameters.

3.3. Degradation during the round robin

An important factor for the success of a RR, is to be able to rule out, or at least understand, possible device degradation, so as to be able to distinguish this from the observed deviations in PV performance.

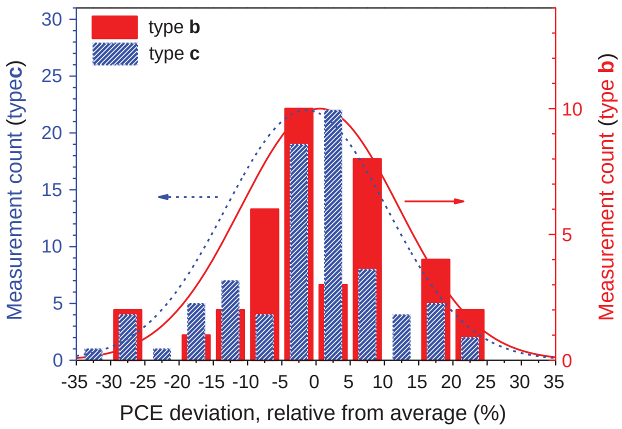

Fig. 5. Histogram over all measurements before light soaking (“initial”) for device types **b** and **c**.

In Fig. 8a we plot the difference in measured I_{sc} of the RR devices, from the initial measurement to the final one, meaning that negative current implies degradation. As all **b**- and **c**-type devices show small, positive and similar current differences, we exclude degradation of these devices, while all **a**-type devices show significant degradation. This is also seen from the plot in Fig. 8b, where the I_{sc} values have been normalized, both to the initial DTU measurement, and then to each laboratory average, as to average out the inter-laboratory deviations. This leads to the exclusion of the **a**-type devices from the RR data treatment presented in Section 3.1.

The failure of this one type of device is linked to the encapsulation procedure, which was done slightly different for the **a**-type, where the allowance of small air pockets between the barrier and solar cell gave rise to delamination in the device over time.

3.3.1. Long term stability studies

To further investigate what device stability could be expected during the RR, a selection of laboratories performed outdoor shelf-life tests on the device type used in the RR. In Fig. 9 we plot the PV parameters recorded at four laboratories in climatically different locations (climate details are listed in Table 5). Four of the five devices show less than 20% degradation in PCE during the >90 days experiment, with the degrading parameter being the I_{sc}. One device shows complete failure after 100 days, possibly due to a failure of either a contact or the encapsulation.

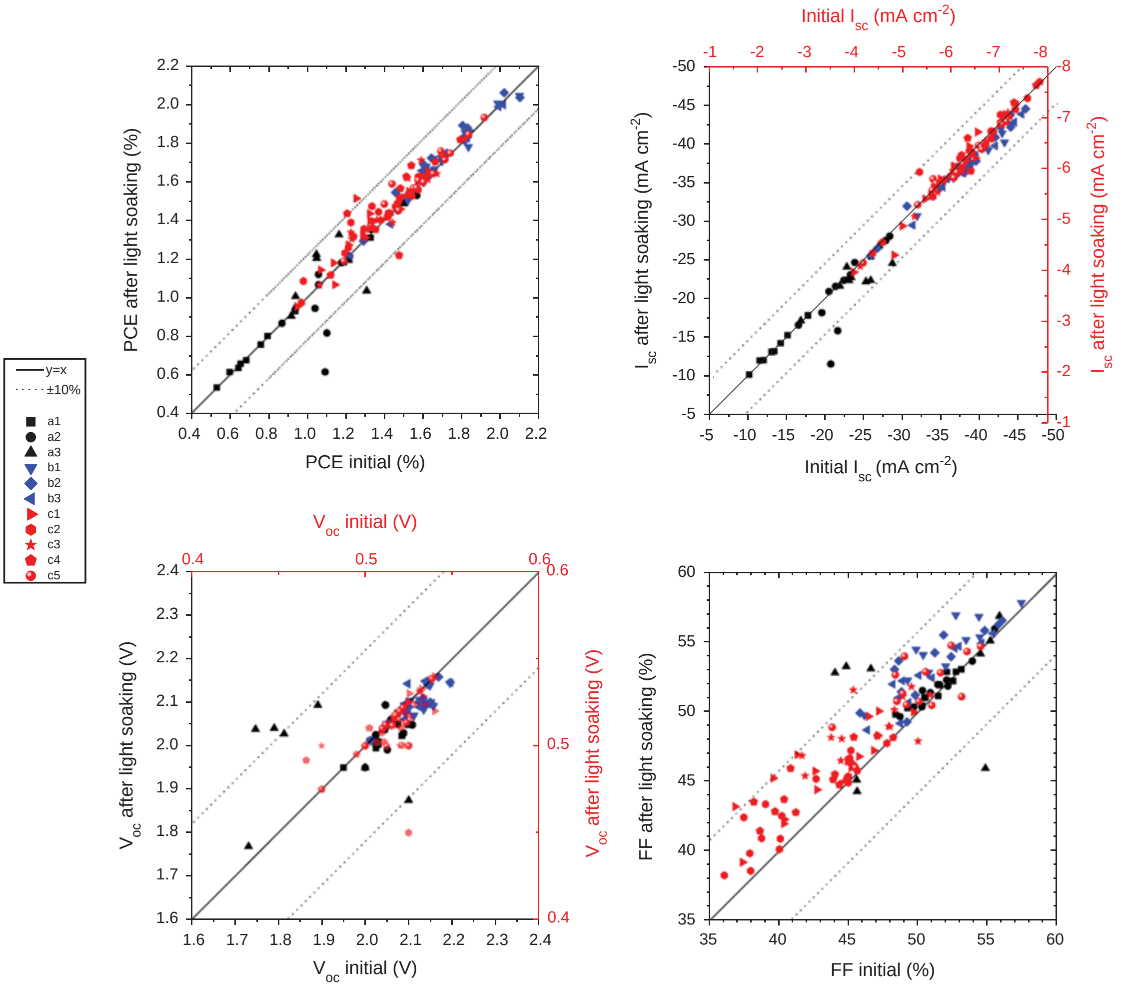

Fig. 6. Correlation plots of PV parameters before and after light 5 min soaking for all laboratories. Each symbol represents a device of either type, where type is shown by color. In the case of I_{sc} and V_{oc} the top+right scale refers to the c-type devices as indicated by the color. The solid line indicates no difference between the initial and soaked measurements, while the dotted lines indicate ± 10% of the (absolute) maximum value in the plot.

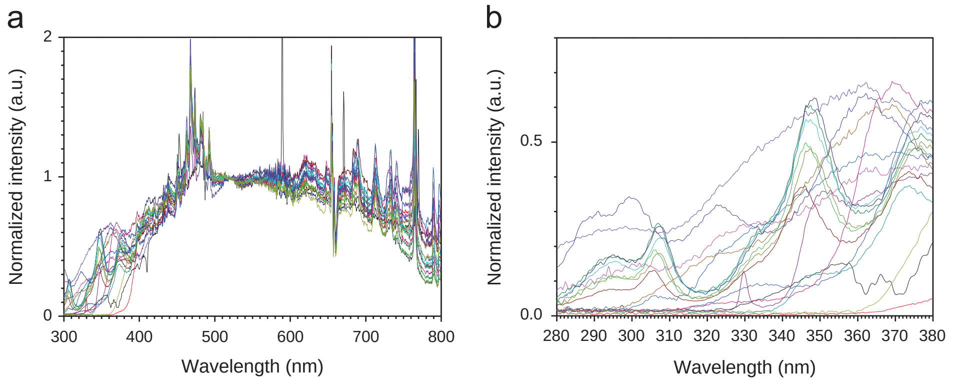

Fig. 7. (a) All light source spectra, normalized to the intensity at 520 nm, where (b) is a zoom-in on the UV relevant range used to extract the relative UV content of the different light sources.

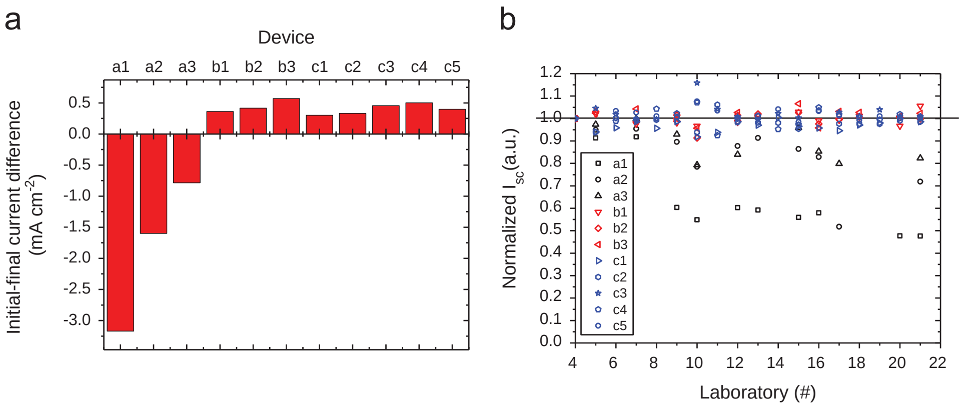

Fig. 8. (a) The difference in J_{sc} between the initial and final characterization at CLOP (DTU) for all devices. (b) The normalized I_{sc} of all devices and all laboratories (lab # proportional with time), where the data has been normalized to the average of the b- and c-type devices at the respective laboratory.

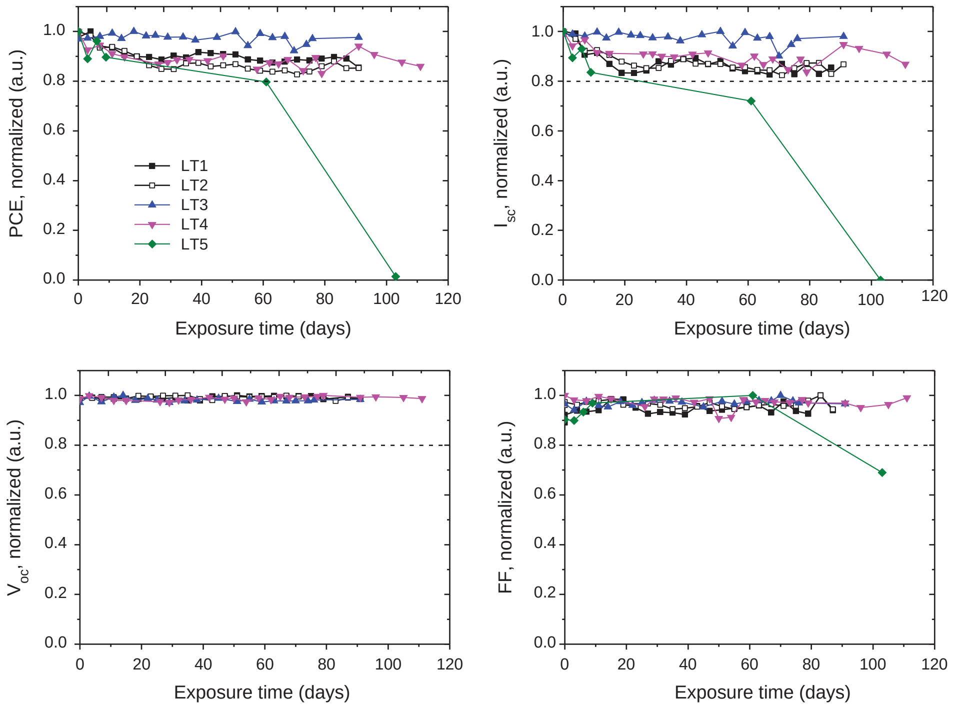

Fig. 9. Data from 3-month long outdoor stability studies at four different locations.

Because the real RR devices were only exposed to extreme temperatures (outdoor conditions) for shorter periods of time during travel, and always kept in stabilizing packaging, these outdoor test conditions represent the worst possible scenario for

Table 5
Details of the stability studies, including minimum, maximum, average temperature and average humidity, recorded in the study period. Data is taken from publically available weather sources.

Device ID (type)	Laboratory	T_{min} (°C)	T_{max} (°C)	T_{avg} (°C)	Avg. RH (%)
LT1 (b)	CIAC	−32	8	−14	72
LT2 (b)	CIAC	−32	8	−14	72
LT3 (b)	NCNST	−18	11	−4	54
LT4 (a)	ZJU	−5	31	10	65
LT5 (b)	NCU	−3	21	7	81

the RR cells. Taking this into account it seems reasonable to conclude that degradation did not contribute significantly to the observed deviations in PV parameters during the RR study, only in the case of the a-type devices which show an obvious deviation from the average trends (Table 5).

3.4. Observations and recommendations

From the results presented in Section 3.1 it is clear that the I_{sc} is the prime contributor to the inter-laboratory variations. This is indeed regardless of the fact that a reference Si-device from the solar simulator manufacture was used regularly by all labs, and most often just prior to the measurements presented here. In several instances it seemed that some error had rooted itself in the calibration procedure at the given lab. Such phenomena would be avoidable, if laboratories routinely would share and exchange their reference devices as well as experimental devices in miniature round robins [17].

Further improvements in accuracy would be given by a future convergence of measurement procedures [13], which might be led by strengthened editorial procedures regarding the reporting of solar cell efficiencies [24]. However, due to the unavoidable parameter variety among laboratories, in regards to device materials, device layouts, measurement temperature, *IV* sweep time etc., much of the observed deviation presumably cannot be avoided, and thus must be considered a standard measurement uncertainty. If we thus consider the PCE standard deviation of 12% and a 95% confidence interval, this leads to a measurement uncertainty of ±24%.

4. Conclusion

By a combined Chinese–Danish collaboration between 15 laboratories, we have conducted a round-robin study of a series of ITO- and vacuum free all R2R coated and printed polymer solar cells and small modules of different sizes. The results show large inter-laboratory variations in photovoltaic parameters obtained in the simulated AM1.5G *IV*-characterizations. Largest were the variations in I_{sc} (up to 33%) thus accounting for the largest source of observed variations in the PCE (up to 30%). The data approached a normal distribution, with resulting average standard deviations for the RR devices of 12% for PCE and I_{sc}, 6% for FF and only 2% for V_{oc}. Also the effect of light soaking was investigated, showing only a small effect on the FF and consequently the PCE. The spectral proportion of UV-light was not seen to influence the performance significantly. Based on the results and general observations, we have given some recommendations, where inter-laboratory exchange of devices and measurement data is seen as the key to improving the mutual agreement of results. All-in-all this extensive round robin study have re-confirmed the large spread in performance data observed for OPV which does seem to be specific to the OPV technology. It is of significant interest and importance to conclude that there are no significant differences between the spread in data as obtained for round robins recorded in Europe/US and as in this case China. The dawning conclusion is that the observable spread is specific to OPV and independent of geographic/cultural region. The implications are significant since they seem to be independent of the nominal performance and should therefore apply to all reported data. The certainty in any reported literature data (past or present) for OPV can thus be assumed to exhibit the significant spread that we also report here.

Acknowledgments

The Authors from DTU and ZJU acknowledge main support from the Danish National Research Foundation and the National Natural Science Foundation of China (Grant no. 51011130028), while the remaining authors acknowledge support from the NSFC (Grants nos. 51225301, 91233104, 51273193 and 50933003), the “100 Talents Program” of Chinese Academy of Sciences, the National High Technology Research and Development Program of China (863 Program), the External Cooperation Program of the Chinese Academy of Sciences under Grant no. GJHZ1220, and the National Basic Research Program of China under Grant no. 2011CBA00700.

References

[1] J. Nelson, Polymer: fullerene bulk heterojunction solar cells, Materials Today 14 (2011) 462–470.

[2] Y. Lin, Y. Li, X. Zhan, Small molecule semiconductors for high-efficiency organic photovoltaics, Chemical Society Reviews 41 (2012) 4245–4272.

[3] J. You, L. Dou, K. Yoshimura, T. Kato, K. Ohya, T. Moriarty, K. Emery, C.-C. Chen, J. Gao, G. Li, Y. Yang, A polymer tandem solar cell with 10.6% power conversion efficiency, Nature Communications 4 (2013) 1446.

[4] M.A. Green, K. Emery, Y. Hishikawa, W. Warta, E.D. Dunlop, Solar cell efficiency tables (version 41), Progress in Photovoltaics: Research and Applications 21 (2013) 1–11.

[5] Heliatek 12% Efficiency record: ⟨www.heliatek.com⟩, (n.d.).

[6] D. Angmo, T.T. Larsen-Olsen, M. Jørgensen, R.R. Søndergaard, F.C. Krebs, Roll-to-roll inkjet printing and photonic sintering of electrodes for ito free polymer solar cell modules and facile product integration, Advanced Energy Materials 3 (2013) 172–175.

[7] P. Sommer-Larsen, M. Jørgensen, R.R. Søndergaard, M. Hösel, F.C. Krebs, It is all in the pattern-high-efficiency power extraction from polymer solar cells through high-voltage serial connection, Energy Technology 1 (2013) 15–19.

[8] M. Hösel, R.R. Søndergaard, M. Jørgensen, F.C. Krebs, Fast inline roll-to-roll printing for indium–tin-oxide-free polymer solar cells using automatic registration, Energy Technology 1 (2013) 102–107.

[9] R.R. Søndergaard, M. Hösel, D. Angmo, T.T. Larsen-Olsen, F.C. Krebs, Roll-to-roll fabrication of polymer solar cells, Materials Today 15 (2012) 36–49.

[10] M.T. Dang, L. Hirsch, G. Wantz, P_3HT:PCBM, Best Seller in polymer photovoltaic research, Advanced Materials 23 (2011) 3597–3602.

[11] M.K. Riede, K.O. Sylvester-Hvid, M. Glatthaar, N. Keegan, T. Ziegler, B. Zimmermann, M. Niggemann, A.W. Liehr, G. Willeke, A. Gombert, High throughput testing platform for organic Solar Cells, Progress in Photovoltaics: Research and Applications 16 (2008) 561–576.

[12] T. Tromholt, S.A. Gevorgyan, M. Jørgensen, F.C. Krebs, K.O. Sylvester-Hvid, Thermocleavable materials for polymer solar cells with high open circuit voltage-a comparative study, ACS Applied Materials & Interfaces 1 (2009) 2768–2777.

[13] S.A. Gevorgyan, J. Eggert Carlé, R.R. Søndergaard, T.T. Larsen-Olsen, M. Jørgensen, F.C. Krebs, Accurate characterization of OPVs: device masking and different solar simulators, Solar Energy Materials and Solar Cells 110 (2013) 24–35.

[14] M.R. Lilliedal, A.J. Medford, M.V. Madsen, K. Norrman, F.C. Krebs, The effect of post-processing treatments on inflection points in current–voltage curves of roll-to-roll processed polymer photovoltaics, Solar Energy Materials and Solar Cells 94 (2010) 2018–2031.

[15] F.C. Krebs, S.A. Gevorgyan, B. Gholamkhass, S. Holdcroft, C. Schlenker, M.E. Thompson, B.C. Thompson, D. Olson, D.S. Ginley, S.E. Shaheen, H.N. Alshareef, J.W. Murphy, W.J. Youngblood, N.C. Heston, J.R. Reynolds, S. Jia, D. Laird, S.M. Tuladhar, J.G.A. Dane, P. Atienzar, J. Nelson, J.M. Kroon, M.M. Wienk, R.A.J. Janssen, K. Tvingstedt, F. Zhang, M. Andersson, O. Inganäs, M. Lira-Cantu, R. de Bettignies, S. Guillerez, T. Aernouts, D. Cheyns, L. Lutsen, B. Zimmermann, U. Würfel, M. Niggemann, H.-F. Schleiermacher, P. Liska, M. Grätzel, P. Lianos, E.A. Katz, W. Lohwasser, B. Jannon, A round robin study of flexible large-area roll-to-roll processed polymer solar cell modules, Solar Energy Materials and Solar Cells 93 (2009) 1968–1977.

[16] J. Gilot, M.M. Wienk, R.A.J. Janssen, Double and triple junction polymer solar cells processed from solution, Applied Physics Letters 90 (2007) 143512.

[17] T.T. Larsen-Olsen, F. Machui, B. Lechene, S. Berny, D. Angmo, R.R. Søndergaard, N. Blouin, W. Mitchell, S. Tierney, T. Cull, P. Tiwana, F. Meyer, M. Carrasco-Orozco, A. Scheel, W. Lövenich, R. de Bettignies, C.J. Brabec, F.C. Krebs, Round-robin studies as a method for testing and validating high-efficiency ito-free polymer solar cells based on roll-to-roll-coated highly conductive and transparent flexible substrates, Advanced Energy Materials 2 (2012) 1091–1094.

[18] H. Ossenbrink, K.. Krebs, R.V. Steenwinckel, Results of the 1984/1985 international round robin calibration summit working group on technology, growth and employment, IEEE (1985) 943–944.

[19] J. Metzdorf, T. Wittchen, K. Heidler, K. Dehne, R. Shimokawa, F. Nagamine, H. Ossenbrink, L. Fornarini, C. Goodbody, M. Davies, K. Emery, R. Deblasio, The results of the PEP'87 Round-Robin Calibration of reference cells and modules, Final Report, PTB Technical Report PTB-Opt-31, , 1990.

[20] T.R. Bets, R. Gottschalg, D.G. Infield, W. Kolodenny, M. Prorok, T. Zdanowicz, N. van der Borg, H. de Moor, G. Friesen, A. Guerin de Montgareuil, W. Herrmann, Round robin comparison of European outdoor measurement systems, in: Proceedings of the 21st European Photovoltaic Solar Energy Conference (2006) pp. 2447–2451.

[21] J.-S. Yu, I. Kim, J.-S. Kim, J. Jo, T.T. Larsen-Olsen, R.R. Søndergaard, M. Hösel, D. Angmo, M. Jørgensen, F.C. Krebs, Silver front electrode grids for ITO-free all printed polymer solar cells with embedded and raised topographies, prepared by thermal imprint, flexographic and inkjet roll-to-roll processes, Nanoscale 4 (2012) 6032–6040.

[22] F.C. Krebs, T. Tromholt, M. Jørgensen, Upscaling of polymer solar cell fabrication using full roll-to-roll processing, Nanoscale 2 (2010) 873–886.

[23] L.J.A. Koster, V.D. Mihailetchi, H. Xie, P.W.M. Blom, Origin of the light intensity dependence of the short-circuit current of polymer/fullerene solar cells, Applied Physics Letters 87 (2005) 203502.

[24] G.P. Smestad, F.C. Krebs, C.M. Lampert, C.G. Granqvist, K.L. Chopra, X. Mathew, H. Takakura, Reporting solar cell efficiencies in, Solar Energy Materials and Solar Cells, Solar Energy Materials and Solar Cells 92 (2008) 371–373.